Lawrence Berkeley Laboratory
UNIVERSITY OF CALIFORNIA

Materials & Chemical Sciences Division

Collisional Energy Transfer from Excited Nitrogen Dioxide

K.O. Patten
(Ph.D. Thesis)

May 1991

LOAN COPY
Circulates
for 4 weeks
Bldg. 50 Library.
LBL-30599
Copy 2

Prepared for the U.S. Department of Energy under Contract Number DE-AC03-76SF00098

DISCLAIMER

This document was prepared as an account of work sponsored by the United States Government. Neither the United States Government nor any agency thereof, nor The Regents of the University of California, nor any of their employees, makes any warranty, express or implied, or assumes any legal liability or responsibility for the accuracy, completeness, or usefulness of any information, apparatus, product, or process disclosed, or represents that its use would not infringe privately owned rights. Reference herein to any specific commercial product, process, or service by its trade name, trademark, manufacturer, or otherwise, does not necessarily constitute or imply its endorsement, recommendation, or favoring by the United States Government or any agency thereof, or The Regents of the University of California. The views and opinions of authors expressed herein do not necessarily state or reflect those of the United States Government or any agency thereof or The Regents of the University of California and shall not be used for advertising or product endorsement purposes.

Lawrence Berkeley Laboratory is an equal opportunity employer.

DISCLAIMER

This document was prepared as an account of work sponsored by the United States Government. While this document is believed to contain correct information, neither the United States Government nor any agency thereof, nor the Regents of the University of California, nor any of their employees, makes any warranty, express or implied, or assumes any legal responsibility for the accuracy, completeness, or usefulness of any information, apparatus, product, or process disclosed, or represents that its use would not infringe privately owned rights. Reference herein to any specific commercial product, process, or service by its trade name, trademark, manufacturer, or otherwise, does not necessarily constitute or imply its endorsement, recommendation, or favoring by the United States Government or any agency thereof, or the Regents of the University of California. The views and opinions of authors expressed herein do not necessarily state or reflect those of the United States Government or any agency thereof or the Regents of the University of California.

LBL-30599

Collisional Energy Transfer from Excited Nitrogen Dioxide

Kenneth Oliver Patten

Ph.D. Thesis

Department of Chemistry

University of California

and

Chemical Sciences Division

Lawrence Berkeley Laboratory

University of California

Berkeley, CA 94720

May 1991

This work was supported by the Director, Office of Energy Research, Office of Basic Energy Sciences, Chemical Sciences Division of the U. S. Department of Energy under Contract No. DE-AC03-76SF00098.

Collisional Energy Transfer from Excited Nitrogen Dioxide

by

Kenneth Oliver Patten

Abstract

The radiative lifetimes of gaseous nitrogen dioxide excited by pulsed, tunable dye laser radiation are determined for excitation wavelengths ranging from 400 to 750 nm. When the data are expressed in the form of zero-pressure radiative rate constants (k_0 / s^{-1}), they fit a linear equation with respect to excitation energy (X_L / cm^{-1}):

$$k_0 = (0.504 \pm 0.168)\,(X_L - X_o) + (7.96 \pm 1.82) \times 10^3,$$

given an origin energy X_o of 9,710 cm^{-1}. This fit predicts a radiative lifetime of 64 μs for 400 nm excitation and 102 μs at 750 nm. The effects of pressure, observation delay time, and wavelength range of the fluorescence detection apparatus are determined for both radiative lifetime and quenching constant.

Dispersed fluorescence spectra from excited nitrogen dioxide are analyzed into three-parameter functions that approximate the corresponding excited state population distributions. Energy transfer from nitrogen dioxide excited at 532 nm and colliding with thirteen buffer gases is studied by this population deconvolution method. The energy removal rate constant for nitrogen dioxide as a buffer gas is $(6.92 \pm 0.66) \times 10^{-8}$ cm^{-1} cm^3 $molecule^{-1}$ s^{-1}, which corresponds to (629 ± 60) cm^{-1} removed per hard-sphere collision based on a collision rate constant of 1.10×10^{-10} cm^3 s^{-1}. Neon

quenches nitrogen dioxide least efficiently among the buffer gases studied; its energy transfer rate constant of $(2.16 \pm 0.18) \times 10^{-8}$ cm^{-1} cm^3 $molecule^{-1}$ s^{-1} gives only (206 ± 17) cm^{-1} removed per hard-sphere collision for a collision rate constant of 1.05×10^{-10} cm^3 s^{-1}. The most efficient quencher is sulfur dioxide with an energy transfer rate constant of $(15.42 \pm 1.43) \times 10^{-8}$ cm^{-1} cm^3 $molecule^{-1}$ s^{-1}, or (1390 ± 130) cm^{-1} removed per hard-sphere collision when the collision rate constant is taken as 1.11×10^{-10} cm^3 s^{-1}. The energy removal rate constants increase in the order Ne < Ar < Kr < Xe < He < CO < N_2 < O_2 < NO < NO_2 < CO_2 < SF_6 < SO_2. The energy transfer rate constant is strongly correlated with the number of degrees of freedom of the buffer molecule and with low vibrational frequencies of the buffer molecule.

Population deconvolution from excited nitrogen dioxide fluorescence spectra is again employed to find energy removal rate constants for the NO_2^*-NO_2 collisions, excited by dye laser at 475.34, 435.04, and 400.00 nm. The energy transfer rate constant increases with decreasing excitation wavelength to $(32.6 \pm 2.2) \times 10^{-8}$ cm^{-1} cm^3 $molecule^{-1}$ s^{-1} at 400.00 nm, or (2960 ± 200) cm^{-1} per hard-sphere collision. The energy removal rate constant between 400 and 532 nm excitation increases as the (3.6 ± 0.4) power of the excitation photon energy.

Table of Contents

Abstract ii

Acknowledgments ix

General Introduction

Effects of Nitrogen Dioxide Properties upon

Radiative Dynamics 1

Figure Captions 4

Figures 5

1. Radiative Lifetimes of Nitrogen Dioxide for

Excitation Wavelengths from 400 to 750 nm

1.1 Introduction 7

1.2 Experimental

1.2.1 Vacuum Fluorescence Cell and Gases 10

1.2.2 Excitation and Observation Optics 12

1.2.3 Electronics and Data Collection 14

1.3 Results

1.3.1 Pressure Dependent Radiative Rate Constants 17

1.3.2 Zero-pressure Radiative Rate Constants 19

1.3.3 Stern-Volmer Quenching Rate Constants 21

1.4 Discussion

1.4.1 Zero-pressure Radiative Rate Constant 22

1.4.2 Density of States 24

1.4.3 Comparison with Previous Radiative Lifetime Measurements 26

1.4.4 Stern-Volmer Quenching Rate Constants 27

1.5 Conclusions 34

Tables 36

Figure Captions 43

Figures 47

2. Collisional Energy Transfer from Nitrogen Dioxide Excited at 532 nm

2.1 Introduction 57

2.2 Experimental Apparatus

2.2.1 Excitation and Fluorescence Collection Systems 58

2.2.2 Electronics 61

2.2.3 Gas Handling and Vacuum System 62

2.3 Data Adjustment and Fitting

2.3.1 Normalization of the Data 63

2.3.2 Method of Population Deconvolution 64

2.3.2.A The Nascent Laser-Induced Fluorescence Function 65

2.3.2.B Fitting General NO_2 Fluorescence Profiles 67

2.3.2.C Populations from Fitting Parameters 70

2.4 Results

2.4.1 Example of Interpretation: NO_2 as a Buffer Gas 74

2.4.2 Correction for NO_2^*-NO_2 Collisions in Experiments with Other Buffer Gases 80

2.4.3 Noble Gas Buffers 81

2.4.4 Diatomic Buffer Gases 83

2.4.5 Polyatomic Buffer Gases 84

2.5 Discussion

2.5.1 Comparison with Other Work 86

2.5.2 Rate Constants versus Physical Properties of Buffers 90

2.5.2.A Buffer Mass 90

2.5.2.B Permanent Dipole Moment 92

2.5.2.C Polarizability 93

2.5.2.D Unpaired Electron Association 94

2.5.2.E Internal Motions 95

2.5.3 Population Form and Mechanism of Energy Transfer 98

2.5.3.A Stepladder Model 101

2.5.3.B Exponential Model 102

2.5.3.C Biased Random-Walk Model 103

2.5.3.D The Intensity Coefficient Function Selection 104

2.6 Conclusions 107

Tables 108

Figure Captions 137

Figures 145

3. Excitation Energy Dependence of NO_2 Energy Transfer Rates

3.1 Introduction 191

3.2 Experimental Apparatus 193

3.2.1 Excitation and Fluorescence Collection 193

3.2.2 NO_2 Sample Handling 195

3.3 Results 196

3.3.1 475.34 nm Excitation 197

3.3.2 435.04 nm Excitation 199

3.3.3 400.00 nm Excitation 200

3.4 Discussion

3.4.1 Energy Removal Rate Dependence on Ensemble Average Energy 201

3.4.2 Energy Removal Rate Dependence on Excitation Energy 203

3.5 Conclusions 206

3.6 Tables 208

Figure Captions 224

Figures 226

4. References 235

Acknowledgments

The guidance of Professor Harold S. Johnston throughout these studies has been absolutely indispensable. His knowledge and insight have many times shown the meaning of the data reported here; yet, his patience and tolerance have permitted me to learn my own way. I predict that his abilities will be missed by the University of California-Berkeley upon his retirement, and am glad to know that he will continue his work on atmospheric chemistry, a vital field which requires individuals of his caliber. Despite my long educational career, I still lack an adequate vocabulary to express fully my gratitude to Professor Johnston.

My current colleagues have given much scientific and non-scientific support to this study. Joel Burley contributed considerable experimental and interpretational work to the Radiative Lifetime study (Chapter 1) and has added suggestions for presentation of the other work. Charles (Chip) Miller worked extensively on the Population Deconvolution Method (Section 2.3) to the benefit of this study as well as his own work and has also provided numerous suggestions for the interpretation of the energy transfer studies in Chapters 2 and 3. Philip Hunter has many times offered assistance with both the experimental equipment and the computational aspects of these studies. The interest by Pamela Chu of the research group of Professor Yuan T. Lee in the energy transfer experiments and her suggestions toward analysis have been directly helpful in this report. In addition, each member of the experimental

research groups of the D-Level of Hildebrand, Latimer, and Giauque Halls has loaned equipment when needed by these studies and has contributed in other ways.

Past colleagues from this research group and others have also rendered much assistance. Dr. Anthony Young, Dr. Daniel Oh, and Dr. Wade Sisk did the experimental work and initial interpretation on the nascent laser-induced fluorescence of nitrogen dioxide (Section 2.2.2) and initially demonstrated the procedures for the apparatus later used by this study. Dr. Douglas Kinnison also worked on the Population Deconvolution Method and later tutored me in the use of the Cray X/MP supercomputer at Lawrence Livermore National Laboratory in an as yet unfinished simulation of energy transfer. Dr. Bongsoo Kim introduced me to the use of the IBM 3090 mainframe computer on the campus of the University of California-Berkeley; this computer proved invaluable in the Population Deconvolution Method.

To all of the above people, I wish to offer my deepest thanks and best wishes in future work. Finally, without one individual, this work would not have existed. This individual knows well the effort and endurance required by any such scientific project and requires no further mention.

This work was supported by the Director, Office of Energy Research, Office of Basic Energy Sciences, Chemical Sciences Division of the United States Department of Energy under Contract Number DE-AC03-76SF00098. The use of the IBM 3090 mainframe was granted by University of California-Berkeley Campus Computing Funds.

General Introduction

Effects of Nitrogen Dioxide Properties upon Radiative Dynamics

The radiative dynamics and spectroscopy of nitrogen dioxide (NO_2) have held the interest of physical chemists for several generations. As one of the smallest polyatomic molecules, its radiative dynamics would be expected to serve as an intermediate case between those of diatomic molecules, which are generally well understood,[1] and those of large polyatomic molecules, which are complicated by intramolecular transitions.[2] Excited NO_2 radiative properties proved more similar to those of a large polyatomic than to those of a diatomic. This behavior of electronically excited nitrogen dioxide, NO_2^*, is exploited in this study of the radiative lifetime and of the collisional energy transfer rate constants with several buffer gases.

When NO_2 is excited by a visible laser, the resulting state is a combination of the Born-Oppenheimer electronic states illustrated in the energy diagram of Figure I-1.[3] The origins of the first excited state, $^2B_2$, and the third excited state, $^2A_2$, are known from photoelectron detachment studies,[4,5] while that of the $^2B_1$ second excited state has been found from absorption spectroscopy.[6] High vibrational levels within the $^2A_1$ state couple with the vibrational levels of the $^2B_2$ state through the Renner-Teller mechanism.[7,8] Figure I-2 illustrates the consequences of this coupling. Each highly excited vibrational level of the $^2A_1$ state obtains transition intensity through

contributions from nearby vibrational levels of the $^2B_2$ state, so that a very large number of transitions are observed in both absorption[9] and fluorescence[10,11] spectroscopy. The coupling also breaks down most quantum-mechanical transition selection rules; only total energy, total angular momentum, and symmetry selection rules are obeyed by many transitions.[12] Absorption spectra taken at room temperature consist of so many transitions as to appear continuous.[13] Spectra obtained after rotational cooling with a supersonic molecular beam[11] show large numbers of lines, though the spectra can be resolved into separate transitions. As a result of the coupling, the variation of spectroscopic constants such as rotational energy spacings among vibronic bands is considerable, and the excited state quantum numbers are assigned for only a small fraction of the total number of excited states.[10,11,14-16]

NO_2 excited to energies greater than 25,132 cm^{-1} dissociates without fluorescence.[17] NO_2 excited by photons to energies less than this always emits one photon for each photon absorbed in the absence of collisions.[18] Figure I-2 indicates that the decay rate of the fluorescence should be affected by the vibronic coupling. The $^2A_1$ component of an excited state cannot contribute to fluorescence due to symmetry, so that the $^2B_2$ contribution to the excited state determines the radiative lifetime. Studies have determined[19-23] that the radiative lifetime is more than an order of magnitude greater than that which would be expected for a pure $^2B_2$ state.[24] The $^2B_2$ contribution to a typical excited state of NO_2 is no greater than ten percent. Variations in the contribution from $^2B_2$ among excited states cause severe variation in radiative lifetimes

from one state to the next, as observed directly by molecular beam lifetime studies[25] and indirectly by gas phase studies.[23] The radiative lifetime investigation of this laboratory[23] is given in Chapter 1.

Excited states of NO_2 consist predominantly of vibrationally excited levels of the ground electronic state. NO_2^* would be expected to behave as a vibrationally hot molecule in energy transfer. NO_2^* can interact with other molecules through the Van der Waals and close-range interelectronic repulsion forces present between all molecules, through its permanent dipole moment, and through its unpaired electron. Chapter 2 presents a study of energy removal from NO_2^* excited with 532 nm light by each of thirteen buffer molecules, including NO_2. These buffers are chosen to provide a range of interaction properties. The dependence of energy removal rates upon the excitation energy of NO_2^* is explored in Chapter 3. Each of these studies utilizes the vibronic coupling of NO_2^* which obstructs state-specific experiments. The fact that total energy is conserved despite the coupling permits analysis of an ensemble containing many NO_2^* states within a small energy range X to X + dX as if it were a single state characterized by the internal energy X.

Figure Captions

Figure I-1. Energy diagram as a function of O-N-O bond angle for NO_2. Adapted from Reference 3.

Figure I-2. Illustration of the effect of vibrational-electronic interaction on the nature of NO_2 excited states.

Figure I-1

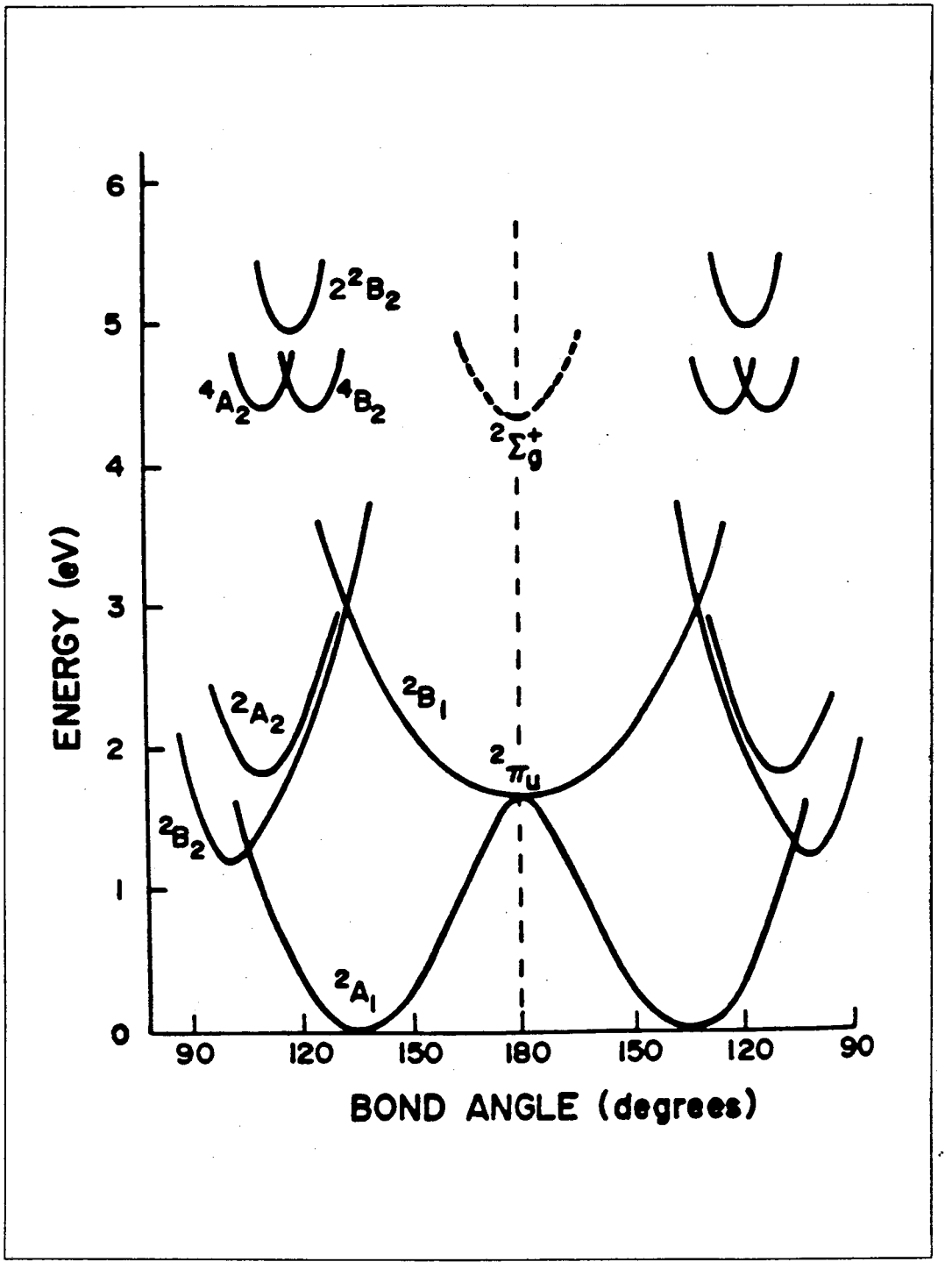
ENERGY (eV)
0
1
2
3
4
5
6
2^2B_2
$^4A_2$
$^4B_2$
$^2\Sigma_g^+$
$^2A_2$
$^2B_1$
$^2\pi_u$
$^2B_2$
$^2A_1$
90
120
150
180
150
120
90
BOND ANGLE (degrees)

Figure I-2

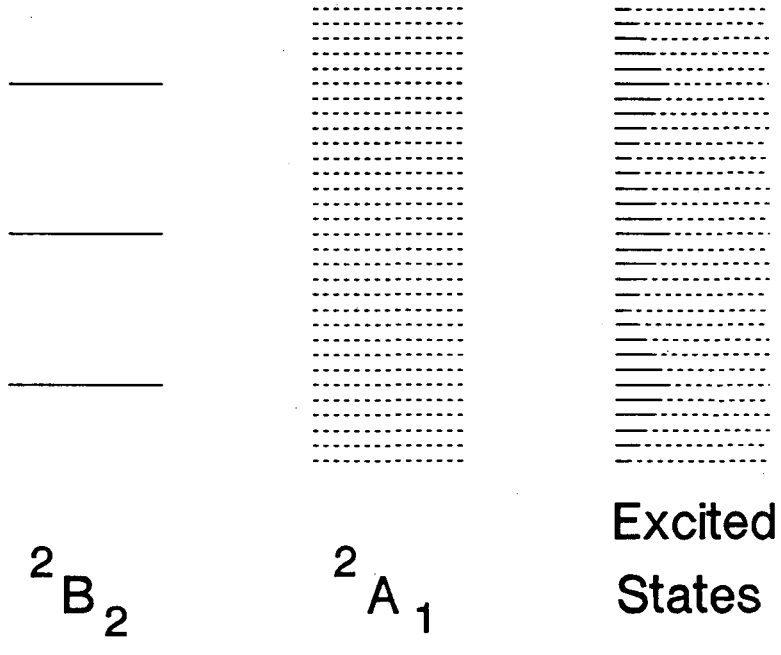

Chapter 1

Radiative Lifetimes of Nitrogen Dioxide for Excitation Wavelengths from 400 to 750 nm

1. Introduction

The radiative fluorescence lifetimes of nitrogen dioxide (NO_2) excited at visible wavelengths have been the subject of considerable research for a period spanning nearly 60 years. The first fluorescence lifetime studies were carried out by Norrish[26] and Baxter,[27] with the first direct measurement coming from Heil in 1932,[28] who obtained a lifetime of 10 μs for excitation with blue light. In a later study, Neuberger and Duncan[19] excited with a mercury line at 435.8 nm and measured a lifetime of 44 μs. Neuberger and Duncan also calculated the lifetime from the integrated absorption coefficient by the method of Mulliken[24] and obtained a value of 0.26 μs. Douglas[7] confirmed Neuberger and Duncan's experimental result and attributed the discrepancy between the measured and calculated lifetimes to coupling between vibrationally excited levels of the $^2A_1$ ground electronic state and the $^2B_2$ excited state.

Following the work of Douglas, experimental and theoretical work on this topic intensified. Keyser, Kaufman, and Zipf[29] measured the fluorescence lifetimes at 435.8, 546.1, and 578.0 nm using phase shift techniques and obtained values of 55, 58, and 53 μs, respectively. Sakurai and Broida[30] estimated a lifetime of 50 μs for

excitation at 488 nm from broadening in their fluorescence beam at low pressures. Keyser, Levine, and Kaufman[31] used phase shift techniques to obtain a lifetime of 55 μs for the range 400 - 600 nm. Sakurai and Capelle[32] used a pulsed dye laser to excite at 422, 451, and 484 nm and obtained lifetimes of 43, 41, and 42 μs, respectively. Bixon and Jortner[8] presented a quantitative theoretical formulation for Douglas' coupling hypothesis. Using a large flask for the experiment and phase shift techniques, Schwartz and Johnston[20] obtained fluorescence lifetimes which increased with excitation wavelength from a value of 55 μs at 400 nm to a value of 90 μs at 600 nm. In addition, Schwartz and Johnston pointed out the problem of restricted observation geometries, whereby observed lifetimes are shortened by collisions between the excited NO_2 molecules and the walls of the cell and by migration of excited NO_2. Sackett and Yardley[21,33,34] further examined the problem of improper observation geometry[21] and measured lifetimes which gradually increase from 70 μs near 440 nm to 82 μs near 490 nm.[33] They also measured a short component (0.5 - 3.7 μs) lifetime for excitation near 455 nm.[34] Several of the early lifetime experiments[7,29,31,32] are probably distorted by the geometric problem mentioned above.[21]

The observation of a short lifetime by Sackett and Yardley[34] indicated that some NO_2 excited states are relatively unaffected by coupling. Stevens et al.[35] measured both the resolved and unresolved fluorescence resulting from excitation at 593.45 nm. In the former case, fluorescence decays were exponential, and two distinct lifetimes of 30 and 115 μs were observed. For the unresolved case, the decay

was non-exponential and a lifetime of 60 μs was obtained. Solarz and Levy[36] determined the lifetime of one spin component of a 5_{24} rotational level of an unknown vibrational level of the $^2B_2$ excited state (488.0 nm excitation). Their linewidth measurement gave a value of less than 3.39 μs. Schwartz and Senum[37] excited at 442 nm and found a lifetime of 36 μs for the K' = 4, N' = 16 $\pm$ 1, $^2B_1$ state. Haas et al.[38] examined some K_a = 0, $^2B_1$ states (454.8 nm excitation) and obtained a lifetime of 33 μs. Hakala and Reeves[39] used ruby laser excitation at 694.3 nm and measured a lifetime of 41 μs. Uselman and Lee[17] excited in the region 399.0 to 455.0 nm and obtained lifetimes in the range of approximately 70 - 80 μs. In a series of 70-liter bulb studies, Kaufman and coworkers[22,40-42] measured NO2 radiative dynamics, observing short-term lifetimes that increased irregularly from 88 μs at 473 nm to 124 μs at 659 nm.[22]

Overall, the consensus of these many bulb and theoretical investigations is that excited states with lifetimes comparable to those predicted from the integrated absorption coefficient contribute only a small fraction to the total NO2 emission.[38] Furthermore, radiative lifetimes of NO2 are seen to vary sharply depending upon the specific state or manifold of states from which the fluorescence occurs. Molecular beam experiments performed since 1975 have confirmed this analysis. Demtröder and co-workers[43] examined the collision-free lifetimes resulting from excitation at 488.0 and 514.5 nm using a single mode argon ion laser. They observed a directly excited state with a lifetime of 1 - 3 μs, which decays into two (or more) vibronic

states with fluorescence lifetimes near 30 and 100 μs. In a later study,[25] sub-Doppler measurements by the same group revealed single exponential lifetimes which ranged from 40 to 96 μs within an 82 cm^{-1} region centered near 593 nm. This study also showed that significant differences in fluorescence lifetimes can exist between hyperfine components of the same rovibronic state. Chen et al.[44] measured fluorescence lifetimes for 18 excitation wavelengths between 572.20 and 596.57 nm, and obtained lifetimes in the range 19 - 37 μs. Cheshnovsky and Amirav[45] found lifetimes varying from 25 to 260 μs in the same interval (571 - 596 nm), and argued that the lifetimes of Chen et al.[44] were shortened by intra-beam and background collisions.

As this summary of previous work indicates, fluorescence lifetimes of excited NO2 depend strongly upon experimental parameters such as excitation light source bandwidth and the time frame for observation. Few measurements exist for wavelengths longer than 600 nm. Because of the need for (1) lifetime data obtained under conditions consistent with previous photolysis-induced fluorescence studies done in this laboratory[46,47] and (2) lifetime data for excitation wavelengths in the red, a new series of NO2 fluorescence lifetime experiments was undertaken. The results presented here were originally published by Patten, Burley, and Johnston in 1990.[23]

2. Experimental

2.1. Vacuum Fluorescence Cell and Gases

The apparatus for observation of NO2 fluorescence decay is illustrated in Figure 1-1. Nitrogen dioxide (Matheson, 99.5% purity) is initially degassed by three freeze-pump-thaw cycles at 77 K. The solid N_2O_4 (NO_2 dimer) is then vacuum distilled from a Dry Ice-isopropanol bath at approximately 203 K to a storage vial at 77 K; only the middle third of the distillate is saved for experimental use, and the resulting white solid is kept in the dark at 203 K. A 50-liter Pyrex bulb serves as the fluorescence chamber and is evacuated to less than 10^{-2} mTorr by a vacuum system consisting of a liquid nitrogen trap, a 2 inch oil diffusion pump, and a reciprocating pump (Welch Duo-Seal). The end windows of the bulb (Suprasil) are mounted at the Brewster angle of 55 degrees to the laser path and face Woods horns, and these mounts are optically isolated from the bulb by O-ring vacuum seals. The bulb gains 0.002 mTorr of pressure per minute when isolated from the rest of the apparatus. This small pressure gain has no significant effect upon the measured lifetimes. To perform an experiment, the bulb is decoupled from the vacuum system, NO_2 is admitted from the storage vial until the desired pressure is reached, and the bulb is then sealed. To permit extrapolation to the zero-pressure limit, fluorescence lifetimes are measured at eight NO_2 pressures between 0.25 and 2.0 mTorr; such a set of fluorescence lifetime measurements will be referred to as a "sequence" below. Empty bulb measurements are also performed to compensate for any fluorescence signal not due to excited NO_2. Pressures were monitored to within 0.02 mTorr using a capacitance manometer (MKS Baratron model 310BHS-1). Since the NO_2 pressure for these

experiments never exceeds two mTorr, no pressure correction for NO_2 dimerization is needed.

2.2. Excitation and observation optics

A dye laser (Lumonics Hyper-Dye 300) pumped by an excimer laser (Lumonics TE-861M: XeCl, 308 nm) is used as the source of exciting radiation. Excimer energies are measured by a calorimeter (Scientech 360001) and typically are on the order of 30 millijoules per pulse for a repetition rate of 30 Hz. Depending on the dye used, the dye laser radiates from 7 mJ/pulse at 400.00 nm to 1 mJ/pulse at 746.00 nm. It is estimated that transmission losses and reflections off of the quartz prisms used in the periscope and from the front window of the bulb reduce the laser power by approximately 50% before it reaches the NO_2 sample, except in experiments where the beam is purposely attenuated by a filter placed before the bulb. (The latter configuration is used to limit signal intensities in some of the photon counting experiments.) During installation, the manufacturer calibrated the dye laser to 0.05 nm using a neon hollow-cathode lamp and measured its linewidth as 0.8 cm^{-1}. Fluorescence is observed by a photomultiplier tube (RCA C31034, designated PMT in Figure 1-1) oriented perpendicular to the path of the laser through the cell. In order to prevent scattered laser radiation from saturating the PMT, colored glass cut-off filters (Corning and Schott) are positioned in front of the photocathode. The shortest wavelengths for which these filters transmit at least 10% are listed in Table 1-1. A

thermoelectric cooler (Products for Research TE-210TS-RF) maintains the PMT at -20°C to suppress dark noise. A high-voltage power supply (Fluke 412B) provides 800 to 1,800 volts for PMT operation, and a 40dB wideband amplifier (Analog Modules 352-1-B-1-50) coupled closely with the PMT amplifies the signal to drive the time resolution electronics.

Since NO_2 has a radiative lifetime on the order of 100 μs, care must be taken to insure that the excited molecules cannot migrate out of the photomultiplier viewing region while the decay is being observed.[20,21] For the experimental configuration used here, the primary geometric factor limiting the viewing region is the filter holder in front of the PMT. As Figure 1-2 shows, the field of view perpendicular to the laser beam (i.e. in the vertical direction in the laboratory frame) is constrained by the filter holder to an umbra half-height of 4.0 cm. At the lowest pressure employed in this experiment, 0.25 mTorr, the mean free path of NO_2 is 10 cm. Under these nearly collisionless conditions, the fraction of excited NO_2 lost to migration can be estimated by calculating the fraction of NO_2 molecules which have velocities sufficient to leave the viewing region defined by this umbra during the 60 μs observation time. The minimum velocity for this process is given by d/t, where d = 4.0 cm and t = 60 μs. Integration of the one-dimensional Boltzmann distribution (pg. 72 of Reference 48) gives the fraction of NO_2 molecules which possess velocities in excess of this value:

$$f = 2 \int_{d/t}^{\infty} \left(\frac{m}{2mkT}\right)^{1/2} e^{-\frac{mv^2}{2kT}} dv$$

$$= 0.0072 \text{ for } NO_2 \text{ at } T = 293 \text{ K.} \qquad (1\text{-}1)$$

This fraction is small enough such that any uncertainty introduced by migration of excited NO_2 out of the viewing region is negligible when compared with other sources of experimental error. The fraction of excited NO_2 lost is reduced with increasing pressure since a collision between an excited NO_2 molecule migrating outward and another NO_2 molecule will tend to send the former back into the viewing region.

2.3. Electronics and Data Collection

To obtain temporal resolution of the observed fluorescence decays, two gated measurements of the fluorescence intensity are made for each laser shot. The reference gate is held at a fixed delay of 0.7 μs after the photodiode pulse. The sample gate is scanned in 12 steps of 5.0 μs, starting at 0.7 μs. Both gates are open for 3.0 μs, during which time the fluorescence signal is either integrated using boxcars or counted with a photon counter, depending on the nature of the signal. A fast photodiode (Hamamatsu S1722-02) viewing scattered laser light and reverse-biased at 90 volts supplies the initial pulse to trigger the time resolution electronics; the pulse width is approximately 20 nanoseconds, the pulse duration of the dye laser.

For each individual time delay in a typical experiment, anywhere from 200 to 5,000 laser shots are collected at a rate of 30 Hz.

For excitation wavelengths from 400 to 580 nm, the signal from the PMT is mostly continuous (in time) and analog boxcar integration is used as the measurement technique. The PMT preamplifier output is sent to the inputs of two analog gated integrators (Stanford Research Systems SR250), one of which collects the reference signal while the other collects the sample signal. Both integrators are operated with DC coupling to prevent distortion of the decay signal. The analog voltages output by the two boxcars are digitized by an analog-digital conversion board (Data Translation DT2801A) controlled by a personal computer (IBM PC-AT) running the program BCARTAU.N2 under the ASYST programming language.[49] In these experimental sequences, no significant signal was noted for the empty bulb experiments. DC offsets are measured by deactivating the PMT high voltage and are then subtracted from the raw fluorescence signal. The computer divides the sample response by the reference response for each laser shot, and obtains the average and the standard deviation of this (I/I_0) quotient for all laser shots taken at a particular delay. The computer also digitizes pressure information and generates an analog voltage to control the sample gate delay. According to the specifications quoted by the manufacturer of the gated integrators, the time delays are accurate to $\pm 3\%$ of the maximum delay utilized (about 60 μs), which is ± 1.8 μs. This estimate of the time base uncertainty was confirmed by direct measurement with an oscilloscope (Tektronix 2245A).

For excitation wavelengths from 550 to 750 nm, the signal from the PMT typically consists of pulses from individual photons and photon counting is used as the measurement technique. For these experiments, the PMT is maintained at 1,600 volts, and the photon counter discriminators are set at 128 millivolts to eliminate radio-frequency interference and ringing after the single-photon pulses. A gated photon counter (Stanford Research Systems SR400) configures and scans the two photon counting gates in the manner outlined above. The photon counting system communicates with the personal computer via an RS-232 serial interface using driver software supplied by the manufacturer (SR465). The photon counter accumulates counts in both channels for each delay, then sends the total number of counts from each gate to the computer, where the number of sample counts is divided by the number of reference counts after subtraction of counts measured in the empty bulb experiment. The standard deviation for this (I/I_0) quotient is determined using standard counting statistics and error propagation techniques.

For the sake of comparison, both the analog boxcar and photon counter methods are used at wavelengths from 489.00 to 612.47 nm. To reduce the normally continuous fluorescence signal to photon counting levels, the laser output is attenuated either by placing a filter in front of the bulb or by partially turning off the amplifier stage of the dye laser. A comparison of these two methods is given below.

3. Results

3.1. Pressure Dependent Radiative Rate Constants

At each excitation wavelength from 400 to 750 nanometers, at least one sequence consisting of fluorescence decays for eight NO_2 pressures ranging from 0.25 to 2.0 mTorr has been obtained, as well as an empty bulb decay. For nearly all of these wavelengths, more than one sequence has been measured as a check upon reproducibility. First-order kinetics are used to model the decays:

$$I(t) = I_0 e^{-kt} \qquad (1\text{-}2a)$$

$$\ln [I(t)/I_0] = - kt = - t / \tau \qquad (1\text{-}2b)$$

where I_0 is the initial fluorescence intensity, I(t) is the fluorescence intensity as a function of time, and k is the (pressure-dependent) radiative rate constant. Data analysis is accomplished by the program ANALYZ.BCT for boxcar experiments or by the program SR4SV.PRO for photon counting experiments, each of which runs under ASYST.[49] The individual decays are each fit to Equation (1-2b) by linear least squares -- weighted by the reciprocal of the square of the standard deviation in $\ln(I/I_0)$ -- in order to obtain the rate constant k. Figure 1-3 demonstrates application of this method to analog boxcar data obtained at 455.00 nm using a CS2-73 scattered-light filter. At 2.07 mTorr sample pressure (Figure 1-3a), the fluorescence signal follows a decay plotted as a solid line with a lifetime of 67 μs. For 0.52 mTorr of NO_2 (Figure 1-3b) the best-fit lifetime is 73 μs. This increase in fluorescence lifetime with decreasing NO_2 pressure indicates that quenching collisions play a significant role

even at these low pressures. Collisions play a greater role for the decays obtained for excitation at 723.50 nm, as demonstrated in Figure 1-4. Here, the data are obtained with the photon counter and an RG780 scattered light filter. The decay at 2.03 mTorr NO_2 pressure (Figure 1-4a) gives a lifetime of 39.2 μs, and the decay at 0.26 mTorr (Figure 1-4b) gives a lifetime of 112.5 μs. Generally, the effect of collisional quenching upon the observed fluorescence lifetime increases with increasing excitation wavelength.

In order to obtain the zero-pressure limit to the fluorescence lifetime, the data are fitted in Figure 1-5 to the Stern-Volmer model for radiative decay in the presence of quenching collisions[50]:

$$A + h\nu(1) \rightarrow A^* \qquad \text{Rate} = a\,[A]\,I_1 \qquad (1\text{-}3)$$

$$A + A^* \rightarrow A + A \qquad \text{Rate} = b\,[A]\,[A^*]$$

$$A^* \rightarrow A + h\nu(2) \qquad \text{Rate} = c\,[A^*] = I_{observed}$$

In laser-flash excitation, the first step sets up the initial concentration of electronically excited molecules, $[A^*]_0$. The subsequent decay of A^* is

$$\frac{d[A^*]}{dt} = -(b[A]+c)[A^*] \qquad (1\text{-}4)$$

The integrated equation is

$$\ln\frac{[A^*]}{[A^*]_0} = -(b[A]+c)t \qquad (1\text{-}5)$$

Since the observed fluorescence is proportional to the concentration of electronically excited molecules, the integrated equations in terms of the mechanism and in terms of the empirical rate coefficients are:

$$\ln\frac{I(t)}{I(t=0)} = -(b[A]+c)t = -k_1 t$$

$$k_q\,[A] + k_0 = k_1 \qquad (1\text{-}6)$$

A plot of ln I(t) against time during one run gives the empirical first-order rate constant, k_1, and a plot of k_1 against [A] for a sequence of runs gives the slope, b = k_q, and intercept, c = k_0. The Stern-Volmer collisional quenching constant is k_q, and k_0 is the radiative rate constant at zero pressure.

3.2. Zero-pressure Radiative Rate Constants

Figure 1-5a applies this analysis to data collected with the analog collection system at 525.71 nm excitation using a CS2-73 scattered light filter. The pressure of NO_2 on the horizontal axis is proportional to NO_2 concentration. The data for the three separate sequences are seen to be nearly coincident and the solid lines representing the weighted linear least squares fits are difficult to distinguish, indicating good reproducibility. For excitation at 746.00 nm using the photon counting system and an RG830 filter, the reproducibility of the decays is not as good, as seen in the two sequences of Figure 1-5b. Table 1-2 lists the results of the fits to all sequences undertaken using the SR250 analog boxcars, and Table 1-3 lists results from fits to

sequences obtained with the SR400 photon counter. All of these radiative lifetime results are plotted logarithmically against wavelength in Figure 1-6.

The radiative lifetimes vary from under 70 μs for excitation near 400.00 nm to approximately 100 μs for excitation at 746.00 nm. Figure 1-6 shows that the lifetime generally increases with increasing excitation wavelength. Some exceptions to this trend are observed, such as the unusually low lifetimes at 612.47 nm and 673.35 nm. The apparent reproducibility of the lifetime measurement decreases abruptly for wavelengths at or above 548 nm to an extent not explained by the increase in uncertainty from the statistical error in the fits as the excitation wavelength increases. This reproducibility loss seems unrelated to the change from the analog system to the photon counting system.

Comparison of the radiative lifetimes obtained by analog time-resolution and by photon-counting time-resolution shows agreement between the two methods better than the agreement among the trials with a single system for many of the excitation wavelengths between 547.79 nm and 612.47 nm. However, for excitation from 489.00 nm to 525.71 nm, the photon counting results are consistently about 5 μs shorter than are the analog results, which is twice the standard deviation in the analog lifetimes throughout this range and thus indicates a systematic deviation between the two methods. The only experimental difference between the photon counting and analog experiments is the use of a Schott BG1 filter for attenuation in each of the sequences in question; this attenuation filter was used at no other excitation wavelength.

Figure 1-7 shows the radiative rate constants (k_0) plotted against the excitation energy (E) minus the energy of the origin (E_0) of the NO_2 $^2B_2$ state,[5] 9710 cm^{-1}, along with the best-fit line from weighted linear least squares,

$$k_0 = (0.504 \pm 0.168)\ cm\ s^{-1}\ (E - E_0) + (7.96 \pm 1.82)x10^3\ s^{-1} \qquad (1\text{-}7)$$

An attempt to fit the data to a second-order polynomial in the excitation energy produced only slightly better overall agreement, but tended to give large deviations for blue excitation wavelengths.

3.3. Stern-Volmer Quenching Rate Constants.

In addition to zero-pressure radiative rate constants, the Stern-Volmer quenching constants are obtained from the linear fit of apparent radiative rate constant to pressure. These quenching constants are also tabulated in Tables 1-2 and 1-3 and are plotted against excitation wavelength in Figure 1-8. Generally, the quenching constant increases with increasing excitation wavelength. However, for excitation wavelengths from 400.00 to 423.50 nm, the quenching constant decreases rapidly with increased excitation wavelength.

The choice of observation filter strongly affects the measured quantity interpreted as the quenching constant, as is seen in the results for 455.00 nm excitation (Table 1-4). While the lifetime result shows minimal dependence upon the choice of observation filter, the quenching constant systematically decreases from $(2.3 \pm 0.2)x10^{-11}$ cm^3 s^{-1} (464 nm filter cut-off) to $(0.43 \pm 0.05)x10^{-11}$ cm^3 s^{-1} (762 nm filter

cut-off). The quenching constant reproducibility decreases for wavelengths of 548 nm or greater, suggesting that the mechanism causing scatter in τ_0 for red excitations may also affect the quenching constant.

4. Discussion

The parameters k_1, b or k_q, and c or k_0 of the Stern-Volmer Equation (1-6) are not elementary rate constants; they are sums and averages over the complicated rovibronic states of NO_2. A formal examination of the nature of these averages is an aid in discussing the experimental results and the literature of the subject. This approach is first used to discuss the zero pressure fluorescence constant k_0, and then the formal method is extended to include fluorescence occurring in the presence of energy-transfer collisions.

4.1. Zero-pressure Radiative Rate Constant

The NO_2 molecules at room temperature are spread over a large number of rotational states. The beam of exciting light has a bandwidth of about 0.8 cm^{-1} in this case. Because of these two sources of energy spread, the initially excited molecules will involve a range of energy states i, $\{A_i\}_0$. The initial concentrations are $[A_i]_0$, and the radiative transition constants to lower energy states j are c_{ij}. The function ϕ_{ij} is defined as one if the energy of emitted fluorescence is in the range of observations, 12000 to 25000 cm^{-1}, and is zero if the emitted photon is not in this range. Aside

from instrumental factors such as solid angle considerations and optical efficiencies, the observed radiation is represented by the double summation over initial and final states of the initial state concentrations multiplied by the molecular fluorescence rate constant and the observability factor ϕ_{ij}:

$$I_{obs} = \sum_j \sum_i \phi_{ij} c_{ij} [A_i]_0 \tag{1-8}$$

This equation may be multiplied on the right by $1 = [A^*]_0/\Sigma_i [A_i]_0$. The actual, non-equilibrium distribution function for electronically excited molecules is $P_i = [A_i] / [A^*]$. The observed fluorescence may be interpreted as follows:

$$I_{obs} = k_0[A^*]_0 = \sum_j \sum_i \phi_{ij} c_{ij0} P_i [A^*] = [A^*] \sum_j \langle \phi_{ij} c_{ij} \rangle_i^{ave} \tag{1-9}$$

Note that k_0 is obtained from a sum over the final states j of the observed average fluorescence rate constant, where the average is taken over the initial excitation distribution.

$$k_0 = \frac{1}{\tau_0} = \sum_j \langle \phi_{ij} c_{ij} \rangle_i^{ave} \tag{1-10}$$

4.2. Density of States.

The energy spacings between the NO_2 states included in the summations of Equations (1-8) to (1-10) must be considered. Calculation of the density of states by the method of Whitten and Rabinovich[51] yields 0.088 vibronic states per cm^{-1} for NO_2 excited to 15,000 cm^{-1} above the ground state, and 0.149 states per cm^{-1} for 20,000 cm^{-1} excitation. Fluorescence excitation spectra taken by Smalley, Wharton, and Levy[10] reveal 140 vibronic states within the excitation interval of 570.8 to 670.8 nm, corresponding to an overall density of vibronic states of 0.054 per cm^{-1} for this spectral region. Absorption spectra from Hsu, Monts, and Zare[9] contain some 18,000 rovibronic peaks within the excitation range of 553 to 648 nm, resulting in a net density of states of 6.8 per cm^{-1}. The state-specific fluorescence lifetime study of Persch, Vedder, and Demtröder[25] lists 28 rovibronic levels within the range 16,810.772 - 16,946.521 cm^{-1}; this yields a density of states of 0.206 per cm^{-1} for this excitation range. Persch and coworkers also observe that several closely spaced rovibronic levels within this energy interval have lifetimes which differ by as much as a factor of two. For example, using the vibronic origin labels of Smalley, Wharton, and Levy,[10] the $5_{0,5}$, S = +1/2 hyperfine component of band 101 and the $9_{0,9}$, S = +1/2 hyperfine component of band 99 (located within 0.5 cm^{-1} of each other) have respective lifetimes of 94.5 and 48.5 μs. Donnelly, Keil, and Kaufman[41] state that above 570 nm "there are regions where closely spaced levels have substantially different radiative lifetimes".

Since the reproducibility of the laser wavelength is estimated by the manufacturer to be on the order of one bandwidth (0.8 cm^{-1}), it is reasonable that lifetime sequences measured at what is nominally the same excitation wavelength will in fact correspond to slightly different excitation energies. Thus, possibly significant shifts in the set of NO_2 rovibronic states produced by the initial laser excitation could result, such that two sequences at the "same" wavelength could give very different lifetime results. For those cases where coupling between different NO_2 rovibronic states is strongest (i.e. for shorter excitation wavelengths[41]), the different sets of states initially produced would have more similar radiative lifetimes. This is partly because the radiative lifetimes of strongly coupled states are usually similar to one another and partly because more states are included in the band of excited states accessed by the laser at higher energies (due to the increasing density of states). For those cases where coupling between different NO_2 rovibronic states is relatively weak (i.e. for longer excitation wavelengths[41]), the different sets of states initially produced could have quite dissimilar lifetimes. Thus, the apparent lack of reproducibility between sequences at the "same" wavelength would be expected to increase with increasing excitation wavelength, as is observed experimentally. If the excitation laser used in this study had the same wavelength reproducibility but a markedly wider bandwidth, then it is expected that the observed lifetimes would have had better overall reproducibility.

4.3. Comparison with Previous Radiative Lifetime Measurements

The present results (Figure 1-6) agree semi-quantitatively with those of Sackett and Yardley,[33] who observed a somewhat smaller increase in the lifetime over the range 440 to 490 nm than is observed here. Uselman and Lee[17] also obtain lifetimes in approximate agreement with the present values for the range 399 - 455 nm, but their data rise more rapidly with increasing wavelength than do the current values. Since Uselman and Lee used different excitation wavelengths and different pressures (15.8 - 50 mTorr) in their Stern-Volmer extrapolation, direct comparisons are difficult. Hakala and Reeves' value[39] of 41 $\pm$ 4 μs for excitation at 694.3 nm disagrees markedly with the current values of 90 and 141 μs. Since this wavelength region is where there are large state-to-state differences in radiative lifetimes and Hakala and Reeves' used an extremely narrow bandwidth (0.006 nm) ruby laser, it is probable that the two experiments were exciting different states. The short-term (τ_s) results of Donnelly and Kaufman[22,40] for wavelengths between 473 and 659 nm are in generally good agreement with the present measurements:

Ref.	λ/nm	τs/μs	Present	λ/nm	τs/μs
22	593.49	71	count	585.4	80
	593.67	75		593.4	105
	612.32	46		612.47	55
23	473.	88	analog	473.99	78
	526.	93		525.71	90
	558.	123		558.00	110
			count	558.00	100
	659.	124		656.20	115

4.4. Stern-Volmer Quenching Rate Constants

The full Stern-Volmer mechanism can be illustrated by a formal analysis using the "stepladder model".[20,41] In this discussion, the index j goes over all states from the highest excited state to the lowest energy level of the molecule. For any value of j, the index i represents all states with energy greater than ϵ_j, and the index k represents all states with energy less than ϵ_j. If one ignores (for this discussion) the concept of time indicated as the abscissa, one can identify some features of this model with Figure 1-9. Seven patterns show 7 values of j including the initial excitation energy of 24,000 cm^{-1}, and a dashed line shows the energy at 12,000 cm^{-1}. When j represents the energy level of 20,000 cm^{-1}, for example, one thinks of all collisions from states i above j that transfer molecules down into j = 20,000 cm^{-1}, and one thinks of all collisions that transfer molecules in state j to any state k below 20,000 cm^{-1}. Also, one thinks of all fluorescence from state j to lower energy states k, down to zero energy of the molecule. Those transitions at wavelengths below the cut-off limit of the detector (formally indicated in these derivations by zero value of ϕ_{jk}) are filled with a solid pattern in Figure 1-9. The detailed Stern-Volmer mechanism and various rate terms are:

$A + h\nu_1$	$\rightarrow A_i$	$a\,[A]$
$A + A_i$	$\rightarrow A + A_j$	$b_{ij}\,[A]\,[A_i]$
$A + A_j$	$\rightarrow A + A_k$	$b_{jk}\,[A]\,[A_j]$
A_j	$\rightarrow A_k + h\nu_2$	$c_{jk}\,[A_j]$

With this mechanism, the rate of change of any selected state j is

$$\frac{d[A_j]}{dt} = \sum_{i>j} b_{ij}[A][A_i] - \sum_{k<j} (b_{jk}+c_{jk})[A_j] \qquad (1\text{-}11)$$

The rate of observed fluorescence is

$$I_{obs} = k_1[A^*] = \sum_j \sum_{k<j} \phi_{jk} c_{jk} [A_j] \qquad (1\text{-}12)$$

$$= [A^*] \sum_j \sum_{k<j} \phi_{jk} c_{jk} P_j \qquad (1\text{-}13)$$

In principle, Equations (1-11) are to be solved for the time-dependent concentrations of excited molecules A_j and substituted in (1-12) to give the lifetime:

$$\tau^{-1} = \sum_j \sum_{k<j} \phi_{jk} c_{jk} P_j \qquad (1\text{-}14)$$

Figure 1-9 can be interpreted in another way. If the rate of collisions is fast relative to rate of fluorescence, the figure gives a zero order model for deactivation by collision as a function of time for molecules initially excited to 24,000 cm^{-1}. With this step-ladder model the initial spread of excited energies is lumped into one level, and (for purposes of illustration) every collision is assumed to remove 2000 cm^{-1} of energy, so that each consecutive pattern in Figure 1-9 represents the situation after

another collision. The photomultiplier is assumed to have uniform quantum response from 24,000 to 12,000 cm^{-1} and zero response at lower energies. The observable fluorescence from 24,000 cm^{-1} is shown to terminate at 7 electronic ground-state energies between 0 and 12,000 cm^{-1} by the first pattern at time zero in Figure 1-9, and this pattern corresponds to 7 values of the index k in Equation 1-13. The letters B, G, and R refer to the colors blue, green, and red. Between zero and time 1 (arbitrary units) in Figure 1-9, a deactivating collision reduces the energy of the excited molecules to 22,000 cm^{-1}. The highest energy of fluorescence, that terminating at zero energy, is 22,000 cm^{-1}. The emission channel terminating at 12,000 cm^{-1} now has a photon energy of only 10,000 cm^{-1}, so that it is not detected by the photomultiplier (ϕ_{jk} is zero). The number of observable emission channels has decreased from 7 to 6. With each unit of time, a collision reduces the energy of the excited molecules by another 2000 cm^{-1}, and a high energy channel becomes no longer possible and another low energy channel falls below the detectivity threshold of the photomultiplier. The numbers across the top of Figure 1-9 correspond to the number of observable fluorescence channels. Other things being equal, it may be assumed that the observed rate of fluorescence from the 7 patterns in Figure 1-9 is proportional to the number of observable channels. It requires 3.5 time units for half of the initial set of open channels to close, but only 1 unit of time for the open channels at 14,000 cm^{-1} to decrease by one-half. Over a long time frame, the apparent rate constant of fluorescence would increase with time. Figure 1-9 does not

show the time-dependent reduction of population of excited molecules due to radiative emission, but it emphasizes the time-dependent reduction of the number of observable fluorescence channels as a function of collisional deactivation. The qualitative features of this analysis should still apply if a more realistic model is used.

The patterns in Figure 1-9 may be interpreted in yet another way (Donnelly, Keil, and Kaufman discussed a similar point[41]): they represent six pairs of initial excitations at different laser energies followed by the collision-modified situation one unit of time later. As one approaches the zero-pressure limit of the Stern-Volmer plot, the degree of collisional energy reduction is more nearly represented by successive pairs of patterns in Figure 1-9 than by the entire sequence. As a zero order approximation, the observable effect of collisional deactivation is given by the change in number of observable channels for fluorescence. The effective quenching rate constant may be estimated as

$$k_q[A] = \frac{1}{\tau} \ln \left\{ \frac{\textit{channels observable at } t = 0}{\textit{channels observable at } t = t} \right\} \qquad (1\text{-}15)$$

By this model, the relative values of the quenching constant k_q as a function of energy of excitation for the cases in Figure 1-9 are:

Excitation energy/1000 cm^{-1}	Relative k_q
24	1.0
22	1.2
20	1.4
18	1.9
16	2.6
14	4.5

This variation in k_q is the same order of magnitude as the change observed between 450 and 746 nm in Figure 1-8. For a given assumed energy-transfer model and rate constants, this analysis shows that one may observe a wide range of apparent quenching rate constants, depending on the wavelength of excitation. A corollary of this discussion is that the observed quenching rate constant could depend on the pressure range of observations or the duration of observations. For example, at a low pressure the usual first-order rate plot might appear linear (within experimental scatter) both for observation times {1, 2, 3, 4 μs} and {10, 20, 30, 40 μs}, but the slopes might differ (Figure 1-9; Equation 1-15).

The reverse of the trend discussed above is seen for excitation energies above 24,000 cm^{-1} (Figure 1-8). The initial vibrational-electronic energy distribution of excited molecules is not a single energy as indicated by Figure 1-9, but rather it is spread about 1,000 cm^{-1} in either direction by facile rotational-vibrational energy exchange under collisions.[17,41] This rotational energy, which is present, can be converted into vibrational energy in the dissociative reaction coordinate, so that the observed fluorescence lifetime is shortened by NO_2 dissociation. As was previously explained by Uselman and Lee,[17] the probability of this conversion increases as the

excitation energy approaches the dissociation limit of 25,132 cm^{-1}. This effect qualitatively explains the increase of apparent quenching rate constant below 420 nm in Figure 1-8.

For excitation at 455 nm and otherwise identical conditions, Table 1-4 shows a six-fold decrease in the apparent quenching rate constant, as the cut-off point of the scattered filter increases from 464 nm to 762 nm. Figure 1-10 provides a qualitative explanation of this filter effect. It is the same as Figure 1-9 except that a filter has been added to remove the three bluest bands of fluorescence. As the next three patterns indicate, collisions bring high energy excited molecules from the source hidden by the filter into the observation window at the same rate as collisions remove excited molecules from the red end of the observation window. The number of observable channels remains constant between 0 and 3 time units in Figure 1-10. The duration of this constancy of initial number of observable channels increases as the wavelength of the filter cut-off is changed to the red, accounting for the decrease in k_q observed with the redder filters (Table 1-5). There will still be a decrease of fluorescence with time as fluorescence reduces the population of excited molecules, but the observable effect of collisional deactivation is masked for various lengths of time, depending on the width of blue light cut off by the filter. The wavelength sensitivity of the light detector and the shape of its long-wavelength fall-off to zero will also affect the observed quenching rate constant in an analogous fashion.

These remarks about experimental difficulties in making interpretable measurements of quenching rate constants apply to systems where the detector covers a wide but not complete range of wavelengths. There are still some difficulties with dispersed radiation or observations of fluorescence at narrow wavelength bands. Figure 1-9 may be used to illustrate one such difficulty. If fluorescence is excited by blue light and observed as green light through a monochromator, the physical transition (upper state and lower state) changes as deactivating collisions lower the energy of the excited molecules (successive panels in Figure 1-9). The constant wavelength of observation therefore does not correspond to a constant observed physical process.

From these considerations of the effects of excitation wavelength, filters, detectors, pressures, and times used in the experiment, there may be little reason to expect our quenching rate constants to agree with those of other investigators, and in general they do not. Keyser, Levine, and Kaufman[31] obtained a vibrational quenching constant of 3.9×10^{-10} cm^3 s^{-1} for excitation wavelengths of 405, 436, 546, and 578 nm, which is more than a factor of three larger than our quenching constants for 579.60 nm excitation, (0.79 and 1.07) $\times 10^{-10}$, and their value appeared to be independent of excitation wavelength. Their quenching constants were distorted by the small size of the fluorescence cell, wall collisions, and small viewing region.[20,21] Later, Donnelly, Keil, and Kaufman[41] gave an extensive report of fluorescence quenching using a 70-liter bulb, pressures down to 0.01 mTorr, and dispersed fluorescence. At 532 nm

(Nd-YAG laser), for example, they found two quenching rate constants, 5.9×10^{-10} cm^3 s^{-1} for up-and-down rotational energy transfer, and 1.1×10^{-10} for vibrational deactivation according to a step-ladder model. In our experiments at 538.3 nm, which observed undispersed fluorescence at all energies down to about 12,000 cm^{-1}, the apparent quenching constant is 0.44×10^{-10}. Our method would not be expected to see the fast redistribution of rotational states, since these states retained about the same average energy before and after collisions and remained in the observation window. Hakala and Reeves[39] report a quenching rate constant of 0.57×10^{-10} cm^3 s^{-1} for excitation at 694.3 nm with a ruby laser. The corresponding quenching constants from this experiment, $(1.32 \text{ and } 2.16) \times 10^{-10}$, are a factor of two to four larger. Uselman and Lee[17] report quenching constants averaging 0.44×10^{-10} cm^3 s^{-1} for excitation wavelengths from 399 to 460 nm with minimal wavelength dependence; we find a decreasing trend from $(0.6 \text{ to } 0.14) \times 10^{-10}$ between 400 and 423.5 nm, which we interpret as dissociation induced by rotational-to-vibrational energy conversion.

5. Conclusions

Nearly nascent radiative rate constants of NO_2 have been found to increase linearly with increasing excitation energy (cm^{-1}) for excitation wavelengths from 400 to 750 nm according to the equation,

$$k_0 = (0.504 \pm 0.168) \text{ cm s}^{-1} (E - E_0) + (7.96 \pm 1.82) \times 10^3 \text{ s}^{-1}.$$

Scatter in the data is small for wavelengths below 548 nm, but becomes large at longer wavelengths. This scatter is attributed to the high sensitivity of NO_2 fluorescence lifetimes to the specific ensemble of rovibronic levels accessed by the excitation radiation. The present results are found to be in fair agreement with a number of previous measurements.

In general, Stern-Volmer collisional quenching rate constants are found to be strongly dependent on experimental conditions, such as bulb size, filters used, duration of observations, the wavelength sensitivity of the detector, and the excitation wavelength. These instrumental perturbations of the quantity measured are so great that most Stern-Volmer quenching rate constants in the literature are strongly affected by them, including those of this article. For near-nascent excited NO_2, we have observed these quenching constants to increase with decreasing excitation energy (except near the 398 nm dissociation threshold); this increase is attributed mostly to the long-wavelength cut-off of the detection system. Near the dissociation limit, the apparent quenching rate increases with increasing excitation energy due to fast collisional conversion of rotational energy (present in the ground-state NO_2 before excitation) to energy in the dissociation coordinate. The present Stern-Volmer quenching constant results are found to be in disagreement (sometimes high and sometimes low) with a number of previous measurements.

Table 1-1

Colored Glass Filters Used in Fluorescence Detection

and Blue-Wavelength Limits for 10% Transmittance

Filter	10% Limit
GG475	464
CS2-73	569
CS2-62	605
RG645	633
RG9	713
CS7-69	724
RG780	762
RG830	811

Wavelengths for cut-off are interpolated from manufacturer specifications (Corning for CS filters, Schott for all other filters) and should be considered accurate to ± 3 nm.

Table 1-2

NO_2 Radiative Lifetimes (τ_0 / μs) and Collisional Quenching Constants (k_q /10^{-10} cm^3s^{-1}) Acquired with SR250 Analog Boxcar Integrator System. Uncertainties of one standard deviation are given.

λ, nm	Filter	τ_0			k_q		
400.00	GG475	68.3	±	2.0	.595	±	.018
400.00	GG475	64.4	±	1.9	.575	±	.050
405.20	GG475	66.4	±	1.9	.421	±	.022
405.20	GG475	68.0	±	2.0	.422	±	.013
415.00	GG475	66.2	±	1.9	.304	±	.015
415.00	GG475	67.1	±	2.0	.309	±	.009
417.50	GG475	66.2	±	1.9	.161	±	.012
423.50	GG475	68.9	±	2.0	.169	±	.009
423.50	GG475	68.1	±	2.0	.140	±	.015
434.80	GG475	67.5	±	2.0	.198	±	.010
434.80	GG475	67.4	±	2.0	.179	±	.009
444.80	GG475	67.1	±	2.0	.212	±	.025
444.80	GG475	67.8	±	2.0	.185	±	.009
455.00	GG475	75.9	±	2.2	.254	±	.015
455.00	GG475	71.1	±	2.1	.215	±	.024
455.00	CS2-73	80.6	±	2.4	.178	±	.011
455.00	CS2-73	78.7	±	2.3	.094	±	.014
455.00	CS2-73	77.0	±	2.3	.174	±	.015
455.00	RG645	77.4	±	2.3	.105	±	.004
455.00	RG780	79.0	±	2.3	.043	±	.005
463.20	CS2-73	73.6	±	2.2	.154	±	.006
463.20	CS2-73	72.0	±	2.1	.155	±	.012
473.99	CS2-73	78.5	±	2.3	.227	±	.022
473.99	CS2-73	77.8	±	2.3	.209	±	.016
473.99	CS2-73	76.1	±	2.2	.223	±	.013
474.35	CS2-73	79.9	±	2.3	.199	±	.013
474.35	CS2-73	79.7	±	2.3	.233	±	.007
479.09	CS2-73	83.3	±	2.5	.198	±	.015
479.09	CS2-73	85.8	±	2.5	.256	±	.010
479.09	CS2-73	79.2	±	2.3	.217	±	.022
479.09	CS2-73	83.1	±	2.4	.209	±	.006
479.09	CS2-73	84.0	±	2.5	.165	±	.005

Table 1-2 continued

λ, nm	Filter	τ_0			k_q		
489.00	CS2-73	76.4	±	2.2	.278	±	.018
489.00	CS2-73	78.6	±	2.3	.192	±	.008
489.00	CS2-73	78.6	±	2.3	.288	±	.012
494.80	CS2-73	77.2	±	2.3	.283	±	.022
494.80	CS2-73	78.1	±	2.3	.270	±	.010
496.09	CS2-73	84.6	±	2.5	.290	±	.009
504.70	CS2-73	84.1	±	2.5	.355	±	.011
504.99	CS2-73	81.9	±	2.4	.332	±	.014
504.99	CS2-73	80.6	±	2.4	.327	±	.016
504.99	CS2-62	84.1	±	2.5	.262	±	.022
512.64	CS2-73	85.0	±	2.5	.342	±	.011
512.64	CS2-73	80.9	±	2.4	.395	±	.015
525.71	CS2-73	90.1	±	2.7	.419	±	.016
525.71	CS2-73	90.8	±	2.7	.425	±	.013
525.71	CS2-73	90.1	±	2.7	.410	±	.012
538.30	CS2-73	97.2	±	2.9	.469	±	.014
538.30	CS2-73	96.1	±	2.8	.467	±	.014
547.79	CS2-73	85.4	±	2.5	.533	±	.023
547.79	CS2-73	84.3	±	2.5	.706	±	.022
547.79	CS2-73	65.7	±	1.9	.714	±	.026
547.79	CS2-73	93.8	±	2.8	.682	±	.020
558.00	CS2-73	118.5	±	3.5	.489	±	.017
558.00	CS2-73	106.1	±	3.1	.493	±	.020
558.00	CS2-62	114.0	±	3.4	.414	±	.013
570.96	CS2-62	59.1	±	1.7	1.36	±	.079
570.96	CS2-62	88.4	±	2.6	.902	±	.027
571.99	CS2-62	86.6	±	2.6	.847	±	.028
571.99	CS2-62	91.0	±	7.6	1.00	±	.158
579.60	CS2-62	101.4	±	3.0	.786	±	.026
579.80	CS2-62	130.0	±	16.0	.882	±	.161
579.80	CS2-62	127.1	±	3.8	.530	±	.034
579.80	CS2-62	130.3	±	3.9	.445	±	.013
585.40	CS2-62	79.9	±	2.3	1.08	±	.081
593.40	CS2-62	104.1	±	3.1	.898	±	.027
593.40	RG645	106.0	±	3.1	.826	±	.025
612.47	RG645	51.2	±	1.5	2.28	±	.105
612.47	RG645	58.2	±	1.7	1.71	±	.093

Table 1-3

NO_2 Radiative Lifetimes (τ_0 / μs) and Collisional Quenching Constants (k_q / 10^{-10} cm^3s^{-1}) acquired with the SR400 Gated Photon Counter System. Uncertainties of one standard deviation are given.

λ, nm	Filter	τ_0			k_q		
489.00[1]	CS2-73	72.1	±	.2	.36	±	.03
494.80[1]	CS2-73	70.9	±	.7	.49	±	.05
504.99[1]	CS2-73	67.0	±	.5	.43	±	.04
504.99[1]	CS2-62	75.2	±	.3	.34	±	.03
512.64[1]	CS2-73	73.3	±	1.3	.48	±	.05
525.71	CS2-73	82.8	±	.6	.55	±	.04
547.79[1]	CS2-73	81.6	±	1.7	.51	±	.06
547.79	CS2-73	84.6	±	.6	.63	±	.02
558.00	CS2-73	100.1	±	1.2	.86	±	.05
570.96	CS2-62	84.7	±	1.6	1.31	±	.08
571.99	CS2-62	79.0	±	1.3	1.25	±	.11
579.60	CS2-62	101.6	±	1.0	1.07	±	.06
579.80	CS2-62	107.5	±	2.5	.81	±	.06
579.80	CS2-62	110.0	±	4.8	.95	±	.11
579.80	CS2-62	120.3	±	1.3	.66	±	.02
585.40	CS2-62	95.7	±	3.4	1.06	±	.11
585.40	CS2-62	68.3	±	1.2	1.60	±	.10
593.40	CS2-62	135.9	±	23.2	2.17	±	.40
593.40	RG645	99.7	±	1.9	1.66	±	.15
600.71[2]	RG645	85.6	±	1.4	1.31	±	.06
600.71	RG645	97.3	±	1.4	1.40	±	.10
612.47[2]	RG645	58.9	±	.2	2.51	±	.05
612.47	RG645	44.7	±	.8	2.41	±	.12
612.47	RG645	56.0	±	1.4	2.16	±	.19
624.20[2]	RG645	110.8	±	2.1	1.39	±	.06
624.20	RG645	124.2	±	2.8	1.59	±	.07
624.20[2]	RG9	108.7	±	12.3	1.26	±	.23
624.20[2]	RG9	102.5	±	1.6	.91	±	.05
624.20	RG9	148.3	±	2.0	1.18	±	.03
634.00[3]	RG9	101.8	±	7.6	1.27	±	.21
634.00	RG9	122.8	±	6.2	.81	±	.17

Table 1-3 continued

λ, nm	Filter	τ_0			k_q		
647.40[2]	RG9	104.0	±	5.6	2.22	±	.18
647.40	RG9	98.0	±	1.9	3.07	±	.12
647.40	RG9	116.9	±	6.7	2.12	±	.14
656.20[2]	RG9	90.6	±	1.5	1.75	±	.08
656.20	RG9	97.4	±	3.4	2.07	±	.12
656.20	RG9	132.6	±	2.6	1.32	±	.06
656.20	RG9	140.4	±	9.4	1.21	±	.15
667.99[3]	RG9	89.4	±	2.5	2.87	±	.12
667.99	RG9	125.1	±	2.4	2.50	±	.08
668.00	RG9	93.8	±	1.0	2.10	±	.08
668.00	RG9	100.7	±	2.0	2.37	±	.15
668.00	RG9	116.5	±	2.0	1.65	±	.09
668.00	RG9	110.5	±	2.0	2.05	±	.10
673.35	RG9	63.0	±	3.8	2.11	±	.23
673.35[3]	RG9	70.7	±	1.3	2.75	±	.13
673.35	RG9	55.9	±	.3	3.19	±	.05
673.35	RG9	54.8	±	.6	3.01	±	.11
679.50	RG9	83.3	±	.6	2.89	±	.07
679.50	RG9	126.1	±	2.3	2.16	±	.08
680.00	RG9	120.9	±	5.5	2.89	±	.18
680.00	RG9	156.8	±	4.5	2.28	±	.08
686.10	RG9	183.2	±	15.9	2.58	±	.22
686.10	CS7-69	111.9	±	13.4	3.22	±	.26
686.11	RG9	126.9	±	5.4	2.87	±	.20
694.30	CS7-69	90.2	±	2.8	1.32	±	.10
694.30	CS7-69	140.5	±	8.8	2.16	±	.12
694.59	CS7-69	94.5	±	2.2	1.77	±	.06
694.59	CS7-69	64.3	±	2.0	3.09	±	.30
705.40	CS7-69	122.8	±	3.5	3.57	±	.07
705.40	RG780	105.3	±	6.7	2.43	±	.20
705.40	RG780	132.5	±	3.6	3.62	±	.08
713.46	RG780	106.5	±	9.9	1.61	±	.42
713.46	RG780	124.5	±	1.7	3.43	±	.10
713.46	RG780	143.4	±	14.9	2.39	±	.13
713.46	RG830	121.1	±	12.5	2.21	±	.20
723.50	RG780	143.0	±	8.2	2.74	±	.11
723.50	RG780	71.5	±	1.4	1.57	±	.06
723.50	RG780	136.4	±	13.3	2.24	±	.24

Table 1-3 continued

λ, nm	Filter	τ_0			k_q		
731.80	RG830	97.7	±	18.0	1.67	±	.41
731.80	RG830	222.8	±	8.1	1.79	±	.04
739.10	RG830	94.9	±	2.7	2.40	±	.08
739.10	RG830	67.2	±	3.6	1.28	±	.16
746.00	RG830	99.3	±	2.9	3.49	±	.09
746.00	RG830	119.4	±	8.4	3.52	±	.24

Notes for Table 3:

[1]Schott BG1 attenuation filter

[2]Corning CS4-70 attenuation filter

[3] Schott RG3 attenuation filter

Table 1-4

Effect of blue cut-off filters on the apparent Stern-Volmer quenching rate constants (k_q / 10^{-11} cm^3 s^{-1}) and zero-pressure fluorescence lifetimes (τ_0 / μs). Excitation wavelength: 455.00 nm. Filter wavelength represents the wavelength of 10% transmission. Uncertainties of one standard deviation are quoted.

Filter λ/nm	τ_0		k_q	
464	75.9	±2.3	2.54	±0.15
464	71.2	±2.1	2.15	±0.24
569	80.7	±2.4	1.78	±0.11
569	78.8	±2.4	0.94	±0.14
569	77.0	±2.3	1.74	±0.15
633	77.5	±2.3	1.05	±0.04
762	79.1	±2.4	0.43	±0.05

Figure Captions

Figure 1-1. Diagram of lifetime apparatus. The path of the laser beam is shown as a dashed line through the 50-liter Pyrex bulb. "Boxcar Time Resolution" refers to either two Stanford Research Systems SR250 gated integrators or to SR400 gated photon counter, depending on fluorescence intensity; see text.

Figure 1-2. Illustration of fluorescence viewing region perpendicular to laser path. The umbra is defined by the solid line, and the dashed line shows the penumbra.

Figure 1-3. Fluorescence decay traces for NO_2 excited at 455.00 nm, observed through a Corning CS2-73 filter (cutoff at 569 nm), and resolved in time with the SR250 analog boxcar system. The error bars shown illustrate one standard deviation about the data points. (a) 2.07 mTorr of NO_2, 67 μs lifetime. (b) 0.52 mTorr of NO_2, 73 μs lifetime.

Figure 1-4. Fluorescence decay traces for NO_2 excited at 723.50 nm, observed through a Schott RG780 filter (cutoff at 762 nm), and resolved in time with the SR400 photon counting system. Error bars represent one standard deviation as calculated from the number of counts. (a) 2.03 mTorr of NO_2, 39.2 μs lifetime. (b) 0.26 mTorr of NO_2, 112.5 μs lifetime.

Figure 1-5. Fluorescence decay rate constant as a function of NO_2 pressure. (a) NO_2 excited at 525.71 nanometers and observed through a CS2-73 filter using the SR250 system. Three separate trials are shown using the symbols □, ○, and Δ, representing 90, 91, and 90 μs zero pressure radiative lifetimes and Stern-Volmer quenching constants of (0.42, 0.43, and 0.41) $\times 10^{-10}$ cm^3 s^{-1}. (b) NO_2 excited at 746.00 nm and observed through an RG830 filter (cut-off at 811 nm) using the SR400 system. Two trials are shown representing 99 and 119 μs zero pressure radiative lifetimes and quenching constants of (3.5 and 3.5) $\times 10^{-10}$ cm^3 s^{-1}. Error bars representing two standard deviations about the rate constants are shown where the bars are larger than the symbols indicating the points.

Figure 1-6. Zero-pressure radiative lifetimes plotted against wavelength. The triangles represent experiments which used the SR250 analog time resolution system; the open circles represent experiments which used the SR400 photon counter. The shown error bar represents twice the maximum standard deviation in any trial; twice the minimum standard deviation of a trial is approximately the same as the size of the symbols.

Figure 1-7. Zero-pressure radiative rate constant (reciprocal lifetime) of NO_2 as a function of energy above the $^2B_2$ excited state origin. Error bars representing

maximum and typical standard deviations are shown. The solid line represents the weighted empirical fit given in Equation 1-7.

Figure 1-8. Collisional quenching rate constants of NO_2 as a function of excitation wavelength. The minimum uncertainty is smaller than the symbols on this scale; the maximum uncertainty is displayed as the set of error bars, representing two standard deviations. Symbols correspond to the scattered-light filters used. Boxcars: ▼ GG-475, ● CS2-73, ▲ CS2-62, ◆ RG-645, ■ RG-780; photon counter: ○ CS2-73, Δ CS2-62, ◇ RG-645, □ RG-780, + RG-9, x RG-830, ▷ CS7-69.

Figure 1-9. Zero order approximation of the changing sets of observed radiative transitions as a function of degree of collisional deactivation of the initially excited NO_2 molecules. The light detector is assumed to have unit quantum efficiency from 24,000 cm^{-1} to 12,000 cm^{-1} and a sharp cut-off to zero for photons with energy less than 12,000 cm^{-1}. The first pattern breaks the observable radiation into 7 equally wide energy bands and shows the ladder of low energy molecular states, which are the final energy levels after emission of radiation at initial time. The subsequent patterns at later times (arbitrary units) retain the same final state energy levels, but the upper molecular energy levels are reduced by a sequence of energy-lowering collisions. This figure does not show the time-dependent reduction of population of excited molecules due to radiative emission, but it emphasizes the time-dependent

number of observable fluorescence channels as a function of collisional deactivation, which are numbered at the top of the figure.

Figure 1-10. The same as Figure 1-9, except that it includes a scattered light filter that blocks the first three channels of fluorescence. To a zero-order approximation, there is no change in number of fluorescence channels, which are numbered at the top of the figure, with time until after collisions have reduced the molecular energy so that the fluorescence is in the observable range. This effect adds to other processes causing the observed quenching rate lifetime to be unduly long (compare Table 1-4).

Figure 1-1

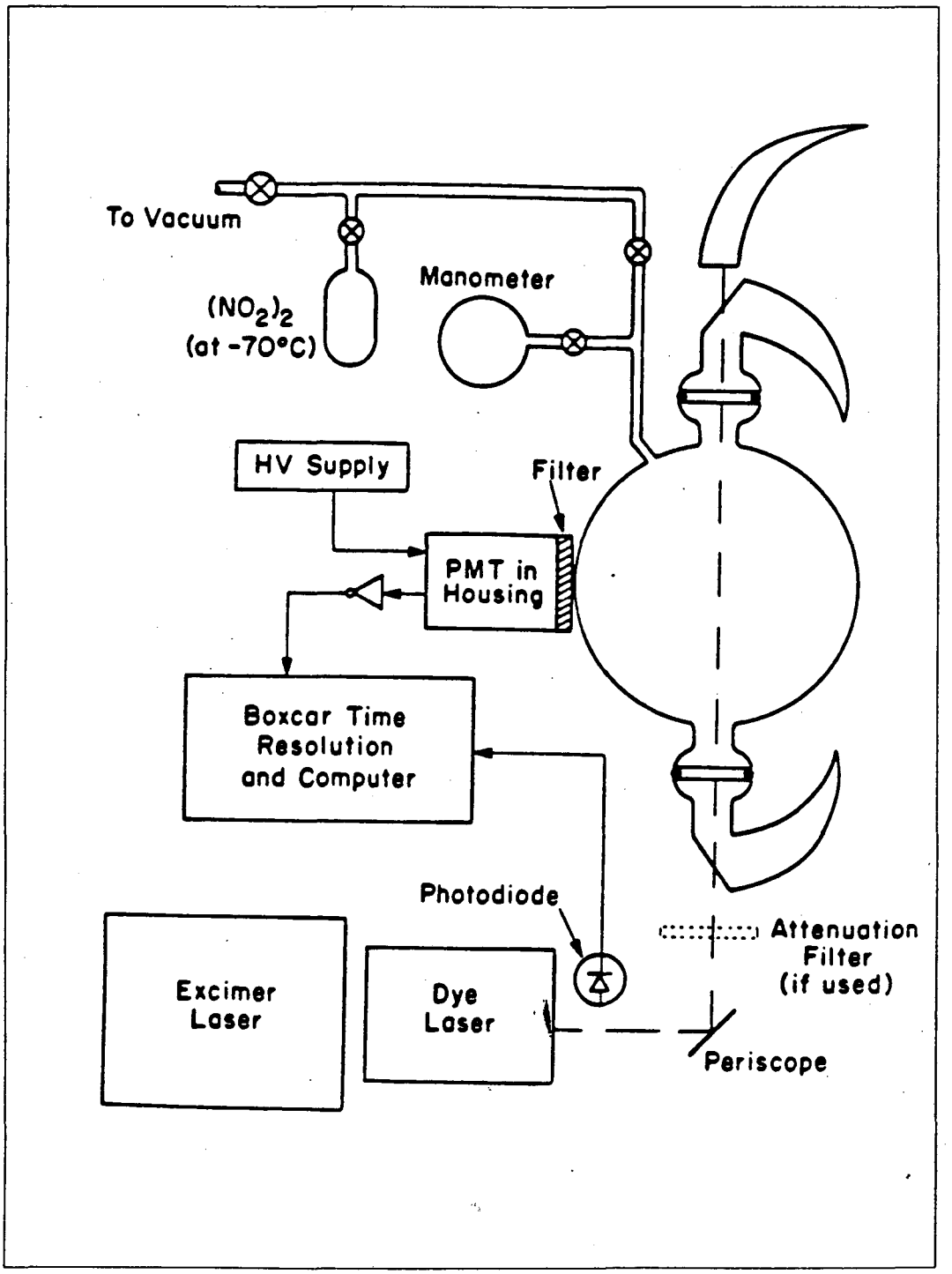
To Vacuum
Manometer
$(NO_2)_2$
(at -70°C)
HV Supply
Filter
PMT in
Housing
Boxcar Time
Resolution
and Computer
Photodiode
Attenuation
Filter
(if used)
Excimer
Laser
Dye
Laser
Periscope

Figure 1-2

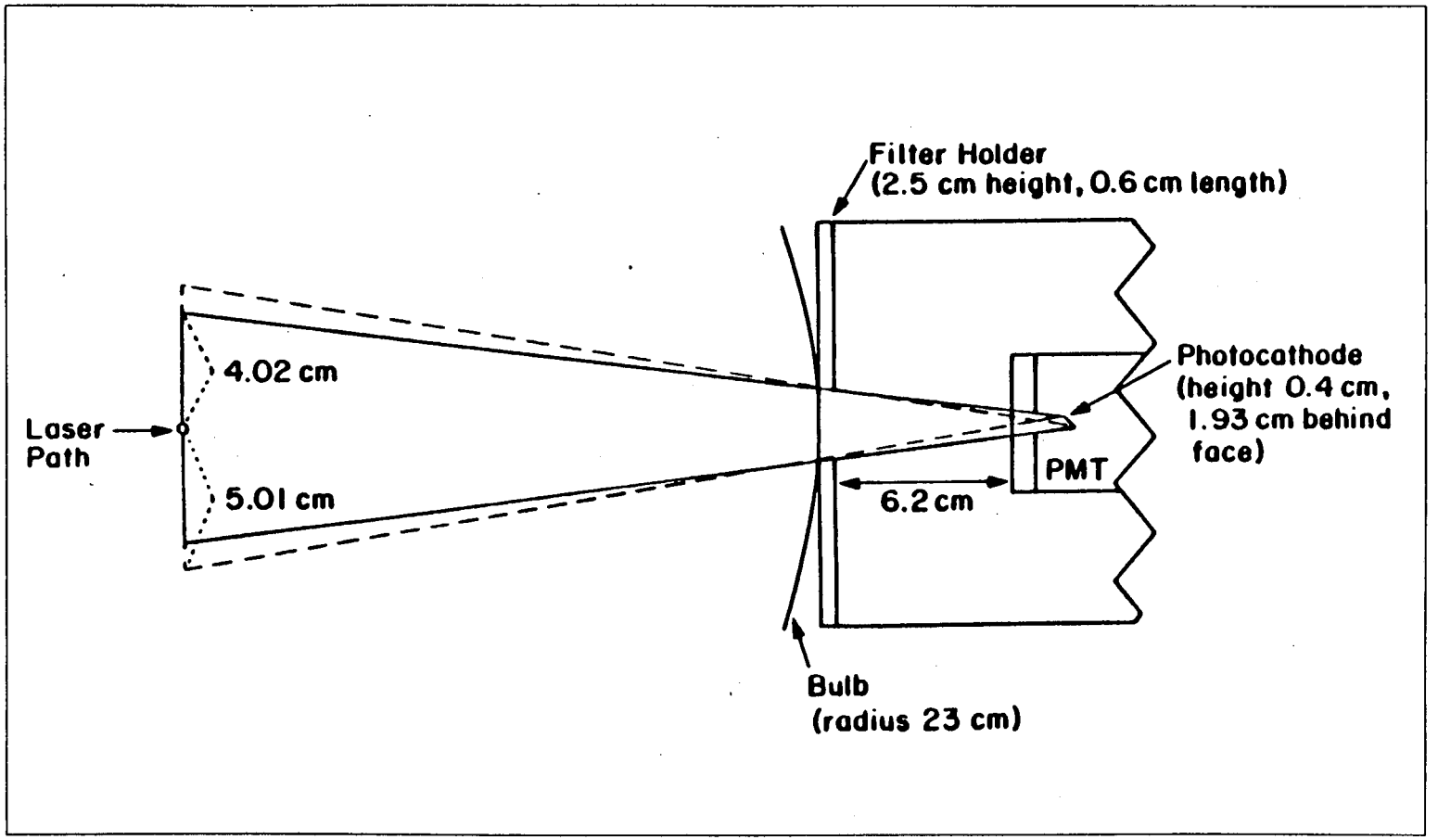
Filter Holder
(2.5 cm height, 0.6 cm length)
Photocathode
(height 0.4 cm,
1.93 cm behind
face)
PMT
6.2 cm
4.02 cm
5.01 cm
Laser
Path
Bulb
(radius 23 cm)

Figure 1-3

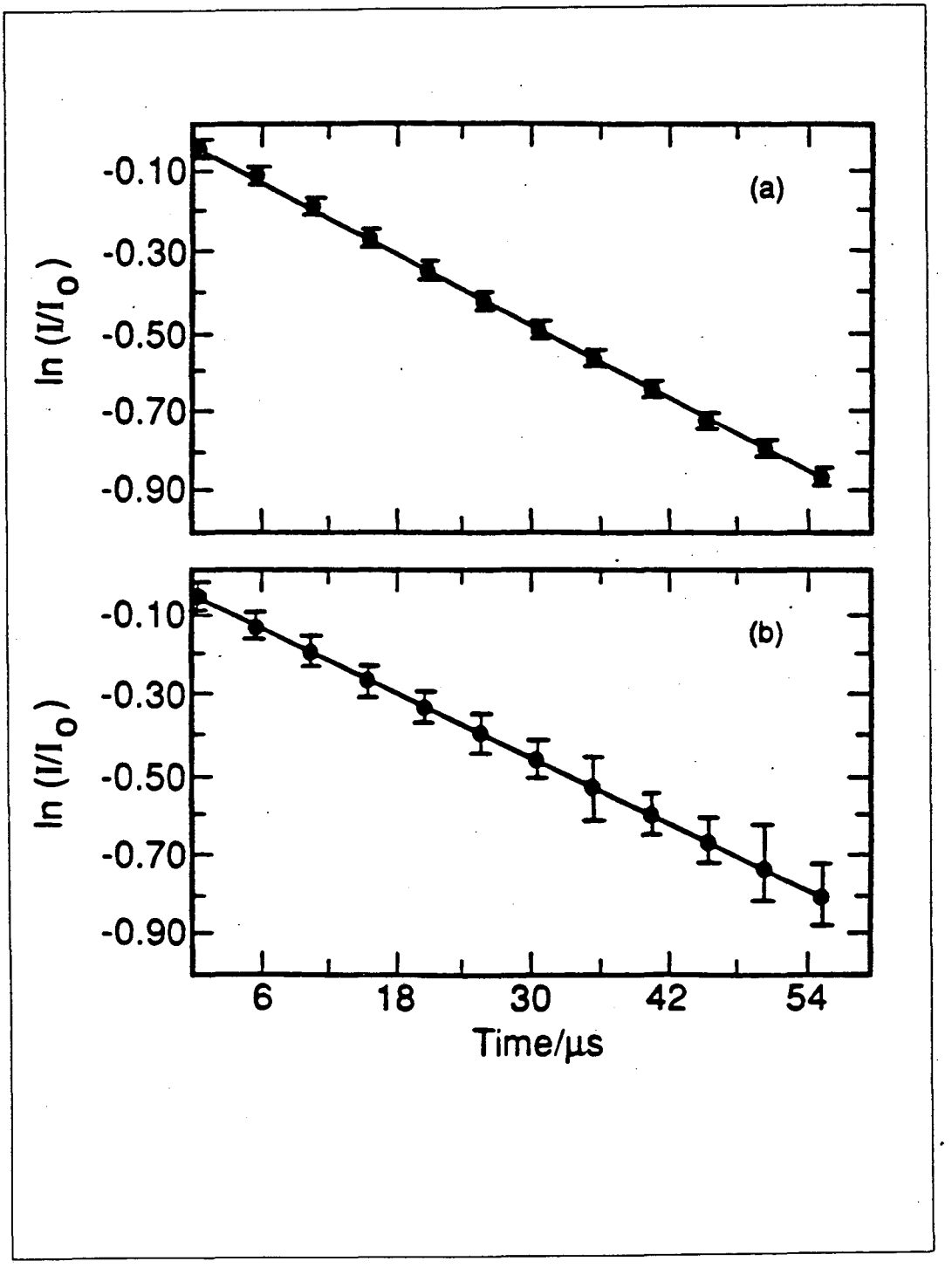
-0.10
-0.30
-0.50
-0.70
-0.90
ln (I/I$_o$)
(a)
-0.10
-0.30
-0.50
-0.70
-0.90
ln (I/I$_o$)
(b)
6
18
30
42
54
Time/µs

Figure 1-4

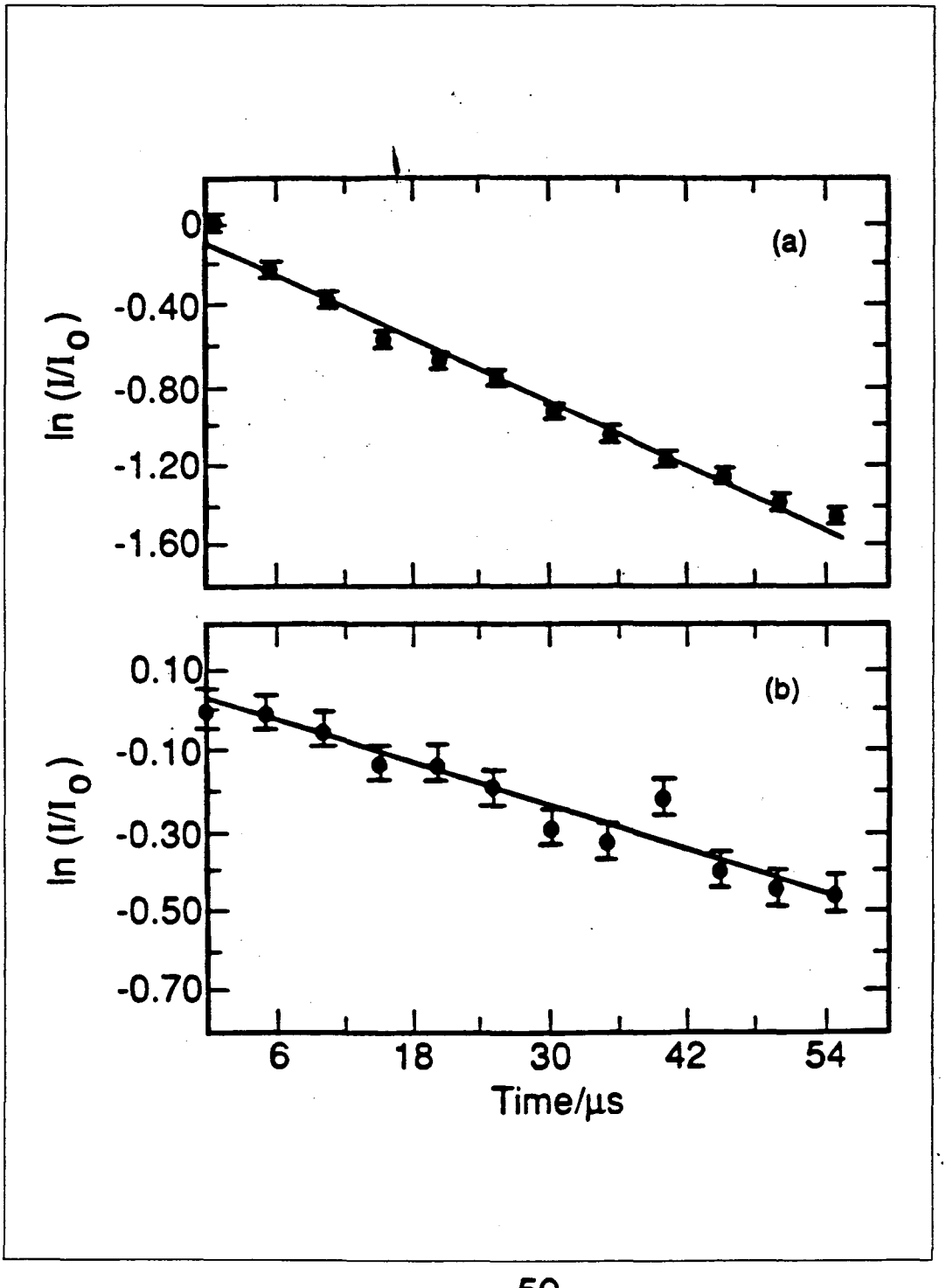
0
-0.40
-0.80
-1.20
-1.60
ln (I/I$_0$)
(a)
0.10
-0.10
-0.30
-0.50
-0.70
ln (I/I$_0$)
(b)
6
18
30
42
54
Time/μs

Figure 1-5

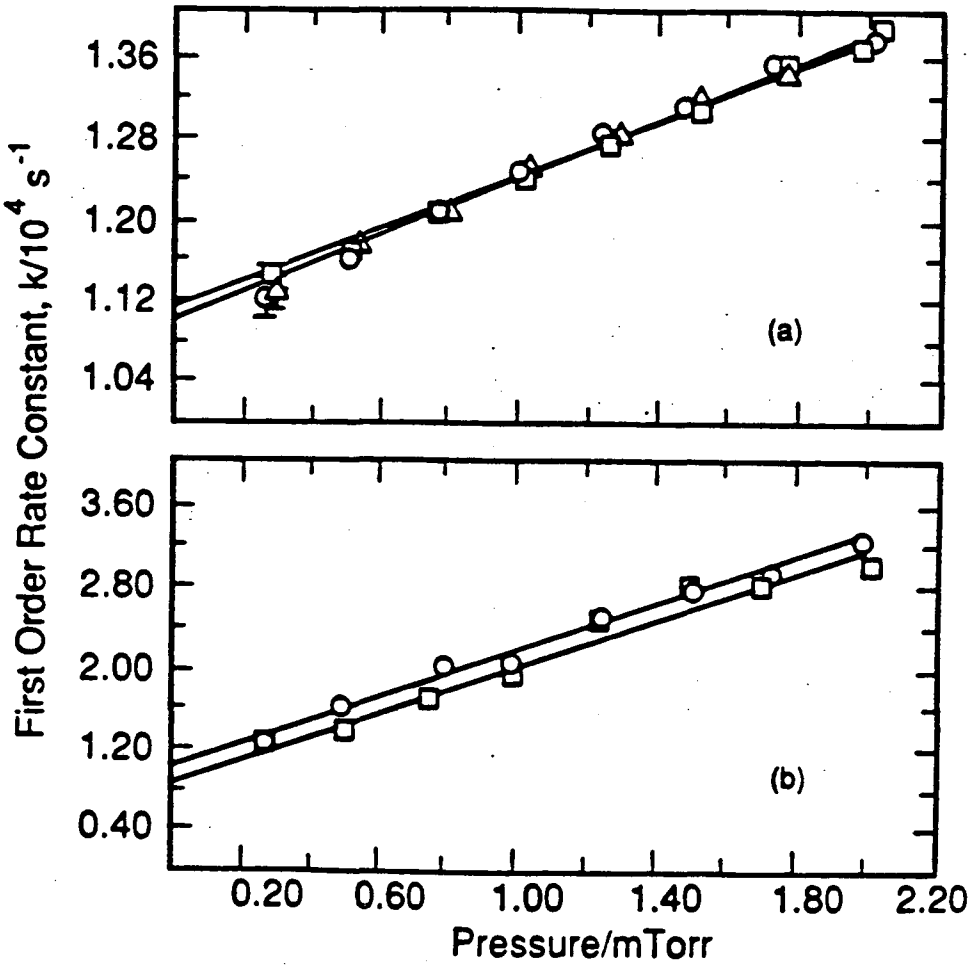
First Order Rate Constant, k/10^4 s^-1
1.36
1.28
1.20
1.12
1.04
(a)
3.60
2.80
2.00
1.20
0.40
(b)
0.20
0.60
1.00
1.40
1.80
2.20
Pressure/mTorr

Figure 1-6

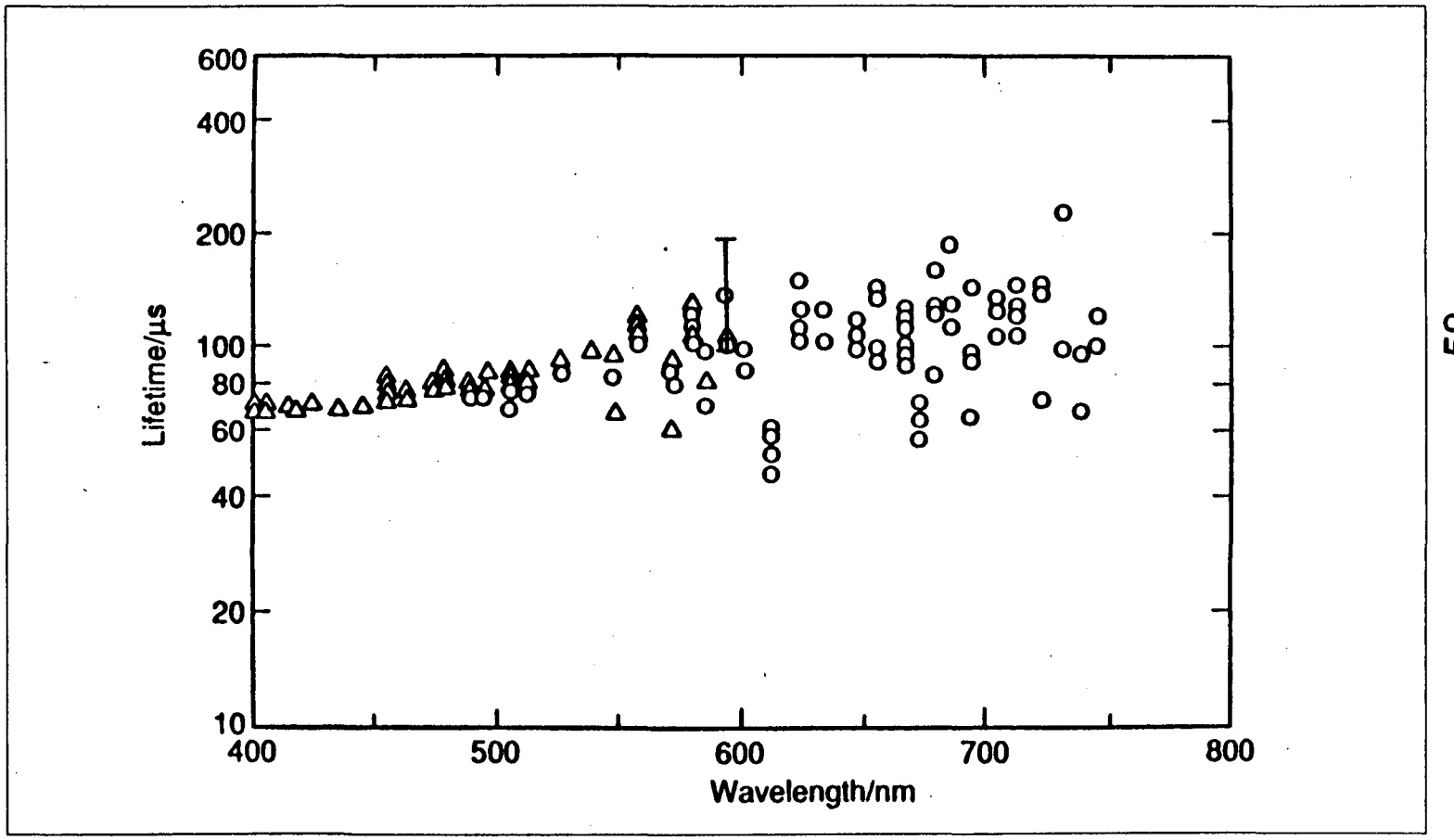
600
400
200
100
80
60
40
20
10
Lifetime/µs
400
500
600
700
800
Wavelength/nm

Figure 1-7

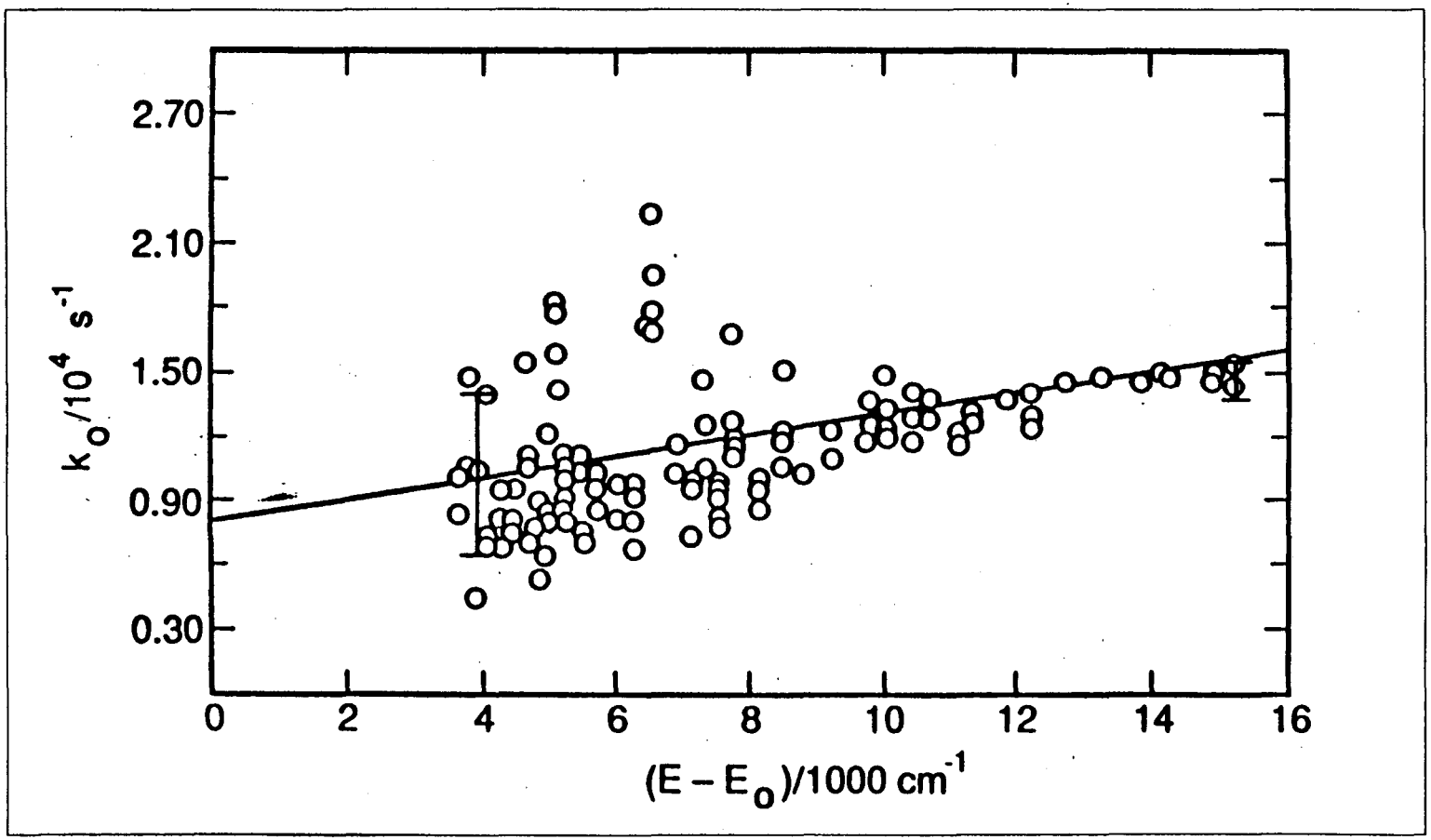

Figure 1-8

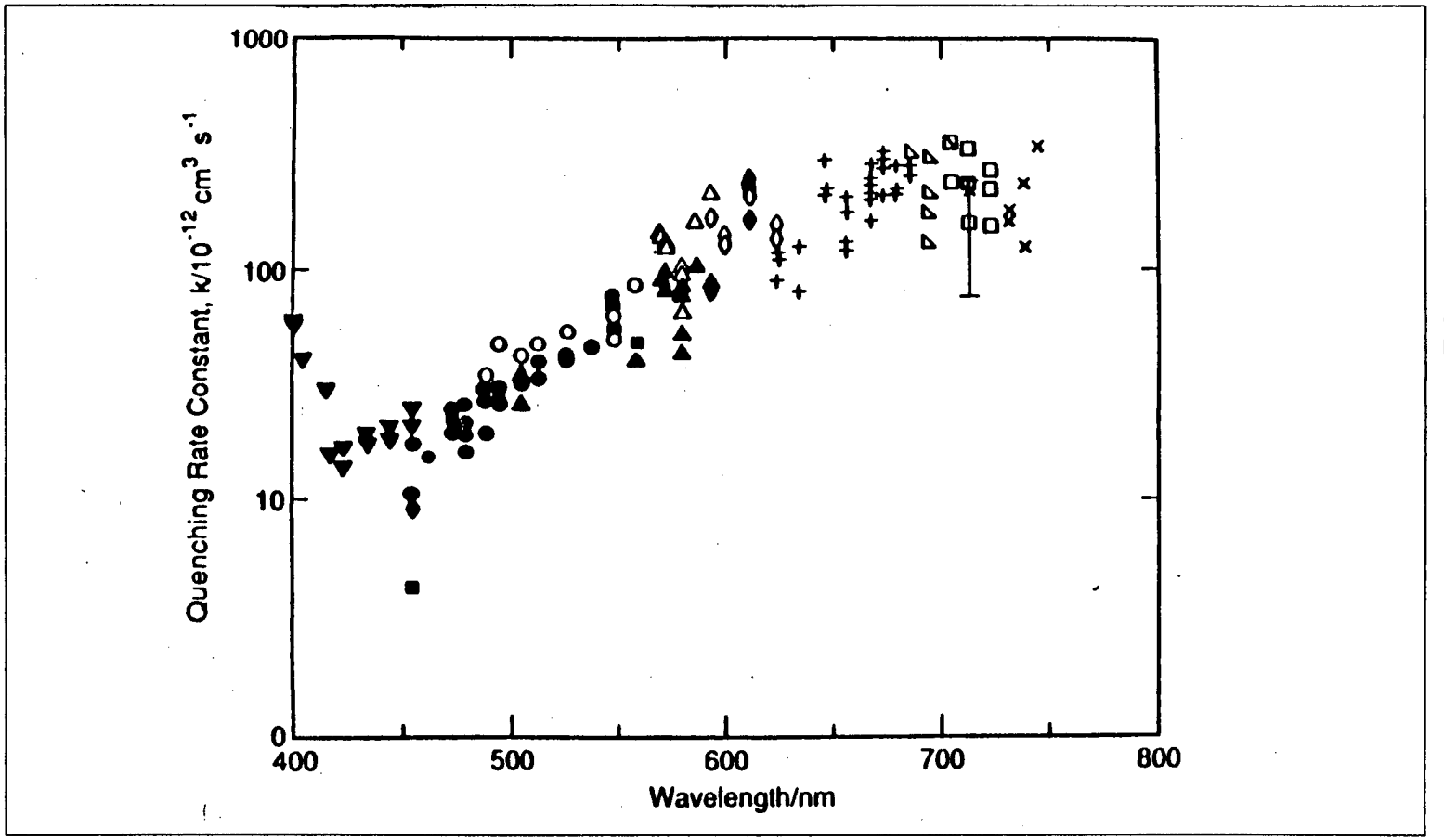
1000
100
10
0
400
500
600
700
800
Wavelength/nm
Quenching Rate Constant, k/10^{-12} cm^3 s^{-1}

Figure 1-9

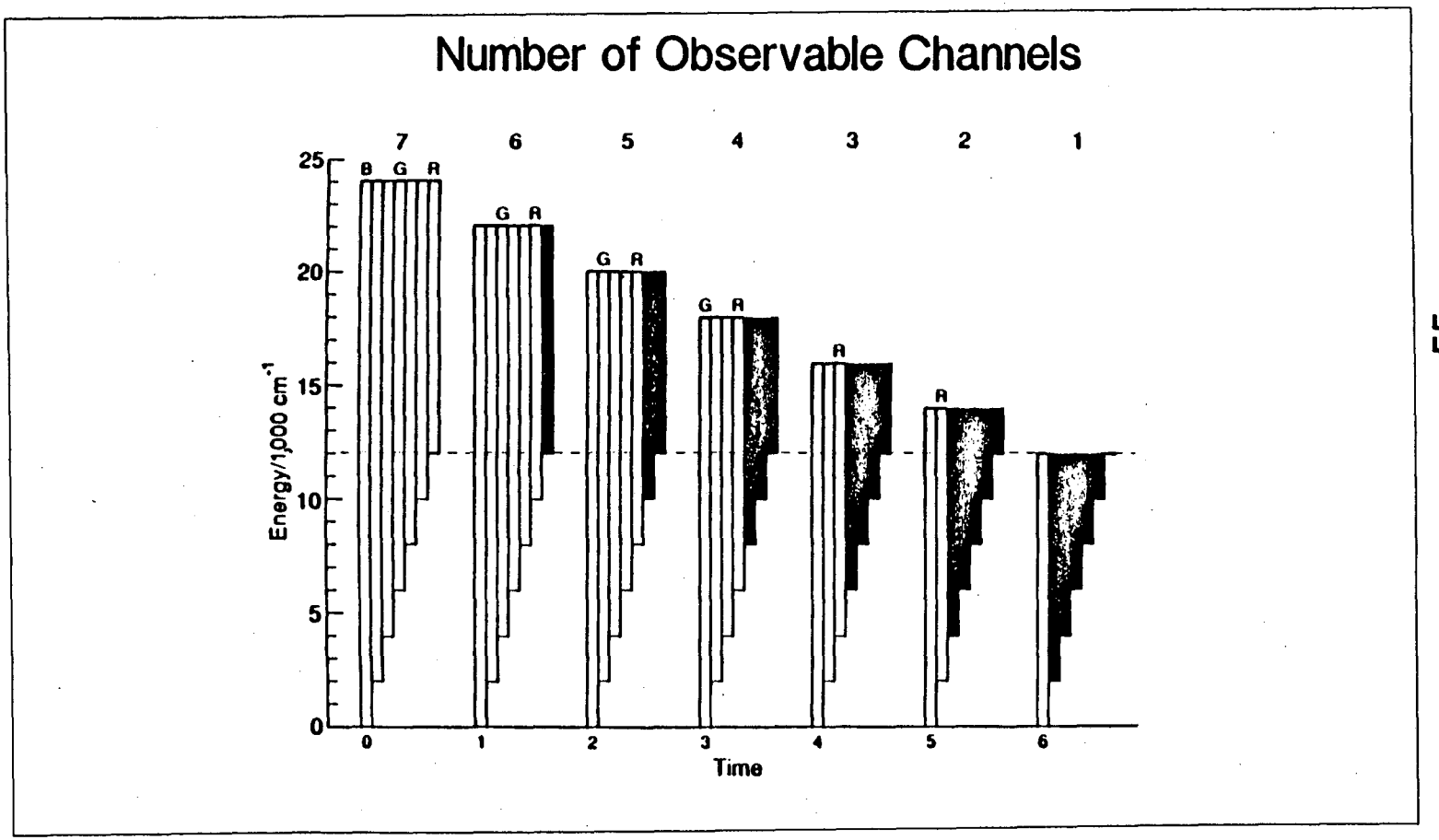
Number of Observable Channels
7
6
5
4
3
2
1
B G R
G R
G R
G R
R
R
25
20
15
10
5
0
Energy/1,000 cm-1
0
1
2
3
4
5
6
Time

Figure 1-10

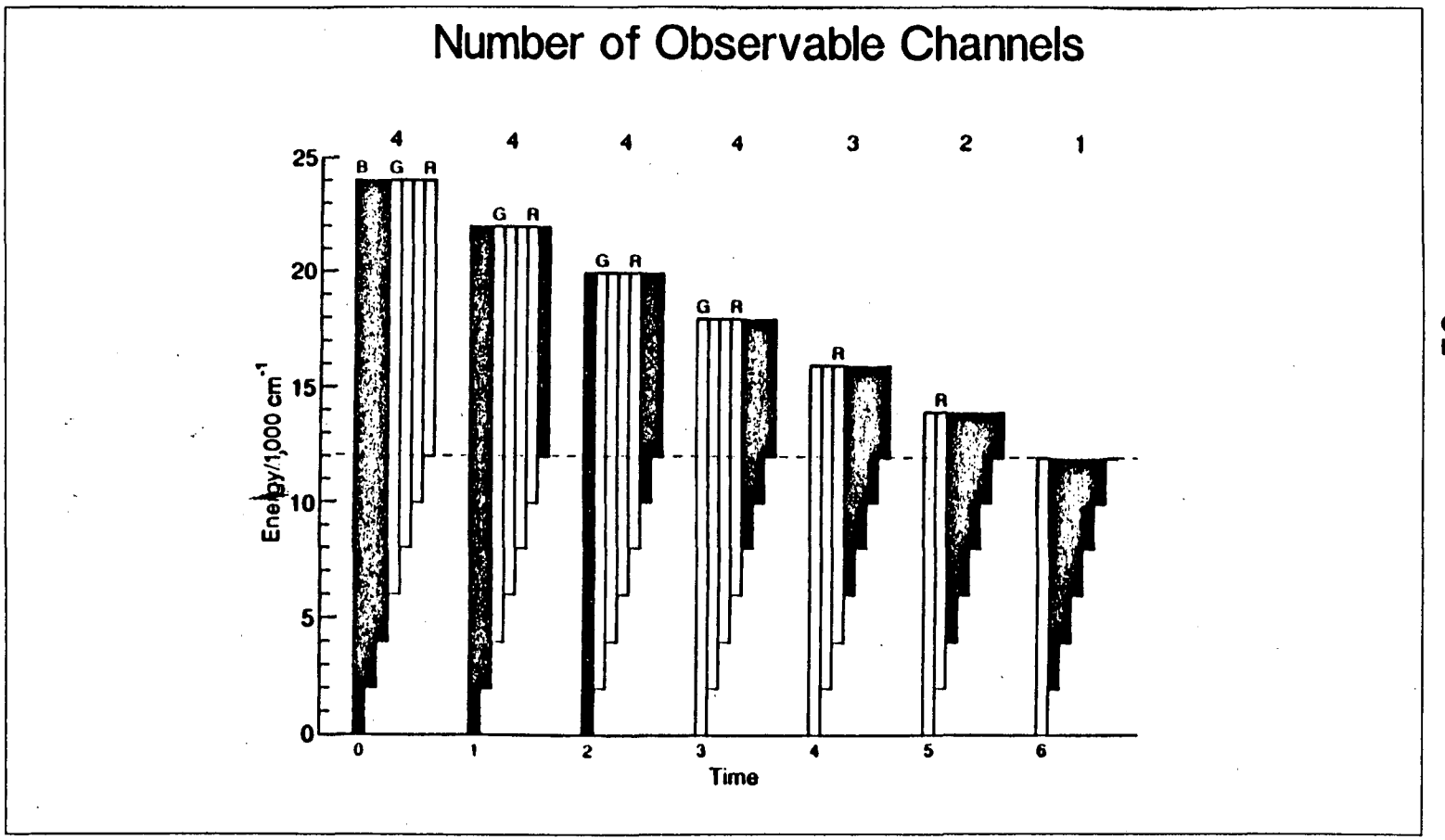
Number of Observable Channels
4
4
4
4
3
2
1
B G R
G R
G R
G R
R
R
25
20
15
10
5
0
Energy/1,000 cm⁻¹
0
1
2
3
4
5
6
Time

Chapter 2

Collisional Energy Transfer from Nitrogen Dioxide Excited at 532 nm

1. Introduction

Nitrogen dioxide (NO_2) is an atmospheric trace constituent whose excited state kinetics remain of great scientific interest despite considerable study.[9,23] This molecule is the most noted example of the transition from the quantum state-specific behavior of diatomics and some triatomics to the statistical behavior of large polyatomic molecules.[7,8] Strong coupling between its lowest excited electronic state, the $\tilde{A}\ ^2B_2$, and its ground state, $\tilde{X}\ ^2A_1$, leads to eigenstates which have predominantly the characteristics of the ground state.[10] The density of states is considerably greater than would be otherwise expected[9,10,52] and the radiative lifetime of these states is considerably longer than would ordinarily occur for an electronically excited state.[20,23]

Studies of the radiative lifetime of NO_2 frequently provide some data concerning the electronic quenching rate constants of NO_2.[23] However, these results are highly phenomenological since they represent a convolution of the energy transfer rates of NO_2 with the red limit of response of the photomultiplier used and are strongly influenced by the specific pressure and time conditions of the experiment.[23] More recent studies of collisional energy transfer from excited NO_2 have used more direct means, including the time-resolved change in infrared absorption of carbon

dioxide, carbon monoxide, and nitrous oxide in vibrationally excited states[53] and time-dependent thermal lensing of noble gases.[54] The former study observed the rate of a specific vibration-to-vibration collisional process for the three colliders while the latter technique is limited to the gases argon, krypton, and xenon.

In this work, a method based upon integrated fluorescence from NO_2^* determines[46,47,55] excited state population changes as NO_2 excited by a 532 nm laser pulse collides with each of thirteen buffer gases, including NO_2. After the experimental section details the apparatus, the results section applies this method to collisional deactivation data. The discussion section interprets the results further, emphasizing differences among the buffer gases and comparing these differences with known properties of the buffers.

2. Experimental Apparatus

2.1. Excitation and Fluorescence Collection Systems

Figure 2-1 illustrates the excitation laser and fluorescence collection apparatus. A Nd:YAG laser (Quanta-Ray DCR-1) with a KDP doubling crystal is set at 50 joules of electrical excitation per flashlamp pulse for both oscillator and amplifier stages to give approximately 50 mJ per pulse of 532 nm light. The pulse duration was < 20 ns, as observed from the photodiode (Hamamatsu S1722-02) signal, and the laser repetition rate was 10 Hz. The wavelength of the light produced was observed as 531.13 ± 0.16 nm (FWHM), based on the scattered light observed through the mono-

chromator. The quoted uncertainty in excitation wavelength arises from the monochromator resolution and does not indicate the bandwidth of the laser. The slit width on the monochromator (Interactive Technology CT-103) was set to 2.5 mm for experiments, corresponding to 2 nm resolution with the 1200 lines/mm, 500 nm blaze angle grating. Fused quartz slit lenses were used at the entrance and exit slits for the monochromator in order to collect more of the fluorescence.[55] Figure 2-2 illustrates the lenses used and the fluorescence collection region at the cell, as well as the cathode of the photomultiplier tube (Hamamatsu R1477).

The laser entrance and exit windows of the fluorescence cell are mounted on glass O-ring seals using high-vacuum epoxy (TorrSeal®). The mounts are equipped with Woods horns in order to trap laser light reflected from the windows, as shown in Figure 2-1. The window mounts and the fluorescence cell are silvered both at the window end and at the O-ring seal, then painted flat black on the outside surface. A larger Woods horn mounted to another O-ring seal opposes the fluorescence viewing window on the cell. While these measures significantly reduce interference from scattered laser light, they do not completely eliminate the intense combination of scattered light, resonance fluorescence, and Rayleigh-scattered light which is observed when the monochromator moves to a wavelength near 532 nm. The high voltage power supply is manually reduced by 400 volts for that datum in order to avoid possible damage to the photomultiplier.

The monochromator readings are calibrated for wavelength using a mercury lamp (Oriel), and the calibration is accurate to within ± 0.1 nm. A standard tungsten ribbon lamp (General Electric) equipped with a fused quartz window and aimed toward the monochromator through the opening for the large Woods horn provides a standard light source to obtain the spectral responsivity for this fluorescence collection system. The standard light source is chopped at 150 Hz using an optical chopper (Stanford Research Systems SR540), and a spectrum is taken in the same manner as in an experimental spectrum (see below) except in that the optical chopper provides the triggering signal for the gated integrators. This spectrum is divided by the Planck blackbody emission, as calculated from the discussion of Castellan on pages 452-5 of Reference 48:

$$I_\lambda d\lambda = \frac{2\pi c}{\lambda^4}\left(e^{\frac{hc}{\lambda kT}}-1\right)^{-1} d\lambda \qquad (2\text{-}1)$$

and by the emissivity of tungsten[56,57] to obtain the responsivity of the fluorescence collection system, which is plotted against observation wavelength in Figure 2-3. The temperature T of the tungsten ribbon lamp was measured by an optical pyrometer (Leeds and Northrop #8622C) calibrated by Lawrence Berkeley Laboratory.

2.2. Electronics

The high-voltage power supply (Fluke 408B) provides from 500 to 800 volts to the photomultiplier (PMT) which is adjusted to maximize the NO_2 fluorescence signal without saturation for a given series of experiments. The photomultiplier amplifier (Analog Modules 352-1-B-1-50) is closely connected to the PMT in order to minimize pickup of radio-frequency interference from the excimer laser. The amplified signal is then led into two gated integrators (Stanford Research Systems SR250) simultaneously, which permits collection of two different delays during a single experiment. The delays of both boxcars with respect to the laser pulse are measured to within 5% using an oscilloscope (Tektronix 2245A). The fluorescence signal at each wavelength of observation and at each delay is collected and averaged over 100 shots. The photodiode signal is collected into a third gated integrator with a delay of 15 ns and width of 10 ns in order to confirm the stability of the laser intensity, which was better than 5% between sets of 100 shots.

An personal computer (IBM PC-AT) equipped with an analog input/output card (Data Translation DT2801A) drives the experiment using the program ROVIB6D.YAG under the ASYST programming language.[49] This program supplies a trigger pulse to the Nd:YAG laser through the digital-to-analog (D/A) port 0 of the DT2801A board, then collects the readings from the gated integrators through the analog-to-digital (A/D) ports 0, 3, and 4 for each laser shot. After half the number of laser shots are taken for a given wavelength, the pressure reading from the capaci-

tance manometer is collected through A/D port 2. Once all of the laser shots have been collected for the current wavelength, the program stops firing the laser and sends pulses to the monochromator to drive it to a wavelength two nanometers greater than the previous one. This process is repeated for the 220 wavelengths from 480 to 918 nm collected in an experiment. In each experiment, the monochromator is first scanned forward briefly by the computer in order to remove backlash in the scanning mechanism. The initial wavelength reading of the monochromator and the pressure reading from the manometer are recorded, and the experiment is then allowed to proceed. After the 220 wavelengths have been collected, the final wavelength and pressure readings are taken for further analysis, and the data are saved to disk as a file for later analysis.

2.3. Gas Handling and Vacuum System

The NO_2 sample (Matheson, 99.5%) is purified by a freeze-pump-thaw cycle using liquid nitrogen, then mixing at room temperature with one-half atmosphere of oxygen gas (Lawrence Berkeley Laboratory, 99.5%) for 12 hr., then removal of the excess O_2 by a second freeze-pump-thaw cycle with liquid nitrogen. Samples thus prepared are maintained in the dark at -70°C. For each NO_2 experiment, an amount of NO_2 is measured into the evacuated cell, then sealed off. The volatile buffer gases helium (LBL, 99.995%), nitrogen (LBL, 99.999%), oxygen, neon (Spectra Gases, Inc. UHP grade, 99.996%), and carbon monoxide (Airco, 99.999%) were used

without further purification. Argon, krypton, and xenon (Airco, grade 4.5, 99.995%), carbon dioxide (Matheson bone dry, 99.8%), sulfur dioxide (Matheson anhydrous, 99.98%), and sulfur hexafluoride (Matheson instrument purity, 99.99%) were subjected to a freeze-pump-thaw cycle at liquid nitrogen temperature before use. Nitric oxide (Matheson CP grade, 99.0%) was exposed to a finger held at dry ice temperature in order to remove possible nonvolatile impurities before use. For a buffer experiment, NO_2 is added to the cell to a pressure from 30 to 50 mTorr; then, the buffer is added to a measured total pressure. All pressures are measured by a capacitance manometer (Baratron 310AHS-10).

3. Data Adjustment and Fitting

Before application of the NO_2 population deconvolution method, the data as collected by the program ROVIB6D.YAG must first be corrected for laser power variations and for the spectral responsivity. Then, the normalized data are fitted by nonlinear least squares to a representation of the NO_2 excited state population responsible for the fluorescence.[46,47,55]

3.1. Normalization of the Data

The program ANALYZ.PRO under ASYST loads data files from ROVIB6D.YAG to prepare them for the population deconvolution method. First, the zero-signal point is obtained by viewing the raw data for each boxcar on a graphics

display; the program provides cursors in order to expand the blue edge of the spectrum, then to select the range of wavelengths which is to be considered to have zero signal. This range typically extends over points corresponding to 480 to 510 nm. Second, the data from each boxcar are corrected for the spectral responsivity shown in Figure 2-3. Since the small responsivity at the red end drives the signal to near zero, the red limit of the data is selected by the program at this step, typically at 840 nm. Finally, the variations in the laser intensity as monitored by the gated photodiode signal are subjected to a four- to eight-point smooth in order to eliminate noise, then divided out of the spectra. The corrected spectra are then each saved to a file in the standard number format of the IBM PC-compatible personal computers and to an ASCII text file for reading by the fitting programs.

3.2. Method of Population Deconvolution

Energy conservation dictates that a molecule, NO_2 in this particular case, may not emit radiation with more energy than the molecule possesses. As has been shown in previous works,[46,47,55] the excited state population responsible for a given fluorescence spectrum may in theory be determined by "peeling" off the contributions of excited molecules from high energies to low when the fluorescence resulting from molecules excited at a given energy is known. For NO_2, the fluorescence profile is an analytical function of the excitation and observation energy, as has been demonstrated in Reference 55, upon which the following discussion is based.

3.2.A. The Nascent Laser-Induced Fluorescence Function

A laser-excited fluorescence spectrum of NO_2, if taken in the gas phase at the resolution of the current experiment under conditions of low pressure and short delay time after the excitation, generally exhibits peaks superimposed upon a continuous broadband fluorescence profile shifted to the red of the excitation energy, such as the dotted line in Figure 2-4. The peaks represent the vibrational structure from the electronic ground state, while the continuum is actually an average intensity of many transitions arising from both NO_2 molecules that had nonzero rotational and vibrational energy before excitation (hot bands) and from the general breakdown of selection rules for transitions due to Douglas coupling.[9,10,12] While this profile seems noisy when expressed as a function of excitation energy because of the structured emission, the running sum of the fluorescence is a considerably smoother function, as shown by the dotted line in Figure 2-5. The running sum, taken from higher observation energies to lower, is defined as:

$$S(X_L,X_k) = \sum_{j=1}^{j=k} s(X_L,X_k) \qquad (2\text{-}2)$$

where k represents an array index which corresponds to the observation energy and $s(X_L,X_k)$ represents the fluorescence excited at energy X_L and observed at energy X_k. The function

$$L(X_L,X)dX = \begin{Bmatrix} C_1 Z^2 \exp(-Z)dX, & X < X_L+X_{hot} \\ 0, & X \geq X_L+X_{hot} \end{Bmatrix} \qquad (2\text{-}3)$$

where X represents the observation energy, dX is the resolution of the monochromator in terms of energy, C_1 is a normalization factor between the fit and the data, and Z is defined as

$$Z = \frac{X_L + X_{hot} - X}{a(X_L + X_{hot})} \qquad (2\text{-}3a)$$

where both X_{hot} and a are fitting parameters. X_{hot} is the difference between the highest energy at which significant NO_2 fluorescence can be detected and the excitation energy X_L. Since Z in Equation 2-3a represents the energy of NO_2 after transition scaled by the initial energy of the excited NO_2, a can be considered a scaling factor.

The fit to the running sum of the data is given by:

$$I(X_L,X_k) = C_1 a(X_L+X_{hot})\left[2 - (2+2Z(X_k)+Z(X_k)^2)\exp(-Z_k)\right] \qquad (2\text{-}4)$$

except when $X_L + X_{hot} > X_{diss}$, the dissociation limit[17] of NO_2 of 25,132 cm^{-1}, in which case the first "2" is replaced by the term $[2 + 2Z(X_{diss}) + Z(X_{diss})^2]\exp(-$

$Z(X_{diss})$). The best values of the fitting parameters X_{hot} and a for 63 nascent LIF spectra at 22 different excitation energies[55] are

$$X_{hot} = 1000 \text{ cm}^{-1} \tag{2-5}$$

$$a = \exp[(7.29 \pm 2.69)\times 10^{-5} X_L/\text{cm}^{-1} - (2.986 \pm 0.623)].$$

3.2.B. Fitting General NO_2 Fluorescence Profiles

Any NO_2 fluorescence spectrum may be represented as a linear combination of nascent fluorescence spectrum functions. Nascent fluorescence spectrum functions (Equation 2-3) for different excitation energies X_L ranging from the dissociation limit of NO_2 to the lowest energy of observation of fluorescence X_r form a basis set for NO_2 fluorescence. Where the coefficients of a linear combination of those basis functions form the function $F(X_L)$, called the intensity coefficient function, the fluorescence fit is

$$PIF(X_i) = \left(\sum_{X_L - X_{diss}}^{X_L - X_i - X_{hot}} L_{nor}(X_L, X_i) F(X_L) \Delta(X_L) \right) \Delta X_i \tag{2-6}$$

where L_{nor} differs from L in Equation 2-3 in that the normalization range, rather than over the data, is from the dissociation energy to zero energy. The fluorescence sum fit is

$$SUM\text{-}PIF\text{-}CALC(X_k) = \sum_{X_i=X_{diss}}^{X_i=X_k} \left(\sum_{X_L=X_{diss}}^{X_L=X_i-X_{hot}} L_{nor}(X_L,X_i)F(X_L)\Delta(X_L) \right) \Delta X_i \tag{2-7}$$

and the function $F(X_L)$ is selected such that the sum error

$$r = \left\{ \frac{1}{N-2} \sum_{X_k=X_{diss}}^{X_k=X_N} \left[SUM\text{-}PIF\text{-}OBS(X_k) - SUM\text{-}PIF\text{-}CALC(X_k) \right]^2 \right\}^{1/2} \tag{2-8}$$

is minimized, where SUM-PIF-OBS is the running sum of the NO_2 fluorescence data and N is the number of data points. This formula is used for consistency with the sum error definition used in the photolysis-induced fluorescence interpretation;[46,47,55] since three parameters will be varied in this fitting procedure (see below) rather than two, the N - 2 denominator term should more properly be replaced by N - 3. For N = 183, the difference in r is not significant and does not affect the determination of the best fit.

Three empirical functions, each of which has three adjustable parameters, are used in fitting the data. The first is the Gamma Kernel,

$$F(X_L) = \frac{\left[\frac{(M-X_L)}{Y_m} \exp\left(-\frac{(M-X_L)}{Y_m} \right) \right]^n \Delta(X_L)}{\sum_{X_L=X_{diss}}^{X_L=X_r} \left[\frac{(M-X_L)}{Y_m} \exp\left(-\frac{(M-X_L)}{Y_m} \right) \right]^n \Delta(X_L)} \tag{2-9}$$

in which M can be interpreted as the maximum energy available for NO_2 fluorescence, Y_m is the difference between the maximum of the function and M, and n controls the spread of the function. The Gaussian,

$$F(X_L)\Delta(X_L) = \begin{cases} \dfrac{\exp\left(-\dfrac{(X_L-\mu)^2}{2\sigma^2}\right)\Delta(X_L)}{\sum_{X_L-X_{diss}}^{X_L-X_r} \exp\left(-\dfrac{(X_L-\mu)^2}{2\sigma^2}\right)\Delta(X_L)}, & X_L \le M \\ 0, & X_L > M \end{cases} \quad (2\text{-}10)$$

is set to zero for any excitation energy greater than M. M must always be less than or equal to X_{diss} for this function. Its other two parameters are μ, the energy for the maximum of the function, and σ, the spread of the function. The third function is the Biexponential,

$$F(X_L)\Delta(X_L) = \frac{\exp\left(-\dfrac{M-X_L}{c_d}\right)\left(1-\exp\left(-\dfrac{M-X_L}{c_r}\right)\right)\Delta(X_L)}{\sum_{X_L-X_{diss}}^{X_L-X_r} \exp\left(-\dfrac{M-X_L}{c_d}\right)\left(1-\exp\left(-\dfrac{M-X_L}{c_r}\right)\right)\Delta(X_L)} \quad (2\text{-}11)$$

which includes a rise constant c_r and a decay constant c_d. Each experiment in this study is represented well by at least one of the above functions, as will be demonstrated.

None of the fit functions permits analytical determination of the equations (2-6 to 2-8). In addition, the sum error $\underline{r}$ has been shown[55] to strongly depend upon the two parameters Y_m and $\underline{n}$ for the Gamma Kernel, consisting of a "valley" in the three-dimensional space of $(Y_m,\underline{n},\underline{r})$ with a shallow best fit point within that valley. This problem cannot be solved by standard numerical methods such as the simplex method[58] because such algorithms oscillate about the valley rather than locating the actual minimum. The parameter search algorithm contained in FITPRO28.FOR for the IBM PC-compatibles and in FP28 FOR for the IBM 3090 mainframe, while computationally intensive, averts the oscillation problem and consistently finds each of the three fit parameters to very good precision when the sum error tolerance is set to 1.0×10^{-6}. The sum errors resulting from each of the three fit functions for a given set of data are then compared, and the function corresponding to the lowest sum error (that is, agreeing best with the data) is selected to represent that data set. Occasionally, two functions will give rise to the same sum error, indicating that both functions have converged to the same distribution profile. In that case, the order of selection priority is arbitrarily defined as Gamma Kernel > Gaussian > Biexponential.

3.2.C. Populations from Fitting Parameters

Two factors remain to be considered in constructing the population of the excited NO_2 from the intensity coefficients $F(X_L)$. Intensity is related to the population through the zero-pressure radiative rate constant by the first-order rate equation,

$$I = -\frac{d[NO_2^*]}{dt} = k_0(X_L)[NO_2^*] \tag{2-12}$$

so that the intensity coefficients must be divided by the radiative rate constant to obtain the population in terms of excitation energies X_L. The rate constant for NO_2 is given to a good approximation by the linear relation, Equation 1-7 above[23]

$$k_0(X_L)/s^{-1} = 0.504\ (X_L/cm^{-1} - 9710) + 7960. \tag{2-13}$$

The resulting quantity represents a contribution to NO_2 excited state population from a given excitation energy. That contribution is the room-temperature rotational-vibrational distribution of NO_2, as given by the equation[55,59]

$$P_0(R)d\left(\frac{R}{kT}\right) = \frac{R}{kT}\exp\left(-\frac{R}{kT}\right)d\left(\frac{R}{kT}\right) \tag{2-14}$$

projected upward in energy by the laser excitation energy X_L. The room-temperature distribution must be convoluted with the $F(X_L)$ and $k_0(X_L)$ to produce the final expression for the population,

$$P(E_{int})dE_{int} = \left(\frac{1}{C}\int_{R=0}^{R-E_{int}-X_r}\left[\frac{F(X_L-E_{int}-R)\left(\frac{R}{kT}\right)\exp-\left(\frac{R}{kT}\right)}{0.504(X_L-9710)+7960}\right]d\left(\frac{R}{kT}\right)\right)dE_{int} \tag{2-15}$$

where the normalization constant C is selected such that

$$1 = \sum_{E_{int}=X_{diss}}^{E_{int}=X_r} P(E_{int})\Delta E_{int} \qquad (2\text{-}15a)$$

The normalized population permits calculation of the energy moments for further analysis of the deactivation data. The average energy of the population,

$$<E> = \sum_{E_{int}=X_{diss}}^{E_{int}=X_r} E_{int}P(E_{int})\Delta(E_{int}) \qquad (2\text{-}16)$$

is a direct and convenient ensemble average of the energy transfer from excited NO_2. Another quantity of relevance is the square root of the second central moment of energy, referred to as the energy spread:

$$(<\Delta E^2>)^{1/2} = \sum_{E_{int}=X_{diss}}^{E_{int}=X_r} (E_{int}-<E>)^2 P(E_{int})\Delta E_{int} \qquad (2\text{-}17)$$

For the purposes of the analysis, the uncertainties in these moments may be estimated from consideration of the experimental data involved in producing them. A deviation in a data point results in a directly proportional change in the intensity coefficient at an excitation energy corresponding to a threshold at that data point. In turn, the deviation in the intensity coefficient creates a directly proportional change in the population at energies corresponding to that intensity coefficient, which then causes a change in the average energy. The uncertainty in the average energy is thus stated as

the average energy obtained from Equation 2-16 times the sum error divided by the average value of the fluorescence sum (typically 0.3 for these experiments). Similarly, the uncertainty in the energy spread is the energy spread times the sum error divided by the average value of the fluorescence sum. These estimates should be considered as minimum estimates for the uncertainties of these derived results.

Finally, for evaluation of whether or not a sufficient fraction of the population is viewed by the experiment, the fraction of the intensity coefficient fit which falls to the red of the viewing region is calculated by

$$f_R = \frac{\int_{X_L=0}^{X_L=X_{red}} F(X_L)\Delta(X_L)}{\int_{X_L=0}^{X_L=M} F(X_L)\Delta(X_L)} \tag{2-18}$$

where the integrations are actually performed by standard numerical methods over an array corresponding to constant spacing in excitation energy X_L. Any experiment for which this fraction is greater than 0.05 is not considered for further analysis since Equations (2-16) and (2-17) no longer provide valid moments of the overall population.

4. Results

4.1. Example of Interpretation: NO_2 as a Buffer Gas

Figure 2-4 demonstrates the energy transfer obtained in this experiment. As collisions start, the strong vibrational progression of the dispersed fluorescence spectrum of NO_2 at 13 mTorr after 0.060 μs delay (dotted line) is markedly smoothed out with relatively little effect on the overall profile for 125 mT NO_2 after 0.472 μs (short-dashed line). Further collisions reduce the total emission intensity, particularly the emission from higher energies, as shown by the spectra at 332 mT, 0.964 μs (long-dashed line) and at 584 mT, 1.998 μs (solid line). The fluorescence sum plot in Figure 2-5 shows even more clearly how the blue edge of the fluorescence is reduced by collisional energy transfer. Each of these spectra, as with all of the spectra in this experiment, is normalized to unit total area and has been corrected for laser intensity and spectral response as discussed above.

Figures 2-6 through 2-11 demonstrate the effects of energy transfer upon relative population profiles for NO_2 as a buffer gas. At the lowest pressure-delay time combinations studied, as in Figures 2-6 and 2-7, the population profile exhibits an abrupt blue edge near the excitation energy. The population then falls less steeply on its red edge, but goes to nearly zero within 4,000 cm^{-1} below the excitation energy. As collisions continue (Figures 2-8, 2-9, 2-10), the most probable energy of the population shifts to the red and the red edge becomes increasingly less steep. Finally, after a sufficiently large collision number (Figure 2-11), the excited NO_2 has

deactivated enough so that a significant fraction is beyond the observation range; f_R from Equation 2-18 is 0.3759 for this experiment, as given in Table 2-2. Experiments where an insignificantly small fraction of the excited NO_2 population falls below the red limit of observations X_R ($f_R \leq 0.05$) may be quantitatively analyzed in terms of the population distribution moments.

A convenient measure of the rate of energy transfer is obtained if the ensemble average energy (Equation 2-16) is plotted against the product of the buffer gas concentration and the delay time between fluorescence excitation and collection. In the simplest approximation for small changes of internal energy, the rate of energy removal is independent of the internal energy of the excited molecule. Since these experiments extend over only a third of the total excitation energy near the dissociation limit for NO_2, this approximation could be expected to be satisfactory, but is subject to confirmation by the data. The plot of average energy versus concentration-time product (or, equivalently, the collision number between an NO_2^* and buffer molecules, which is the concentration-time product times a collision rate constant) should fit a line:

$$\langle E \rangle = k_E(M)\, c(M)\, t + \langle E \rangle_0. \qquad (2\text{-}19)$$

The initial average energy $\langle E \rangle_0$, expressed in cm^{-1}, is expected to be the laser excitation energy plus the average energy of the room-temperature rotational-vibrational distribution of NO_2, which for T = 20°C is

$$<E>_0 = X_L + \int_{R=0}^{R=\infty} \frac{R}{kT} e^{-\frac{R}{kT}} dR \qquad (2\text{-}20)$$
$$= 18828 + kT = 19032 cm^{-1}$$

The slope and y-intercept of the plot are determined from the data for which $f_R \leq 0.05$ by weighted linear least squares.[58] Comparison of the initial average energy with this value provides a check upon the physical consistency of the fit. The slope of the line is the energy removal rate constant $k_E(M)$ with the dimensions of energy change per unit concentration per unit time, which for this experiment will have the units $cm^{-1} \cdot cm^3\ s^{-1}$. Nonlinearity of the data points reflects a breakdown of the approximation of constant $k_E(M)$ with respect to internal energy E. In particular, a positive curvature in the plot indicates a decrease in $k_E(M)$ with decreasing E. If positive curvature is observed, then the $k_E(M)$ obtained from the linear fits above should be considered as averaged $k_E(M)$ over the observation energy range, and the $k_E(M)$ at the initial internal energy $<E>_0$ should be larger than given by the fit.

The rate constant for energy removal $k_E(M)$ may be divided by any of a choice of collisional rate constants in order to obtain the energy removed from the ensemble per collision. For this analysis, the hard-sphere collision rate constant

$$k_{HS} = \pi \sigma_{HS}^2 \left(\frac{8kT}{\pi \mu}\right)^{1/2} \qquad (2\text{-}21)$$

and the Lennard-Jones close collision rate constant (Page 144, Reference 60):

$$k_{close} = 2\,\Gamma\left(\frac{2}{3}\right)\pi\sigma_{LJ}^{2}\left(\frac{\epsilon}{kT}\right)^{1/3}\left(\frac{8kT}{\pi\mu}\right)^{1/2} \qquad (2\text{-}22)$$

are used. σ_{HS} and σ_{LJ} in the above equations represent the hard-sphere collision diameter and the Lennard-Jones collision diameter, respectively. ϵ is the Lennard-Jones well depth, T represents the absolute temperature in degrees Kelvin, k is Boltzmann's constant, μ is the reduced mass of the colliders (see below), and $\Gamma(2/3) = 1.35412$ can be found in standard mathematical tables. The Lennard-Jones close collision rate constant represents the rate constant for collisions which overcome the rotational pseudopotential between the two approaching molecules and thus contact the inner, strongly repulsive potential between the two molecules.[60] This collision rate constant is the more appropriate choice of basis for the vibrational energy transfer process.[61] However, as has been pointed out,[41,62,63] the choice of a given type of collision rate constant leads to a dependence of the energy removed per collision upon the type of collision specified, and comparison of results between different types of collisions is not possible. As with other experiments which have directly observed energy transfer,[53,54] this experiment can only determine the rate of energy removal per unit concentration per unit time and lacks any independent means of determining an "effective" collision number for vibrational energy transfer. Quantitative results of this study based upon the Lennard-Jones close collision number should be treated with this restriction in mind. The hard-sphere collision diameter σ_{HS} and the Lennard-

Jones potential well depth ϵ and crossing point σ_{LJ} for each of the buffer gases used in this study are given in Table 2-1. The approximate mutual collision diameter σ_{ab} for two gases a and b is obtained from the diameters for the two gases with themselves by the equation[64]

$$\sigma_{ab} = \frac{\sigma_{aa}+\sigma_{bb}}{2} \tag{2-23}$$

and the combination rule for the Lennard-Jones well depth ϵ is

$$\epsilon_{ab} = (\epsilon_{aa}\epsilon_{bb})^{1/2} \tag{2-24}$$

The reduced mass μ is obtained from the masses of the two colliders m_a and m_b by:

$$\mu = \frac{m_a\, m_b}{m_a+m_b} \tag{2-25}$$

For the purposes of this study, one of the gases in the above combination rules is always NO_2. The rate constants for collision used are also given in Table 2-1. In the particular case of NO_2 as a buffer gas, each expression for collision number uses the NO_2 parameters directly.

The average energies of all NO_2-buffered experiments are plotted against the hard-sphere collision number in Figure 2-12. Twenty-four combinations of NO_2

pressure and observation delay time were collected in this experiment, and the conditions, best fit parameters, and energy moments are given in Table 2-2. f_R is greater than 0.05 for three of the 24 combinations of pressure and time, which are shown as hollow squares in the following figures. The linear least squares fit of Equation 2-19 for those experiments with $f_R \leq 0.05$ (filled squares) is:

$$\langle E \rangle / \mathrm{cm}^{-1} = (18590 \pm 240) - (6.92 \pm 0.66) \times 10^{-8}\, c(NO_2) \cdot t \qquad (2\text{-}26)$$

which is represented by the solid line. Dividing the slope above by the hard-sphere collision rate constant in Table 2-1 gives 629 ± 60 cm^{-1} removed per hard-sphere collision, while dividing by the close collision rate constant gives 123 ± 12 cm^{-1} removed per close collision. The experiments with $f_R > 0.05$ are also shown as hollow squares for comparison; only for Z_{HS} greater than three is any significant deviation from the trend shown by the 21 experiments with $f_R \leq 0.05$ apparent. However, some nonlinearity in the average energy appears in Figure 2-12. First, the initial energy $\langle E \rangle_0$ in Equation 2-26 is lower than the expected initial energy in Equation 2-20, although the uncertainty in the fit is such that the expected initial energy is within two standard deviations. More significantly, the points of average energy themselves show significant curvature. As noted above, the above energy removal rates should be considered as minimum values for this excitation energy.

Figure 2-13 shows the energy spread as a function of hard-sphere collision number. The energy spread increases quickly at first with collisions, but then increases more slowly as collisions proceed. This negative curvature is also exhibited in Figure 2-14, which shows that the square of the energy spread (the second central moment of energy) for the 21 experiments for which f_R is less than 0.05 is also not linear. A log-log plot of the energy spread versus Z_{HS}, shown in Figure 2-15, is nearly linear except for the point corresponding to Experiment 1 in Table 2-2, which is fit by a near-nascent population and thus is unusual. The solid line in the figure is the linear least squares fit:

$$\ln\left(\langle \Delta E^2 \rangle\right)^{1/2} = (0.336 \pm 0.040)\ \ln[c(NO_2)\cdot t] - (0.5 \pm 32.8) \qquad (2\text{-}27)$$

The y-intercept of the above fit has no physical significance, but the slope indicates that the energy spread increases approximately as the cube root of the concentration-time product. For comparison, Gaussian populations increasing in width with increased concentration-time product would produce a slope of 0.5 when the energy spreads are subjected to the log-log fit above.

4.2. Correction for NO_2^*-NO_2 Collisions in Other Buffer Experiments

The effect of NO_2^*-NO_2 collisions must be considered before the average energy and energy spread results are analyzed for the buffer gases, even though the

experiments were conducted under conditions of minimum NO_2 pressure in order to limit this effect. The corrected average energy $<E>_c$ is obtained from the average energy yielded by the fitting method $<E>_o$ by adding the energy removed by NO_2 at the delay time of the experiment:

$$<E>_c = <E>_o + k_E(NO_2)\, c(NO_2)\, t \qquad (2\text{-}28)$$

While the energy spread is not as straightforward to separate into contributions from NO_2 and from the buffer, it is compensated for the effect of the average energy change by the equation:

$$(<\Delta E^2>)_c = (<\Delta E^2>)_o + (k_E(NO_2)\, c(NO_2)\, t)^2 \qquad (2\text{-}29)$$

4.3. Noble Gas Buffers

The noble gas pressure, pressure of NO_2, delay time, best fit parameters and sum error, and averaged parameters are listed in Table 2-3 for buffer gas experiments. Unlike the case with NO_2 as a buffer, most of these fluorescence data are best fit by the Gaussian function, indicating the relative absence of the red "tail" which is present in most of the NO_2 experiments even at large collision numbers. Also, the rate of energy removal is less than is the case for NO_2. Figures 2-16 to 2-20 plot the average energy versus hard-sphere collision number for the noble gases in order of increasing collider mass. The data for helium (Figure 2-16) show significant scatter about its linear fit of:

$$<E> = (19480 \pm 110) - (2.77 \pm 0.21)\times 10^{-8}\, c(He)\cdot t \qquad (2\text{-}30)$$

Neon (Figure 2-17) shows a considerably greater rate of energy removal in terms of hard-sphere collisions, even though its fit in terms of concentration-time product is:

$$\langle E \rangle = (19562 \pm 79) - (2.16 \pm 0.18) \times 10^{-8}\ c(Ne) \cdot t \qquad (2\text{-}31)$$

for which the slope is the lowest energy removal rate of any buffer in this study. Argon (Figure 2-18) exhibits approximately the same energy removal per hard-sphere collision as does neon, and its linear fit is:

$$\langle E \rangle = (19420 \pm 110) - (2.59 \pm 0.24) \times 10^{-8}\ c(Ar) \cdot t \qquad (2\text{-}32)$$

Krypton (Figure 2-19) removes energy from NO_2^* at the same rate as does xenon (Figure 2-20):

$$\langle E \rangle = (19175 \pm 97) - (2.60 \pm 0.20) \times 10^{-8}\ c(Kr) \cdot t \qquad (2\text{-}33)$$

$$\langle E \rangle = (19090 \pm 120) - (2.65 \pm 0.23) \times 10^{-8}\ c(Xe) \cdot t \qquad (2\text{-}34)$$

to within the uncertainty of this experiment. The initial energy from the fit is within agreement with the expected initial energy (Equation 2-20) for Kr and Xe, but significantly higher than the expected initial energy for the other noble gases. In no case is significant deviation from linearity apparent.

Figures 2-21 through 2-25 plot the natural logarithm of the energy spread versus the natural logarithm of the hard-sphere collision number for the noble gases. Experimental scatter prohibits determination of a general power law for all of these buffers. The energy spread increases as the fourth root of the buffer concentration-delay time product to within experimental uncertainty for He, Ar, and Xe, as demonstrated by the fit equations:

He: $\ln(<\Delta E>^2)^{1/2} = (0.237 \pm 0.121)\ln(c(He)t) + (1.4 \pm 64.9)$ (2-35)

Ne: $\ln(<\Delta E>^2)^{1/2} = (0.461 \pm 0.045)\ln(c(Ne)t) - (4.3 \pm 40.3)$ (2-36)

Ar: $\ln(<\Delta E>^2)^{1/2} = (0.267 \pm 0.079)\ln(c(Ar)t) + (0.7 \pm 118.0)$ (2-37)

Kr: $\ln(<\Delta E>^2)^{1/2} = (0.0705 \pm 0.0356)\ln(c(Kr)t) + (5.6 \pm 20.0)$ (2-38)

Xe: $\ln(<\Delta E>^2)^{1/2} = (0.192 \pm 0.054)\ln(c(Xe)t) + (2.7 \pm 39.4)$ (2-39)

Ne, however, increases nearly as the square root, which would be expected from a population distribution which is symmetric about its mean. Krypton, on the other hand, increases as the tenth root. Figures 2-21 through 2-25 indicate the large experimental uncertainty in these results.

4.4. Diatomic Buffer Gases

The conditions and fit parameters of experiments for which nitrogen, oxygen, carbon monoxide, and nitric oxide are used as buffers are listed in Table 2-4. Each of these gases relaxes NO_2^* more quickly than do the noble gases. The initial energy for each of the fit of average energy versus concentration-time product matches to within three standard deviations the expected value (Equation 2-20) for each of these gases:

N_2: $<E> = (19190 \pm 110) - (3.89 \pm 0.24)\times 10^{-8}\, c(N_2)\cdot t$ (2-40)

O_2: $<E> = (19000 \pm 64) - (4.70 \pm 0.25)\times 10^{-8}\, c(O_2)\cdot t$ (2-41)

CO: $<E> = (18740 \pm 190) - (3.77 \pm 0.56)\times 10^{-8}\, c(CO)\cdot t$ (2-42)

$$\text{NO:}\quad \langle E \rangle = (18859 \pm 97) - (6.45 \pm 0.60)\times 10^{-8}\, c(NO)\cdot t \qquad (2\text{-}43)$$

The agreement of the linear fit with the average energy is good for all diatomic buffer gases (Figures 2-26 to 2-29, in order) for those points corresponding to $f_R \leq 0.05$; however, curvature in the average energy is detected for all of the buffers.

The log-log plots of energy spread versus hard-sphere collision number (Figures 2-30 to 2-33, in order) bear considerably fewer points corresponding to near-nascent fit parameters than do the plots for the noble gases. The energy spread increases approximately as the fourth root of the buffer concentration-delay time product for each of the diatomic gases, as the slopes of the linear fits show:

$$N_2:\quad \ln(\langle \Delta E \rangle^2)^{1/2} = (0.284 \pm 0.052)\ln(c(N_2)t) + (0.5 \pm 35.5) \qquad (2\text{-}44)$$

$$O_2:\quad \ln(\langle \Delta E \rangle^2)^{1/2} = (0.258 \pm 0.030)\ln(c(O_2)t) + (1.1 \pm 41.6) \qquad (2\text{-}45)$$

$$CO:\quad \ln(\langle \Delta E \rangle^2)^{1/2} = (0.283 \pm 0.030)\ln(c(CO)t) + (0.6 \pm 36.1) \qquad (2\text{-}46)$$

$$NO:\quad \ln(\langle \Delta E \rangle^2)^{1/2} = (0.306 \pm 0.036)\ln(c(NO)t) + (0.2 \pm 34.1) \qquad (2\text{-}47)$$

The energy spread is in better agreement with linear fits than is the case for the noble gases.

4.5. Polyatomic Buffer Gases

The polyatomic gases carbon dioxide, sulfur dioxide, and sulfur hexafluoride each remove energy from NO_2^* faster than does NO_2 itself based on the buffer

concentration-delay time product, the hard-sphere collision number, or the effective collision number. Figures 2-34, 2-35, and 2-36 display the average energy versus hard-sphere collision number for these gases in order, along with the fits:

$$CO_2: \ \langle E \rangle = (18919 \pm 93) - (10.09 \pm 0.86) \times 10^{-8}\, c(CO_2) \cdot t \qquad (2\text{-}48)$$

$$SO_2: \ \langle E \rangle = (19180 \pm 140) - (15.4 \pm 1.4) \times 10^{-8}\, c(SO_2) \cdot t \qquad (2\text{-}49)$$

$$SF_6: \ \langle E \rangle = (19110 \pm 160) - (14.8 \pm 1.4) \times 10^{-8}\, c(SF_6) \cdot t \qquad (2\text{-}50)$$

As above, each of the hollow squares reflects a fit for which f_R is greater than 0.05 which is not included in calculating the fits given. In each case, scatter among fit points of nearly the same collision number is greater than any apparent deviation from linearity in the plot. The initial energy of the fit agrees well in each case with the expected initial energy of Equation 2-20.

The energy spread for CO_2 increases as the fourth root of the concentration-delay product, as shown by the fit in Figure 2-37:

$$CO_2: \ \ln(\langle \Delta E \rangle^2)^{1/2} = (0.247 \pm 0.054) \ln(c(CO_2)t) + (1.7 \pm 109.1) \qquad (2\text{-}51)$$

However, the energy spreads for both SO_2 and SF_6 (Figures 2-38 and 2-39) increase as the third root of the concentration-delay product, similar to NO_2:

SO_2: $\ln(<\Delta E>^2)^{1/2} = (0.348 \pm 0.084)\ln(c(SO_2)t) - (0.6 \pm 117.1)$ (2-52)

SF_6: $\ln(<\Delta E>^2)^{1/2} = (0.314 \pm 0.059)\ln(c(SF_6)t) + (0.1 \pm 66.0)$ (2-53)

Table 2-6 summarizes the fitted initial energy, energy removal rate constant, energy removed per hard-sphere collision, energy removed per effective collision, and the power law for the energy spread for all of the buffer gases.

5. Discussion

5.1. Comparison with Other Work

Most of the studies related to collisional energy transfer obtained Stern-Volmer collisional quenching constants during efforts to obtain the zero-pressure radiative lifetime of NO_2^*.[23] However, these rate constants are only indirectly related to the energy transfer rate constants derived in this study. The Stern-Volmer rate constant is the rate constant for reduction of the population of NO_2^* such that its emission falls to an energy below the red cutoff of the photomultiplier tube or other detection system used to collect the fluorescence. Additionally, this rate constant can depend upon the blue cutoff of the fluorescence detection system, which is always at a lower energy than the excitation energy in order to suppress scattered light in such experiments. Due to the phenomenological quality of these quenching constants and to the lack of information on the absolute number of excited molecules present in this experiment, comparison of these results and the Stern-Volmer quenching constants is not possible.

The experiments at 532 nm of Donnelly, Keil, and Kaufman in 1979[41] measured the quenching rate constant for dispersed fluorescence, but did not measure the excited state population directly, so that their quenching rate constants are also not directly comparable with those of this experiment. Their experiment also obtained a energy step per quenching collision $\Delta\epsilon_{vib}$ of 1000 $\pm$ 500 cm^{-1} by interpreting collisionally deactivated, dispersed fluorescence spectra of NO_2 in terms of the stepladder model (Figure 2-40). If the vibrational quenching rate constants k_C obtained in their experiment (Table III of Ref. 41) are multiplied by that energy step, then the products semi-quantitatively agree with the energy transfer rate constants in Table 2-6:

Buffer	This work $k_E(M)/10^{-8}$ $cm^{-1}\ cm^3\ s^{-1}$	Reference 41 $k_C \cdot \Delta\epsilon_{vib}/10^{-8}$ $cm^{-1}\ cm^3\ s^{-1}$
He	2.77 $\pm$ 0.21	3.5
Ar	2.59 $\pm$ 0.24	3.9
O_2	4.70 $\pm$ 0.25	5.4
N_2	3.89 $\pm$ 0.24	6.0
NO_2	6.92 $\pm$ 0.66	11
CO_2	10.09 $\pm$ 0.86	13
SF_6	14.84 $\pm$ 1.44	18

Despite the uncertainty of 50% in the k_E results from Reference 41 arising from the uncertainty in ϵ_{vib}, they reproduce the observation by this study that the energy transfer rate constant increases in the order $NO_2 < CO_2 < SF_6$.

Chou et al.[53] have studied energy transfer from NO_2^* by monitoring the rise of the infrared absorption intensity of singly excited high-frequency vibrational modes of CO_2, N_2O, and CO after excitation of NO_2 at 495 nm. Their study determined that

approximately three percent of the excitation energy in NO_2 is transferred into the ν_3 vibration of CO_2 and one percent of the excitation energy is transferred into the vibration of CO by finding the number of buffer molecules promoted into the v=1 state. Since that measurement found the total for the entire cascade of NO_2^* back to the ground state, this figure should not be expected to correspond meaningfully to the relatively nascent conditions of this study. However, the infrared absorption study also found that CO_2 appeared in the 00^01 state with a rate constant of 420 $\pm$ 100 $Torr^{-1}$ ms^{-1}, while v=1 CO appeared with a rate constant of 130 $\pm$ 80 $Torr^{-1}$ ms^{-1}. When the rate constant for CO_2 is converted to cm^3 s^{-1}, then multiplied by the CO_2 ν_3 frequency[65] of 2349.3 cm^{-1}, the resulting energy transfer rate constant is (3.0 $\pm$ 0.7) $\times$ 10^{-8} cm^{-1} cm^3 s^{-1}, or approximately 30% of the energy transfer rate constant determined in the current experiment. When the rate constant for CO is converted and multiplied by the fundamental frequency[66] of 2143.2 cm^{-1}, the energy transfer rate constant of (8.6 $\pm$ 5.3) $\times$ 10^{-9} cm^{-1} cm^3 s^{-1} is 20 percent of the energy transfer rate constant found by this experiment. The experiment of Reference 53 detects only energy which appears as v=1 CO, whereas the current experiment observes energy removal from NO_2 regardless of the channel responsible for the energy transfer. Further, though the uncertainty is large enough that this is not proven, this rate constant for transfer into the vibrational degree of freedom could make up the difference between the observed CO energy transfer rate constant and the energy

transfer rate constant observed for Ar, which has a comparable mass but no internal degrees of freedom.

The energy transferred into translational degrees of freedom from NO_2^* excited at 21631 cm^{-1} was measured by Toselli, Walunas, and Barker in 1989 using time-dependent thermal lensing of the gases Ar, Kr, and Xe.[54] Figure 11 of that report shows that Ar, Kr, and Xe remove approximately 25, 40, and 40 cm^{-1} per Lennard-Jones collision at energies corresponding to those of 532 nm excitation. The Lennard-Jones collision rate constants used were 3.19, 3.03, and 3.21 $\times$ 10^{-10} cm^3 s^{-1} for Ar, Kr, and Xe respectively. The TDTL results are consistently lower than the current results on the basis of energy removal rate constants:

Buffer	Current $k_E(M)/10^{-8}$ cm^{-1} cm^3 s^{-1}	TDTL buffer $k_E(M)/10^{-8}$ cm^{-1} cm^3 s^{-1}
Ar	2.59 $\pm$ 0.24	0.80 $\pm$ 0.16
Kr	2.60 $\pm$ 0.20	1.21 $\pm$ 0.24
Xe	2.65 $\pm$ 0.23	1.28 $\pm$ 0.26

The TDTL study monitored translation energy in the noble gas atoms for pressures of 10 to 500 Torr and delay times up to 500 μs. For the first several μs, the TDTL experiment may not obey the theoretical model used in data interpretation due to the non-Gaussian spatial profile of the excitation laser beam. The TDTL study is thus not as sensitive to the energy transfer occurring a few collisions after the laser excitation as to the deactivation at much larger collision numbers, which can account for the discrepancy of this study.

5.2. Rate Constants Versus Physical Properties of Buffers

The removal of vibrational and electronic energy from NO_2^* is expected to depend upon several properties of the buffer gas considered. Among these[61] are the molecular mass through the reduced mass of the two colliding molecules, the presence and magnitude of a permanent dipole moment, the polarizability of the buffer molecule, and the presence and energies of internal motions of the buffer. The buffer molecules in this experiment have been selected to provide a sampling of these properties.

5.2.A. Buffer Mass

Figure 2-41 plots the rate constant for energy removal against the reduced mass of the NO_2-buffer molecule system in atomic mass units. This provides for comparison of the buffers with respect to a property which is shared by all molecules. For this and Figures 2-42, 2-43, and 2-44, the circles correspond to noble gases, which lack internal degrees of freedom. The diamonds represent the diatomic gases, which have two rotational degrees of freedom and one vibrational mode ranging from 1554.7 cm^{-1} for O_2 to 2330.7 cm^{-1} for CO.[66] The squares are polyatomic buffers, which have three rotational degrees of freedom except for CO_2 and each have three or more vibrational modes, at least one of which has a fundamental frequency of less than 750 cm^{-1}. Both CO_2 and SF_6 have vibrational degeneracy, as well. In particular, the filled square represents NO_2. Figure 2-42 plots the energy removed per hard-

sphere collision against reduced mass, Figure 2-43 plots the energy removed per close collision against reduced mass, and Figure 2-44 plots the power law for the energy spread against reduced mass.

A comparison of the points for noble gases in Figures 2-41, 2-42, and 2-43 shows relatively little dependence upon the reduced mass. The rate of energy removal is nearly constant in Figure 2-41 for all of the gases except neon at 2.6×10^{-8} cm^{-1} cm^3 s^{-1}, and even neon agrees with this figure to within three standard deviations. In terms of hard-sphere collisions (Figure 2-42), Ar, Kr, and Xe again agree with one another at 270 cm^{-1} removed, while neon is reduced to 200 cm^{-1} and helium is reduced still further to 120 cm^{-1}. This is due primarily to the larger collision rate constants for the lighter gases (Table 2-1): more NO_2^*-He collisions occur for a given concentration-time product than do NO_2^*-Xe collisions since the mean relative velocity of NO_2 and He is greater than that for NO_2 and Xe. The phenomenological quality of the "hard-sphere collision" must be noted while interpreting Figure 2-42, however. As discussed above, the close collision should be the more satisfactory basis for consideration of energy removed by a buffer molecule. Figure 2-43 shows that all of the noble gases agree to within one standard deviation with 54 cm^{-1} removed per close collision except for He, which is four standard deviations away from that value. In this case, the close collision rate constant for He is considerably greater than for the other noble gases. No significant dependence of the energy transfer rate upon reduced mass is demonstrated by these experiments.

5.2.B. Permanent Dipole Moment

Of the molecules studied in this series of experiments, the noble gases, N_2, O_2, CO_2, and SF_6 have no permanent dipole moment, while CO, NO, NO_2, and SO_2 possess dipole moments of increasing magnitude:[67]

Buffer	Dipole Moment, Debyes
CO	0.112
NO	0.153
NO_2	0.316
SO_2	1.63

The most striking comparison of two buffers is between N_2 and CO, which have nearly identical masses. For all four of the Figures 2-41 through 2-44, the points for these two gases are superimposed upon each other to within experimental uncertainty. A further indication of the relative independence of energy transfer rates from dipole moment is the comparison of CO_2 (no dipole moment by symmetry) with NO_2, which has a lower energy removal rate in all terms presented despite its dipole. The energy removal rate constant for NO is about 1.5 times that of CO, nearly the same as the factor of increase in the permanent dipole moment, but other factors may contribute in this difference. SO_2, however, has both the largest dipole moment and the largest rate of energy removal of any buffer presented. While the permanent dipole seems to have little effect, it is not conclusively eliminated by this study as one of many terms involved in energy transfer.

5.2.C. Polarizability

Some polarizability data may be derived[68] from the first dielectric virial coefficient by the equation

$$\epsilon_1 = \frac{4}{3}\pi N_o \alpha \tag{2-54}$$

where N_o is Avogadro's number. The first dielectric virial coefficient ϵ_1 has been obtained[68] for the following gases:

Buffer	Polarizability /Å^3	$k_E(M)/10^{-8}$ cm^{-1} cm^3 s^{-1}
He	0.2051	2.77 ± 0.21
Ne	0.3946	2.16 ± 0.18
Ar	1.642	2.59 ± 0.24
Kr	2.484	2.60 ± 0.20
N_2	1.740	3.89 ± 0.24

In addition, Reference 64 lists values of polarizability for:

Buffer	Polarizability /Å^3	$k_E(M)/10^{-8}$ cm^{-1} cm^3 s^{-1}
N_2	1.76	3.89 ± 0.24
O_2	1.60	4.70 ± 0.25
CO	1.95	3.77 ± 0.56
CO_2	2.65	10.09 ± 0.86
SO_2	3.72	15.42 ± 1.43

No significant change in $k_E(M)$ occurs despite a factor of 12 increase in polarizability for the noble gases from He to Kr. An effect of polarizability upon the energy removal rates is not found.

5.2.D. Unpaired Electron Association

The presence of an unpaired electron on the buffer molecule in the ground state is expected to allow for a high mutual attraction with NO_2^*, which has an unpaired electron. Chemical reactions of NO_2 with itself and with NO based upon pairing of the unpaired electrons of the separated molecules have been extensively documented. Such association could possibly allow collisions of low relative velocity to last for several orbits, during which energy could be continuously removed from the excited molecule. Though most models of vibrational energy transfer require a hard encounter with the repulsive internal potential barrier,[61] chemical association could give rise to a collision complex in which the NO_2^* fragment loses energy through local-mode coupling to normal modes of the complex.

If chemical association contributed strongly to collisional energy transfer, then NO_2 should remove energy more readily than polyatomic molecules lacking unpaired electrons. $k_E(NO_2)$ in Table 2-6, however, is markedly lower than the $k_E(M)$ for the other three polyatomics, none of which possess unpaired electrons. Energy removal from NO_2^* should not be enhanced significantly by chemical association with NO_2 because the proportion of associative collisions is small. Orbiting collisions require

small ranges of both relative velocity and impact parameter out of the total range of these variables available,[60] so that such collisions are only a small fraction of the total number of collisions. The observation also requires that hard encounters with the internal repulsive barrier predominate in the transfer of vibrational energy, in agreement with theory. The enhancement in $k_E(O_2)$ and $k_E(NO)$ compared with $k_E(N_2)$ and $k_E(CO)$ will be better explained through a different mechanism below.

5.2.E. Internal Motions

The diatomic buffer molecules and CO_2 have two rotational degrees of freedom available, whereas the nonlinear polyatomic buffers NO_2, SO_2, and SF_6 have three rotational degrees of freedom. The order of magnitude of a rotational transition for these molecules is at most 10 cm^{-1},[1,2,65,66] and most collisions do not change the magnitude of any quantum number of an individual participant molecule by more than one, so that an individual collision involving rotational energy change cannot be expected to remove significantly more than this. Rotation-to-vibration and rotation-to-translation energy transfer are expected to occur faster than vibration-to-translation or vibration-to-vibration transfer due to the possibility of such transfer in glancing collisions--collisions in which the molecules do not approach closely enough to contact the inner repulsion term.[61,69] If each rotational degree of freedom is assumed to contribute the same increase in $k_E(M)$ as does each translational degree of freedom for any buffer molecule, then a diatomic should have an energy transfer rate constant 5/3 that

of a noble gas, or $5(2.55)/3 = 4.3 \times 10^{-8}$ cm^{-1} cm^3 s^{-1}. Table 2-6 shows that $k_E(N_2) = (3.89 \pm 0.24) \times 10^{-8}$ cm^{-1} cm^3 s^{-1} and $k_E(CO) = (3.77 \pm 0.56) \times 10^{-8}$ cm^{-1} cm^3 s^{-1} are lower than this model of energy transfer equipartition, but agree within experimental uncertainty. $k_E(O_2) = (4.70 \pm 0.25) \times 10^{-8}$ cm^{-1} cm^3 s^{-1} is higher than the model, but is still with experimental uncertainty. However, $k_E(NO) = (6.45 \pm 0.60) \times 10^{-8}$ cm^{-1} cm^3 s^{-1} is enhanced beyond this simple theory. Further, the energy transfer rate constant for a nonlinear polyatomic is predicted as $6(2.55)/3 = 5.1 \times 10^{-8}$ cm^{-1} cm^3 s^{-1}, which is significantly less than the $k_E(M)$ value in Table 2-6 for any of the four polyatomic buffer gases.

The unpaired electrons of NO, O_2, and NO_2 provide opportunities for energy-level splitting in the ground-state molecules due to interaction between the electron spin and the orbital angular momentum.[65] However, due to the symmetries of the electronic ground state for O_2 and NO_2, only NO possesses a spin-orbit excited state. The $^2\Pi_{1/2}$ spin-orbit state is 119.82 cm^{-1} above the $^2\Pi_{-1/2}$ ground state.[66] This electronic excited state could readily enhance the energy removal rate for NO beyond that of other diatomics.

A collision which involves transfer of vibrational energy from the NO_2^* to vibrational modes of the buffer molecule, while less likely than collisions involving V-to-T or V-to-R transfer,[61,69] will remove considerably more energy from the NO_2^*. The probability of V-to-V transfer, as with all other transfers, decreases as the amount of energy to be transferred increases. For such transfers, the minimum

amount of energy to transfer corresponds to the lowest vibrational fundamental frequency of the buffer molecule except for small contributions from changes in rotation and relative translation. The fundamental frequencies and symmetries of the buffer molecules are given in Table 2-7.

Among the diatomics, N_2, CO, and NO have vibrational fundamentals of ten percent or more of the excitation energy of the NO_2^* and only O_2 has a fundamental of under 10 percent. NO has its spin-orbit excited state of 119.82 cm^{-1}, which could be treated as an additional vibrational fundamental in energy transfer. The comparison of this study with the results of the infrared absorption study[53] of CO energy removal above indicates that V-to-V transfer could act in concert with the V-to-T transfer to produce the observed energy removal per effective collision, but the V-to-R transfer mode could also explain the energy removal, as it can for N_2 in the equipartition model presented above. For O_2, the spin-orbit states do not contribute significantly, but the V-to-V transfer will be seen as a probable significant contributor. The NO energy removal rate is most likely to be enhanced by the spin-orbit excited state plus some amount of V-to-V transfer.

The plausible contribution of V-to-V transfer is most striking in the comparison of energy removed per collision between CO_2, for which V-to-V transfer has been shown by the infrared absorption study[53], and NO_2. CO_2 removes 164 cm^{-1} per close collision (Table 2-6), or approximately 90 cm^{-1} more than does N_2. NO_2 removes 126 cm^{-1} per close collision, some 50 cm^{-1} more than N_2. The frequencies of

the O-C-O bend and the O-N-O bend are roughly comparable, but the O-C-O bend of CO_2 is doubly degenerate, whereas the O-N-O bend is singly degenerate. The frequency of the O-S-O bend in SO_2 is lower in frequency, which should lead to a greater amount of energy removed per collision than NO_2. Not all of the vibrations of a buffer need be activated by collision: all 15 of the fundamental modes of SF_6 have frequencies less than 1000 cm^{-1}, but SF_6 removes essentially the same amount of energy as does SO_2 (three fundamentals) per close collision. The SF_6 mode ν_1 (totally symmetric S-F stretch) in particular should be difficult to activate by collision with NO_2^* since such activation would require the simultaneous stretching (or contraction) of all six S-F bonds by contact with the NO_2^*.

5.3. Population Form and Mechanism of Energy Transfer

The process of collisional energy transfer obeys the rotation-independent master equation,[62] as written for NO_2:

$$\frac{dc(NO_2^*(E_i))}{dt} = -k_0(E_i)c(NO_2(E_i)) + \int_{E_j=0}^{D_0} k(E_i,E_j)c(NO_2^*(E_j))c(M)dE_j$$

$$- \int_{E_j=0}^{\infty} k(E_j,E_i)c(NO_2^*(E_i))c(M)dE_j \qquad (2\text{-}55)$$

for which $c(NO_2^*(E))$ is the concentration of NO_2^* with energy ranging from E to E + dE, c(M) is the concentration of buffer molecules, $k_0(E_i)$ is the zero-pressure radiative rate constant for NO_2, and $k(E_j,E_i)$ is the rate constant for collisional conversion of NO_2^* molecules from an initial energy E_i to a final energy E_j. This system of coupled linear differential equations is most conveniently solved[62,63] when the microscopic energy transfer rate constants $k(E_j,E_i)$ are assumed to be a total collision rate constant k_c times probabilities $f(E_j,E_i)$ for energy transfer from initial energy E_i to final energy E_j. When a nearly-nascent population distribution, which is narrow compared with the total range of energies available, loses energy, the resulting relative population distribution is the convolution of the initial population with $f(E_j,E_i)$, or $f(E_j,E_i)$ to a good approximation.

Collisional energy transfer, as measured in this experiment, is an average over an ensemble of relative velocities between excited and ground state molecules. Each collision also involves an impact parameter (distance of closest approach); this distance is one of the two initial parameters which determine whether or not vibra-

tional energy transfer occurs.[60,61] If the molecules have little relative translational energy, then the molecules will not be able to pass the rotational pseudopotential barrier, so that only rotational-translational and rotational-rotational energy exchange can occur to a classical approximation, as shown in Figure 2-45. However, once the molecules possess enough relative energy to overcome the pseudopotential, the collision is guaranteed to encounter the steeper section of the intermolecular potential where vibrational-translational and vibrational-vibrational energy transfer occurs. The samples in this series of experiments constitute ensembles of relative velocities and of impact parameters, some of which will cause significant energy to leave the vibrational motions of NO_2^* while others cause relatively little change in the total energy of the NO_2^* involved.

In the approximation that the initially excited population is narrow and that the population resulting from deactivation is the same as $f(E_j,E_i)$, the energy removal rate constant $k_E(M)$ is the negative of the average change in energy over $f(E_j,E_i)$ times k_c:

$$k_E(M) = -k_c \int_0^\infty (E_j - E_i)\, f(E_j,E_i)\, dE_j \qquad (2\text{-}56)$$

Information beyond that provided by the ensemble-average energy is available in this experiment. The result of the NO_2^* population deconvolution method from Section 3.2 above is a relative population distribution. Since the initial population distribution is narrow compared to that after several collisions, the population distribution is

identical to $f(E_j,E_i)$ under the approximation. Three models of energy transfer probability are considered.

5.3.A. Stepladder Model

The stepladder model of energy transfer, used extensively in past studies[20,41] due to the relative ease of computation, is illustrated in Figure 2-40. An excited species is represented as having n units of internal energy, and the internal energy is always present in an integer number of units. The species, upon collision, has a rate constant k_- of losing one unit of energy and a rate constant k_+ for gaining one unit. These rate constants are related to each other via the principle of microscopic reversibility,

$$k_c(E_i)f(E_j,E_i)\rho(E_i)\exp\left(-\frac{E_i}{kT}\right) = k_c(E_j)f(E_i,E_j)\rho(E_j)\exp\left(-\frac{E_j}{kT}\right) \quad (2\text{-}57)$$

where the $k_c(E)$ are the total collision rate constants and $\rho(E)$ are the densities of states. This relation originates from the fact that equilibrium is established in a gas at room temperature.[62] When the difference in energies $E_i - E_j$ is one energy unit ϵ, the product $k_c(E_i)f(E_j,E_i)$ is k_- and $k_c(E_j)f(E_i,E_j)$ is k_+. The densities of states $\rho(E_i)$ and $\rho(E_j)$ are commonly taken as equal for small differences in energy, which is a good approximation for highly excited molecules. Note that the two rate constants k_- and k_+ are not required to add up to the total rate constant for collision; that is, collisions

which do not transfer energy are permitted. The probability function form for this model consists of three Dirac delta functions at $E_j = E_i - \epsilon$, $E_j = E_i$, and $E_j = E_i + \epsilon$ with areas k/k_c, $(1 - k/k_c - k_+/k_c)$, and k_+/k_c respectively.

5.3.B. Exponential Model

The Troe exponential model,[62]

$$f(E_j,E_i) = \frac{1}{N}\begin{Bmatrix} \exp\left(-\frac{E_i-E_j}{\alpha}\right), & E_j<E_i \\ \exp\left(-\frac{E_j-E_i}{\beta}\right), & E_j>E_i \end{Bmatrix} \qquad (2\text{-}58)$$

where α is the parameter, $N = \alpha + \beta$ for normalization, and the relation of β to α is set by the microscopic reversibility relation in Equation 2-57, provides for the redistribution of an excited species to all possible values of final internal energy E_j. This probability of energy transfer has a maximum at zero energy transferred, which is consistent with the experimental observation that weak collisions predominate, and favors collisions which remove energy over those which add energy. The probability function is illustrated for $\alpha = 80\ cm^{-1}$ and $kT = 200\ cm^{-1}$ as the solid line in Figure 2-46.

5.3.C. Biased Random-Walk Model

The final model is based upon the idea that energy leaves excited species in a manner similar to diffusion except that the reduction of the excited species energy is favored over its increase. This biased random walk model[63] is:

$$f(E_j,E_i) = \frac{1}{2}(s^2\pi)^{-\frac{1}{2}}\exp\left(-\frac{(s^2z+E_j-E_i)^2}{4s^2}\right) \qquad (2\text{-}59)$$

where s is a diffusion coefficient and z is defined as

$$z = -\frac{\partial}{\partial E_j}\left[\ln\left(\rho(E_j)\exp\left(-\frac{E_j}{kT}\right)\right)\right] \qquad (2\text{-}59a)$$

which collapses to $(kT)^{-1}$ when the density of states $\rho(E_j)$ is assumed not to vary significantly with E_j. The model, shown in Figure 2-46 for kT = 200 cm^{-1} and s = 50 cm^{-1} as a dashed line, has a maximum probability at negative changes in energy, but a nonzero probability of elastic collision ($E_j - E_i = 0$). This model was originally applied[63] to vibrational energy removal from large polyatomic molecules, in which a buffer molecule encounters and exchanges energy with several local vibrations of the excited molecule during the course of the collision.

5.3.D. The Intensity Coefficient Function Selection

During the calculation of the fluorescence fit, the intensity coefficient function which best represents the data is selected from among the Gamma Kernel (Equation 2-9), the Chopped Gaussian (Equation 2-10), and the Biexponential (Equation 2-11). Even though each of these functions can resemble any other function for certain parameters, a function which is identical to the data which it represents yields a lower error than does a different function which has adapted to the data. The profile of the population does not differ severely from that of the intensity coefficient function. The linear $k_0(X_L)$ (Equation 2-13) contributes the larger change by enhancing the red edge of the population over that of the intensity coefficients. Room-temperature rotational-vibrational distributions are narrow compared with most of the $F(X_L)$ determined as optimum for these experiments. The net effect of convoluting the room-temperature distribution with $F(X_L)$ is to shift the coefficient function 200 cm^{-1} to the blue. The choice of the intensity coefficient function thus reflects the actual function form of the relative population distribution, which in turn approximately reflects the energy transfer probability function $f(E_j,E_i)$.

Consideration of the form of $F(X_L)$ for low collision numbers with the various buffer gases (Tables 2-2 through 2-5) reveals two classes of buffer molecules and two buffer molecules intermediate between these. The noble gases and N_2 are typically best fit by Chopped Gaussian functions throughout the range of collision numbers observed. The various experiments of CO are best fit by either Chopped Gaussian or

Biexponential functions, but in no consistent pattern, indicating that the choice may be subject to experimental uncertainty. NO_2 is generally but not always fit by the red-shifted Biexponential function for hard-sphere collision numbers up to two, but then is typically fit for larger collision numbers by more symmetric Chopped Gaussian functions (Equation 2-10) with μ within the range of observation and M near the excitation energy. The other buffer gases O_2, NO, CO_2, SO_2, and SF_6 consistently display population shifting to the red in the form of Biexponential best fits or of Chopped Gaussian fits with large μ and σ values, but M values near the excitation energy, parameters which approximate a Biexponential function.

The observation that the noble gases and N_2 have primarily Chopped Gaussian $F(X_L)$ indicates that the probability of the energy transfer process is relatively symmetric about the mean energy removed per collision event. The biased random walk model[63] describes exactly such a process. The collision encounter consists of an approach to distances comparable with the molecular diameter, during which close contacts between the buffer molecule and the atoms of the excited molecule allow vibration-to-translation energy transfer. The biased random walk model was expected to apply only to molecules considerably larger than NO_2 which had a sufficient number of vibrational fundamentals to behave statistically. However, NO_2 has been shown to behave statistically,[52] and the ability to average the fluorescence over multiple excited states within an energy range allows the NO_2^* population deconvolution method presented[55] to work. Thus, energy diffusion from NO_2^* into the

translational motions of the noble gases and N_2 and into the rotational and vibrational motions of N_2 are suggested as the predominant mechanism of energy transfer. The vibrational modes of N_2 and CO cannot participate as strongly in deactivation of NO_2^* as could those of O_2 and NO since the vibrational frequencies of the former are higher (Table 2-7).

In addition to translational and rotational degrees of freedom, the diatomic and polyatomic buffer molecules possess vibrational degrees of freedom of various frequencies. NO has an unpaired electron which may remove energy into its spin-orbit excited state. Unlike the rotational and translational modes, the energy for one quantum of a vibrational motion is a significant fraction of the excitation energy of NO_2^*. A collision involving vibrational-to-vibrational energy transfer must remove at least one quantum of buffer vibrational energy from the NO_2^*. Compared to the biased random walk model above, the energy transfer probability distribution function is skewed to the red by these V-to-V events. The probability of a given transfer decreases as the amount of energy to be transferred increases,[61] giving rise to an energy transfer probability function resembling a Biexponential. Buffers such as N_2 and CO with a single high-frequency fundamental will not as readily remove energy as will buffers with multiple, degenerate low-frequency fundamentals such as SF_6. SO_2 has fundamentals of considerably lower frequency than those of NO_2, while CO_2 has a doubly degenerate vibration which NO_2 in its ground electronic state lacks. The

contribution of vibration-to-vibration energy transfer may therefore play a more significant role in the initial relaxation of NO_2^* than has been indicated.[53]

6. Conclusions

The populations arising from energy removal by 13 buffer gases from NO_2^* excited to 18,828 cm^{-1} by a doubled Nd:YAG laser have been determined by NO_2 population deconvolution applied to dispersed fluorescence spectra. Each of the noble gases removes energy from NO_2^* at the same rate to within experimental uncertainty. The diatomic molecules remove energy at a faster rate than the noble gases due to the transfer of energy into the rotational and possibly vibrational modes of the diatomic molecule. The polyatomic molecules studied generally remove energy from NO_2^* even more quickly than do diatomic buffers, due at least in part to the presence of more vibrational degrees of freedom at lower frequencies. No consistent dependence of energy transfer rate upon collider mass, dipole moment, polarizability, or presence of an unpaired electron could be detected; however, contributions from these factors for individual gases cannot be ruled out. The energy transfer rate is a combination of vibrational-to-translational transfer for all gases, vibrational-to-rotational energy transfer for diatomic and polyatomic buffers, and vibrational-to-vibrational energy transfer when vibrational modes in the buffer readily accept energy from the NO_2^*. The energy spread increases as the third or fourth root of the collision number for most buffer gases studied.

Table 2-1

Collision Parameters and Rate Constants of the Buffer Gases

Temperature = 20 °C

Buffer	σ_{HS}, Å	k_{HS}, $cm^3\ s^{-1}$	σ_{LJ}, Å	ϵ/k, K	k_{close}, $cm^3\ s^{-1}$
NO_2	2.60	$1.10 \cdot 10^{-10}$	3.73[a]	226	$5.64 \cdot 10^{-10}$
He[b]	2.11	$2.26 \cdot 10^{-10}$	2.556	10.22	$5.97 \cdot 10^{-10}$
Ne	1.89	$1.05 \cdot 10^{-10}$	2.79	33.4	$4.01 \cdot 10^{-10}$
Ar	2.34	$1.03 \cdot 10^{-10}$	3.42	120	$4.83 \cdot 10^{-10}$
Kr	2.51	$9.37 \cdot 10^{-11}$	3.60	173	$4.58 \cdot 10^{-10}$
Xe	2.73	$9.52 \cdot 10^{-11}$	4.04	222	$5.01 \cdot 10^{-10}$
N_2	2.49	$1.21 \cdot 10^{-10}$	3.61	90.6	$5.39 \cdot 10^{-10}$
CO	2.51	$1.22 \cdot 10^{-10}$	3.69	99.4	$5.59 \cdot 10^{-10}$
NO	2.23	$1.07 \cdot 10^{-10}$	3.41	113.7	$5.18 \cdot 10^{-10}$
O_2	2.33	$1.09 \cdot 10^{-10}$	3.50	109.1	$5.17 \cdot 10^{-10}$
CO_2	2.57	$1.10 \cdot 10^{-10}$	4.11	199	$6.17 \cdot 10^{-10}$
SO_2	2.82	$1.11 \cdot 10^{-10}$	4.290	252	$6.15 \cdot 10^{-10}$
SF_6	2.57[c]	$8.84 \cdot 10^{-11}$	5.51	200.9	$6.87 \cdot 10^{-10}$

Lennard-Jones parameters are from Reference 64 and hard sphere diameters are from Reference 70 unless otherwise specified:

[a]Lennard-Jones parameters for NO_2 are from Reference 71.

[b]The quantum-mechanical Lennard-Jones parameters given in Reference 64 are used for this light gas.

[c]The hard-sphere collision diameter for SF_6 is based on viscosity data from Reference 72.

Table 2-2

Experimental conditions for NO_2^*-NO_2 excited at 532 nm

index	$P(NO_2)$, mT	t, μs	$c(NO_2) \cdot t$, 10^9 cm^{-3} s	Z_{HS}	Z_{close}
1	125.0 ± 8.2	0.4718 ± 0.0350	1.91 ± 0.19	0.21 ± 0.02	1.08 ± 0.11
2	143 ± 8	0.4646 ± 0.0364	2.15 ± 0.21	0.24 ± 0.02	1.21 ± 0.12
3	273.2 ± 0.3	0.4646 ± 0.0364	4.11 ± 0.32	0.45 ± 0.04	2.32 ± 0.18
4	140 ± 8	0.9205 ± 0.0514	4.18 ± 0.33	0.46 ± 0.04	2.36 ± 0.19
5	144.4 ± 13.9	0.9574 ± 0.0555	4.48 ± 0.50	0.49 ± 0.06	2.53 ± 0.28
6	327.7 ± 34.8	0.4653 ± 0.0424	4.94 ± 0.69	0.54 ± 0.08	2.79 ± 0.39
7	265.6 ± 13.3	0.9524 ± 0.0552	8.20 ± 0.63	0.90 ± 0.07	4.62 ± 0.36
8	549.9 ± 19.0	0.4653 ± 0.0424	8.29 ± 0.81	0.91 ± 0.09	4.68 ± 0.46
9	566.5 ± 3.2	0.4577 ± 0.0349	8.40 ± 0.64	0.92 ± 0.07	4.74 ± 0.36
10	138 ± 2	1.9770 ± 0.1015	8.84 ± 0.47	0.97 ± 0.05	4.99 ± 0.27
11	145.6 ± 11.2	1.9844 ± 0.1031	9.36 ± 0.87	1.03 ± 0.10	5.28 ± 0.49
12	322.7 ± 16.8	0.9639 ± 0.0599	10.08 ± 0.82	1.11 ± 0.09	5.69 ± 0.46
13	1024.5 ± 7.0	0.4666 ± 0.0346	15.49 ± 1.15	1.70 ± 0.13	8.74 ± 0.65
14	1042 ± 22	0.4648 ± 0.0340	15.69 ± 1.19	1.73 ± 0.13	8.85 ± 0.67
15	534.6 ± 5.9	0.9569 ± 0.0554	16.57 ± 0.98	1.82 ± 0.11	9.35 ± 0.55
16	548.0 ± 23.9	0.9679 ± 0.0600	17.18 ± 1.30	1.89 ± 0.14	9.69 ± 0.73
17	281.0 ± 7.4	1.9844 ± 0.1031	18.07 ± 1.05	1.99 ± 0.12	10.19 ± 0.59
18	333.0 ± 27.9	2.0159 ± 0.1069	21.75 ± 2.16	2.39 ± 0.24	12.27 ± 1.22
19	1096.0 ± 8.9	0.9624 ± 0.0545	34.17 ± 1.96	3.76 ± 0.22	19.27 ± 1.11
20	538.6 ± 5.0	1.9844 ± 0.1031	34.63 ± 1.83	3.81 ± 0.20	19.53 ± 1.03
21	1123 ± 22	0.9597 ± 0.0535	34.92 ± 2.06	3.84 ± 0.23	19.69 ± 1.16
22	584.5 ± 38.1	1.9979 ± 0.1060	37.83 ± 3.18	4.16 ± 0.35	21.34 ± 1.79
23	1096.4 ± 7.4	1.9844 ± 0.1025	70.49 ± 3.67	7.75 ± 0.40	39.76 ± 2.07
24	1165.7 ± 61.1	1.9997 ± 0.1028	75.53 ± 5.54	8.31 ± 0.61	42.60 ± 3.12

Note: extra figures beyond significant are included for both $P(NO_2)$ and t for use in calculations.

(Fit parameters and energy moments are provided on the next page.)

Table 2-2 continued: Fit parameters and energy moments for NO_2^*-NO_2 energy transfer

index	fit method	parameters[a] 1	2	M, cm^{-1}	$10^3 \times$ sum error	f_R[b]	<E> cm^{-1}	$<\Delta E^2>$ cm^{-1}
1	Gauss.	1.9145E+4	2.3438E+1	19750	3.8945	0.00	19559 ±183	292.99 ± 2.75
2	Biexp.	2.4414E+1	9.9219E+2	19750	4.3573	6.01E-05	19130 ±208	1053.6 ± 11.5
3	Biexp.	7.8125	9.9023E+2	19453	1.3486	7.80E-05	18842 ± 65	1049.1 ± 3.6
4	Biexp.	9.7656	9.9219E+2	19438	1.4554	8.09E-05	18837 ± 71	1051.0 ± 3.9
5	Biexp.	7.3242	1.6514E+3	19688	2.3233	2.98E-03	18447 ±119	1532.9 ± 9.9
6	Gauss.	2.3926E+4	2.7500E+3	19250	1.1584	5.21E-06	18482 ± 57	1065.2 ± 3.3
7	Gauss.	1.9104E+4	1.7812E+3	19563	2.2487	3.31E-07	18354 ±111	1218.7 ± 7.4
8	Gamma	5.8765E+2	4.4922E-1	19469	0.88638	2.20E-03	17964 ± 44	1532.2 ± 3.8
9	Biexp.	3.1738E+1	1.6055E+3	19375	1.8543	3.10E-03	18152 ± 92	1529.7 ± 7.7
10	Gauss.	1.9861E+4	2.0000E+3	19438	0.77524	1.20E-06	18366 ± 38	1188.4 ± 2.5
11	Gauss.	1.7982E+4	8.8672E+2	25132	2.5158	2.37E-19	18374 ±125	933.65 ± 6.35
12	Gauss.	1.9559E+4	2.3750E+3	19297	0.86370	7.20E-05	17854 ± 44	1431.7 ± 3.5
13	Gauss.	1.9141E+4	1.4062E+3	19684	1.6210	6.94E-04	17525 ± 88	1633.7 ± 8.2
14	Biexp.	3.6011E+1	2.9102E+3	19250	0.67087	0.0421	17183 ± 34	1970.5 ± 3.9
15	Gauss.	1.8844E+4	2.6172E+3	19344	0.55249	7.04E-04	17438 ± 28	1681.8 ± 2.7
16	Gauss.	1.7444E+4	2.2656E+3	19516	0.48923	6.97E-04	17076 ± 26	1759.2 ± 2.6
17	Gamma	1.3088E+4	4.4375E+3	29500	1.4087	3.23E-03	16515 ± 79	1897.5 ± 9.0
18	Gamma	3.5342E+2	3.4922	21000	0.67436	0.0102	16936 ± 35	1923.4 ± 4.0
19	Gamma	1.3092E+4	4.3984E+2	29500	1.4233	3.38E-03	16509 ± 79	1903.4 ± 9.2
20	Gamma	3.2764E+3	1.6602	20219	0.87211	*0.0795*	*16205 ± 47*	*2094.2 ± 6.0*
21	Gauss.	1.6331E+4	2.4531E+3	19672	0.58744	5.89E-03	16354 ± 32	1960.6 ± 3.8
22	Gauss.	1.5867E+4	2.3164E+3	22375	0.80374	6.22E-03	16287 ± 43	2134.1 ± 5.6
23	Gauss.	1.2500E+3	4.3750E+4	19828	2.0274	*0.5201*	*15842 ±106*	*2418.1 ± 16.1*
24	Biexp.	1.1719E+1	1.7383E+4	19625	1.7336	*0.3759*	*16095 ± 90*	*2356.7 ± 13.2*

[a]fit method determines identity of parameters 1 and 2; see Equations 2-9, 2-10, and 2-11.

[b]<E> and $<\Delta E^2>$ are invalid if this number is over 0.05; such entries are italicized.

Table 2-3

Experiment and Fit Parameters for NO_2^* Relaxation by Noble Gases

A. Pressures and Delay Times for Helium

index	$P(NO_2)$[a]	P(He)[a]	total P[a]	t, μs
1	25.6	342.9	373.0 ±4.0	0.4276 ±0.0293
2	25.2	686.9	715.3 ±1.7	0.4320 ±0.0299
3	25.6	342.9	373.0 ±4.0	0.9532 ±0.0538
4	29.5	959.2	989.5 ±0.9	0.4320 ±0.0299
5	51.4	1274.4	1333.7 ±2.3	0.4283 ±0.0287
6	22.3	329.8	353.8 ±0.8	1.9779 ±0.1022
7	25.2	686.9	715.3 ±1.7	0.9539 ±0.0537
8	47.6	1556.5	1609.2 ±1.6	0.4300 ±0.0290
9	29.5	959.2	989.5 ±0.9	0.9539 ±0.0537
10	51.4	1274.4	1333.7 ±2.3	0.9519 ±0.0536
11	25.1	639.6	671.7 ±2.9	1.9742 ±0.1018
12	47.6	1556.5	1609.2 ±1.6	0.9518 ±0.0538
13	30.2	964.1	997.1 ±1.2	1.9724 ±0.1018
14	49.6	1235.7	1288.5 ±2.5	1.9724 ±0.1018
15	52.2	1562.3	1620.2 ±2.3	1.9780 ±0.1027

[a]All pressures are given in mTorr. The NO_2 and He pressures are as metered into the sample cell; the total pressure measurement is read by the computer during the experiment, along with the standard deviation shown.

B. Concentration-Time Products and Collision Numbers for NO_2-He Deactivation

index	c(He) • t /10^8 cm^{-3} s	c(NO_2) • t /10^8 cm^{-3} s	Z_{HS} NO_2^*-He	Z_{HS} NO_2^*-NO_2
1	47.8 ±3.3	3.94 ±0.27	1.08 ±0.07	0.042 ±0.003
2	96.5 ±6.7	3.67 ±0.25	2.18 ±0.15	0.040 ±0.003
3	106.6 ±6.1	8.60 ±0.49	2.41 ±0.14	0.095 ±0.005
4	134.3 ±9.3	4.26 ±0.30	3.04 ±0.21	0.047 ±0.003
5	177.6 ±11.9	7.46 ±0.50	4.01 ±0.27	0.082 ±0.005
6	211.4 ±10.9	15.33 ±0.79	4.78 ±0.25	0.169 ±0.009
7	213.0 ±12.0	8.11 ±0.46	4.81 ±0.27	0.089 ±0.005
8	217.3 ±14.6	6.86 ±0.46	4.91 ±0.33	0.075 ±0.005
9	296.4 ±16.7	9.41 ±0.53	6.70 ±0.38	0.103 ±0.006
10	394.7 ±22.3	16.59 ±0.94	8.92 ±0.50	0.182 ±0.010
11	412.8 ±21.4	16.86 ±0.87	9.33 ±0.48	0.185 ±0.010
12	481.1 ±27.2	15.18 ±0.86	10.87 ±0.61	0.167 ±0.009
13	617.3 ±31.9	19.96 ±1.03	13.95 ±0.72	0.220 ±0.011
14	790.4 ±40.8	33.05 ±1.71	17.86 ±0.92	0.364 ±0.019
15	1004. ±52.1	34.69 ±1.80	22.69 ±1.18	0.382 ±0.020

Table 2-3 continued

C. Fit parameters and energy moments for NO_2^*-He energy transfer

index	fit method	parameters[a] 1	2	M, cm^{-1}	$10^3 \times$ sum error	f_R[b]	$<E>$ cm^{-1}	$<\Delta E^2>^{1/2}$ cm^{-1}
1	Gauss.	1.9084E+4	2.3438E+1	25132	3.7395	0.00	19497 ±177	292.57 ±109.66
2	Gamma	1.9727E+2	3.5000E+1	19688	10.333	0.00	19905 ±479	291.19 ±799.03
3	Gauss.	1.8800E+4	3.8125E+2	20500	2.0845	0.00	19213 ±100	479.55 ± 23.41
4	Gauss.	2.1371E+4	2.6562E+3	19922	3.7588	3.31E-05	18618 ±183	1414.3 ± 37.6
5	Gauss.	1.9047E+4	1.5625E+1	20250	11.077	0.00	19460 ±521	290.98 ±955.26
6	Gauss.	1.8555E+4	2.9687E+2	25132	4.8358	0.00	18970 ±233	415.95 ±140.45
7	Gauss.	1.8994E+4	2.7344E+1	20500	5.0037	0.00	19407 ±237	291.64 ±199.88
8	Gauss.	1.8354E+4	8.7946E+2	23000	3.0461	2.37E-21	18749 ±148	927.24 ± 31.05
9	Gauss.	1.8475E+4	2.1094E+3	19922	3.7837	4.10E-05	17943 ±190	1591.9 ± 39.6
10	Gauss.	1.8318E+4	2.6562E+2	20000	7.4946	0.00	18733 ±365	394.28 ±360.71
11	Gauss.	1.8168E+4	7.5000E+2	21500	5.3894	1.86E-27	18566 ±265	804.49 ± 99.73
12	Gauss.	1.7562E+4	1.2812E+3	25132	2.8266	2.55E-09	17930 ±143	1315.3 ± 26.2
13	Gauss.	1.7231E+4	1.7617E+3	20625	2.9865	2.21E-05	17452 ±155	1670.7 ± 29.2
14	Gauss.	1.6766E+4	1.5957E+3	25132	2.2361	1.58E-05	17109 ±119	1618.6 ± 20.1
15	Gauss.	1.6565E+4	1.4492E+3	25000	5.5859	3.76E-06	16919 ±300	1477.1 ± 88.3

[a]fit method determines identity of parameters 1 and 2; see Equations 2-9, 2-10, and 2-11.

[b]$<E>$ and $<\Delta E^2>^{1/2}$ are invalid if this number is over 0.05; such entries are italicized.

Table 2-3 continued

D. Pressures and Delay Times for Neon

index	$P(NO_2)$[a]	P(Ne)[a]	total P[a]	t, μs
1	25.7	347.2	375.3 ±1.6	0.4515 ±0.0299
2	28.1	659.9	690.6 ±2.3	0.4515 ±0.0299
3	25.7	347.2	375.3 ±1.6	0.9728 ±0.0556
4	31.1	945.1	979.8 ±2.7	0.4506 ±0.0297
5	40.7	1300.5	1342.8 ±1.2	0.4506 ±0.0297
6	28.1	659.9	690.6 ±2.3	0.9728 ±0.0556
7	29.3	337.5	369.4 ±3.1	1.9599 ±0.1016
8	45.4	1606.9	1657.3 ±2.3	0.4453 ±0.0297
9	31.1	945.1	979.8 ±2.7	0.9656 ±0.0545
10	40.7	1300.5	1342.8 ±1.2	0.9656 ±0.0545
11	30.5	680.1	713.7 ±2.2	1.9802 ±0.1027
12	45.4	1606.9	1657.3 ±2.3	0.9678 ±0.0554
13	32.0	927.8	962.7 ±1.8	1.9802 ±0.1027
14	41.4	1215.3	1260.2 ±1.8	1.9767 ±0.1029
15	44.0	1581.2	1631.2 ±2.9	1.9767 ±0.1029

[a]All pressures are given in mTorr. The NO_2 and Ne pressures are as metered into the sample cell; the total pressure measurement is read by the computer during the experiment, along with the standard deviation shown.

E. Concentration-Time Products and Collision Numbers for NO_2-Ne Deactivation

index	c(Ne) • t /10^8 cm^{-3} s	c(NO_2) • t /10^8 cm^{-3} s	Z_{HS} NO_2^*-Ne	Z_{HS} NO_2^*-NO_2
1	50.84 ±3.37	4.06 ±0.27	0.53 ±0.04	0.045 ±0.003
2	96.72 ±6.41	4.30 ±0.29	1.02 ±0.07	0.047 ±0.003
3	109.5 ±6.3	8.76 ±0.50	1.15 ±0.07	0.096 ±0.006
4	138.3 ±9.1	4.71 ±0.31	1.45 ±0.10	0.052 ±0.003
5	189.9 ±12.5	6.14 ±0.40	1.99 ±0.13	0.067 ±0.004
6	208.4 ±11.2	9.27 ±0.53	2.19 ±0.12	0.102 ±0.006
7	214.2 ±11.3	20.36 ±1.07	2.25 ±0.12	0.224 ±0.012
8	232.4 ±15.5	6.76 ±0.45	2.44 ±0.16	0.074 ±0.005
9	296.4 ±16.7	10.09 ±0.57	3.11 ±0.18	0.111 ±0.006
10	407.0 ±23.0	13.15 ±0.74	4.27 ±0.24	0.145 ±0.008
11	437.4 ±22.7	20.53 ±1.07	4.59 ±0.24	0.226 ±0.012
12	505.0 ±28.9	14.68 ±0.84	5.30 ±0.30	0.162 ±0.009
13	596.3 ±31.0	21.30 ±1.11	6.26 ±0.33	0.234 ±0.012
14	779.6 ±40.6	27.49 ±1.43	8.19 ±0.43	0.302 ±0.016
15	1016. ±52.9	29.07 ±1.52	10.67 ±0.55	0.320 ±0.017

Table 2-3 continued

F. Fit parameters and energy moments for NO_2^*-Ne energy transfer

index	fit method	parameters[a] 1	2	M, cm^{-1}	$10^3 \times$ sum error	f_R[b]	$<E>$ cm^{-1}	$<\Delta E^2>^{1/2}$ cm^{-1}
1	Gamma	8.3984E+1	1.0000E+1	19406	7.2573	0.00	19764 ±338	290.5 ±398.8
2	Gauss.	1.9206E+4	2.3438E+1	21000	7.2018	0.00	19647 ±337	292.3 ±394.2
3	Gauss.	1.9010E+4	2.3438E+1	21000	5.5427	0.00	19501 ±262	285.7 ±243.3
4	Gauss.	1.8859E+4	2.8125E+2	21000	2.5900	0.00	19305 ±123	402.7 ± 40.4
5	Gauss.	1.9025E+4	1.0312E+3	19844	2.8387	2.53E-18	19077 ±136	832.5 ± 28.3
6	Gauss.	1.8843E+4	2.3438E+1	21000	5.8902	0.00	19318 ±280	286.6 ±277.8
7	Gauss.	1.8591E+4	2.3437E+2	21000	6.0782	0.00	19147 ±292	345.9 ±252.5
8	Gauss.	1.8685E+4	3.7500E+2	21000	2.8549	0.00	19146 ±137	473.1 ± 43.1
9	Gauss.	1.8675E+4	1.0391E+3	19781	2.0647	4.92E-17	18853 ±101	883.1 ± 16.2
10	Gauss.	1.8062E+4	1.1055E+3	25132	3.2691	2.50E-13	18532 ±161	1140.4 ± 32.9
11	Gauss.	1.7862E+4	1.2773E+3	25132	5.4543	4.23E-10	18371 ±272	1303.5 ± 76.2
12	Gauss.	1.8220E+4	1.3047E+3	19875	2.4658	1.87E-10	18451 ±123	1144.8 ± 20.8
13	Gauss.	1.7948E+4	1.4453E+3	19875	2.5559	2.81E-08	18212 ±129	1273.3 ± 22.1
14	Gauss.	1.7364E+4	1.2969E+3	23500	3.1057	7.60E-09	17917 ±160	1316.3 ± 31.4
15	Gauss.	1.7022E+4	1.6133E+3	25132	3.4929	7.21E-06	17562 ±182	1624.9 ± 37.5

[a]fit method determines identity of parameters 1 and 2; see Equations 2-9, 2-10, and 2-11.

[b]$<E>$ and $<\Delta E^2>^{1/2}$ are invalid if this number is over 0.05; such entries are italicized.

Table 2-3 continued

G. Pressures and Delay Times for Argon

index	$P(NO_2)$[a]	P(Ar)[a]	total P[a]	t, μs
1	26.5	340.8	369.0 ±1.5	0.4323 ±0.0295
2	30.8	630.9	663.3 ±2.0	0.4323 ±0.0295
3	26.5	340.8	369.0 ±1.5	0.9580 ±0.0541
4	32.8	918.0	952.3 ±2.3	0.4332 ±0.0292
5	29.3	1175.7	1209.5 ±2.2	0.4332 ±0.0292
6	30.8	630.9	663.3 ±2.0	0.9580 ±0.0541
7	49.8	1472.5	1540.1 ±1.6	0.4276 ±0.0293
8	26.1	344.2	372.4 ±0.9	1.9762 ±0.1022
9	32.8	918.0	952.3 ±2.3	0.9540 ±0.0535
10	29.3	1175.7	1209.5 ±2.2	0.9540 ±0.0535
11	25.2	630.6	658.2 ±1.6	1.9859 ±0.1026
12	49.8	1472.5	1540.1 ±1.6	0.9532 ±0.0538
13	33.9	1214.7	1253.5 ±2.6	1.9780 ±0.1019
14	49.8	1472.5	1528.4 ±2.5	1.9780 ±0.1019

[a]All pressures are given in mTorr. The NO_2 and Ar pressures are as metered into the sample cell; the total pressure measurement is read by the computer during the experiment, along with the standard deviation shown.

H. Concentration-Time Products and Collision Numbers for NO_2-Ar Deactivation

index	c(Ar) • t /10^8 cm^{-3} s	c(NO_2) • t /10^8 cm^{-3} s	Z_{HS} NO_2^*-Ar	Z_{HS} NO_2^*-NO_2
1	47.7 ±3.3	4.02 ±0.27	0.49 ±0.03	0.044 ±0.003
2	88.4 ±6.0	4.54 ±0.31	0.91 ±0.06	0.050 ±0.003
3	105.6 ±6.0	8.91 ±0.50	1.09 ±0.06	0.098 ±0.006
4	128.9 ±8.7	4.78 ±0.32	1.33 ±0.09	0.053 ±0.004
5	165.5 ±11.2	4.23 ±0.29	1.70 ±0.12	0.047 ±0.003
6	195.8 ±11.1	10.05 ±0.57	2.02 ±0.11	0.111 ±0.006
7	206.2 ±14.1	7.22 ±0.49	2.12 ±0.15	0.079 ±0.005
8	220.4 ±11.4	18.08 ±0.94	2.27 ±0.12	0.199 ±0.010
9	283.8 ±15.9	10.52 ±0.59	2.92 ±0.16	0.116 ±0.006
10	364.5 ±20.5	9.32 ±0.52	3.75 ±0.21	0.102 ±0.006
11	406.6 ±21.0	16.92 ±0.88	4.19 ±0.22	0.186 ±0.010
12	459.6 ±26.0	16.09 ±0.91	4.73 ±0.27	0.177 ±0.010
13	780.9 ±40.3	22.42 ±1.16	8.04 ±0.42	0.247 ±0.013
14	946.4 ±48.8	33.13 ±1.71	9.75 ±0.50	0.364 ±0.019

Table 2-3 continued

I. Fit parameters and energy moments for NO_2^*-Ar energy transfer

index	fit method	parameters[a] 1	2	M, cm^{-1}	$10^3 \times$ sum error	f_R[b]	$\langle E \rangle$ cm^{-1}	$\langle \Delta E^2 \rangle^{1/2}$ cm^{-1}
1	Gauss.	1.9179E+4	2.3438E+1	25132	6.8519	0.00	19632 ±322	290.4 ±361.3
2	Gauss.	1.9092E+4	2.3438E+1	25132	5.5767	0.00	19532 ±263	290.6 ±242.2
3	Biexp.	9.7656	4.1016E+1	18813	5.4951	2.76E-93	19240 ±263	285.7 ±245.6
4	Gauss.	1.8879E+4	2.3438E+1	18953	5.9682	0.00	19324 ±284	289.6 ±282.0
5	Gauss.	1.8437E+4	8.7109E+2	25132	3.8301	3.97E-22	18859 ±186	918.3 ± 46.8
6	Gauss.	1.8581E+4	5.2344E+2	25132	4.3051	1.01E-58	19059 ±208	595.0 ± 79.1
7	Biexp.	2.0000E+4	2.0508E+1	18672	4.4822	0.00	19091 ±216	288.7 ±164.9
8	Gauss.	1.8303E+4	8.8672E+2	23000	3.6609	8.45E-21	18820 ±179	925.2 ± 43.7
9	Gauss.	1.8263E+4	8.1250E+2	23000	4.5368	3.42E-24	18731 ±222	860.2 ± 67.6
10	Gauss.	1.7629E+4	1.4258E+3	25132	3.5284	5.84E-08	18048 ±178	1455.0 ± 36.3
11	Gauss.	1.7638E+4	1.5469E+3	25000	2.6614	5.06E-07	18101 ±134	1571.0 ± 23.2
12	Gauss.	1.7824E+4	1.0820E+3	25000	3.7594	2.83E-13	18319 ±189	1116.3 ± 43.5
13	Gauss.	1.6948E+4	1.5312E+3	25000	3.2271	3.58E-06	17449 ±169	1550.1 ± 33.8
14	Gauss.	1.6646E+4	1.6484E+3	25000	3.8117	2.95E-05	17213 ±203	1650.3 ± 45.0

[a]fit method determines identity of parameters 1 and 2; see Equations 2-9, 2-10, and 2-11.

[b]$\langle E \rangle$ and $\langle \Delta E^2 \rangle^{1/2}$ are invalid if this number is over 0.05; such entries are italicized.

Table 2-3 continued

J. Pressures and Delay Times for Krypton

index	$P(NO_2)$[a]	P(Kr)[a]	total P[a]	t, μs
1	24.8	318.4	346.0 ±1.5	0.4485 ±0.0297
2	25.0	639.2	667.8 ±2.2	0.4485 ±0.0297
3	24.8	318.4	346.0 ±1.5	0.9431 ±0.0543
4	33.3	923.1	961.8 ±1.9	0.4471 ±0.0293
5	33.5	1231.9	1268.3 ±1.6	0.4471 ±0.0293
6	25.0	639.2	667.8 ±2.2	0.9431 ±0.0543
7	25.9	346.7	375.4 ±1.4	1.9807 ±0.1020
8	47.4	1533.0	1588.6 ±2.7	0.4478 ±0.0295
9	33.3	923.1	961.8 ±1.9	0.9601 ±0.0550
10	33.5	1231.9	1268.3 ±1.6	0.9601 ±0.0550
11	24.6	626.4	656.2 ±1.7	1.9892 ±0.1028
12	47.4	1533.0	1588.6 ±2.7	0.9686 ±0.0553
13	32.4	923.6	960.3 ±2.6	1.9685 ±0.1016
14	42.4	1205.3	1252.5 ±1.7	1.9859 ±0.1028
15	45.2	1512.1	1562.4 ±2.3	1.9859 ±0.1028

[a]All pressures are given in mTorr. The NO_2 and Kr pressures are as metered into the sample cell; the total pressure measurement is read by the computer during the experiment, along with the standard deviation shown.

K. Concentration-Time Products and Collision Numbers for NO_2-Kr Deactivation

index	c(Kr) • t /10^8 cm^{-3} s	c(NO_2) • t /10^8 cm^{-3} s	Z_{HS} NO_2^*-Kr	Z_{HS} NO_2^*-NO_2
1	46.4 ±3.1	3.92 ±0.26	0.43 ±0.03	0.043 ±0.003
2	93.2 ±6.2	3.80 ±0.25	0.87 ±0.06	0.042 ±0.003
3	97.5 ±5.6	8.23 ±0.48	0.91 ±0.05	0.091 ±0.005
4	134.3 ±8.8	5.03 ±0.33	1.26 ±0.08	0.055 ±0.004
5	178.7 ±11.7	5.00 ±0.33	1.67 ±0.11	0.055 ±0.004
6	196.1 ±11.3	7.98 ±0.46	1.84 ±0.11	0.088 ±0.005
7	222.9 ±11.5	18.00 ±0.93	2.09 ±0.11	0.198 ±0.010
8	223.3 ±14.7	7.13 ±0.47	2.09 ±0.14	0.078 ±0.005
9	288.4 ±16.5	10.79 ±0.62	2.70 ±0.15	0.119 ±0.007
10	383.8 ±22.0	10.73 ±0.62	3.60 ±0.21	0.118 ±0.007
11	406.3 ±21.0	16.61 ±0.86	3.81 ±0.20	0.183 ±0.009
12	483.1 ±27.6	15.41 ±0.88	4.53 ±0.26	0.170 ±0.010
13	591.0 ±30.6	21.49 ±1.11	5.54 ±0.29	0.236 ±0.012
14	777.6 ±40.3	28.35 ±1.47	7.29 ±0.38	0.312 ±0.016
15	975.3 ±50.5	30.05 ±1.56	9.14 ±0.47	0.331 ±0.017

Table 2-3 continued

L. Fit parameters and energy moments for NO_2^*-Kr energy transfer

index	fit method	parameters[a] 1	2	M, cm^{-1}	$10^3 \times$ sum error	f_R[b]	$<E>$ cm^{-1}	$<\Delta E^2>^{1/2}$ cm^{-1}
1	Biexp.	2.7466E+1	1.1484E+3	20063	2.8536	1.71E-04	19310 ±142	1192.0 ± 25.6
2	Gauss.	1.8915E+4	4.6875E+1	20250	5.6581	0.00	19357 ±268	292.5 ±249.8
3	Biexp.	2.2583E+1	1.5898E+3	20063	1.8072	1.89E-03	18923 ± 91	1523.8 ± 12.7
4	Gauss.	1.8795E+4	2.3438E+1	20250	4.3876	0.00	19245 ±209	289.8 ±154.3
5	Biexp.	3.2349E+1	1.3945E+3	19516	1.6660	1.17E-03	18520 ± 82	1393.0 ± 10.9
6	Gauss.	1.8502E+4	7.6562E+2	24000	5.4688	1.73E-28	18956 ±264	817.5 ± 96.7
7	Gauss.	1.9434E+4	1.9844E+3	19672	2.8868	1.93E-06	18494 ±143	1288.5 ± 25.8
8	Gauss.	1.8474E+4	4.6875E+2	21000	5.8288	3.69E-72	18933 ±282	549.5 ±152.6
9	Gauss.	1.8212E+4	9.2578E+2	24000	4.0050	7.45E-19	18677 ±197	968.1 ± 50.2
10	Gauss.	1.9805E+4	2.6875E+3	19453	2.9292	3.26E-04	17862 ±148	1584.7 ± 27.0
11	Gauss.	1.7452E+4	1.4648E+3	25132	4.7416	2.37E-07	17918 ±241	1490.1 ± 59.2
12	Gauss.	1.7609E+4	1.2187E+3	23500	4.0645	3.16E-10	18087 ±206	1249.6 ± 48.2
13	Gauss.	1.7161E+4	1.4629E+3	23500	2.9191	7.55E-07	17660 ±151	1484.7 ± 28.3
14	Gauss.	1.6392E+4	1.8242E+3	24500	3.4956	2.96E-04	16926 ±187	1807.5 ± 39.8
15	Gauss.	1.6276E+4	1.7812E+3	24500	2.5379	2.77E-04	16827 ±138	1764.2 ± 25.5

[a]fit method determines identity of parameters 1 and 2; see Equations 2-9, 2-10, and 2-11.

[b]$<E>$ and $<\Delta E^2>^{1/2}$ are invalid if this number is over 0.05; such entries are italicized.

Table 2-3 continued: M. Pressures and Delay Times for Xenon

index	$P(NO_2)$[a]	P(Xe)[a]	total P[a]	t, μs
1	18.4	278.6	304.3 ±3.2	0.4679 ±0.0341
2	24.5	518.2	551.5 ±3.4	0.4425 ±0.0312
3	21.2	291.7	305.0 ±3.4	0.9566 ±0.0539
4	48.0	672.1	727.5 ±2.9	0.4280 ±0.0296
5	55.4	852.9	915.3 ±2.6	0.4280 ±0.0296
6	24.5	518.2	551.5 ±3.4	0.9652 ±0.0560
7	59.4	1240.3	1315.4 ±1.7	0.4390 ±0.0300
8	23.1	290.2	319.2 ±4.6	1.9855 ±0.1023
9	48.0	672.1	727.5 ±2.9	0.9450 ±0.0543
10	57.5	1659.5	1720.5 ±2.8	0.4390 ±0.0300
11	55.4	852.9	915.3 ±2.6	0.9450 ±0.0543
12	24.3	518.9	548.9 ±5.2	1.9905 ±0.1026
13	24.5	520.7	556.9 ±5.7	1.9905 ±0.1026
14	59.4	1240.3	1315.4 ±1.7	0.9482 ±0.0543
15	57.5	673.0	734.2 ±2.6	1.9935 ±0.1037
16	57.5	1659.5	1720.5 ±2.8	0.9482 ±0.0543
17	57.3	883.8	949.6 ±3.0	1.9758 ±0.1027
18	59.4	1240.3	1301.5 ±2.5	1.9772 ±0.1026
19	57.5	1659.5	1720.5 ±2.8	1.9968 ±0.1037

[a]All pressures are given in mTorr. The NO_2 and Xe pressures are as metered into the sample cell; the total pressure measurement is read by the computer during the experiment, along with the standard deviation shown.

N. Concentration-Time Products and Collision Numbers for NO_2-Xe Deactivation

index	$c(Xe) \cdot t$ $/10^8$ cm^{-3} s	$c(NO_2) \cdot t$ $/10^8$ cm^{-3} s	Z_{HS} NO_2^*-Xe	Z_{HS} NO_2^*-NO_2
1	43.1 ±3.2	3.05 ±0.22	0.41 ±0.03	0.034 ±0.002
2	75.3 ±5.3	3.74 ±0.26	0.72 ±0.05	0.041 ±0.003
3	87.7 ±5.0	6.87 ±0.39	0.83 ±0.05	0.076 ±0.004
4	93.7 ±6.5	7.21 ±0.50	0.89 ±0.06	0.079 ±0.005
5	118.7 ±8.2	8.25 ±0.57	1.13 ±0.08	0.091 ±0.006
6	164.3 ±9.6	8.15 ±0.48	1.56 ±0.09	0.090 ±0.005
7	178.1 ±12.2	8.96 ±0.61	1.70 ±0.12	0.099 ±0.007
8	189.0 ±10.2	16.35 ±0.87	1.80 ±0.10	0.180 ±0.010
9	206.8 ±11.9	15.91 ±0.92	1.97 ±0.11	0.175 ±0.010
10	236.2 ±16.1	8.48 ±0.58	2.25 ±0.15	0.093 ±0.006
11	262.0 ±15.1	18.20 ±1.05	2.49 ±0.14	0.200 ±0.012
12	337.4 ±17.7	16.58 ±0.87	3.21 ±0.17	0.182 ±0.010
13	342.3 ±18.0	16.90 ±0.89	3.26 ±0.17	0.186 ±0.010
14	384.8 ±22.0	19.35 ±1.11	3.66 ±0.21	0.213 ±0.012
15	433.7 ±22.6	40.52 ±2.11	4.13 ±0.22	0.446 ±0.023
16	510.3 ±29.2	18.32 ±1.05	4.86 ±0.28	0.201 ±0.012
17	568.5 ±29.6	39.41 ±2.05	5.41 ±0.28	0.434 ±0.023
18	793.8 ±41.2	39.93 ±2.07	7.56 ±0.39	0.439 ±0.023
19	1074.5 ±55.8	38.57 ±2.00	10.23 ±0.53	0.424 ±0.022

Table 2-3 continued

O. Fit parameters and energy moments for NO_2^*-Xe energy transfer

index	fit method	parameters[a] 1	2	M, cm^{-1}	$10^3 \times$ sum error	f_R[b]	$<E>$ cm^{-1}	$<\Delta E^2>^{1/2}$ cm^{-1}
1	Biexp.	9.7656	1.2295E+03	19781	4.2492	3.75E-04	18922 ±205	1268.5 ± 46.9
2	Gauss.	1.8698E+04	9.8437E+02	25132	4.1236	9.69E-19	19112 ±198	1027.0 ± 48.8
3	Gauss.	1.8695E+04	1.8750E+01	25132	1.9824	0.00	19151 ± 95	286.6 ± 33.2
4	Gauss.	1.9096E+04	9.0625E+02	19563	3.9020	1.70E-23	19085 ±188	696.9 ± 57.5
5	Gauss.	1.9160E+04	1.1875E+03	19656	2.2204	1.49E-14	18938 ±108	858.9 ± 18.4
6	Gauss.	1.8352E+04	7.1094E+02	25132	7.6784	1.22E-31	18810 ±374	766.5 ±197.4
7	Gauss.	1.8435E+04	5.8594E+02	21500	4.9293	1.64E-46	18902 ±239	651.0 ± 96.3
8	Gauss.	2.0840E+04	2.7812E+03	19594	1.7703	1.67E-04	18246 ± 88	1503.9 ± 12.5
9	Gamma	8.7805E+03	5.9766E+01	27000	3.5856	9.54E-09	18559 ±177	1182.3 ± 38.0
10	Gauss.	1.8274E+04	1.2734E+03	20063	3.1430	6.52E-11	18512 ±155	1148.6 ± 30.7
11	Gauss.	1.8109E+04	1.4766E+03	20016	2.5419	2.93E-08	18318 ±127	1286.1 ± 21.6
12	Gauss.	1.7637E+04	1.6344E+03	20688	1.9849	1.92E-06	17985 ±101	1551.8 ± 15.2
13	Gamma	2.3096E+03	6.7969	20250	5.8197	4.08E-07	18105 ±296	995.2 ±104.3
14	Gauss.	1.7636E+04	1.2148E+03	25000	3.9313	2.42E-10	18140 ±199	1242.9 ± 45.7
15	Gauss.	1.7419E+04	1.3828E+03	25000	4.1105	5.44E-08	18057 ±210	1386.1 ± 48.8
16	Gauss.	1.7198E+04	1.5098E+03	25132	3.0918	1.19E-06	17671 ±160	1532.7 ± 30.7
17	Gauss.	1.6678E+04	1.6836E+03	24000	2.9056	4.39E-05	17288 ±155	1677.7 ± 29.8
18	Gauss.	1.6564E+04	1.7187E+03	25132	3.3238	7.98E-05	17176 ±178	1706.9 ± 36.7
19	Gauss.	1.5854E+04	2.0664E+03	20563	2.4476	2.61E-03	16457 ±136	1890.2 ± 25.7

[a]fit method determines identity of parameters 1 and 2; see Equations 2-9, 2-10, and 2-11.

[b]$<E>$ and $<\Delta E^2>^{1/2}$ are invalid if this number is over 0.05; such entries are italicized.

Table 2-4

Experiment and Fit Parameters for NO_2^* Relaxation by Diatomic Gases

A. Pressures and Delay Times for Nitrogen

index	$P(NO_2)$[a]	$P(N_2)$[a]	total P[a]	t, μs
1	26.4	359.7	388.2 ±0.8	0.4464 ±0.0300
2	28.7	700.1	730.8 ±1.0	0.4464 ±0.0300
3	26.4	359.7	388.2 ±0.8	0.9737 ±0.0563
4	35.0	914.4	953.9 ±1.1	0.4425 ±0.0292
5	35.5	1217.8	1259.5 ±3.2	0.4425 ±0.0292
6	27.4	319.1	346.4 ±6.4	1.9680 ±0.1033
7	42.7	1516.8	1570.0 ±2.3	0.4420 ±0.0295
8	28.7	700.1	730.8 ±1.0	0.9737 ±0.0563
9	35.0	914.4	953.9 ±1.1	0.9668 ±0.0558
10	35.5	1217.8	1259.5 ±3.2	0.9668 ±0.0558
11	29.2	680.3	711.7 ±1.8	1.9688 ±0.1027
12	42.7	1516.8	1570.0 ±2.3	0.9626 ±0.0552
13	36.5	917.7	957.4 ±1.5	1.9688 ±0.1027
14	34.7	1219.5	1257.4 ±1.4	1.9770 ±0.1029
15	42.7	1516.8	1563.8 ±1.3	1.9770 ±0.1029

[a]All pressures are given in mTorr. The NO_2 and N_2 pressures are as metered into the sample cell; the total pressure measurement is read by the computer during the experiment, along with the standard deviation shown.

B. Concentration-Time Products and Collision Numbers for NO_2-N_2 Deactivation

index	$c(N_2) \cdot t$ /10^8 cm^{-3} s	$c(NO_2) \cdot t$ /10^8 cm^{-3} s	Z_{HS} NO_2^*-N_2	Z_{HS} NO_2^*-NO_2
1	52.0 ±3.5	4.12 ±0.28	0.63 ±0.04	0.045 ±0.003
2	101.4 ±6.8	4.33 ±0.29	1.23 ±0.08	0.048 ±0.003
3	113.5 ±6.6	8.99 ±0.52	1.37 ±0.08	0.099 ±0.006
4	131.5 ±8.7	5.24 ±0.35	1.59 ±0.11	0.058 ±0.004
5	175.3 ±11.6	5.26 ±0.35	2.12 ±0.14	0.058 ±0.004
6	201.9 ±11.4	18.97 ±1.06	2.44 ±0.14	0.209 ±0.012
7	218.5 ±14.6	6.33 ±0.42	2.64 ±0.18	0.070 ±0.005
8	221.1 ±12.8	9.45 ±0.55	2.68 ±0.15	0.104 ±0.006
9	287.4 ±16.6	11.44 ±0.66	3.48 ±0.20	0.126 ±0.007
10	383.0 ±22.1	11.50 ±0.66	4.63 ±0.27	0.127 ±0.007
11	434.5 ±22.7	19.49 ±1.02	5.26 ±0.27	0.214 ±0.011
12	475.9 ±27.3	13.78 ±0.79	5.76 ±0.33	0.152 ±0.009
13	586.4 ±30.6	24.29 ±1.27	7.10 ±0.37	0.267 ±0.014
14	782.5 ±40.7	22.92 ±1.19	9.47 ±0.49	0.252 ±0.013
15	973.5 ±50.7	28.20 ±1.47	11.78 ±0.61	0.310 ±0.016

Table 2-4 continued

C. Fit parameters and energy moments for NO_2^*-N_2 energy transfer

index	fit method	parameters[a] 1	2	M, cm^{-1}	$10^3 \times$ sum error	f_R[b]	$\langle E \rangle$ cm^{-1}	$\langle \Delta E^2 \rangle^{1/2}$ cm^{-1}
1	Gamma	1.2891E+2	2.0000E+1	19063	4.5013	0.00	19376 ±213	289.5 ±160.1
2	Gauss.	1.8637E+4	6.0156E+2	23000	3.5501	2.70E-46	19071 ±171	667.1 ± 49.7
3	Gauss.	1.8530E+4	6.6406E+2	23000	4.2595	7.15E-38	18994 ±205	722.1 ± 66.3
4	Gauss.	2.0777E+4	2.2812E+3	19750	4.0698	4.11E-06	18665 ±198	1257.6 ± 44.6
5	Gauss.	2.4570E+4	3.6875E+3	19672	3.0618	4.59E-04	18357 ±150	1527.5 ± 27.3
6	Gauss.	1.7776E+4	1.2539E+3	23500	4.9112	3.17E-10	18274 ±246	1281.4 ± 64.6
7	Gauss.	1.7789E+4	1.2461E+3	23000	3.5985	2.32E-10	18200 ±180	1279.5 ± 38.1
8	Gauss.	1.8375E+4	1.3984E+3	19781	3.6130	1.74E-09	18409 ±179	1153.1 ± 39.2
9	Gauss.	1.7522E+4	1.4375E+3	25132	4.8144	1.10E-07	17953 ±244	1465.5 ± 60.6
10	Gauss.	1.7224E+4	1.9844E+3	20281	3.3917	1.68E-04	17386 ±175	1777.3 ± 35.2
11	Gauss.	1.7032E+4	1.6602E+3	20438	2.8245	1.42E-05	17430 ±148	1598.8 ± 27.3
12	Gauss.	1.6714E+4	1.6016E+3	25132	3.4917	1.48E-05	17148 ±185	1620.2 ± 38.8
13	Gauss.	1.6208E+4	1.9062E+3	23500	3.6351	6.47E-04	16720 ±196	1870.2 ± 42.8
14	Gauss.	1.5809E+4	2.5078E+3	20094	2.1451	0.0110	16246 ±117	2037.8 ± 21.5
15	Gauss.	1.5364E+4	2.2812E+3	25132	6.0363	0.0102	16067 ±332	2057.9 ± 96.8

[a]fit method determines identity of parameters 1 and 2; see Equations 2-9, 2-10, and 2-11.

[b]$\langle E \rangle$ and $\langle \Delta E^2 \rangle^{1/2}$ are invalid if this number is over 0.05; such entries are italicized.

Table 2-4 continued

D. Pressures and Delay Times for Oxygen

index	$P(NO_2)$[a]	$P(O_2)$[a]	total P[a]	t, μs
1	22.9	344.5	367.9 ±1.6	0.4487 ±0.0298
2	27.7	621.9	651.4 ±1.7	0.4487 ±0.0298
3	22.9	344.5	367.9 ±1.6	0.9658 ±0.0557
4	42.3	912.6	957.1 ±4.1	0.4425 ±0.0297
5	47.7	1258.5	1307.1 ±1.5	0.4446 ±0.0293
6	27.7	621.9	651.4 ±1.7	0.9658 ±0.0557
7	45.9	1514.1	1559.7 ±3.2	0.4446 ±0.0293
8	23.2	344.0	374.9 ±6.8	1.9690 ±0.1022
9	42.3	912.6	957.1 ±4.1	0.9658 ±0.0557
10	47.7	1258.5	1307.1 ±1.5	0.9577 ±0.0553
11	29.1	624.9	656.7 ±2.3	1.9675 ±0.1026
12	45.9	1514.1	1559.7 ±3.2	0.9577 ±0.0553
13	38.3	912.9	951.7 ±1.2	1.9675 ±0.1026
14	47.9	1245.9	1294.9 ±1.7	1.9750 ±0.1028
15	45.6	1501.3	1548.9 ±1.4	1.9813 ±0.1032

[a]All pressures are given in mTorr. The NO_2 and O_2 pressures are as metered into the sample cell; the total pressure measurement is read by the computer during the experiment, along with the standard deviation shown.

E. Concentration-Time Products and Collision Numbers for NO_2-O_2 Deactivation

index	$c(O_2) \cdot t$ /10^8 cm^{-3} s	$c(NO_2) \cdot t$ /10^8 cm^{-3} s	Z_{HS} NO_2^*-O_2	Z_{HS} NO_2^*-NO_2
1	49.9 ±3.3	3.56 ±0.24	0.54 ±0.04	0.039 ±0.003
2	90.5 ±6.0	4.22 ±0.28	0.99 ±0.07	0.046 ±0.003
3	107.5 ±6.2	7.65 ±0.44	1.17 ±0.07	0.084 ±0.005
4	130.9 ±8.8	6.36 ±0.43	1.43 ±0.10	0.070 ±0.005
5	181.2 ±12.0	7.14 ±0.47	1.98 ±0.13	0.079 ±0.005
6	194.8 ±11.2	9.08 ±0.52	2.12 ±0.12	0.100 ±0.006
7	217.9 ±14.4	6.81 ±0.45	2.38 ±0.16	0.075 ±0.005
8	223.0 ±12.4	16.13 ±0.89	2.43 ±0.14	0.177 ±0.010
9	285.6 ±16.5	13.88 ±0.80	3.11 ±0.18	0.153 ±0.009
10	390.2 ±22.5	15.37 ±0.89	4.25 ±0.25	0.169 ±0.010
11	399.1 ±20.9	19.49 ±1.02	4.35 ±0.23	0.214 ±0.011
12	469.3 ±27.1	14.67 ±0.85	5.12 ±0.30	0.161 ±0.009
13	581.2 ±30.3	25.45 ±1.33	6.34 ±0.33	0.280 ±0.015
14	796.7 ±41.5	31.86 ±1.66	8.68 ±0.45	0.350 ±0.018
15	964.1 ±50.2	30.20 ±1.57	10.51 ±0.55	0.332 ±0.017

Table 2-4 continued

F. Fit parameters and energy moments for NO_2^*-O_2 energy transfer

index	fit method	parameters[a] 1	2	M, cm^{-1}	$10^3 \times$ sum error	f_R[b]	$<E>$ cm^{-1}	$<\Delta E^2>^{1/2}$ cm^{-1}
1	Biexp.	2.7466E+1	9.1016E+2	19469	2.6759	3.38E-05	18955 ±127	974.2 ± 23.0
2	Biexp.	2.5024E+1	1.0586E+3	19266	1.7119	1.73E-04	18608 ± 82	1109.5 ± 11.1
3	Biexp.	1.0986E+1	1.2871E+3	19344	1.7509	7.57E-04	18491 ± 84	1304.4 ± 11.4
4	Gauss.	1.8690E+4	1.7109E+3	19688	2.0455	3.32E-07	18318 ±100	1276.5 ± 14.7
5	Gauss.	4.0808E+4	5.7812E+3	19109	1.0461	6.01E-04	18170 ± 51	1333.1 ± 5.7
6	Biexp.	2.2583E+1	1.6953E+3	19125	1.8898	4.84E-03	17909 ± 93	1560.3 ± 13.7
7	Biexp.	2.5024E+1	2.0078E+3	19266	1.8883	0.0103	17780 ± 93	1724.5 ± 14.0
8	Gauss.	1.7940E+4	1.5312E+3	19688	2.1044	1.91E-07	18064 ±105	1301.3 ± 16.0
9	Gauss.	1.7269E+4	1.5430E+3	20219	1.9317	1.61E-06	17613 ± 98	1469.0 ± 14.8
10	Gauss.	1.7529E+4	2.1240E+3	19328	1.1269	2.80E-04	17251 ± 58	1641.3 ± 7.6
11	Gamma	1.8608E+3	1.4531	19594	1.1617	0.0106	17078 ± 60	1766.8 ± 8.3
12	Biexp.	9.4849E+2	3.9062E+3	19453	1.8450	*0.1051*	*16558 ± 95*	*2053.2 ± 16.3*
13	Biexp.	3.0078E+3	3.1250E+3	19422	3.5681	*0.0929*	*16365 ±188*	*2005.8 ± 41.1*
14	Gauss.	1.4670E+4	3.6523E+3	19563	2.2847	*0.1172*	*15723 ±124*	*2129.4 ± 24.3*
15	Biexp.	1.5479E+3	3.8500E+4	19797	1.9711	*0.4926*	*15628 ±107*	*2162.1 ± 20.2*

[a]fit method determines identity of parameters 1 and 2; see Equations 2-9, 2-10, and 2-11.

[b]$<E>$ and $<\Delta E^2>^{1/2}$ are invalid if this number is over 0.05; such entries are italicized.

Table 2-4 continued

G. Pressures and Delay Times for Carbon Monoxide

index	$P(NO_2)$[a]	P(CO)[a]	total P[a]	t, μs
1	26.6	257.3	286.9 ±1.8	0.4440 ±0.0291
2	30.3	527.9	561.9 ±2.3	0.4440 ±0.0291
3	26.6	257.3	286.9 ±1.8	0.9615 ±0.0549
4	42.7	806.0	852.0 ±1.3	0.4464 ±0.0309
5	46.9	1022.8	1074.1 ±1.7	0.4429 ±0.0301
6	30.3	527.9	561.9 ±2.3	0.9615 ±0.0549
7	26.5	267.6	297.0 ±2.2	1.9683 ±0.1028
8	53.2	1257.6	1315.0 ±2.3	0.4429 ±0.0301
9	42.7	806.0	852.0 ±1.3	0.9623 ±0.0558
10	46.9	1022.8	1074.1 ±1.7	0.9645 ±0.0558
11	28.0	558.2	590.0 ±1.7	1.9730 ±0.1030
12	53.2	1257.6	1315.0 ±2.3	0.9645 ±0.0558
13	43.8	834.8	883.7 ±1.5	1.9730 ±0.1030
14	49.4	1025.4	1078.5 ±2.8	1.9617 ±0.1021
15	56.6	1268.7	1328.3 ±0.9	1.9683 ±0.1023

[a]All pressures are given in mTorr. The NO_2 and CO pressures are as metered into the sample cell; the total pressure measurement is read by the computer during the experiment, along with the standard deviation shown.

H. Concentration-Time Products and Collision Numbers for NO_2-CO Deactivation

index	$c(CO) \cdot t$ $/10^8$ cm^{-3} s	$c(NO_2) \cdot t$ $/10^8$ cm^{-3} s	Z_{HS} NO_2^*-CO	Z_{HS} NO_2^*-NO_2
1	37.0 ±2.4	4.27 ±0.28	0.45 ±0.03	0.047 ±0.003
2	76.2 ±5.0	4.64 ±0.30	0.93 ±0.06	0.051 ±0.003
3	80.1 ±4.6	9.24 ±0.53	0.98 ±0.06	0.102 ±0.006
4	116.7 ±8.1	6.53 ±0.45	1.42 ±0.10	0.072 ±0.005
5	147.1 ±10.0	7.07 ±0.48	1.79 ±0.12	0.078 ±0.005
6	165.0 ±9.4	10.05 ±0.58	2.01 ±0.11	0.111 ±0.006
7	170.6 ±9.0	18.76 ±0.99	2.08 ±0.11	0.206 ±0.011
8	180.7 ±12.3	7.98 ±0.54	2.20 ±0.15	0.088 ±0.006
9	251.6 ±14.6	14.07 ±0.82	3.07 ±0.18	0.155 ±0.009
10	320.3 ±18.5	15.39 ±0.89	3.91 ±0.23	0.169 ±0.010
11	358.2 ±18.7	18.92 ±0.99	4.37 ±0.23	0.208 ±0.011
12	393.6 ±22.8	17.38 ±1.01	4.80 ±0.28	0.191 ±0.011
13	535.3 ±28.0	29.64 ±1.55	6.53 ±0.34	0.326 ±0.017
14	652.5 ±34.0	33.02 ±1.72	7.96 ±0.41	0.363 ±0.019
15	809.3 ±42.0	37.79 ±1.96	9.87 ±0.51	0.416 ±0.022

Table 2-4 continued

I. Fit parameters and energy moments for NO_2^*-CO energy transfer

index	fit method	parameters[a] 1	2	M, cm^{-1}	$10^3 \times$ sum error	f_R[b]	$\langle E \rangle$ cm^{-1}	$\langle \Delta E^2 \rangle^{1/2}$ cm^{-1}
1	Gauss.	1.8858E+4	1.9531E+1	21000	4.0963	0.00	19320 ±196	288.7 ±136.1
2	Biexp.	2.8687E+1	1.1172E+3	19266	2.7155	2.61E-04	18547 ±134	1161.7 ± 23.9
3	Gauss.	1.8510E+4	4.2969E+2	21000	1.3148	3.46E-87	18984 ± 64	514.5 ± 9.7
4	Biexp.	1.4038E+1	1.4844E+3	19281	1.2896	1.97E-03	18234 ± 64	1445.0 ± 8.0
5	Gauss.	1.7935E+4	9.2578E+2	23000	1.6845	4.01E-18	18374 ± 85	969.7 ± 11.9
6	Biexp.	5.7373E+1	1.6641E+3	19125	2.3929	4.35E-03	17907 ±121	1542.4 ± 20.0
7	Biexp.	3.7231E+1	1.4062E+3	19125	2.7065	1.58E-03	18213 ±136	1377.8 ± 23.9
8	Biexp.	5.0659E+1	1.8867E+3	19125	1.4306	7.99E-03	17723 ± 73	1654.1 ± 10.0
9	Biexp.	1.0522E+3	1.8984E+3	19391	1.4270	0.0114	17422 ± 74	1719.9 ± 10.5
10	Gauss.	1.7281E+4	1.5469E+3	19469	0.8859	1.26E-06	17508 ± 47	1380.5 ± 5.3
11	Gamma	3.0237E+3	4.3579	20563	1.2743	1.17E-03	17350 ± 67	1586.7 ± 9.0
12	Gamma	1.8516E+3	1.1641	19406	1.4379	0.0234	16740 ± 77	1856.4 ± 11.8
13	Gamma	3.4590E+3	2.9141	20188	1.4840	0.0263	16431 ± 82	1872.7 ± 13.1
14	Gamma	1.1494E+4	3.1689E+1	27750	0.8515	5.56E-03	16565 ± 48	1912.6 ± 6.7
15	Gamma	5.6250E+4	0.23633	19188	1.4261	*0.5876*	*15478 ± 81*	*2117.9 ± 14.3*

[a]fit method determines identity of parameters 1 and 2; see Equations 2-9, 2-10, and 2-11.

[b]$\langle E \rangle$ and $\langle \Delta E^2 \rangle^{1/2}$ are invalid if this number is over 0.05; such entries are italicized.

Table 2-4 continued

J. Pressures and Delay Times for Nitric Oxide

index	$P(NO_2)$[a]	P(NO)[a]	total P[a]	t, μs
1	21.2	237.3	259.9 ±1.0	0.4407 ±0.0302
2	31.7	413.9	447.6 ±0.7	0.4423 ±0.0304
3	21.2	237.3	259.9 ±1.0	0.9615 ±0.0555
4	35.1	621.8	658.4 ±1.7	0.4423 ±0.0304
5	36.1	859.9	901.9 ±2.6	0.4434 ±0.0301
6	31.7	413.9	447.6 ±0.7	0.9613 ±0.0549
7	57.1	1020.4	1080.0 ±1.8	0.4400 ±0.0304
8	21.0	235.7	258.0 ±0.6	1.9680 ±0.1020
9	35.1	621.8	658.4 ±1.7	0.9613 ±0.0549
10	36.1	859.9	901.9 ±2.6	0.9609 ±0.0555
11	30.5	425.1	458.1 ±1.1	1.9702 ±0.1019
12	57.1	1020.4	1080.0 ±1.8	0.9575 ±0.0544
13	36.0	641.8	681.0 ±2.4	1.9685 ±0.1027
14	37.6	857.6	898.7 ±1.9	1.9685 ±0.1027
15	50.4	1036.1	1087.7 ±2.3	1.9685 ±0.1027

[a]All pressures are given in mTorr. The NO_2 and NO pressures are as metered into the sample cell; the total pressure measurement is read by the computer during the experiment, along with the standard deviation shown.

K. Concentration-Time Products and Collision Numbers for NO_2-NO Deactivation

index	$c(NO) \cdot t$ $/10^8$ cm^{-3} s	$c(NO_2) \cdot t$ $/10^8$ cm^{-3} s	Z_{HS} NO_2^*-NO	Z_{HS} NO_2^*-NO_2
1	33.8 ±2.3	3.32 ±0.23	0.36 ±0.02	0.036 ±0.003
2	59.2 ±4.1	4.91 ±0.34	0.63 ±0.04	0.054 ±0.004
3	73.7 ±4.3	7.23 ±0.42	0.79 ±0.05	0.080 ±0.005
4	89.0 ±6.1	5.33 ±0.37	0.95 ±0.07	0.059 ±0.004
5	124.1 ±8.4	5.44 ±0.37	1.33 ±0.09	0.060 ±0.004
6	128.7 ±7.4	10.68 ±0.61	1.38 ±0.08	0.117 ±0.007
7	145.3 ±10.1	8.62 ±0.60	1.55 ±0.11	0.095 ±0.007
8	149.8 ±7.8	14.66 ±0.76	1.60 ±0.08	0.161 ±0.008
9	193.5 ±11.1	11.58 ±0.66	2.07 ±0.12	0.127 ±0.007
10	269.0 ±15.5	11.79 ±0.68	2.88 ±0.17	0.130 ±0.007
11	271.4 ±14.1	20.98 ±1.09	2.90 ±0.15	0.231 ±0.012
12	316.3 ±18.0	18.75 ±1.07	3.38 ±0.19	0.206 ±0.012
13	410.0 ±21.4	24.36 ±1.27	4.39 ±0.23	0.268 ±0.014
14	548.0 ±28.6	25.13 ±1.31	5.86 ±0.31	0.276 ±0.014
15	660.0 ±34.5	33.74 ±1.76	7.06 ±0.37	0.371 ±0.019

Table 2-4 continued

L. Fit parameters and energy moments for NO_2^*-NO energy transfer

index	fit method	parameters[a] 1	2	M, cm^{-1}	$10^3 \times$ sum error	f_R[b]	$\langle E \rangle$ cm^{-1}	$\langle \Delta E^2 \rangle^{1/2}$ cm^{-1}
1	Biexp.	2.2583E+1	9.4922E+2	19473	1.7945	4.85E-05	18912 ± 87	1010.5 ± 12.2
2	Biexp.	5.1270E+1	9.9609E+2	19219	1.1087	1.03E-04	18597 ± 55	1052.2 ± 6.0
3	Biexp.	2.5635E+1	1.1641E+3	19258	0.7979	3.67E-04	18510 ± 40	1200.5 ± 3.9
4	Biexp.	2.3193E+1	1.5820E+3	19344	1.5349	2.72E-03	18188 ± 77	1511.6 ± 10.3
5	Biexp.	3.3569E+1	1.7344E+3	19195	0.8370	5.15E-03	17905 ± 42	1586.7 ± 4.9
6	Gamma	1.1792E+3	1.3750	19625	1.6595	3.51E-04	18036 ± 84	1351.0 ± 11.6
7	Gauss.	1.9566E+4	2.3926E+3	19297	1.1104	8.06E-05	17899 ± 57	1438.3 ± 6.8
8	Biexp.	5.1880E+1	1.9766E+3	19258	1.5538	9.55E-03	17823 ± 79	1704.6 ± 11.2
9	Biexp.	6.4087E+1	2.5859E+3	19125	1.2860	0.0292	17297 ± 66	1875.8 ± 9.6
10	Gauss.	1.9489E+4	3.7695E+3	19203	0.9117	0.0128	16916 ± 48	1947.3 ± 6.7
11	Gamma	2.7207E+3	3.1172	20375	1.3188	2.98E-03	17325 ± 70	1694.2 ± 9.7
12	Gamma	3.8335E+3	5.0049	21000	1.4810	4.65E-03	16950 ± 79	1763.0 ± 11.9
13	Gauss.	1.6777E+4	2.7246E+3	19203	1.3347	8.10E-03	16537 ± 73	1913.1 ± 11.3
14	Gamma	3.8203E+3	1.7422	20375	1.4452	*0.1157*	*16171 ± 79*	*2123.7 ± 13.3*
15	Gamma	5.1270E+3	1.8359	21000	1.1257	*0.2065*	*16061 ± 62*	*2238.1 ± 10.3*

[a]fit method determines identity of parameters 1 and 2; see Equations 2-9, 2-10, and 2-11.

[b]$\langle E \rangle$ and $\langle \Delta E^2 \rangle^{1/2}$ are invalid if this number is over 0.05; such entries are italicized.

Table 2-5

Experiment and Fit Parameters for NO_2^* Relaxation by Polyatomic Gases

A. Pressures and Delay Times for Carbon Dioxide

index	$P(NO_2)$[a]	$P(CO_2)$[a]	total P[a]	t, μs
1	21.3	134.2	158.3 ±1.0	0.4451 ±0.0304
2	21.9	208.7	233.4 ±1.4	0.4422 ±0.0301
3	21.3	134.2	158.3 ±1.0	0.9575 ±0.0554
4	22.9	346.4	372.5 ±1.4	0.4437 ±0.0311
5	26.0	419.6	447.9 ±1.4	0.4422 ±0.0301
6	21.9	208.7	233.4 ±1.4	0.9562 ±0.0549
7	20.1	112.5	134.9 ±0.6	1.9560 ±0.1019
8	31.9	527.1	562.2 ±1.5	0.4437 ±0.0311
9	22.9	346.4	372.5 ±1.4	0.9588 ±0.0556
10	26.0	419.6	447.9 ±1.4	0.9562 ±0.0549
11	19.1	209.1	230.3 ±1.4	1.9672 ±0.1023
12	31.9	527.1	562.2 ±1.5	0.9588 ±0.0556
13	23.8	340.5	367.9 ±1.7	1.9560 ±0.1019
14	25.8	413.3	442.9 ±1.7	1.9675 ±0.1026
15	32.9	530.7	567.8 ±1.3	1.9627 ±0.1017

[a]All pressures are given in mTorr. The NO_2 and CO_2 pressures are as metered into the sample cell; the total pressure measurement is read by the computer during the experiment, along with the standard deviation shown.

B. Concentration-Time Products and Collision Numbers for NO_2-CO_2 Deactivation

index	$c(CO_2) \cdot t$ /10^8 cm^{-3} s	$c(NO_2) \cdot t$ /10^8 cm^{-3} s	Z_{HS} NO_2^*-CO_2	Z_{HS} NO_2^*-NO_2
1	19.2 ±1.3	3.62 ±0.25	0.21 ±0.01	0.040 ±0.003
2	29.9 ±2.0	3.51 ±0.24	0.33 ±0.02	0.039 ±0.003
3	41.3 ±2.4	7.79 ±0.45	0.45 ±0.03	0.086 ±0.005
4	50.0 ±3.5	3.54 ±0.25	0.55 ±0.04	0.039 ±0.003
5	60.2 ±4.1	3.98 ±0.27	0.66 ±0.05	0.044 ±0.003
6	64.7 ±3.7	7.59 ±0.44	0.71 ±0.04	0.083 ±0.005
7	70.2 ±3.7	15.27 ±0.80	0.77 ±0.04	0.168 ±0.009
8	75.9 ±5.3	4.89 ±0.34	0.83 ±0.06	0.054 ±0.004
9	108.1 ±6.3	7.65 ±0.44	1.19 ±0.07	0.084 ±0.005
10	130.2 ±7.5	8.60 ±0.49	1.43 ±0.08	0.095 ±0.005
11	133.4 ±7.0	13.41 ±0.70	1.47 ±0.08	0.147 ±0.008
12	164.1 ±9.5	10.57 ±0.61	1.81 ±0.10	0.116 ±0.007
13	216.9 ±11.4	16.30 ±0.85	2.39 ±0.13	0.179 ±0.009
14	264.7 ±13.9	17.62 ±0.92	2.91 ±0.15	0.194 ±0.010
15	338.7 ±17.6	22.38 ±1.16	3.73 ±0.19	0.246 ±0.013

Table 2-5 continued

C. Fit parameters and energy moments for NO_2^*-CO_2 energy transfer

index	fit method	parameters[a] 1	2	M, cm^{-1}	$10^3 \times$ sum error	f_R[b]	$\langle E \rangle$ cm^{-1}	$\langle \Delta E^2 \rangle^{1/2}$ cm^{-1}
1	Biexp.	2.9907E+1	9.1406E+2	19484	2.5709	3.30E-05	18966 ±125	977.9 ± 22.4
2	Biexp.	2.6245E+1	1.2187E+3	19625	2.9838	3.86E-04	18784 ±146	1256.2 ± 26.6
3	Biexp.	3.8452E+1	1.3555E+3	19422	1.8203	1.00E-03	18477 ± 90	1359.6 ± 12.6
4	Biexp.	3.1128E+1	1.4922E+3	19500	2.5537	1.79E-03	18402 ±126	1463.0 ± 20.9
5	Biexp.	1.4038E+1	1.5195E+3	19344	1.2921	2.20E-03	18250 ± 64	1473.4 ± 8.0
6	Biexp.	3.2349E+1	1.6484E+3	19422	1.8979	3.39E-03	18215 ± 95	1557.4 ± 13.8
7	Biexp.	2.6245E+1	1.6289E+3	19281	1.2721	3.45E-03	18153 ± 64	1532.8 ± 8.1
8	Gauss.	3.1055E+4	3.8750E+3	19047	1.1255	3.00E-05	18404 ± 56	1066.9 ± 6.2
9	Biexp.	4.2725E+1	2.2227E+3	19250	0.9712	0.0159	17607 ± 49	1799.7 ± 6.4
10	Biexp.	4.4556E+1	2.6797E+3	19203	1.8221	0.0324	17316 ± 93	1916.1 ± 14.9
11	Biexp.	4.0894E+1	1.8516E+3	19125	2.3700	7.26E-03	17797 ±121	1635.4 ± 20.0
12	Gamma	1.5352E+3	1.3203	19656	1.4767	4.06E-03	17448 ± 77	1668.0 ± 10.9
13	Gauss.	1.7218E+4	2.5391E+3	19344	1.7309	2.72E-03	16840 ± 92	1856.3 ± 14.9
14	Biexp.	6.5186E+2	6.6875E+3	19406	2.6438	*0.2135*	*16228 ±142*	*2131.5 ± 28.2*
15	Biexp.	3.3569E+2	2.3500E+4	19281	1.6393	*0.4297*	*15841 ± 89*	*2179.2 ± 16.1*

[a]fit method determines identity of parameters 1 and 2; see Equations 2-9, 2-10, and 2-11.

[b]$\langle E \rangle$ and $\langle \Delta E^2 \rangle^{1/2}$ are invalid if this number is over 0.05; such entries are italicized.

Table 2-5 continued

D. Pressures and Delay Times for Sulfur Dioxide

index	$P(NO_2)$[a]	$P(SO_2)$[a]	total P[a]	t, μs
1	16.1	131.8	150.3 ±1.3	0.4414 ±0.0301
2	23.4	218.5	244.6 ±4.2	0.4425 ±0.0309
3	16.1	131.8	150.3 ±1.3	0.9620 ±0.0551
4	30.0	316.1	348.2 ±0.9	0.4414 ±0.0301
5	33.9	419.0	453.1 ±1.7	0.4425 ±0.0309
6	23.4	218.5	244.6 ±4.2	0.9622 ±0.0552
7	42.7	512.2	555.9 ±1.2	0.4414 ±0.0301
8	13.7	131.4	145.1 ±1.2	1.9645 ±0.1022
9	30.0	316.1	348.2 ±0.9	0.9620 ±0.0551
10	33.9	419.0	453.1 ±1.7	0.9622 ±0.0552
11	22.0	215.9	238.7 ±1.5	1.9572 ±0.1024
12	42.7	512.2	555.9 ±1.2	0.9620 ±0.0551
13	28.7	325.8	357.1 ±1.2	1.9587 ±0.1020
14	35.6	437.1	468.0 ±4.3	1.9645 ±0.1022
15	42.2	505.9	549.7 ±1.5	1.9645 ±0.1022

[a]All pressures are given in mTorr. The NO_2 and SO_2 pressures are as metered into the sample cell; the total pressure measurement is read by the computer during the experiment, along with the standard deviation shown.

E. Concentration-Time Products and Collision Numbers for NO_2-SO_2 Deactivation

index	$c(SO_2) \cdot t$ /10^8 cm^{-3} s	$c(NO_2) \cdot t$ /10^8 cm^{-3} s	Z_{HS} NO_2^*-SO_2	Z_{HS} NO_2^*-NO_2
1	18.9 ±1.3	2.63 ±0.18	0.21 ±0.01	0.029 ±0.002
2	31.3 ±2.3	3.76 ±0.27	0.35 ±0.03	0.041 ±0.003
3	41.1 ±2.4	5.72 ±0.33	0.46 ±0.03	0.063 ±0.004
4	45.1 ±3.1	4.73 ±0.32	0.50 ±0.03	0.052 ±0.004
5	59.7 ±4.2	5.26 ±0.37	0.66 ±0.05	0.058 ±0.004
6	68.1 ±4.1	8.17 ±0.49	0.76 ±0.05	0.090 ±0.005
7	72.9 ±5.0	6.63 ±0.45	0.81 ±0.06	0.073 ±0.005
8	82.7 ±4.4	9.63 ±0.51	0.92 ±0.05	0.106 ±0.006
9	98.2 ±5.6	10.30 ±0.59	1.09 ±0.06	0.113 ±0.006
10	129.8 ±7.5	11.43 ±0.66	1.44 ±0.08	0.126 ±0.007
11	135.9 ±7.2	15.42 ±0.81	1.51 ±0.08	0.170 ±0.009
12	158.8 ±9.1	14.44 ±0.83	1.76 ±0.10	0.159 ±0.009
13	206.7 ±10.8	19.96 ±1.04	2.29 ±0.12	0.220 ±0.011
14	273.6 ±14.5	24.26 ±1.28	3.04 ±0.16	0.267 ±0.014
15	320.7 ±16.7	29.18 ±1.52	3.56 ±0.19	0.321 ±0.017

Table 2-5 continued

F. Fit parameters and energy moments for NO_2^*-SO_2 energy transfer

index	fit method	parameters[a] 1	2	M, cm^{-1}	$10^3 \times$ sum error	f_R[b]	$\langle E \rangle$ cm^{-1}	$\langle \Delta E^2 \rangle^{1/2}$ cm^{-1}
1	Gauss.	1.8714E+4	2.3438E+1	21000	1.8112	0.00	19157 ± 88	289.4 ± 27.8
2	Biexp.	3.9063E+1	8.9453E+2	19258	1.5195	3.44E-05	18746 ± 75	957.7 ± 9.6
3	Biexp.	3.9673E+1	8.6719E+2	19203	1.4277	2.51E-05	18735 ± 70	931.1 ± 8.8
4	Biexp.	1.0986E+1	1.7734E+3	19359	1.7728	5.18E-03	18045 ± 89	1623.6 ± 12.8
5	Biexp.	3.8452E+1	1.5586E+3	19203	1.1431	2.84E-03	18056 ± 58	1486.8 ± 7.0
6	Gauss.	1.8982E+4	1.8164E+3	19422	1.1306	6.85E-05	18231 ± 57	1229.5 ± 6.5
7	Biexp.	3.9673E+1	2.1094E+3	19250	1.6246	0.0128	17677 ± 82	1758.3 ± 12.1
8	Gauss.	1.8052E+4	1.2695E+3	19781	1.4121	1.40E-10	18286 ± 71	1137.4 ± 8.9
9	Biexp.	2.6123E+3	1.8281E+3	19625	1.4914	0.0125	17314 ± 77	1811.6 ± 11.4
10	Gamma	1.6646E+3	1.2109	19656	1.1652	0.0102	17188 ± 61	1796.5 ± 8.5
11	Gamma	2.7227E+3	2.9219	20375	1.3866	4.11E-03	17238 ± 73	1741.1 ± 10.4
12	Biexp.	1.3940E+3	2.8281E+3	19438	1.3901	*0.0520*	*16770 ± 74*	*1954.6 ± 11.4*
13	Biexp.	2.7500E+4	2.4062E+3	19559	1.9862	*0.0794*	*16366 ± 107*	*2024.4 ± 19.1*
14	Biexp.	7.9834E+2	2.0500E+4	19594	2.3374	*0.4200*	*15844 ± 127*	*2187.4 ± 25.2*
15	Biexp.	2.1704E+3	8.3750E+3	19906	1.2856	*0.3052*	*15974 ± 70*	*2182.4 ± 11.9*

[a]fit method determines identity of parameters 1 and 2; see Equations 2-9, 2-10, and 2-11.

[b]$\langle E \rangle$ and $\langle \Delta E^2 \rangle^{1/2}$ are invalid if this number is over 0.05; such entries are italicized.

Table 2-5 continued

G. Pressures and Delay Times for Sulfur Hexafluoride

index	$P(NO_2)$[a]	$P(SF_6)$[a]	total P[a]	t, μs
1	21.4	148.0	173.0 ±1.9	0.4430 ±0.0300
2	26.4	255.5	285.0 ±1.4	0.4432 ±0.0301
3	21.4	148.0	173.0 ±1.9	0.9534 ±0.0550
4	30.7	328.2	362.9 ±1.6	0.4430 ±0.0300
5	33.3	419.6	458.9 ±2.1	0.4432 ±0.0301
6	54.3	529.4	588.8 ±1.9	0.4430 ±0.0300
7	26.4	255.5	285.0 ±1.4	0.9618 ±0.0546
8	20.4	132.3	154.7 ±0.9	1.9730 ±0.1030
9	30.7	328.2	362.9 ±1.6	0.9534 ±0.0550
10	33.3	419.6	458.9 ±2.1	0.9618 ±0.0546
11	25.4	235.0	260.3 ±2.0	1.9717 ±0.1026
12	54.3	529.4	588.8 ±1.9	0.9534 ±0.0550
13	36.6	318.7	359.8 ±1.4	1.9650 ±0.1018
14	33.1	414.4	451.6 ±1.4	1.9573 ±0.1015
15	50.2	505.2	560.0 ±1.5	1.9573 ±0.1015

[a]All pressures are given in mTorr. The NO_2 and SF_6 pressures are as metered into the sample cell; the total pressure measurement is read by the computer during the experiment, along with the standard deviation shown.

H. Concentration-Time Products and Collision Numbers for NO_2-SF_6 Deactivation

index	$c(SF_6) \cdot t$ /10^8 cm^{-3} s	$c(NO_2) \cdot t$ /10^8 cm^{-3} s	Z_{HS} NO_2^*-SF_6	Z_{HS} NO_2^*-NO_2
1	21.2 ±1.5	3.59 ±0.25	0.19 ±0.01	0.039 ±0.003
2	36.7 ±2.5	4.23 ±0.29	0.32 ±0.02	0.047 ±0.003
3	45.7 ±2.7	7.73 ±0.45	0.40 ±0.02	0.085 ±0.005
4	47.2 ±3.2	4.87 ±0.33	0.42 ±0.03	0.054 ±0.004
5	60.7 ±4.1	5.23 ±0.36	0.54 ±0.04	0.058 ±0.004
6	75.8 ±5.2	8.67 ±0.59	0.67 ±0.06	0.095 ±0.006
7	79.6 ±4.5	9.18 ±0.52	0.70 ±0.04	0.101 ±0.006
8	83.6 ±4.4	15.25 ±0.80	0.74 ±0.04	0.168 ±0.009
9	101.6 ±5.9	10.49 ±0.61	0.90 ±0.05	0.115 ±0.007
10	131.7 ±7.5	11.35 ±0.65	1.16 ±0.07	0.125 ±0.007
11	148.3 ±7.8	17.97 ±0.94	1.31 ±0.07	0.198 ±0.010
12	163.2 ±9.4	18.66 ±1.08	1.44 ±0.08	0.205 ±0.012
13	202.8 ±10.5	26.31 ±1.37	1.79 ±0.09	0.289 ±0.015
14	263.5 ±13.7	22.87 ±1.19	2.33 ±0.12	0.252 ±0.013
15	319.8 ±16.6	35.29 ±1.83	2.83 ±0.15	0.388 ±0.020

Table 2-5 continued

I. Fit parameters and energy moments for NO_2^*-SF_6 energy transfer

index	fit method	parameters[a] 1	2	M, cm^{-1}	$10^3 \times$ sum error	f_R[b]	$\langle E \rangle$ cm^{-1}	$\langle \Delta E^2 \rangle^{1/2}$ cm^{-1}
1	Gamma	5.2734E+2	2.5000E+1	19250	2.8108	0.00	19142 ±136	308.4 ± 62.2
2	Gauss.	2.0145E+4	1.1875E+3	19063	1.6583	4.24E-17	18851 ± 81	620.2 ± 13.3
3	Biexp.	4.3335E+1	1.0898E+3	19219	1.8888	2.25E-04	18529 ± 94	1135.4 ± 13.5
4	Gauss.	1.9714E+4	2.2852E+3	19516	2.0717	2.39E-05	18157 ±104	1393.4 ± 15.8
5	Gauss.	4.9963E+4	7.1875E+3	19141	1.0088	1.54E-03	18029 ± 51	1449.7 ± 5.9
6	Biexp.	7.3242	2.4316E+3	19281	2.5912	0.0219	17552 ±132	1874.5 ± 23.3
7	Gauss.	2.0071E+4	2.3242E+3	19203	1.7250	2.16E-05	18066 ± 87	1304.4 ± 12.2
8	Gauss.	1.7861E+4	1.5195E+3	19891	1.2887	1.38E-07	18058 ± 66	1336.2 ± 8.1
9	Gamma	2.9805E+3	3.5034	20625	1.9147	3.07E-03	17266 ±100	1730.3 ± 15.9
10	Gauss.	1.7975E+4	2.6855E+3	19281	1.1387	2.24E-03	17055 ± 60	1806.2 ± 8.4
11	Gauss.	1.6875E+4	2.0430E+3	19813	0.9631	4.32E-04	17034 ± 52	1770.7 ± 6.9
12	Biexp.	6.9214E+2	6.0312E+3	19594	1.1918	*0.1934*	*16407 ± 63*	*2171.7 ± 10.2*
13	Biexp.	3.0518E+1	1.3750E+4	19063	4.0989	*0.3591*	*16049 ±221*	*2187.3 ± 52.9*
14	Biexp.	3.5840E+3	8.5000E+3	19938	2.3159	*0.3459*	*15724 ±128*	*2165.2 ± 25.3*
15	Gauss.	3.4180E+2	1.8594E+4	19359	2.8671	*0.5822*	*15692 ±157*	*2247.1 ± 33.8*

[a]fit method determines identity of parameters 1 and 2; see Equations 2-9, 2-10, and 2-11.

[b]$\langle E \rangle$ and $\langle \Delta E^2 \rangle^{1/2}$ are invalid if this number is over 0.05; such entries are italicized.

Table 2-6

Energy Transfer Rate Constants and Energy Removal per Collision

buffer	initial energy/cm^{-1}	$k(M)/10^{-8}$ $cm^{-1}cm^3s^{-1}$	$-\Delta<E>$ per collision/cm^{-1}: Hard-Sphere	close	$(<\Delta E^2>)^{1/2}$ exponent
NO_2	18590 ±240	6.92± 0.66	629 ± 60	123 ±12	0.336± 0.040
He	19480 ±110	2.77± 0.21	122.6 ± 9.3	46.3 ± 3.5	0.237± 0.121
Ne	19562 ± 79	2.16± 0.18	206 ± 17	53.8 ± 4.4	0.461± 0.045
Ar	19420 ±110	2.59± 0.24	251 ± 23	53.7 ± 5.0	0.267± 0.079
Kr	19175 ± 97	2.60± 0.20	277 ± 21	56.8 ± 4.4	0.071± 0.036
Xe	19090 ±120	2.65± 0.23	278 ± 24	52.8 ± 4.5	0.192± 0.054
N_2	19190 ±110	3.89± 0.24	321 ± 19	72.1 ± 4.5	0.284± 0.052
O_2	18995 ± 64	4.70± 0.25	431 ± 23	90.8 ± 4.8	0.258± 0.030
CO	18740 ±190	3.77± 0.56	309 ± 46	67 ±10	0.283± 0.030
NO	18859 ± 97	6.45± 0.60	603 ± 56	124 ±12	0.306± 0.036
CO_2	18919 ± 93	10.09± 0.86	917 ± 78	164 ±14	0.247± 0.054
SO_2	19180 ±140	15.42± 1.43	1390 ±130	251 ±23	0.348± 0.084
SF_6	19110 ±160	14.84± 1.44	1680 ±160	215 ±21	0.314± 0.059

Table 2-7

Vibrational Frequencies for the Buffer Molecules

Fundamental information is from Reference 66 for diatomic buffers and Reference 65 for polyatomic buffers unless otherwise indicated.

buffer	point group	designation	fundamental species	frequency, cm^{-1}
N_2	$D_{\infty h}$	ν	σ_g^+	2358.6
O_2	$D_{\infty h}$	ν	σ_g^+	1580.2
CO	$C_{\infty v}$	ν	σ^+	2169.8
NO	$C_{\infty v}$	ν	σ^+	1904.2
CO_2	$D_{\infty h}$	ν_1	σ_g^+	1388.3
		ν_2	π_u	667.3
		ν_3	σ_u^+	2349.3
NO_2[a]	C_{2v}	ν_1	a_1	1320.2
		ν_2	a_1	749.6
		ν_3	b_2	1618.
SO_2	C_{2v}	ν_1	a_1	1151.2
		ν_2	a_1	519.
		ν_3	b_2	1361.
SF_6	O_h	ν_1	a_{1g}	775
		ν_2	e_g	644
		ν_3	t_{1u}	965
		ν_4	t_{1u}	617
		ν_5	t_{2g}	524
		ν_6	t_{2u}	363

[a]from Reference 73.

Figure Captions

Figure 2-1. Apparatus for energy transfer experiments. The laser path through the cell is represented by the dotted line, and the fluorescence path is enclosed by dashed lines. On the gated integrators, T represents the trigger input, I represents the signal input, and O represents the output.

Figure 2-2. Fluorescence collection configuration diagram. The dashed line shows the limits of the light collection path. The laser path is shown as the dotted line; the region of light collection within the cell is 0.98 mm wide perpendicular to the beam. Monochromator slits are 50 mm in height. Distance measurements are in cm.

Figure 2-3. Spectral responsivity of the fluorescence collection system is plotted against wavelength of fluorescence collected. All fluorescence data are limited to a maximum wavelength of 840 nm due to the steep decrease in responsivity.

Figure 2-4. Fluorescence data for NO_2 excited by the doubled Nd:YAG laser. Dotted line: 13 mT, 0.060 μs delay. Short dashes: 125 mT, 0.472 μs delay (Experiment 1, Table 2-2). Long dashes: 322 mT, 0.964 μs (Experiment 12, Table 2-2). Solid: 584 mT, 1.998 μs (Experiment 22, Table 2-2). All fluorescence profiles have been normalized such that the total area under each curve is unity.

Figure 2-5. Running sum of NO_2^* fluorescence data for the same experiments as shown in Figure 2-4.

Figures 2-6 through 2-11 plot the relative populations obtained by the method of Ref. 55 (see Section 2.3) versus internal energy of NO_2^* for the following NO_2 pressures and delay times:

Figure 2-6. 143 mT, 0.465 μs (Experiment 2, Table 2-2)

Figure 2-7. 273 mT, 0.465 μs (Experiment 3, Table 2-2)

Figure 2-8. 550 mT, 0.465 μs (Experiment 6, Table 2-2)

Figure 2-9. 548 mT, 0.968 μs (Experiment 16, Table 2-2)

Figure 2-10. 1123 mT, 0.960 μs (Experiment 22, Table 2-2)

Figure 2-11. 1166 mT, 1.995 μs (Experiment 24, Table 2-2).

Figure 2-12. Average energy vs. hard-sphere collision number for NO_2^*-NO_2 excited at 532 nm is shown by the squares. Filled squares are incorporated in the linear fit shown as the solid line, Equation 2-26. Open squares indicate experiments for which f_R was more than 0.05. Error bars are included in the vertical direction when their size is greater than the size of the square; the uncertainty of the hard-sphere collision number ranges from five to ten percent.

Figure 2-13. Energy spread versus hard-sphere collision number for NO_2^*-NO_2. Open squares again indicate $f_R > 0.05$; uncertainties are smaller than the size of the square on this scale for all experiments.

Figure 2-14. Square of energy spread versus hard-sphere collision number for NO_2^*-NO_2.

Figure 2-15. Plot of natural logarithm of energy spread versus natural logarithm of hard-sphere collision number. The solid line represents the linear fit in Equation 2-27.

Figures 2-16 through 2-20 show the average energy versus hard-sphere collision number for the noble gas buffers. In each case, the solid line represents the fit given in the numbered equation in the text; error bars corresponding to one standard deviation are shown.

Figure 2-16. Helium; Equation 2-30.

Figure 2-17. Neon; Equation 2-31.

Figure 2-18. Argon; Equation 2-32.

Figure 2-19. Krypton; Equation 2-33.

Figure 2-20. Xenon; Equation 2-34.

Figures 2-21 through 2-25 are log-log plots of energy spread against hard-sphere collision number for the noble gases. Filled squares with error bars (one standard deviation) represent all points except those for which the error is greater than the range of the vertical scale in both directions; these points are represented by open squares. Solid lines give the linear fits corresponding to the numbered equations.

Figure 2-21. Helium; Equation 2-35.

Figure 2-22. Neon; Equation 2-36.

Figure 2-23. Argon; Equation 2-37.

Figure 2-24. Krypton; Equation 2-38.

Figure 2-25. Xenon; Equation 2-39.

Figures 2-26 through 2-29 display the average energy versus hard-sphere collision number for the diatomic buffers. The solid line represents the fit given in the numbered equation in the text; error bars corresponding to one standard deviation are shown except when the bars would be smaller than the size of the square on the scale. Filled squares represent individual experiments in Table 2-4 except when the f_R value is greater than 0.05; such points are represented as hollow squares.

Figure 2-26. Nitrogen; Equation 2-40.

Figure 2-27. Oxygen; Equation 2-41.

Figure 2-28. Carbon monoxide; Equation 2-42.

Figure 2-29. Nitric oxide; Equation 2-43.

Figures 2-30 through 2-33 plot the natural logarithm of energy spread versus that of hard-sphere collision number for the diatomic buffers. Filled squares represent the points, and error bars are added where their size exceeds that of the square, except those for which the f_R is greater than 0.05; these points are represented by open squares. Solid lines give the linear fits corresponding to the numbered equations.

Figure 2-30. Nitrogen; Equation 2-44.

Figure 2-31. Oxygen; Equation 2-45.

Figure 2-32. Carbon monoxide; Equation 2-46.

Figure 2-33. Nitric oxide; Equation 2-47.

Figures 2-34 through 2-36 show the average energy versus hard-sphere collision number for the polyatomic buffers carbon dioxide, sulfur dioxide, and sulfur hexafluoride. The solid line represents the fit given in the numbered equation in the text; error bars of one standard deviation are shown except when the bars would be smaller than the size of the square on the scale. Filled squares represent individual experiments in Table 2-5 except for those where the f_R value is greater than 0.05, which are given as hollow squares.

Figure 2-34. Carbon dioxide; Equation 2-48.

Figure 2-35. Sulfur dioxide; Equation 2-49.

Figure 2-36. Sulfur hexafluoride; Equation 2-50.

Figures 2-37 through 2-39 plot the natural logarithm of energy spread versus that of hard-sphere collision number for the polyatomic buffers. Filled squares with error bars (one standard deviation) are given for all points except those for which f_R is greater than 0.05; these points are represented by open squares. Solid lines give the linear fits corresponding to the numbered equations.

Figure 2-37. Carbon dioxide; Equation 2-51.

Figure 2-38. Sulfur dioxide; Equation 2-52.

Figure 2-39. Sulfur hexafluoride; Equation 2-53.

Figure 2-40. The stepladder model of excited state relaxation as used in References 20 and 41. The excited states are separated from each other by the energy step ϵ_{vib}. Energy transfer from state n to state n + 1 occurs with the rate constant k_+ and that from state n to state n - 1 occurs with the rate constant k_-.

Figure 2-41. Energy removal rate constant versus collider mass in atomic mass units for all buffers. The noble gases are represented by circles, the diatomics by diamonds, and the polyatomics by squares; the filled square is NO_2. Error bars represent one standard deviation unless their size would be less than that of the symbol.

Figure 2-42. Energy removed per hard-sphere collision versus collider mass for all buffers. Circles are noble gas buffers, diamonds represent diatomic buffers, and

squares are polyatomic buffers, with NO_2 shown as a filled square. Error bars are shown when needed.

Figure 2-43. Energy removed per effective collision versus collider mass for all buffers. The circles, diamonds, and squares correspond to monatomic, diatomic, and polyatomic buffers respectively. NO_2 is shown as a filled square, and error bars of one standard deviation are shown.

Figure 2-44. Power law for the energy spread versus buffer mass in atomic mass units. Error bars represent one standard deviation. The circles are noble gases, diamonds are diatomic gases, and squares are polyatomic gases, with NO_2 shown as a filled square.

Figure 2-45. A Lennard-Jones potential (dashed line) and the potential plus angular momentum pseudopotential (solid line) scaled by the Lennard-Jones ϵ are plotted against the reduced distance between molecules (the distance between the molecular centers of mass divided by σ_{LJ}). Values of parameters are: $\sigma_{LJ} = 3\text{Å}$, reduced impact parameter $b/\sigma_{LJ} = 1$, reduced angular energy $\mu g^2/2\epsilon = 1$. Adapted from Reference 60.

Figure 2-46. Probability of energy transfer $P(E_j,E_i)$ from initial energy E_i to final energy E_j is plotted against the energy change E_j - E_i for two models: (solid line) Exponential model of Reference 62; (dashed line) Biased random walk model of Reference 63. Parameters for the models are kT = 200 cm^{-1} (corresponding to approximately 20 °C) and:

Exponential (Equation 2-58): α = 80 cm^{-1}

Biased Random Walk (Equation 2-59; $\rho(E_j)$ is constant with respect to E_j): s = 50 cm^{-1}.

Figure 2-1

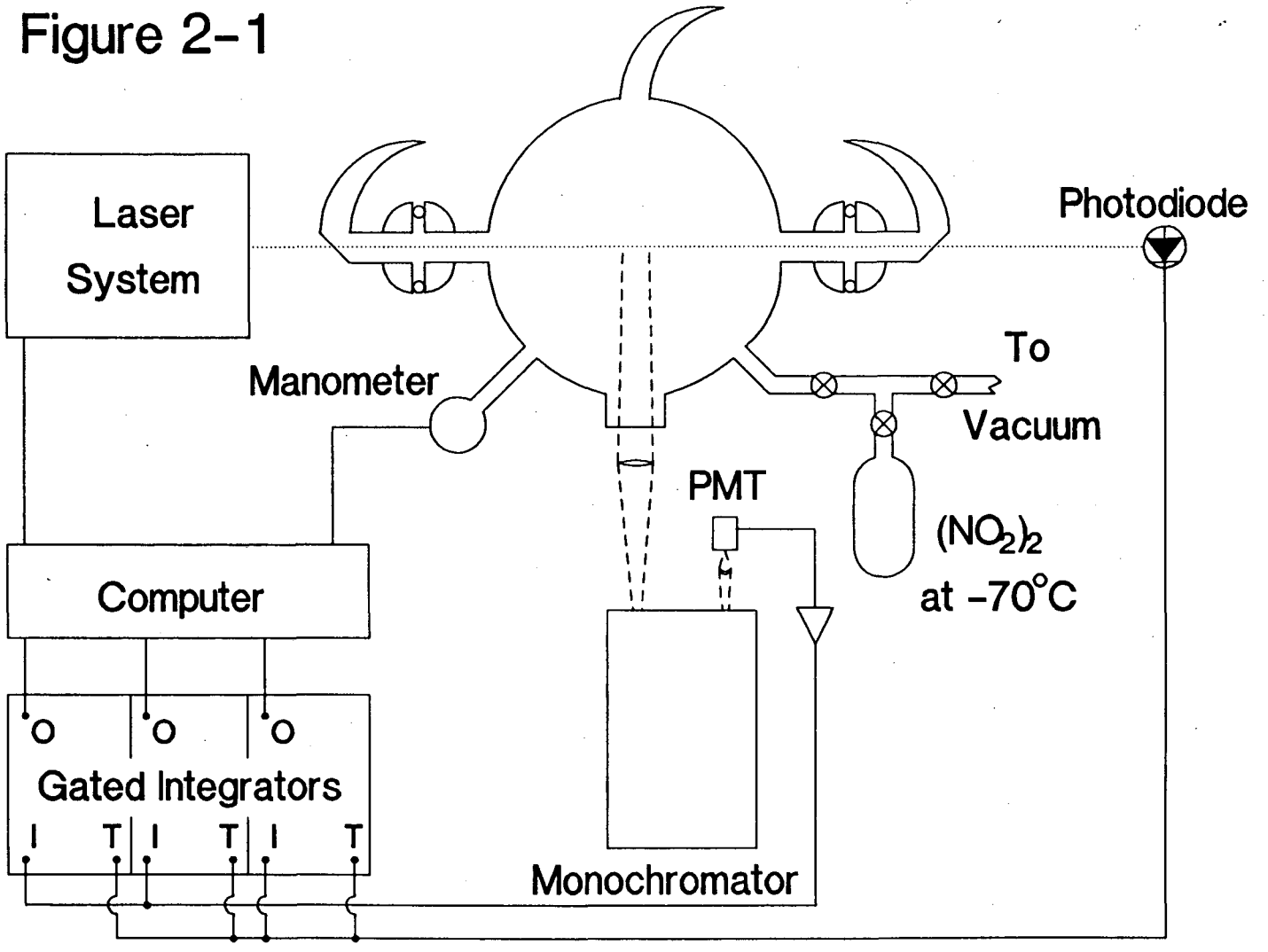
Laser System
Photodiode
Manometer
To Vacuum
PMT
$(NO_2)_2$ at -70°C
Computer
Gated Integrators
I T I T I T
Monochromator

Figure 2-2

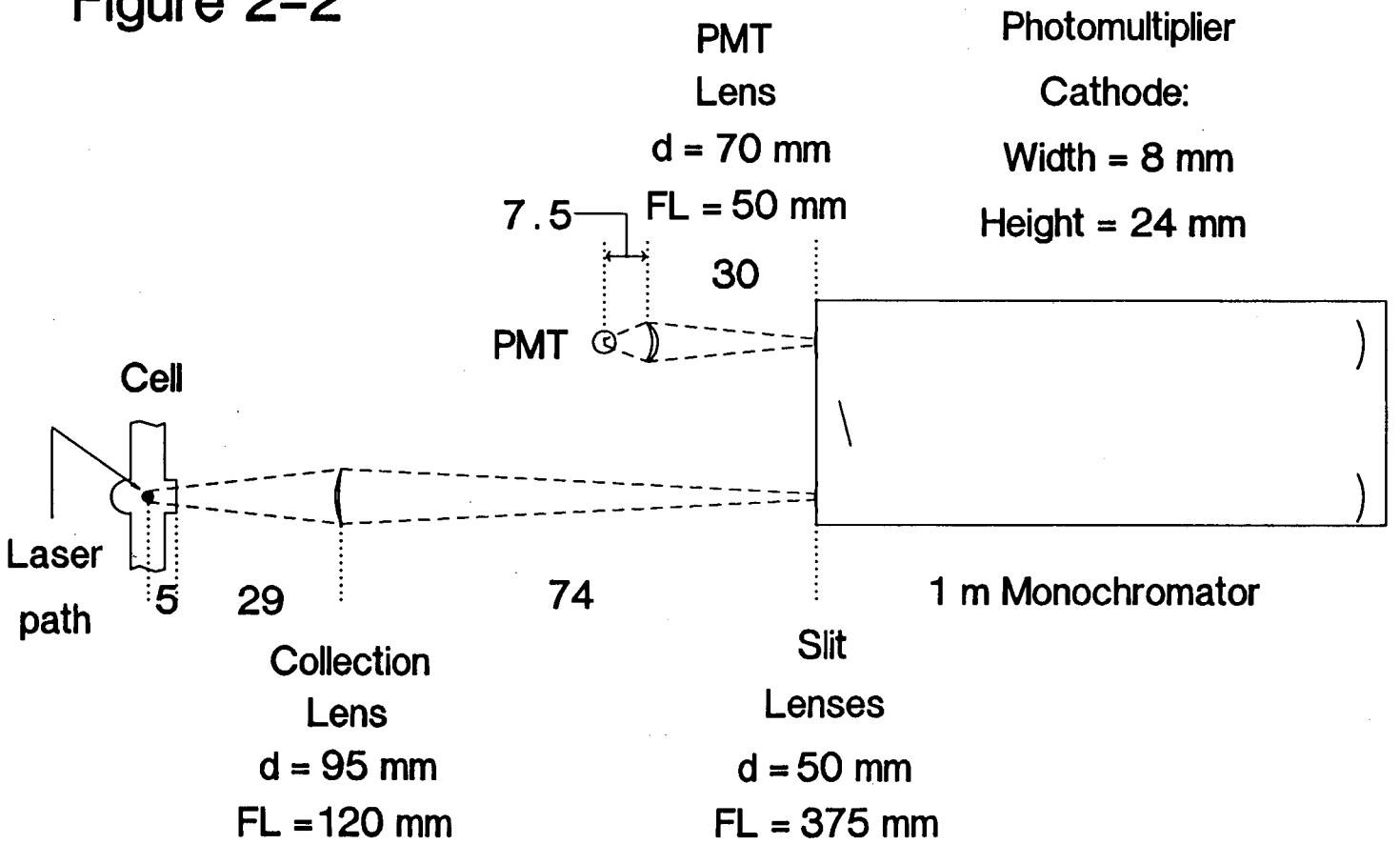
PMT
Lens
d = 70 mm
FL = 50 mm
Photomultiplier
Cathode:
Width = 8 mm
Height = 24 mm
7.5
30
PMT
Cell
Laser
path
5
29
74
1 m Monochromator
Collection
Lens
d = 95 mm
FL = 120 mm
Slit
Lenses
d = 50 mm
FL = 375 mm

Figure 2-3

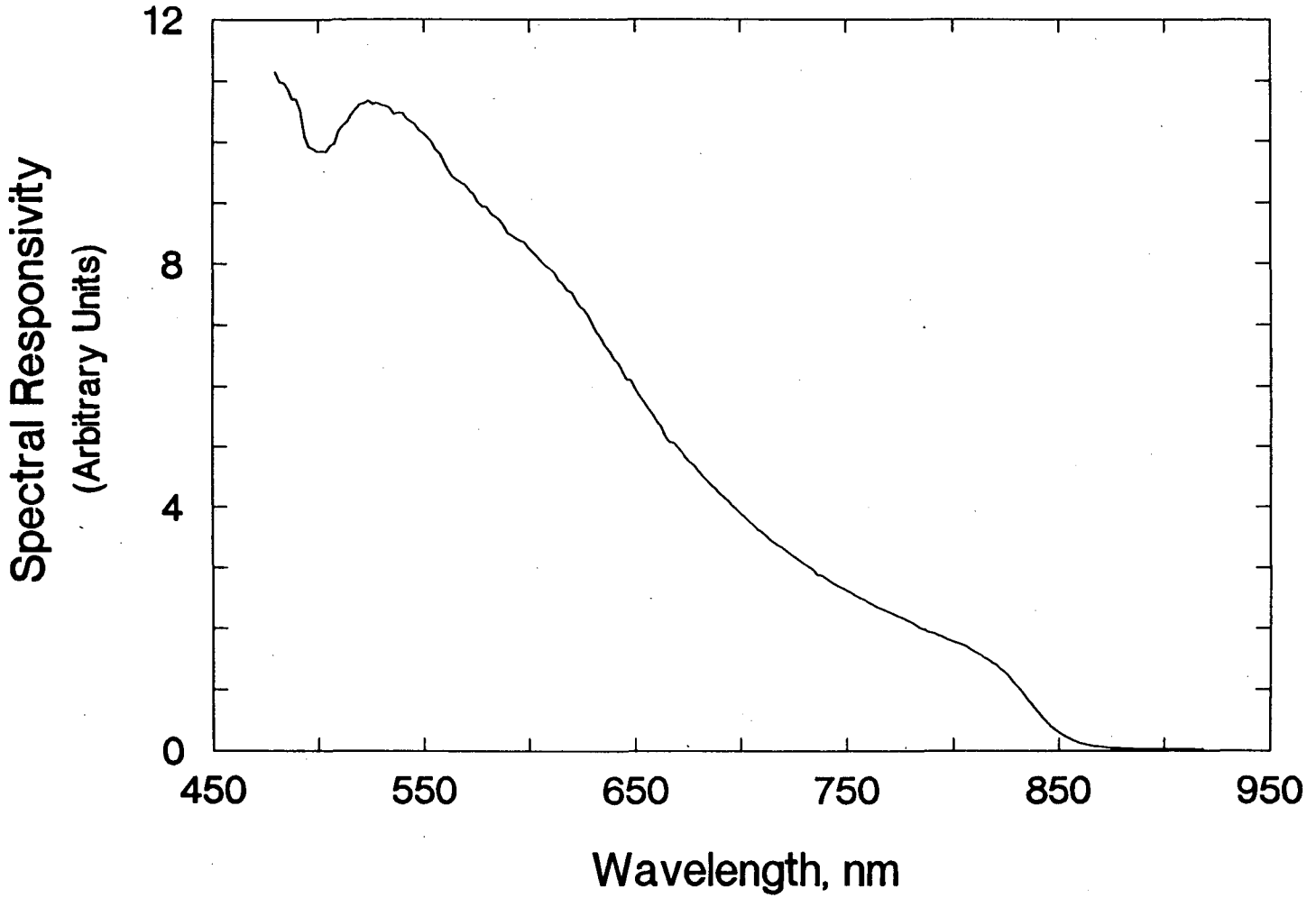
Spectral Responsivity
(Arbitrary Units)
12
8
4
0
450
550
650
750
850
950
Wavelength, nm

Figure 2-4

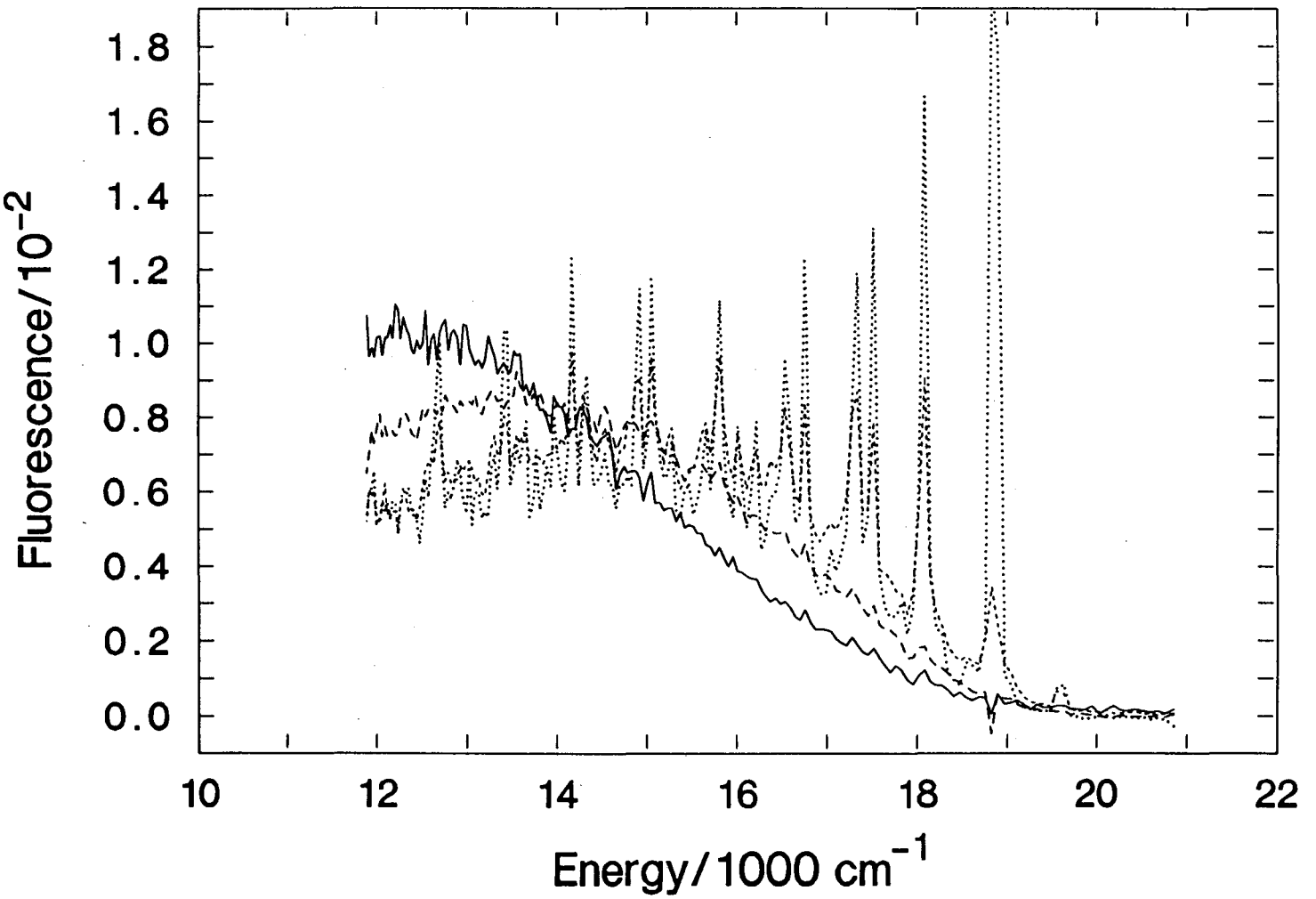
Fluorescence/10^{-2}
1.8
1.6
1.4
1.2
1.0
0.8
0.6
0.4
0.2
0.0
10
12
14
16
18
20
22
Energy/1000 cm^{-1}

Figure 2-5

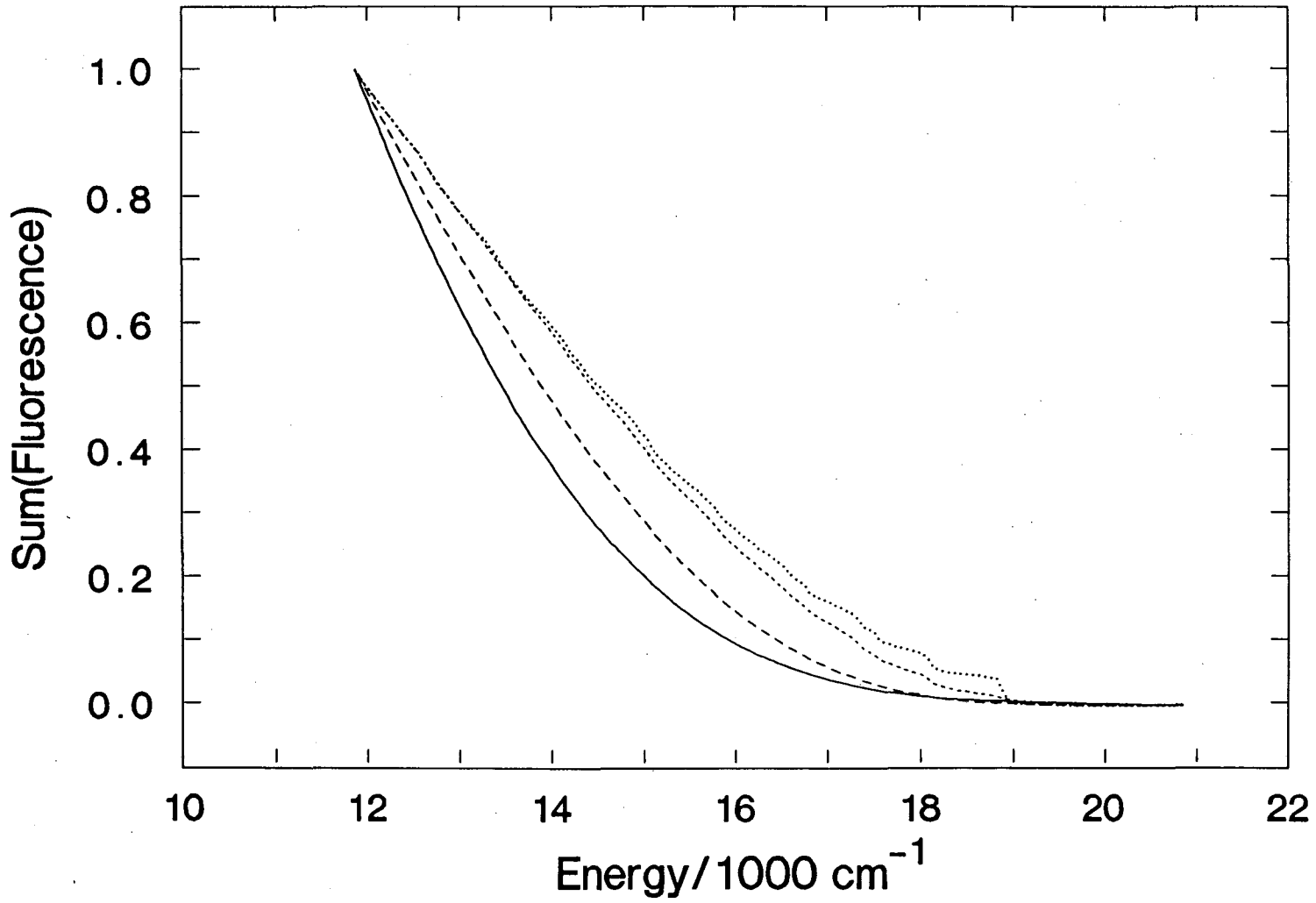
1.0
0.8
0.6
0.4
0.2
0.0
Sum(Fluorescence)
10
12
14
16
18
20
22
Energy/1000 cm^{-1}

Figure 2-6

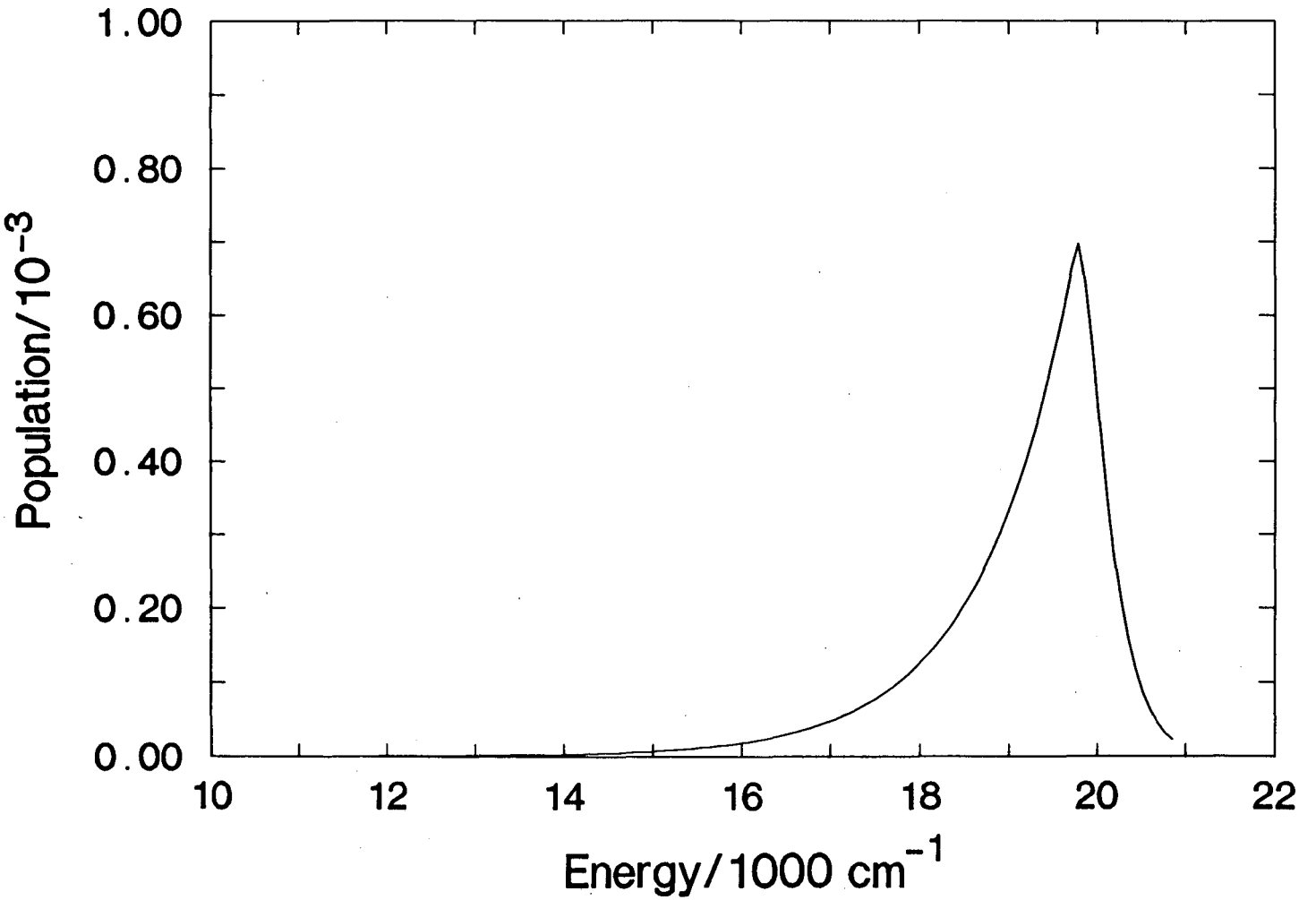
1.00
0.80
0.60
0.40
0.20
0.00
Population/10^{-3}
10
12
14
16
18
20
22
Energy/1000 cm^{-1}

Figure 2-7

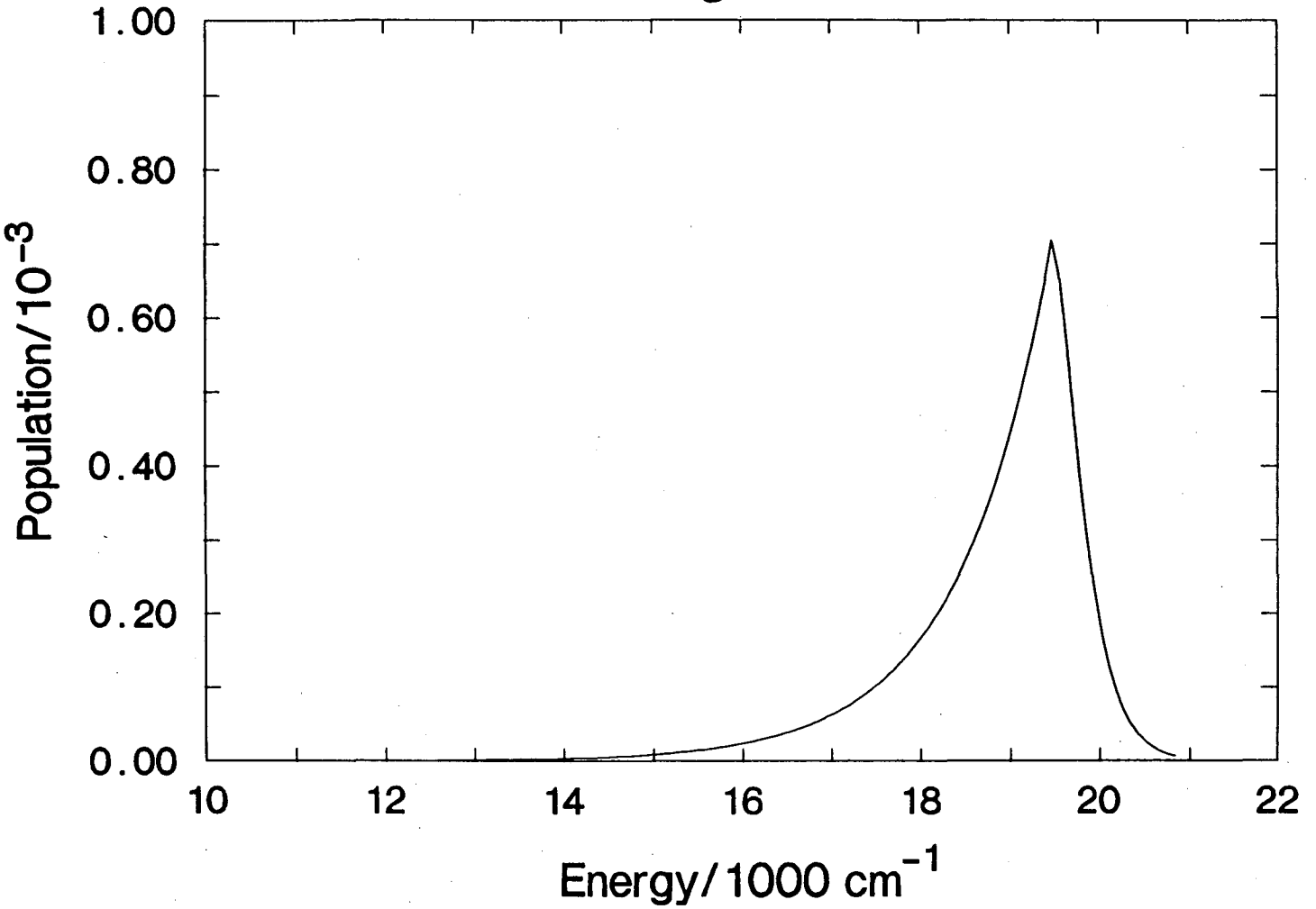
1.00
0.80
0.60
0.40
0.20
0.00
Population/10^{-3}
10
12
14
16
18
20
22
Energy/1000 cm^{-1}

Figure 2-8

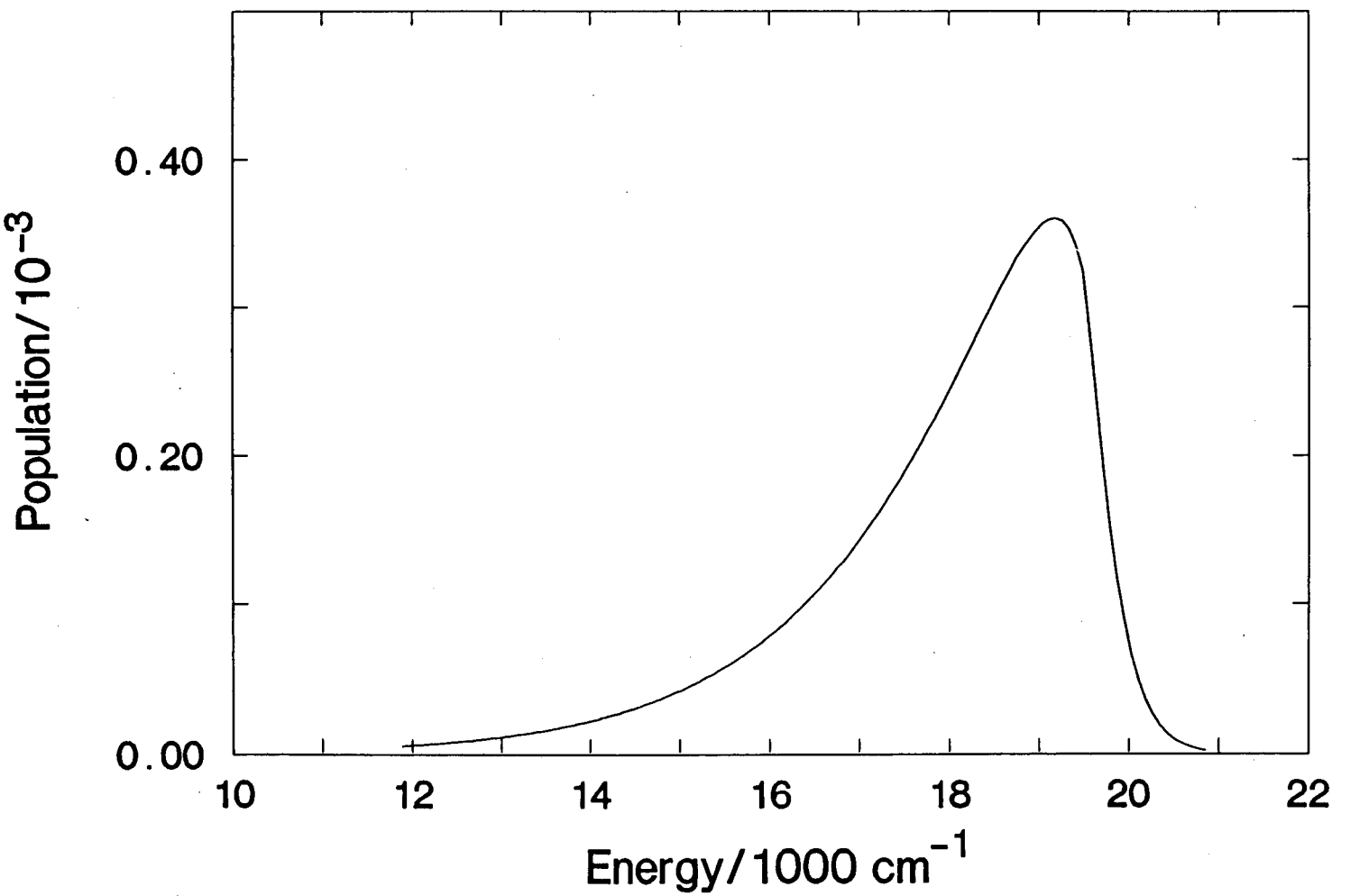

Figure 2-9

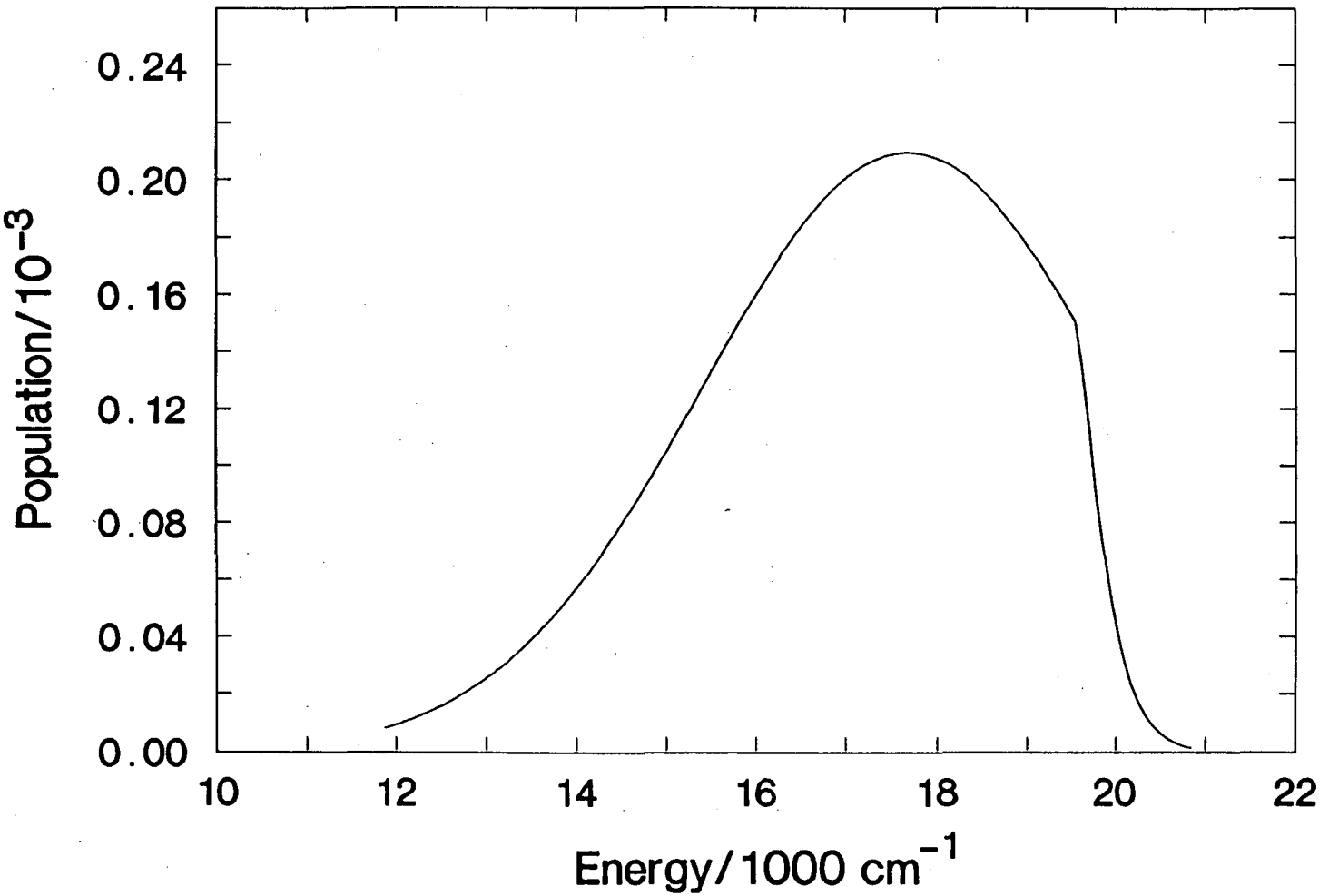
0.24
0.20
0.16
0.12
0.08
0.04
0.00
Population/10^{-3}
10
12
14
16
18
20
22
Energy/1000 cm^{-1}

Figure 2-10

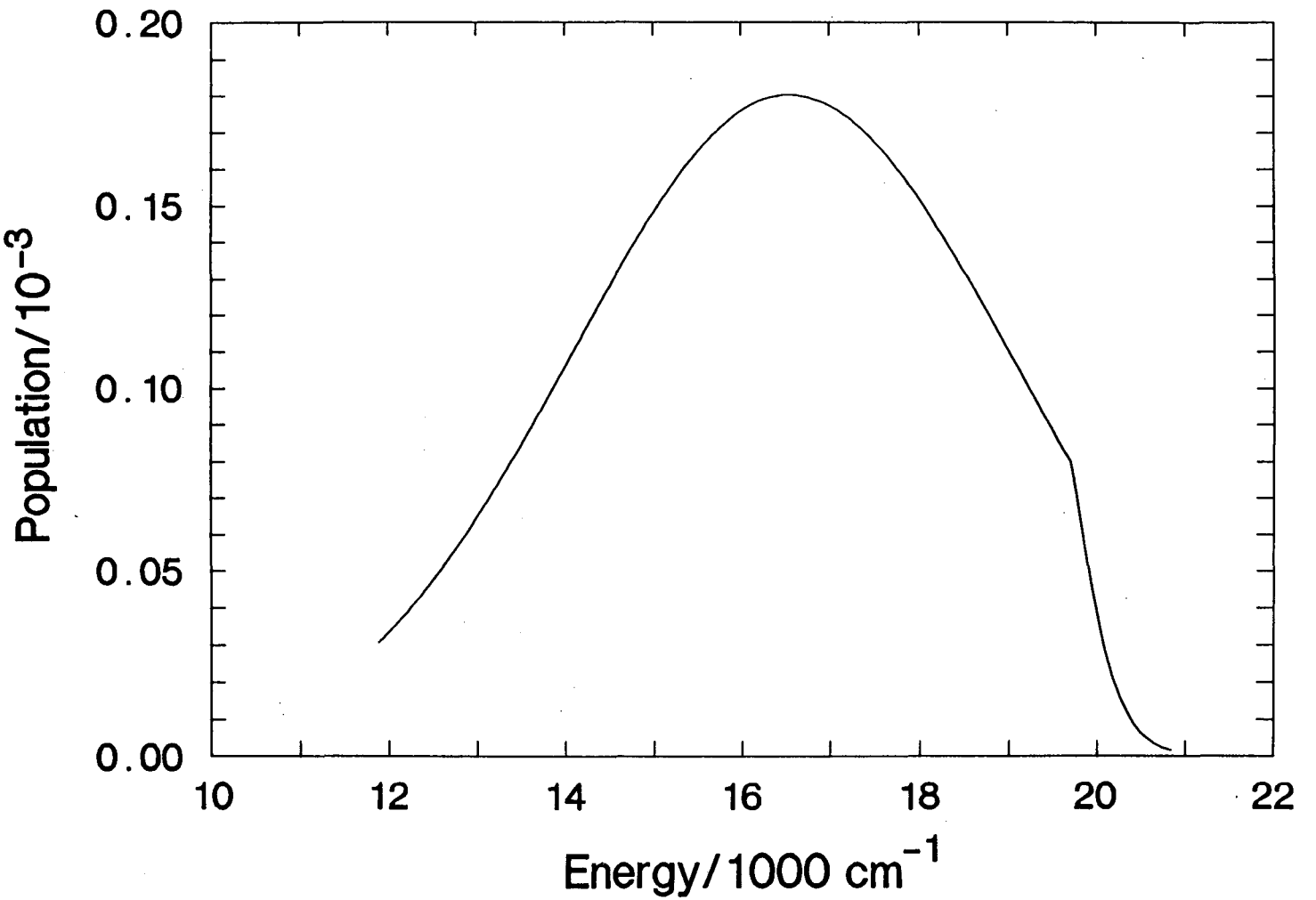
0.20
0.15
0.10
0.05
0.00
Population/10^{-3}
10
12
14
16
18
20
22
Energy/1000 cm^{-1}

Figure 2-11

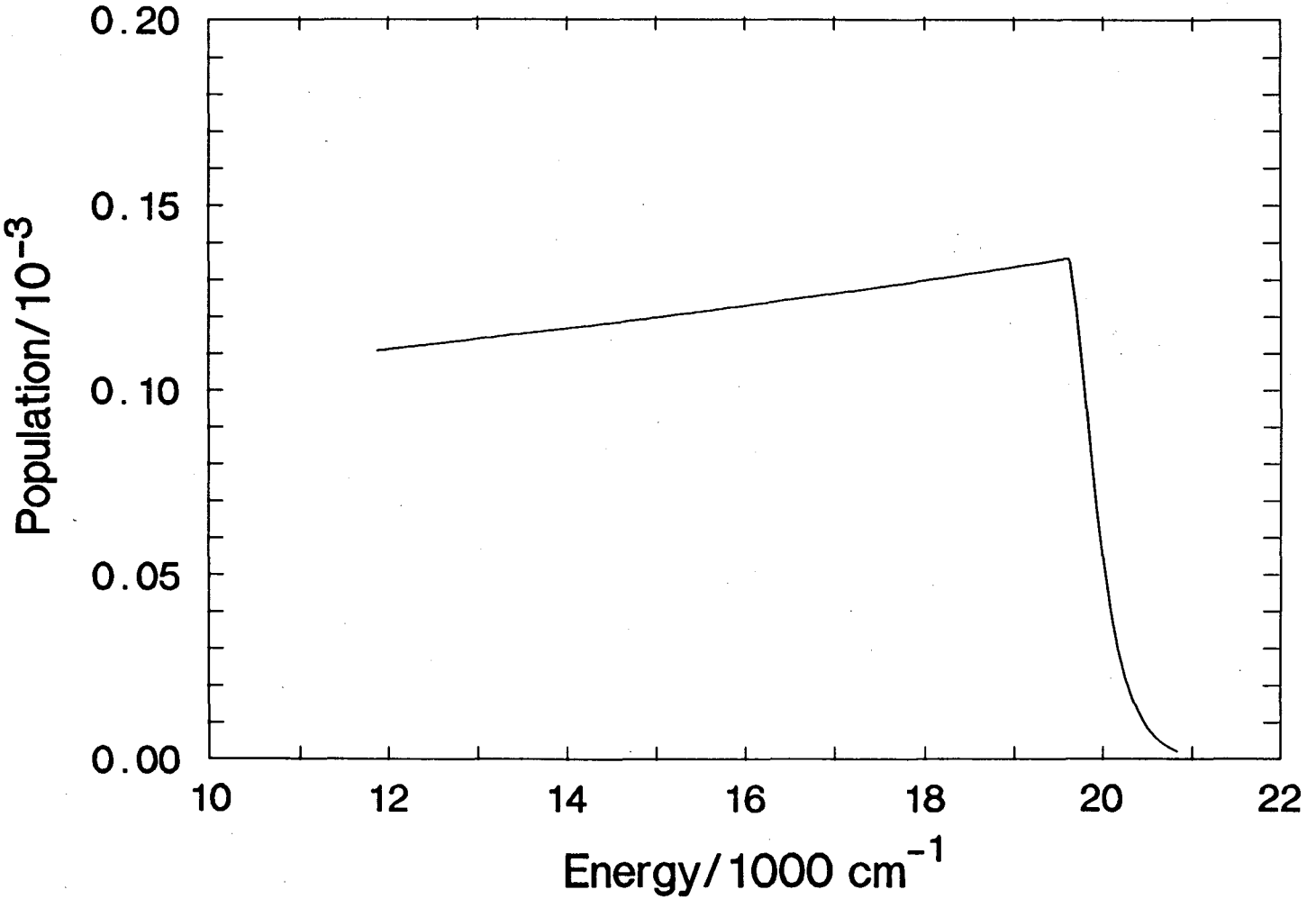
0.20
0.15
0.10
0.05
0.00
Population/10^{-3}
10
12
14
16
18
20
22
Energy/1000 cm^{-1}

Figure 2-12

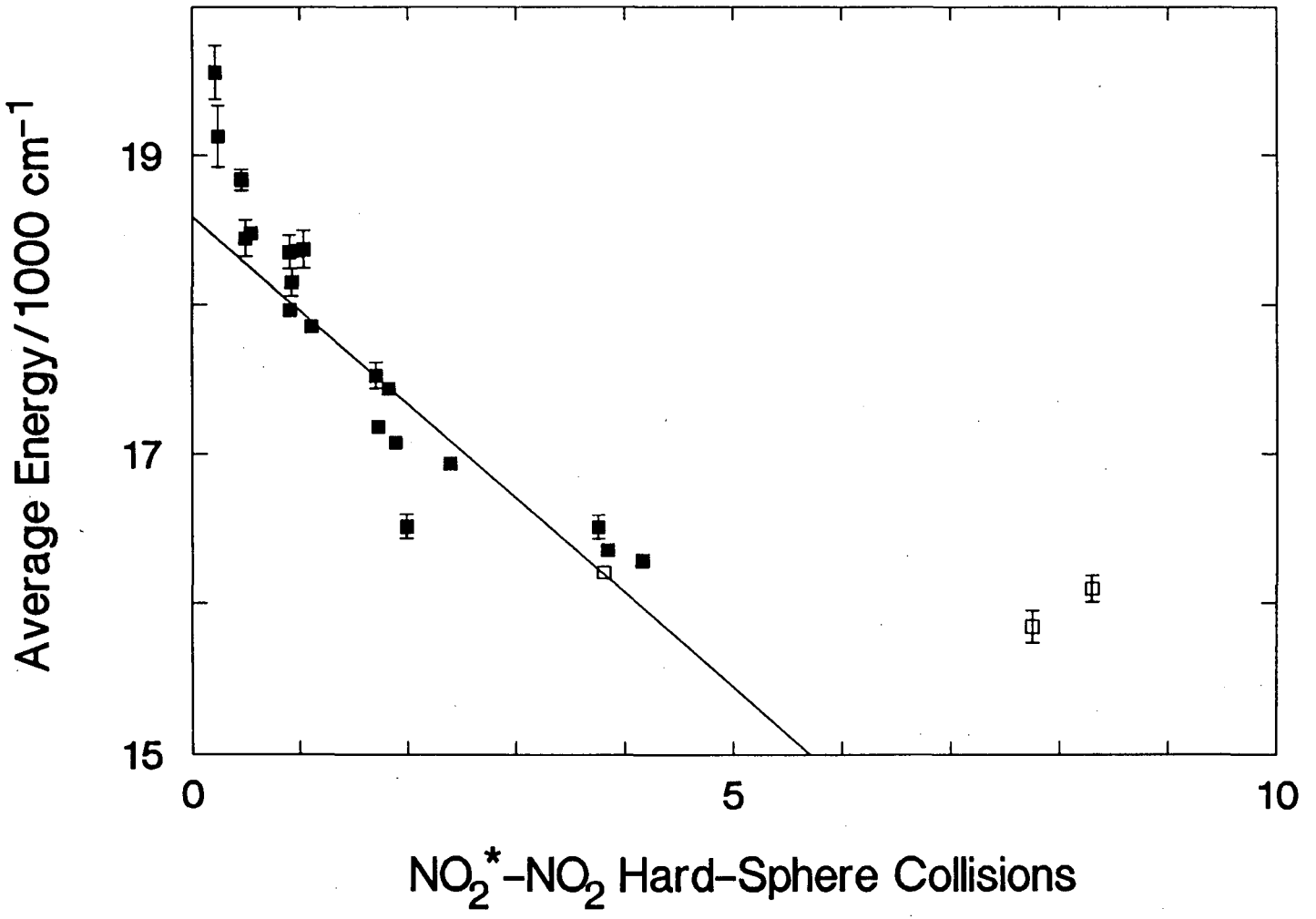
Average Energy/1000 cm^{-1}
19
17
15
0
5
10
NO_2^*-NO_2 Hard-Sphere Collisions

Figure 2-13

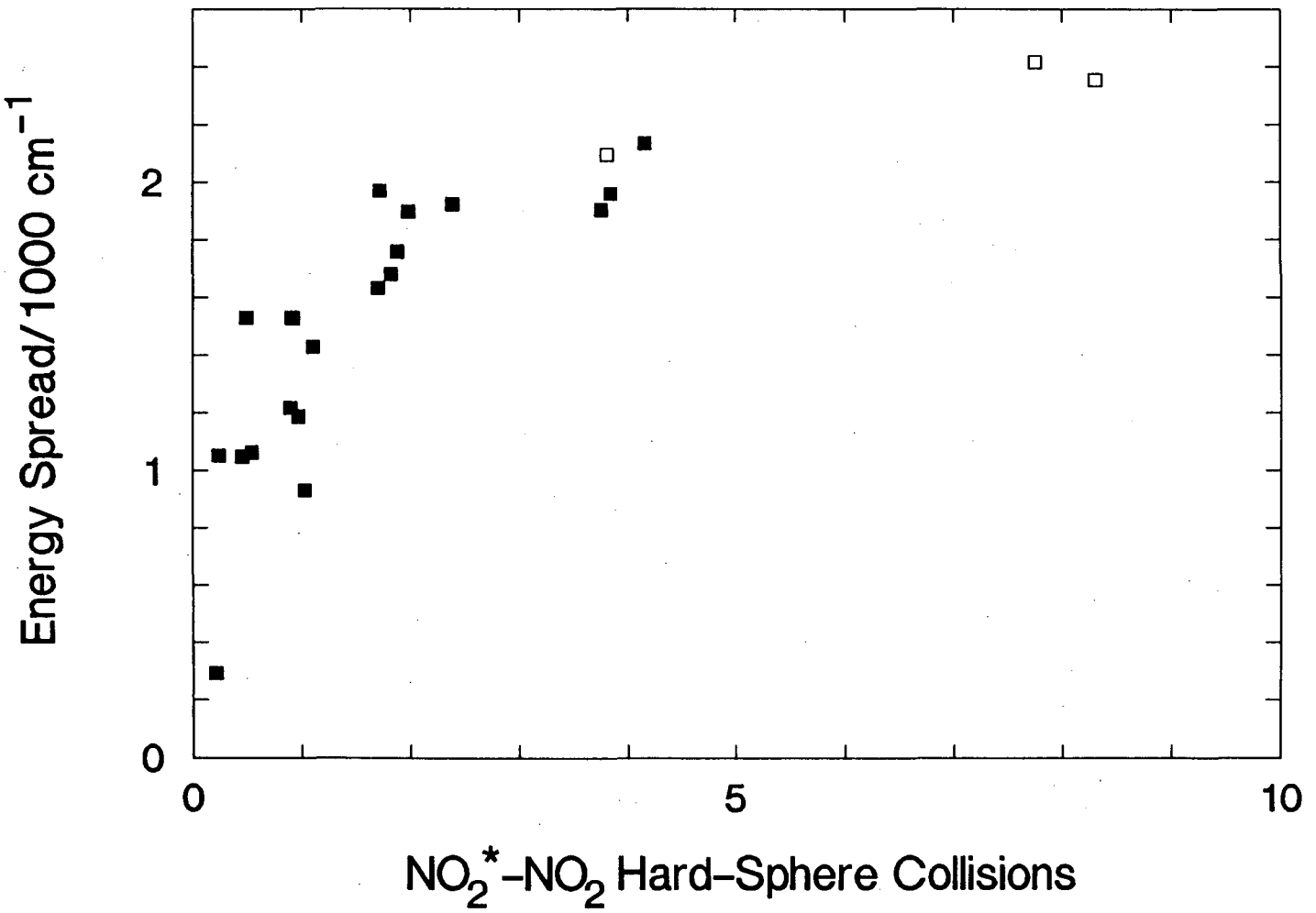
Energy Spread/1000 cm^{-1}
0
1
2
0
5
10
NO_2^*-NO_2 Hard-Sphere Collisions

Figure 2-14

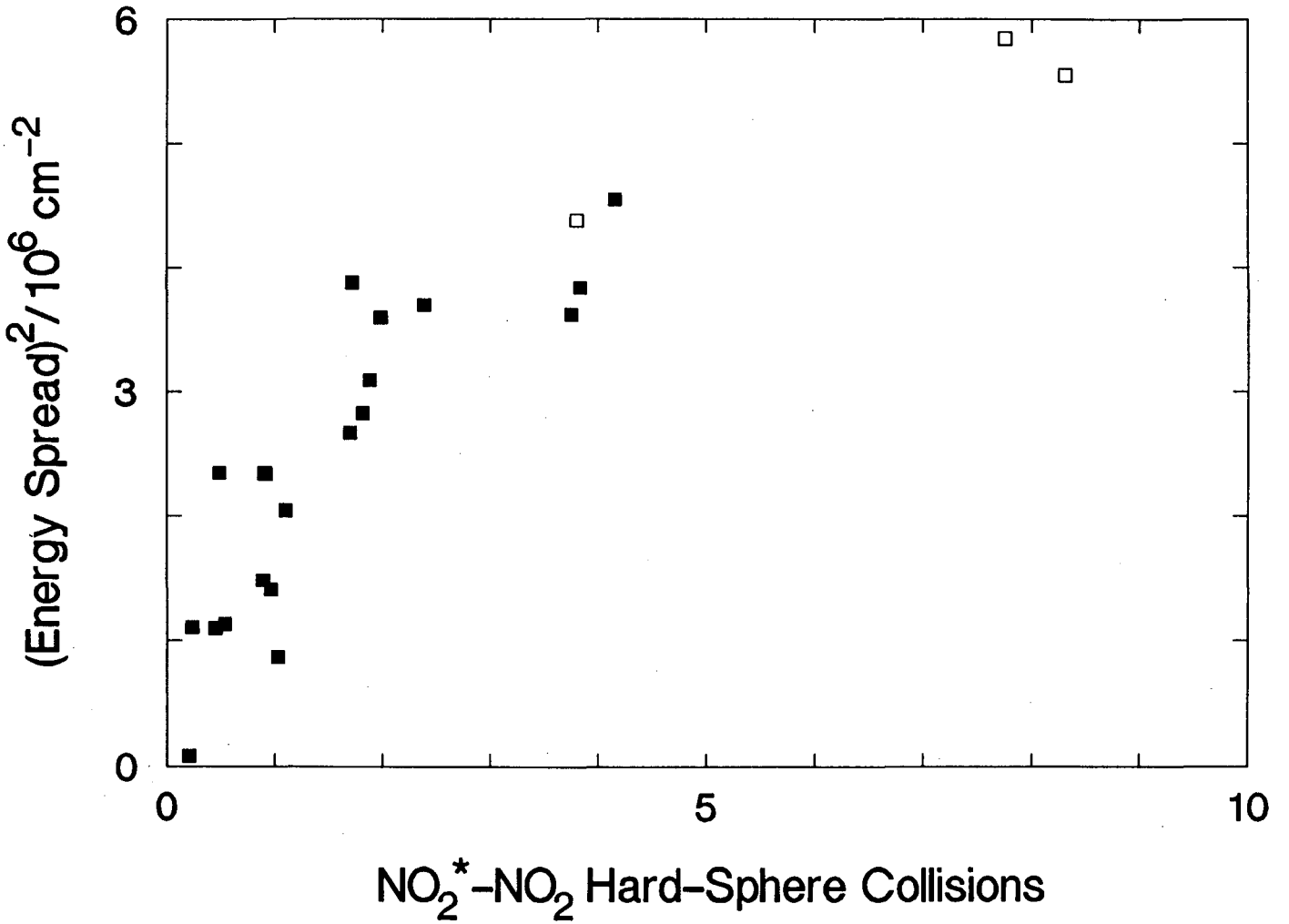
6
3
0
0
5
10
(Energy Spread)^2/10^6 cm^{-2}
NO_2^*-NO_2 Hard-Sphere Collisions

Figure 2-15

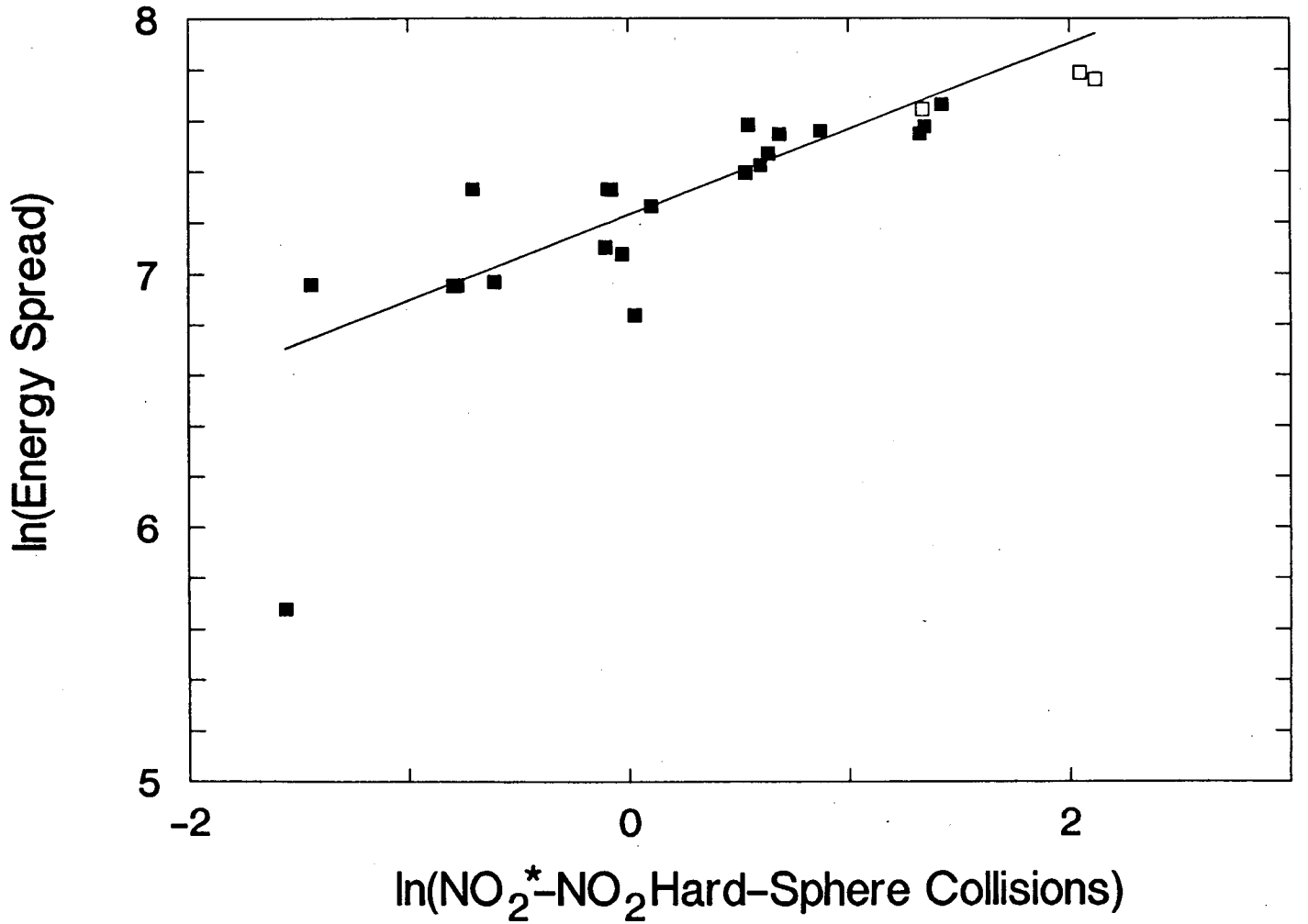

Figure 2-16

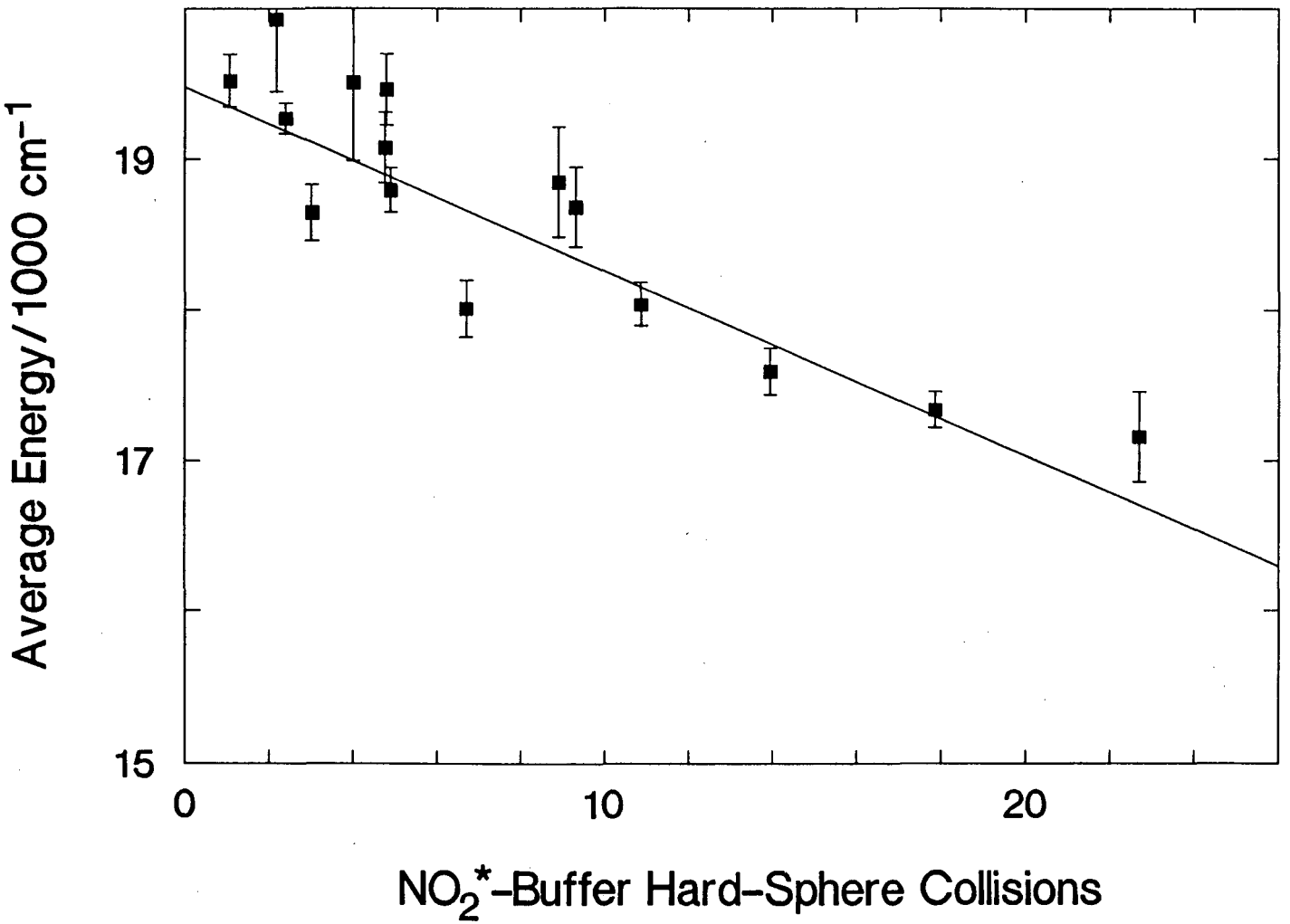
Average Energy/1000 cm^{-1}
19
17
15
0
10
20
NO_2^*-Buffer Hard-Sphere Collisions

Figure 2-17

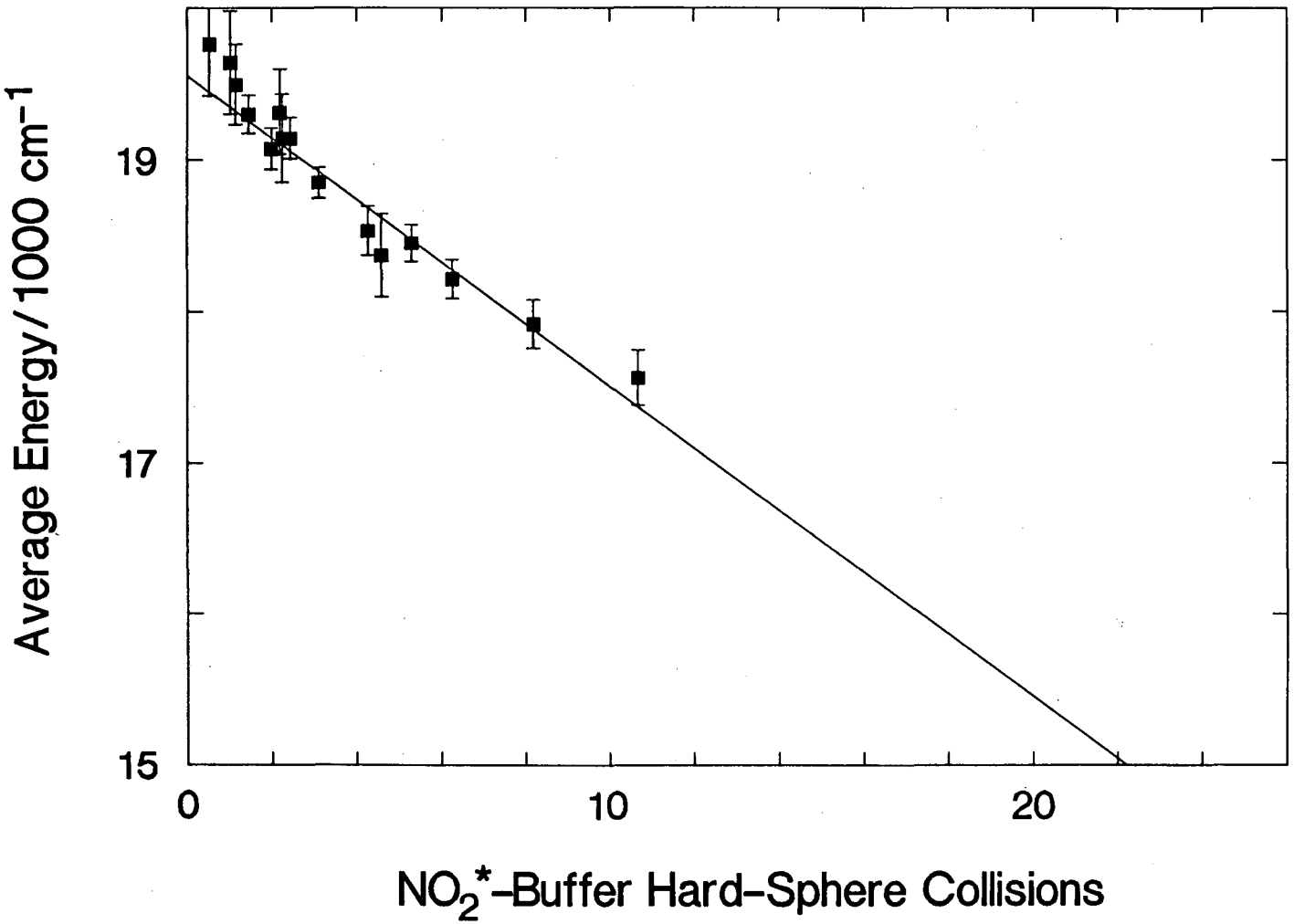
Average Energy/1000 cm^{-1}
19
17
15
0
10
20
NO_2^*-Buffer Hard-Sphere Collisions

Figure 2-18

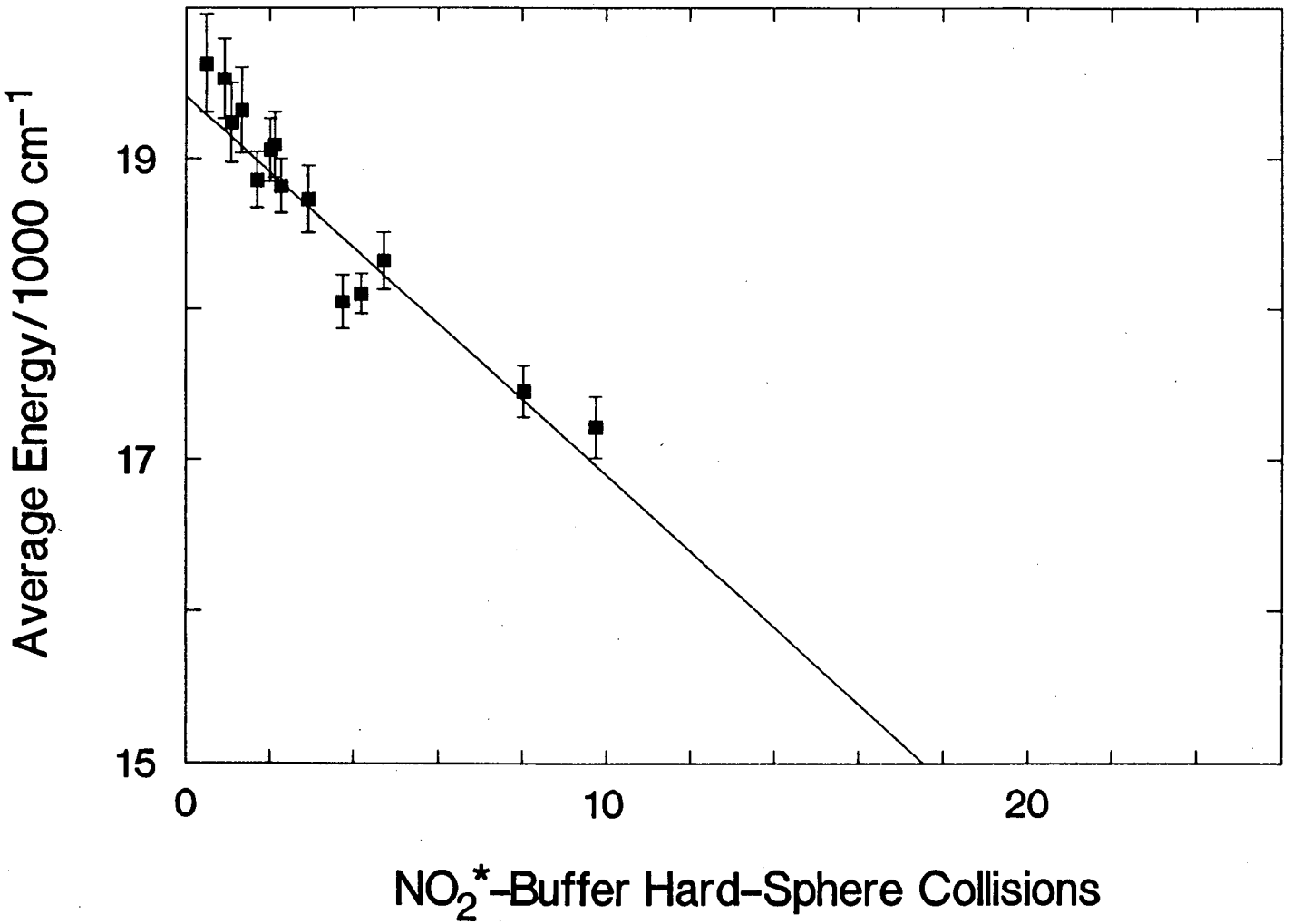
Average Energy/1000 cm^{-1}
19
17
15
0
10
20
NO_2^*-Buffer Hard-Sphere Collisions

Figure 2-19

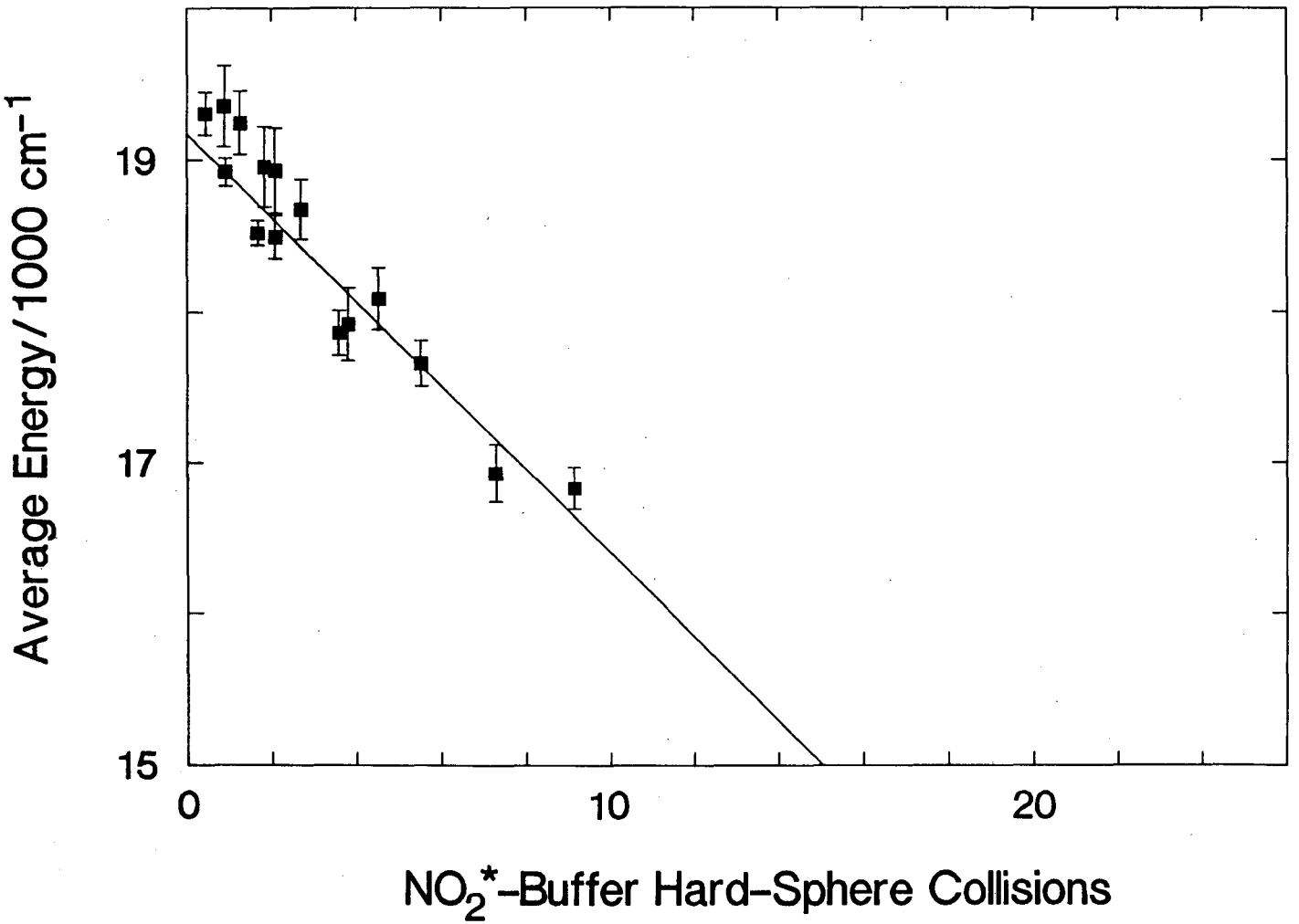
Average Energy/1000 cm^{-1}
19
17
15
0
10
20
NO_2^*-Buffer Hard-Sphere Collisions

Figure 2-20

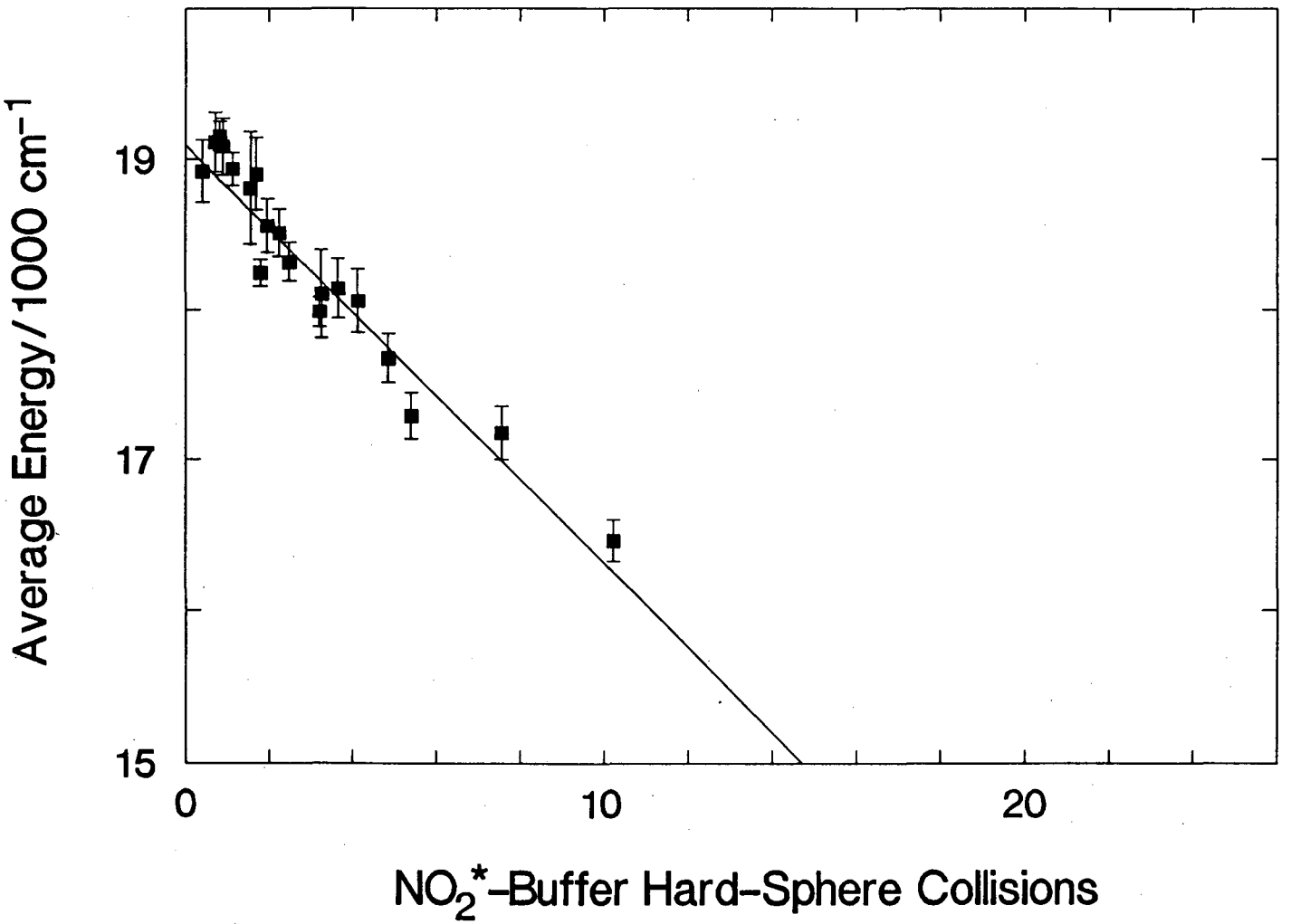
Average Energy/1000 cm^{-1}
19
17
15
0
10
20
NO_2^*-Buffer Hard-Sphere Collisions

Figure 2-21

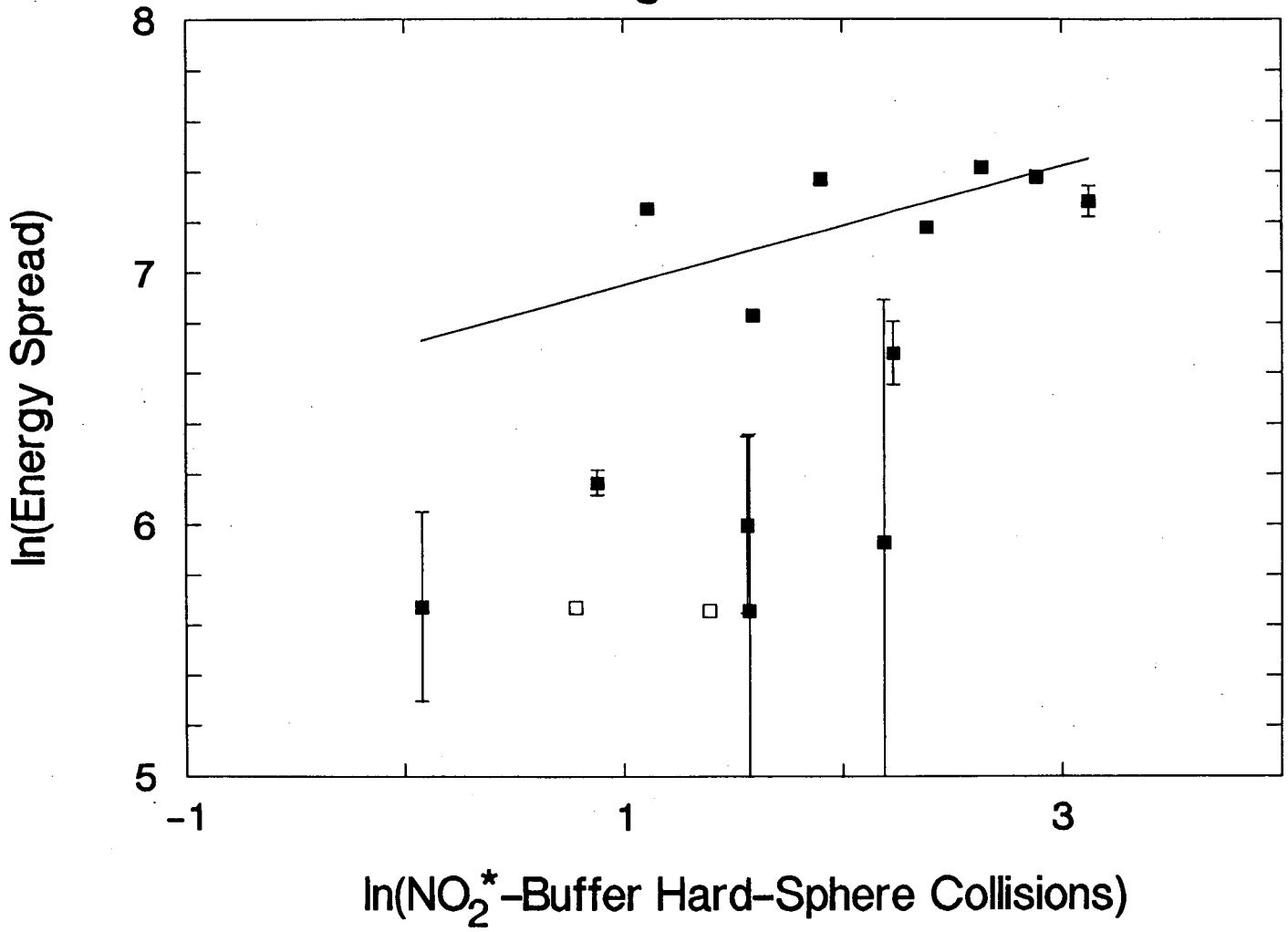
8
7
6
5
-1
1
3
ln(Energy Spread)
ln(NO_2^*-Buffer Hard-Sphere Collisions)

Figure 2-22

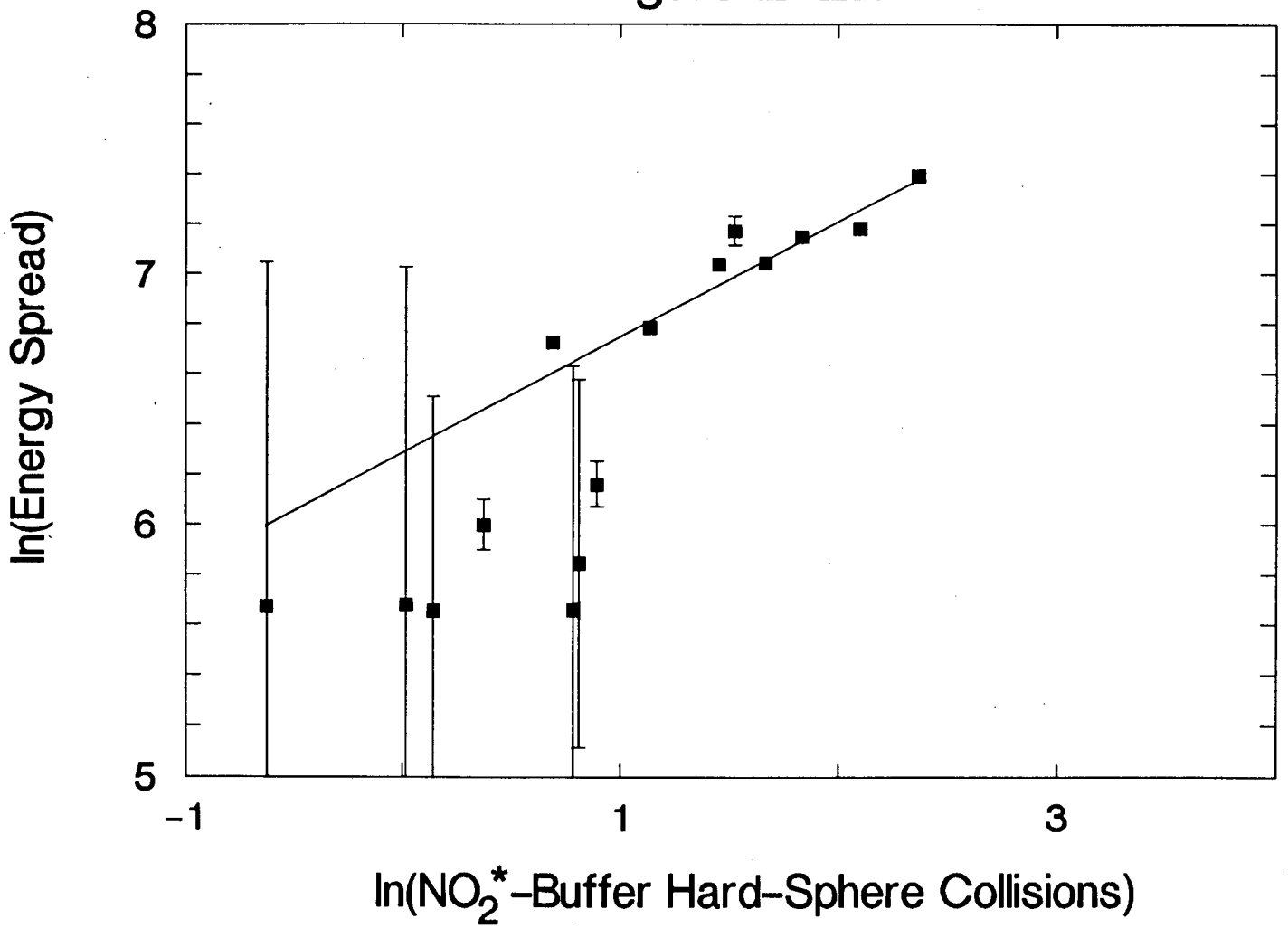
8
7
6
5
-1
1
3
ln(Energy Spread)
ln(NO_2^*-Buffer Hard-Sphere Collisions)

Figure 2-23

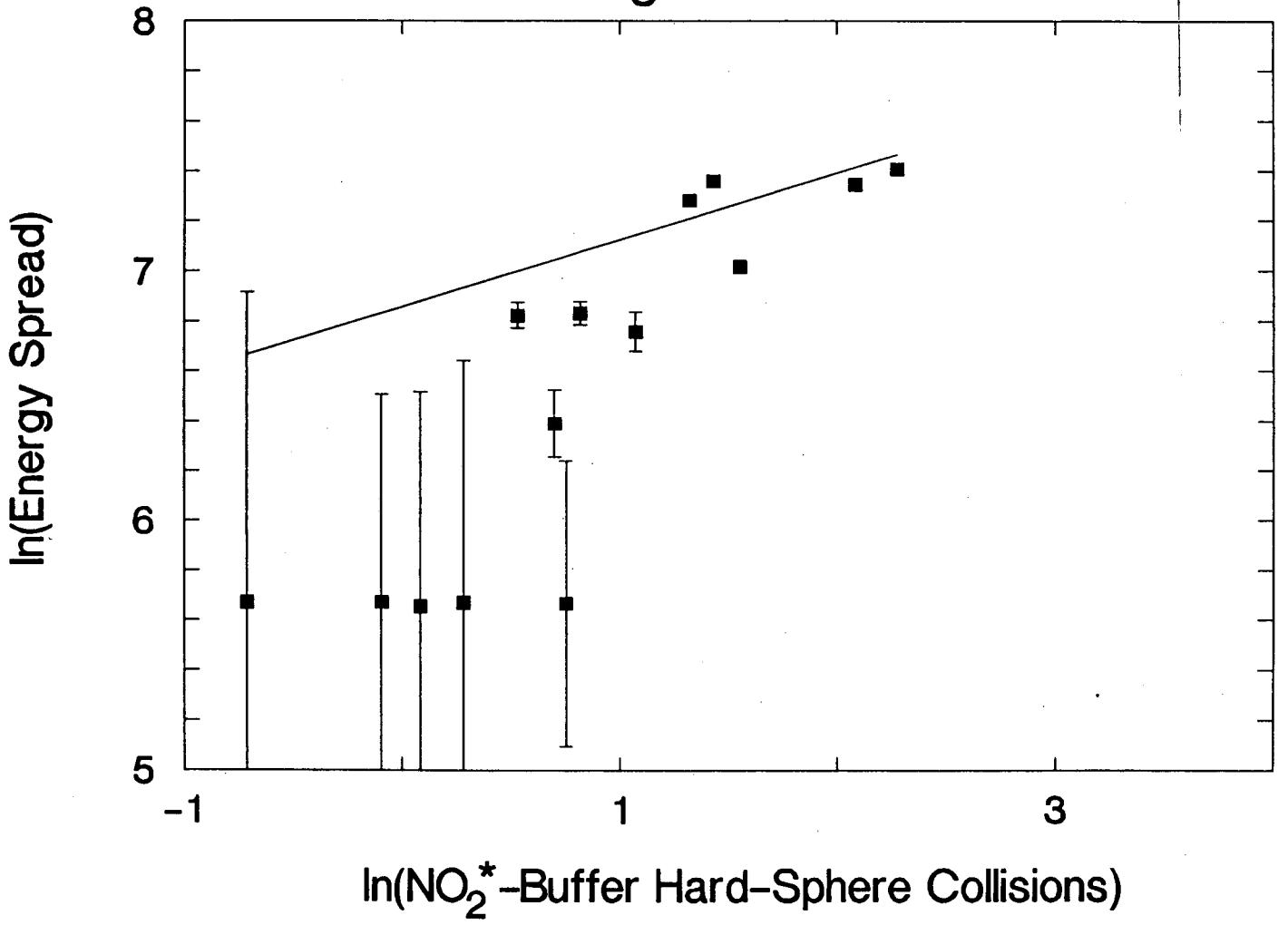
8
7
6
5
-1
1
3
ln(Energy Spread)
ln(NO_2^*-Buffer Hard-Sphere Collisions)

Figure 2-24

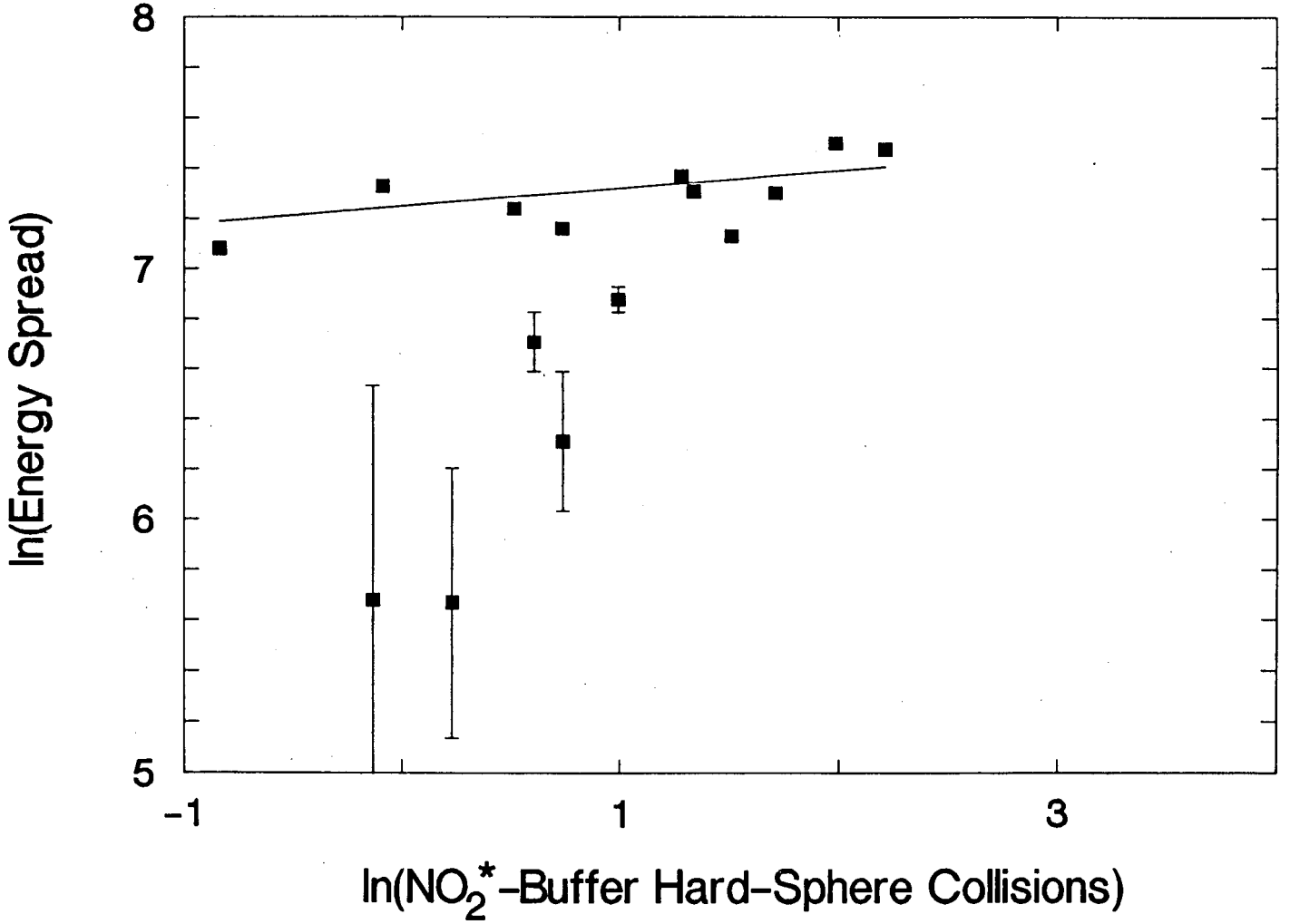
8
7
6
5
-1
1
3
ln(Energy Spread)
ln(NO_2^*-Buffer Hard-Sphere Collisions)

Figure 2-25

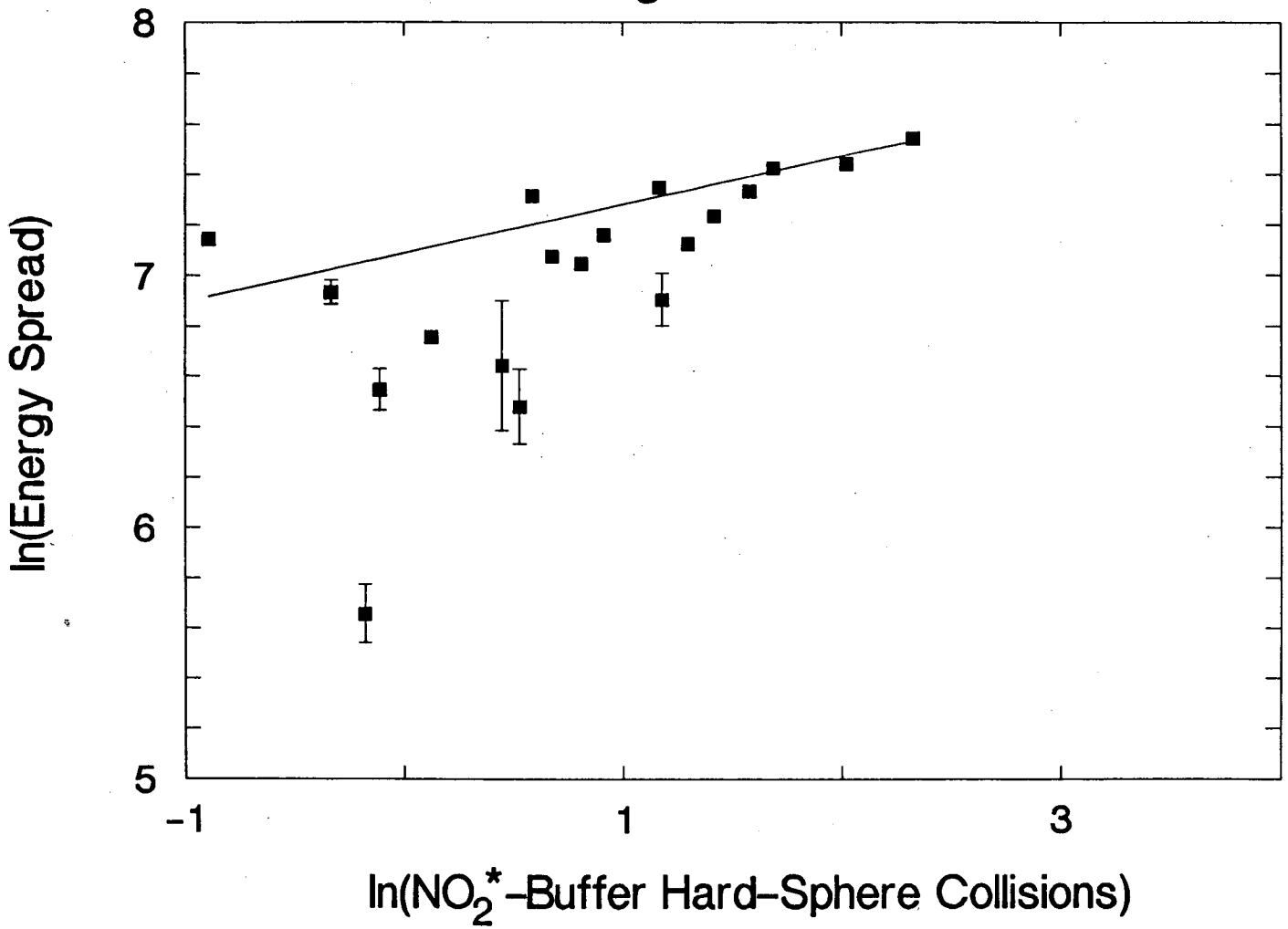
8
7
6
5
-1
1
3
ln(Energy Spread)
ln(NO_2^*-Buffer Hard-Sphere Collisions)

Figure 2-26

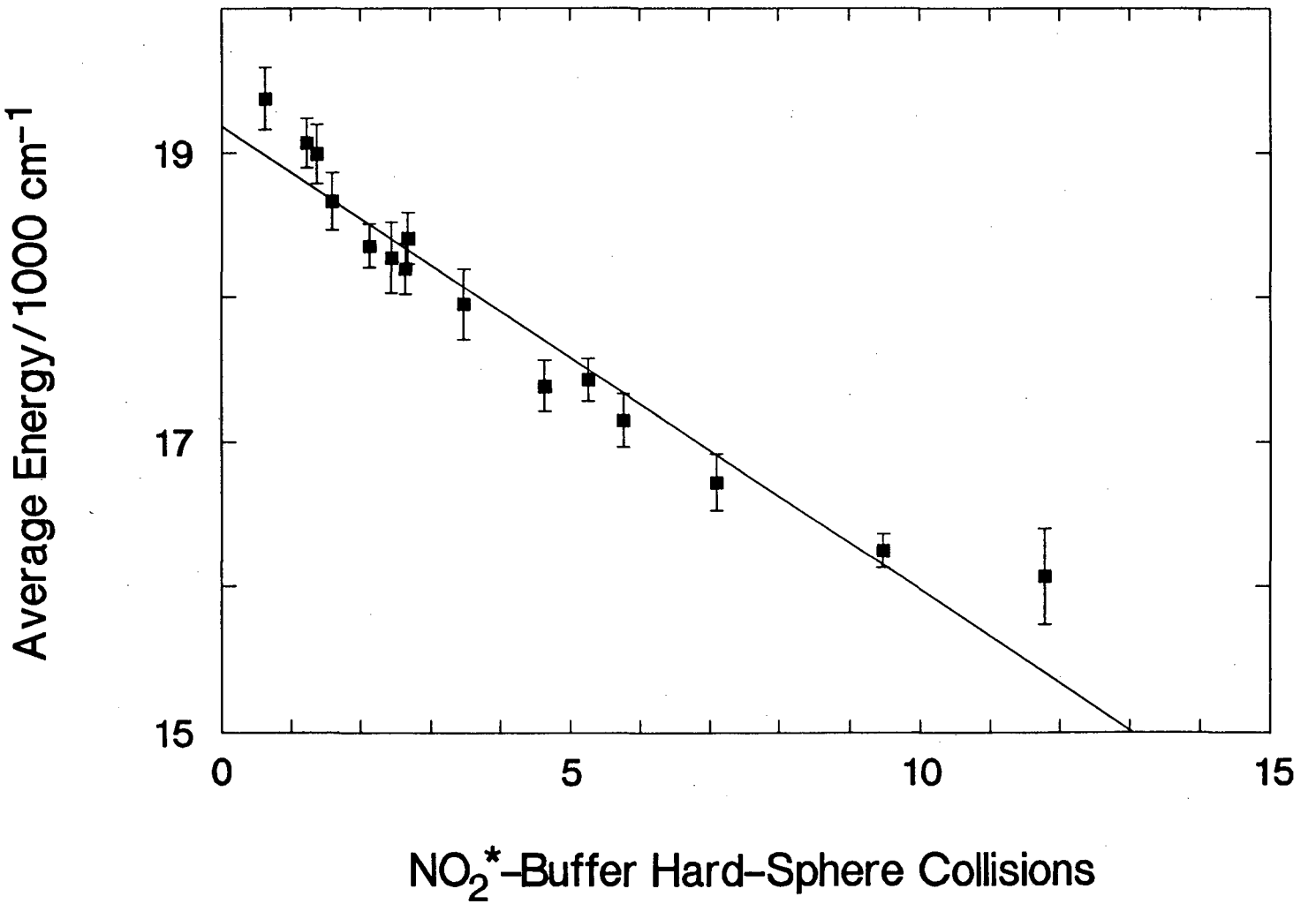
Average Energy/1000 cm^{-1}
19
17
15
0
5
10
15
NO_2^*-Buffer Hard-Sphere Collisions

Figure 2-27

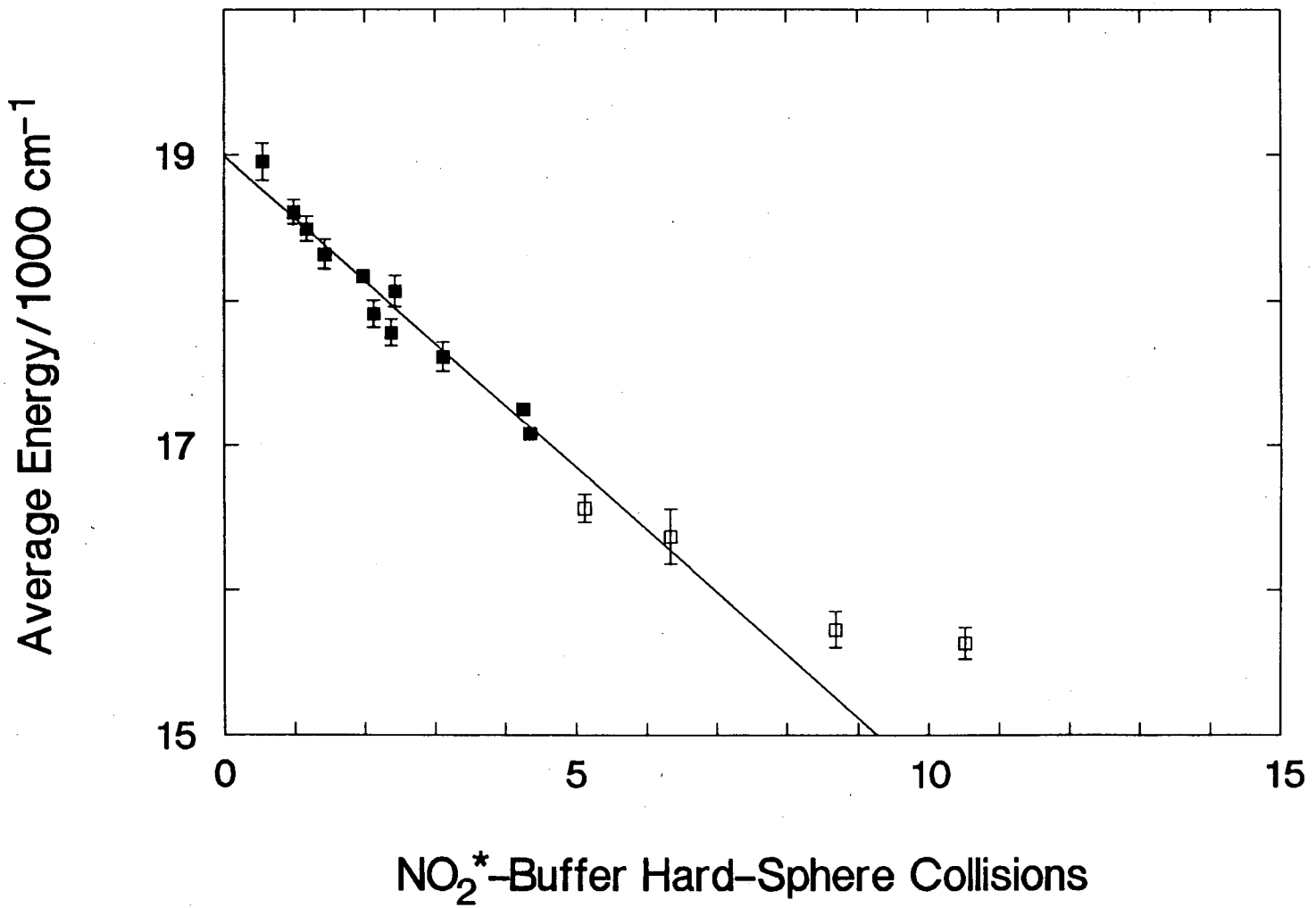
Average Energy/1000 cm^{-1}
19
17
15
0
5
10
15
NO_2^*-Buffer Hard-Sphere Collisions

Figure 2-28

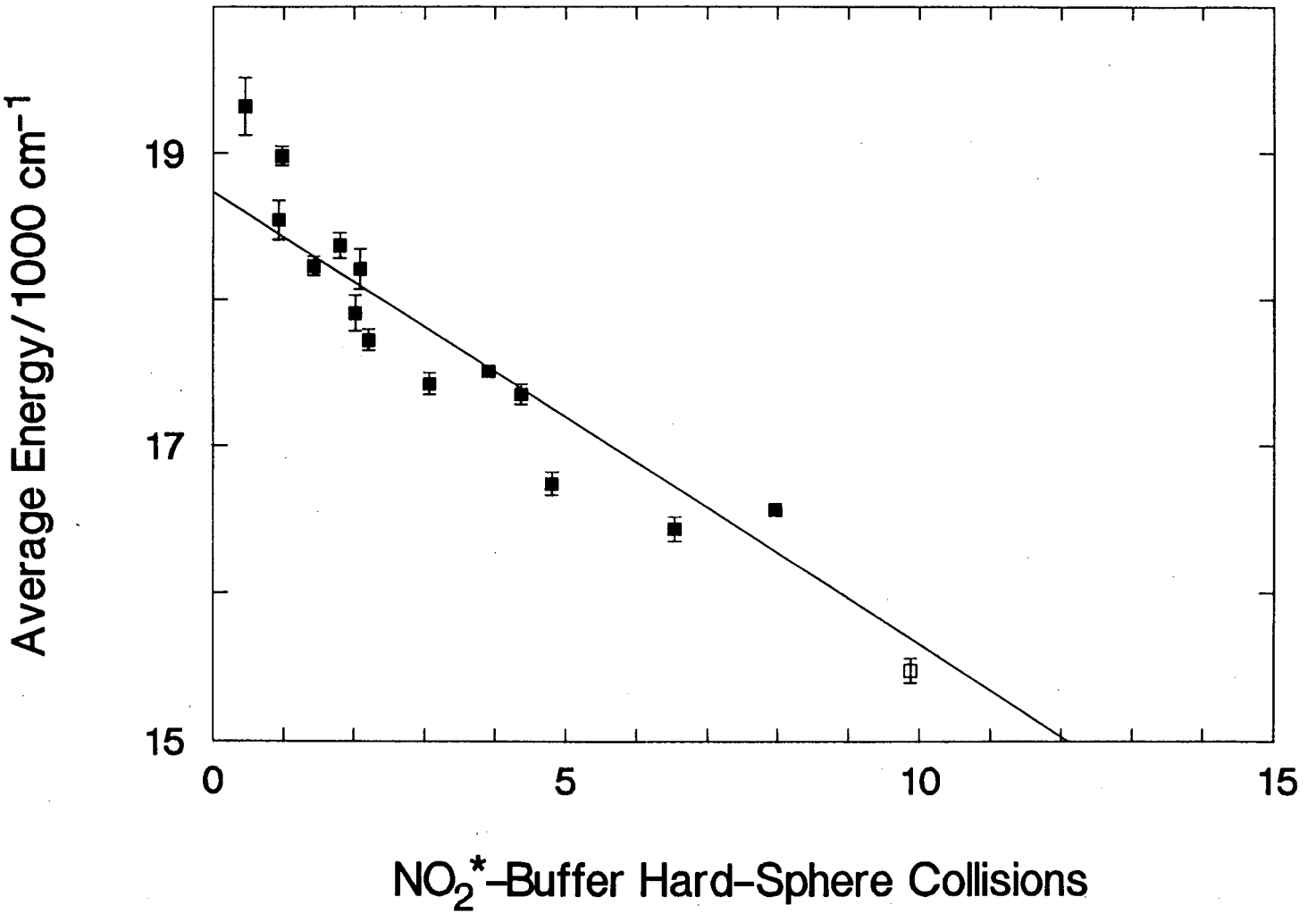
Average Energy/1000 cm^{-1}
19
17
15
0
5
10
15
NO_2^*–Buffer Hard–Sphere Collisions

Figure 2-29

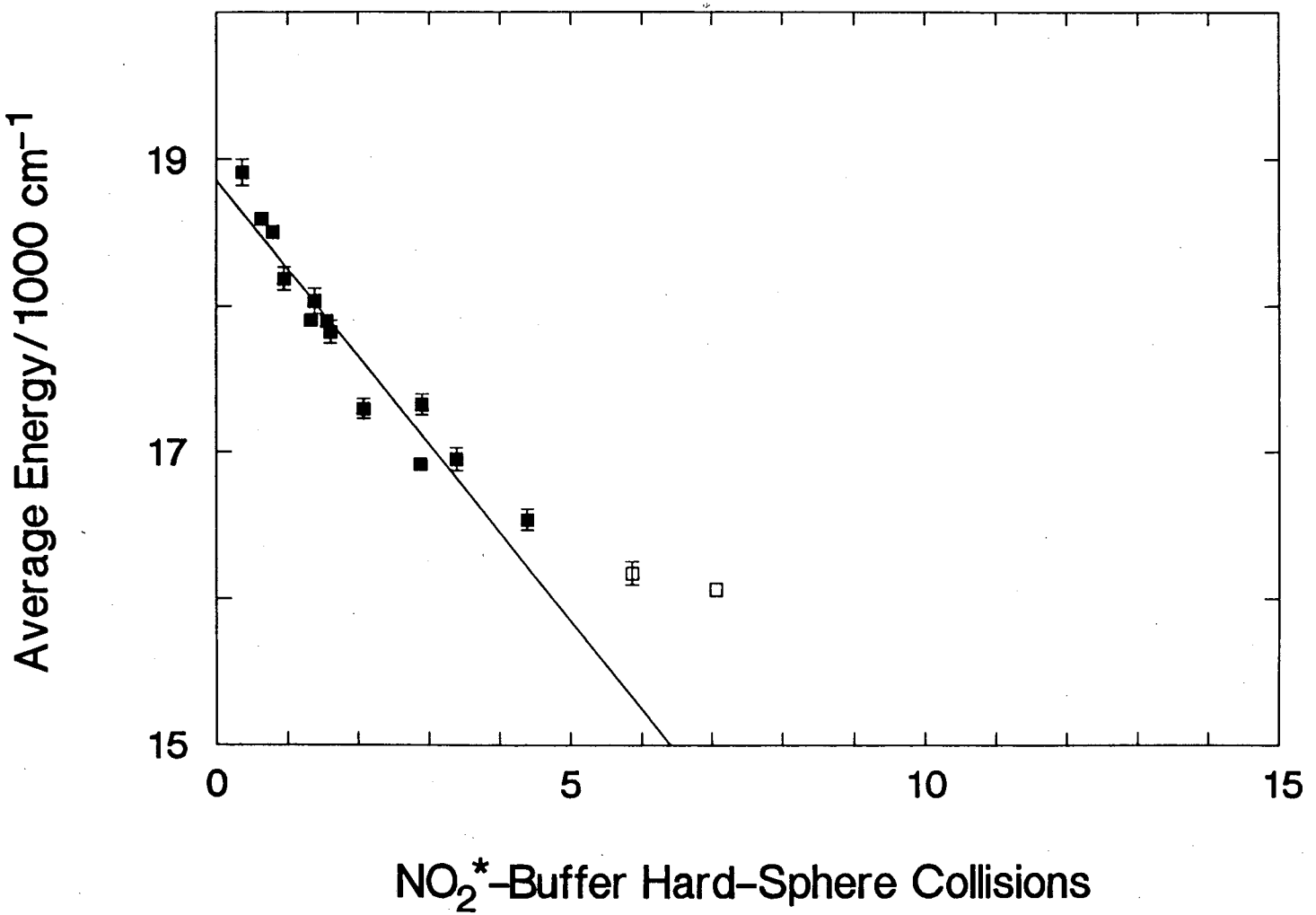
Average Energy/1000 cm^{-1}
19
17
15
0
5
10
15
NO_2^*-Buffer Hard-Sphere Collisions

Figure 2-30

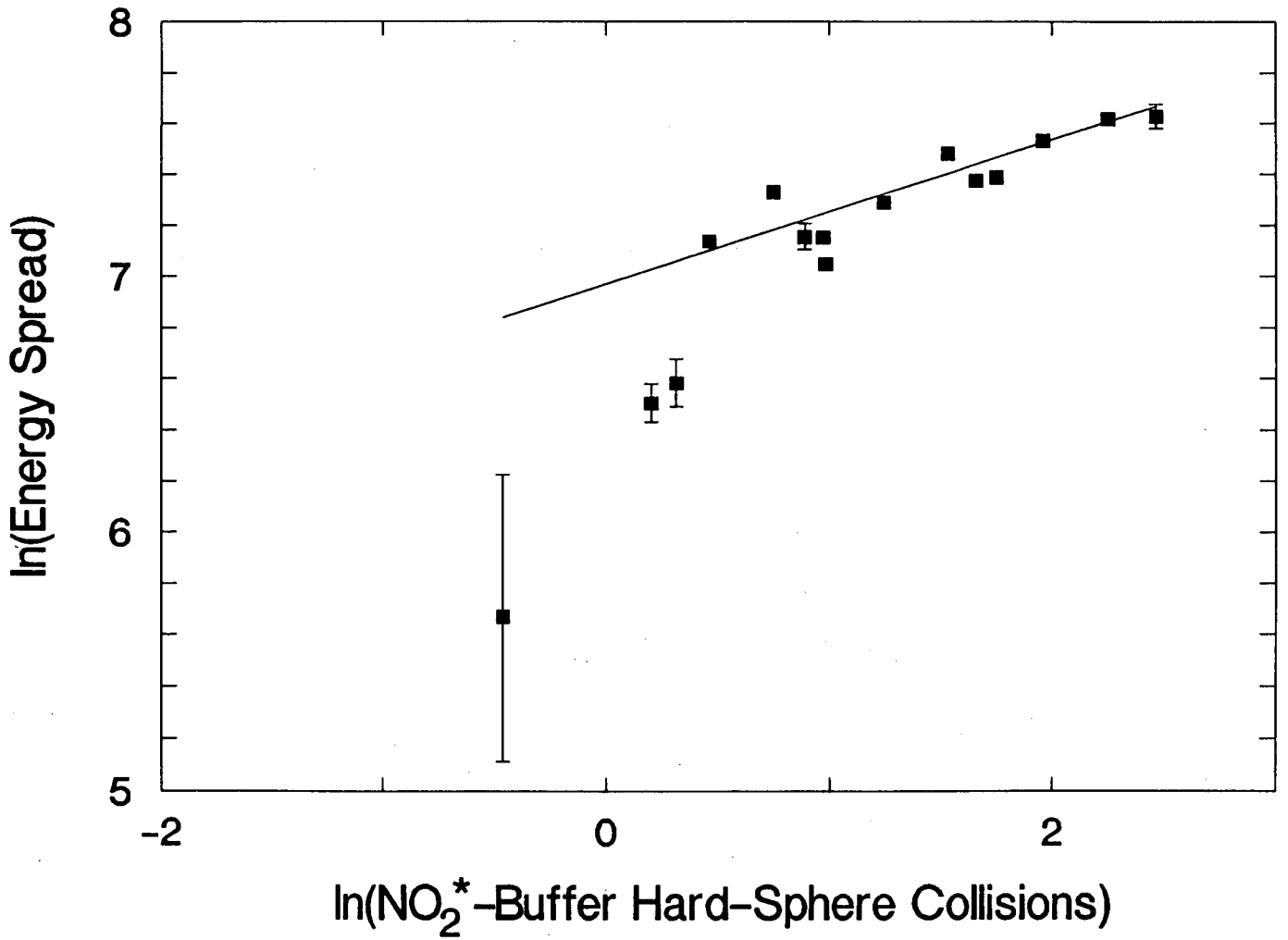
8
7
6
5
-2
0
2
ln(Energy Spread)
ln(NO_2^*-Buffer Hard-Sphere Collisions)

Figure 2-31

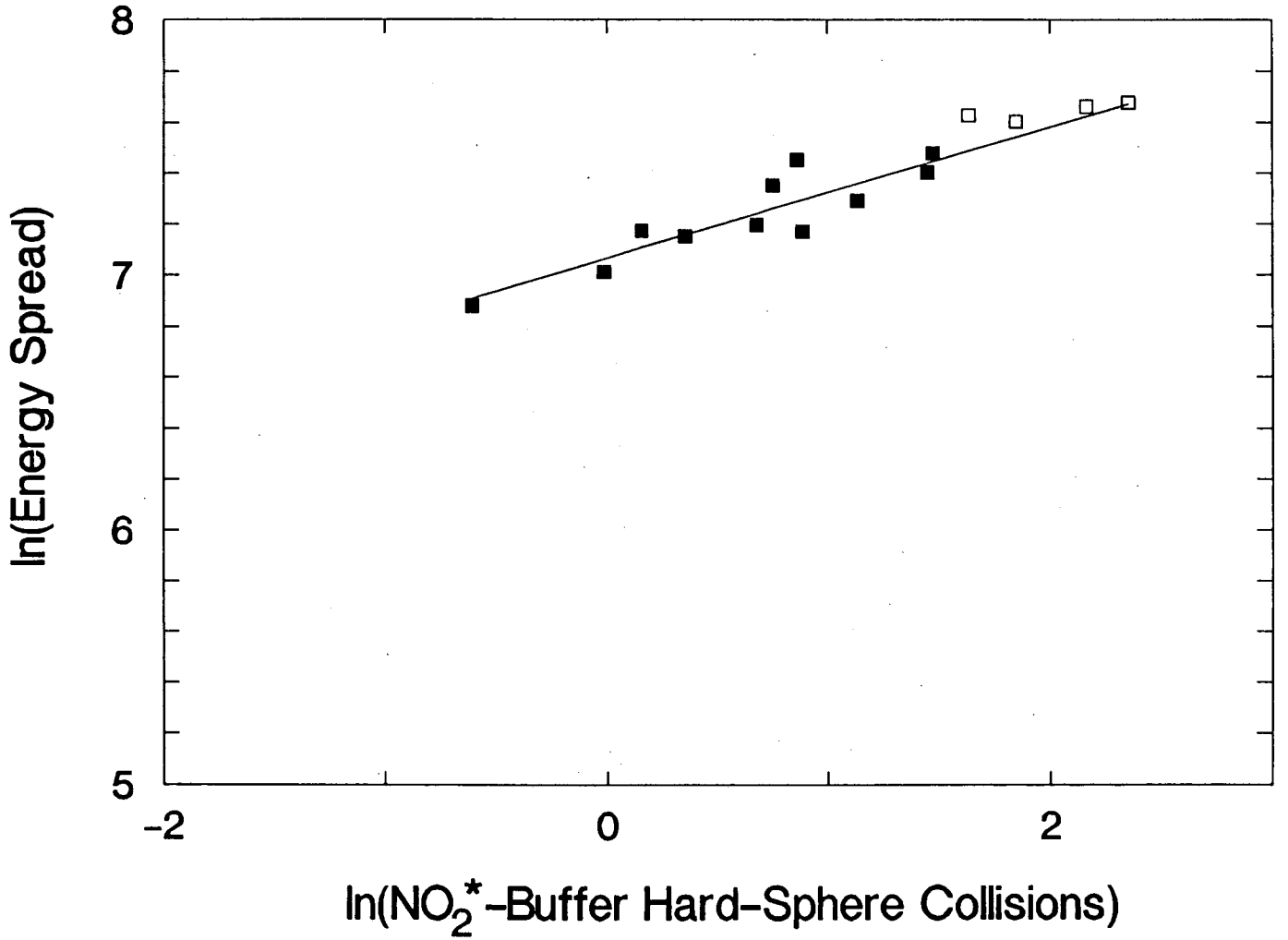
8
7
6
5
-2
0
2
ln(Energy Spread)
ln(NO_2^*-Buffer Hard-Sphere Collisions)

Figure 2-32

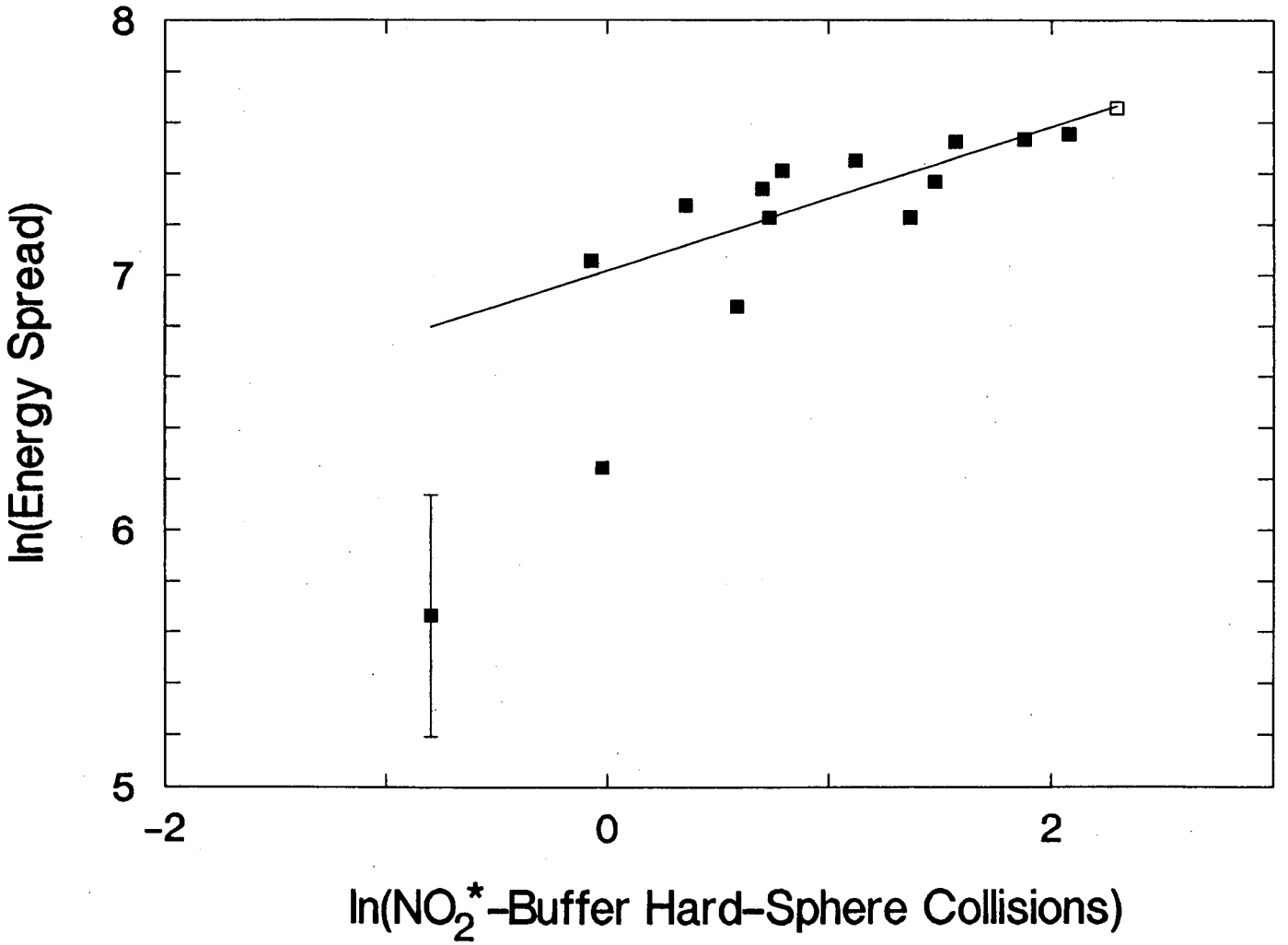
8
7
6
5
-2
0
2
ln(Energy Spread)
ln(NO_2^*-Buffer Hard-Sphere Collisions)

Figure 2-33

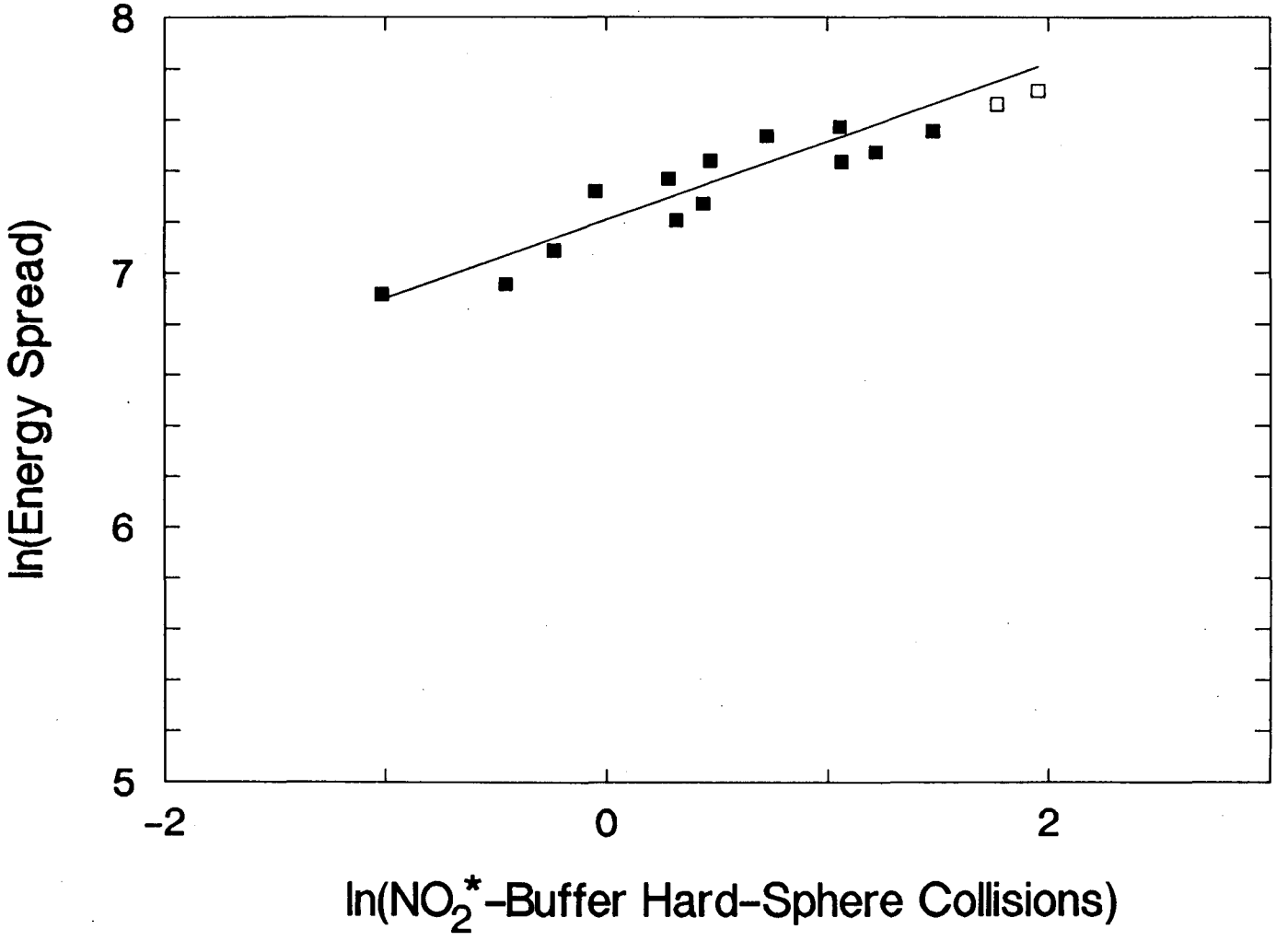
8
7
6
5
-2
0
2
ln(Energy Spread)
ln(NO_2^*-Buffer Hard-Sphere Collisions)

Figure 2-34

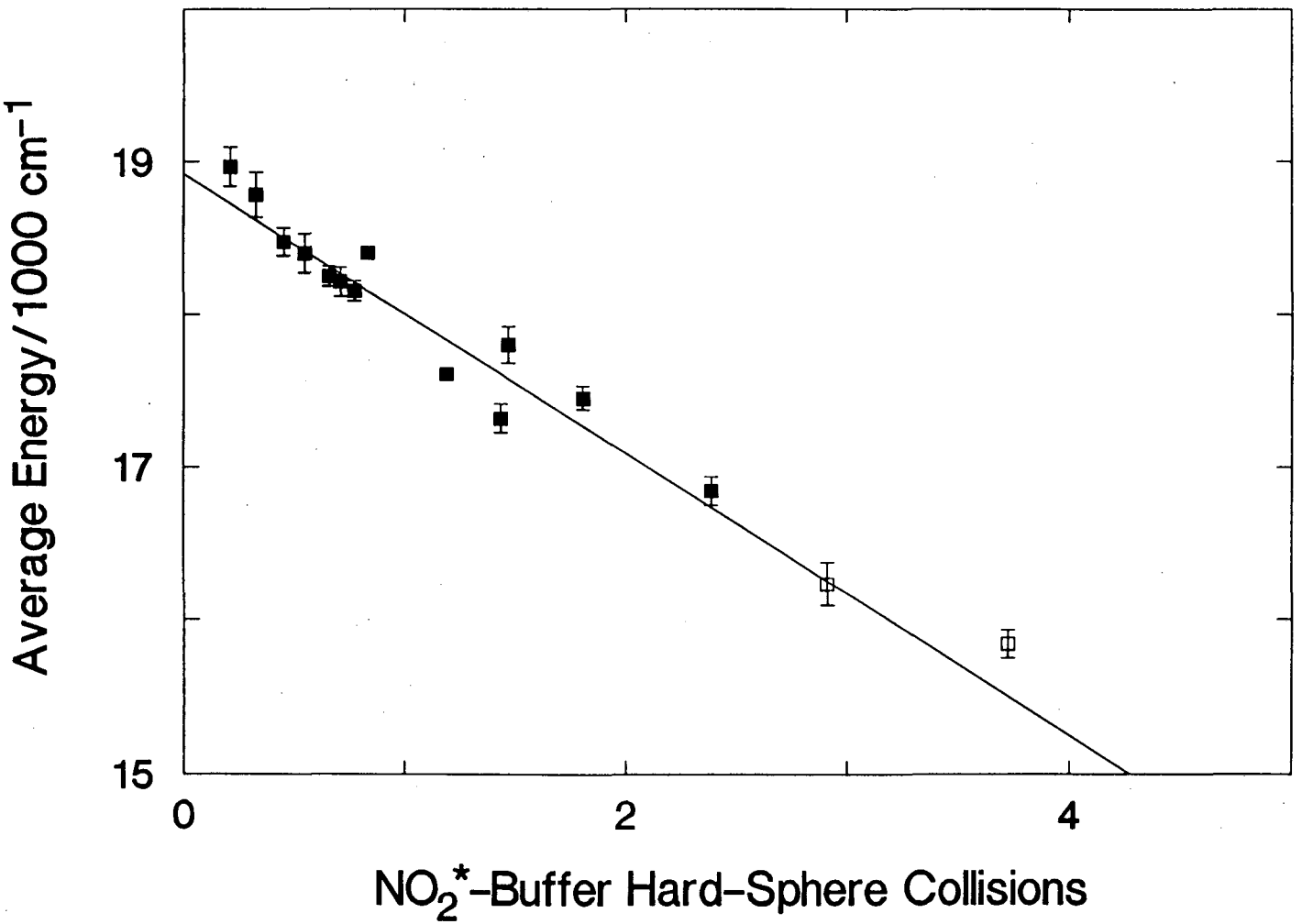
Average Energy/1000 cm^{-1}
19
17
15
0
2
4
NO_2^*-Buffer Hard-Sphere Collisions

Figure 2-35

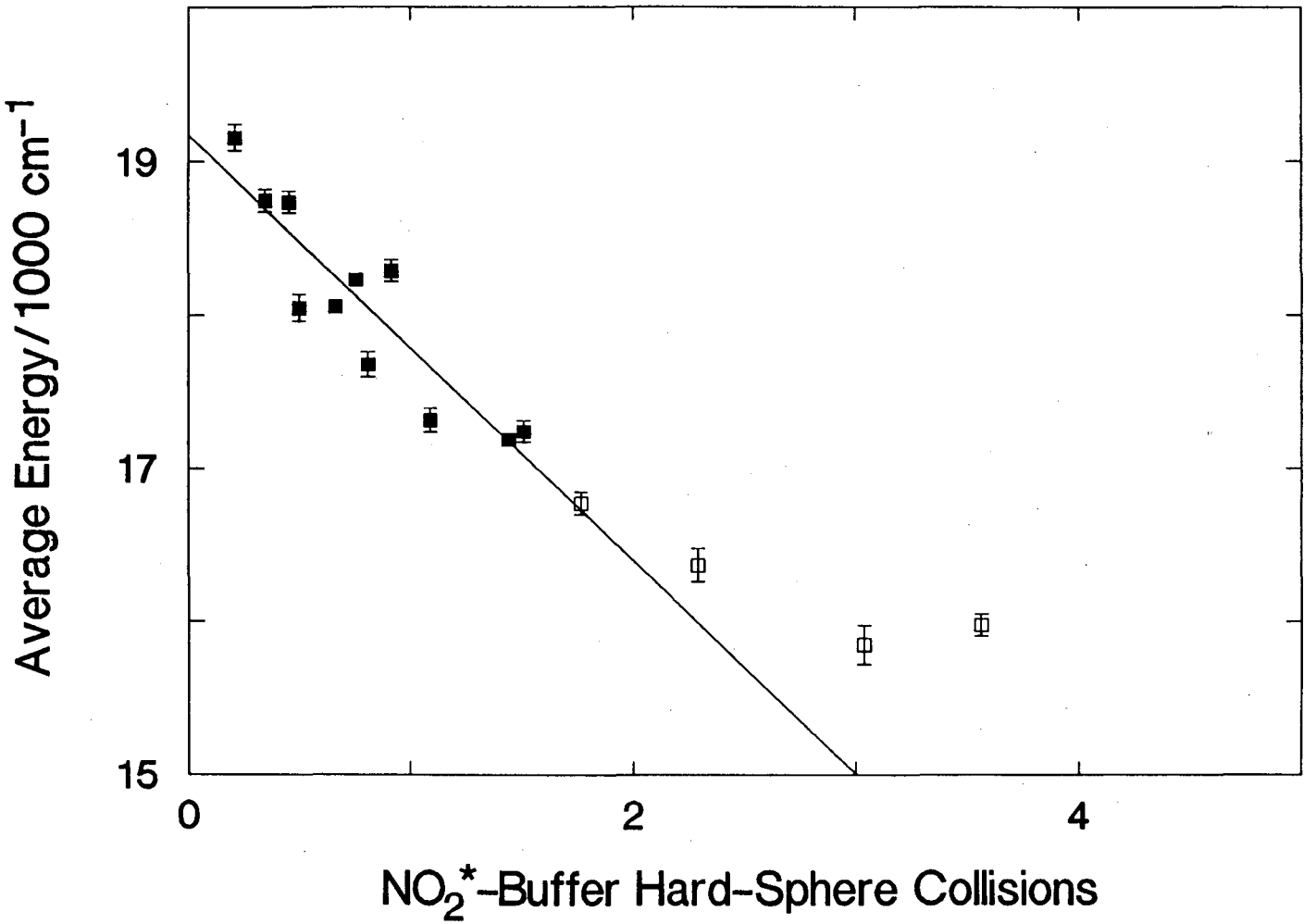
Average Energy/1000 cm^{-1}
19
17
15
0
2
4
NO_2^*-Buffer Hard-Sphere Collisions

Figure 2-36

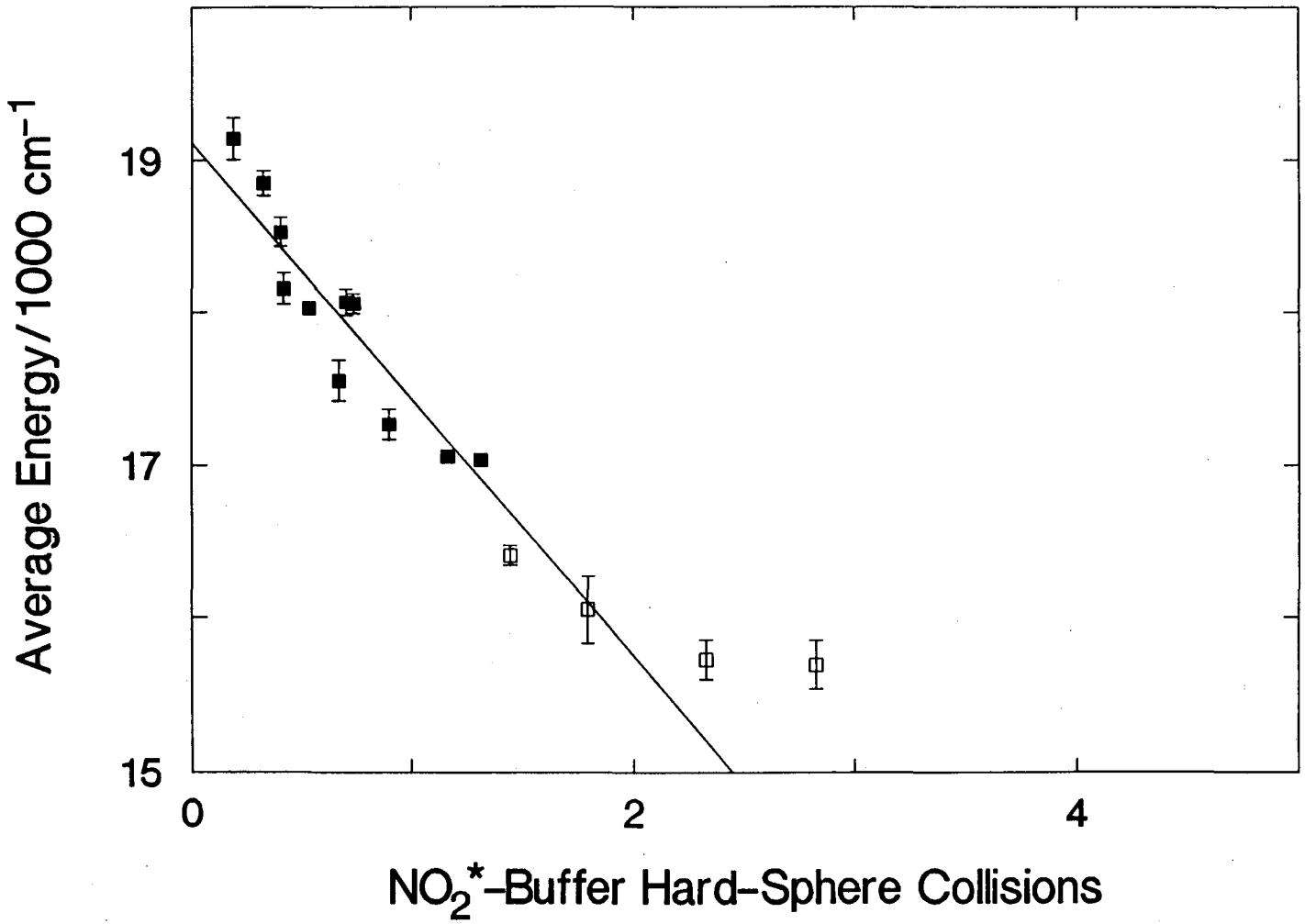
Average Energy/1000 cm^{-1}
19
17
15
0
2
4
NO_2^*-Buffer Hard-Sphere Collisions

Figure 2-37

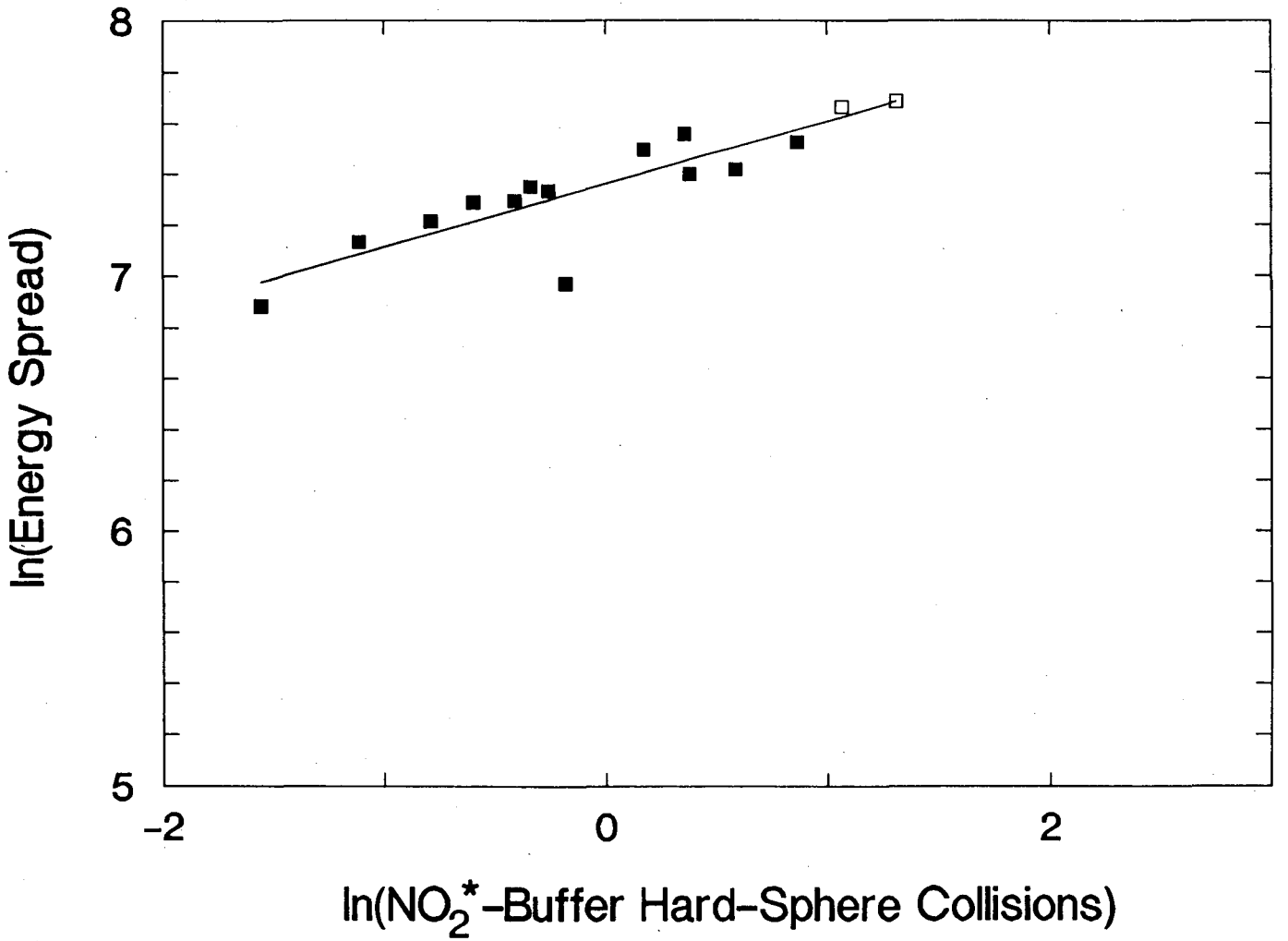
8
7
6
5
-2
0
2
ln(Energy Spread)
ln(NO_2^*-Buffer Hard-Sphere Collisions)

Figure 2-38

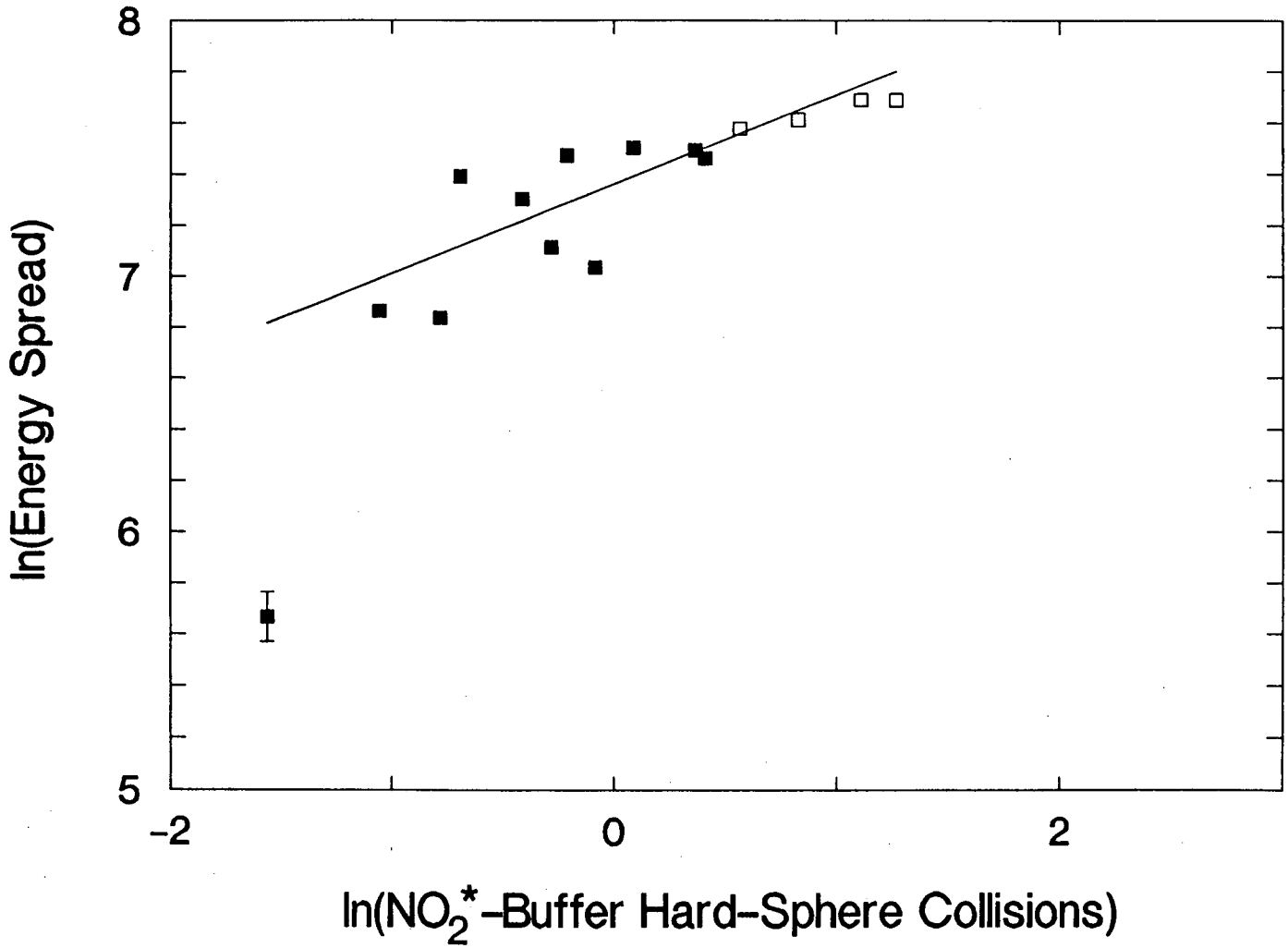
8
7
6
5
-2
0
2
ln(Energy Spread)
ln(NO_2^*-Buffer Hard-Sphere Collisions)

Figure 2-39

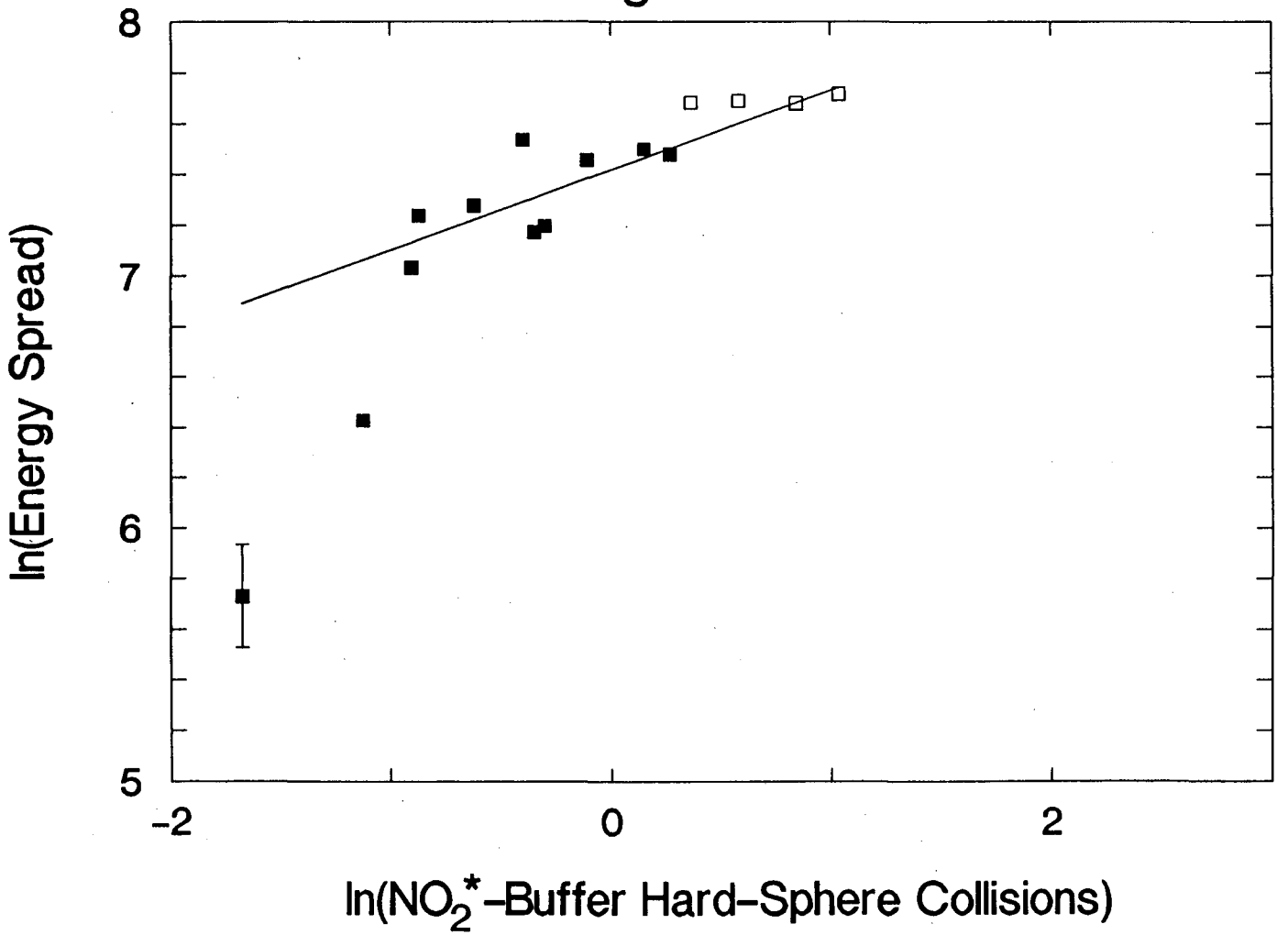
8
7
6
5
-2
0
2
ln(Energy Spread)
ln(NO_2^*-Buffer Hard-Sphere Collisions)

Figure 2–40

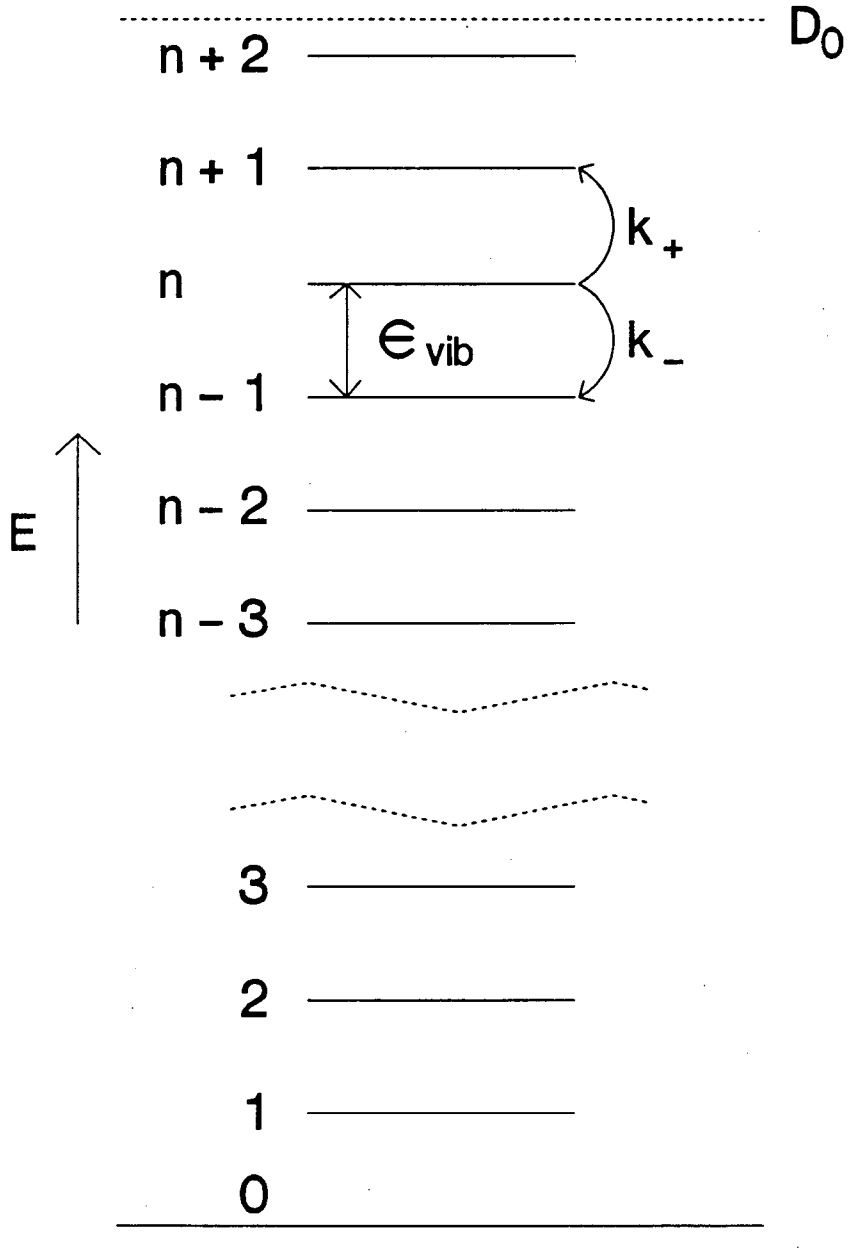

Figure 2-41

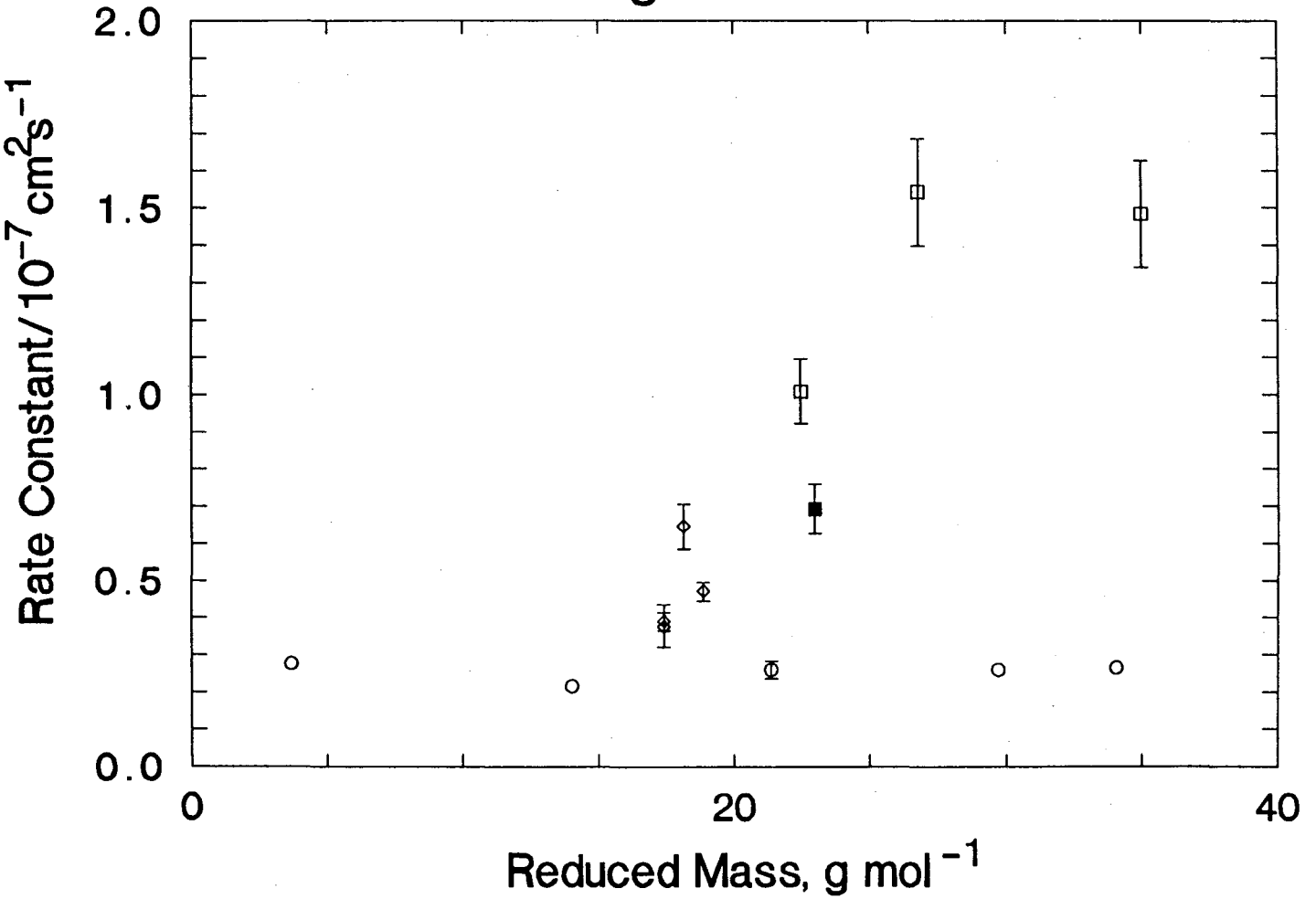
2.0
1.5
1.0
0.5
0.0
Rate Constant/10^{-7} cm^2s^{-1}
0
20
40
Reduced Mass, g mol^{-1}

Figure 2-42

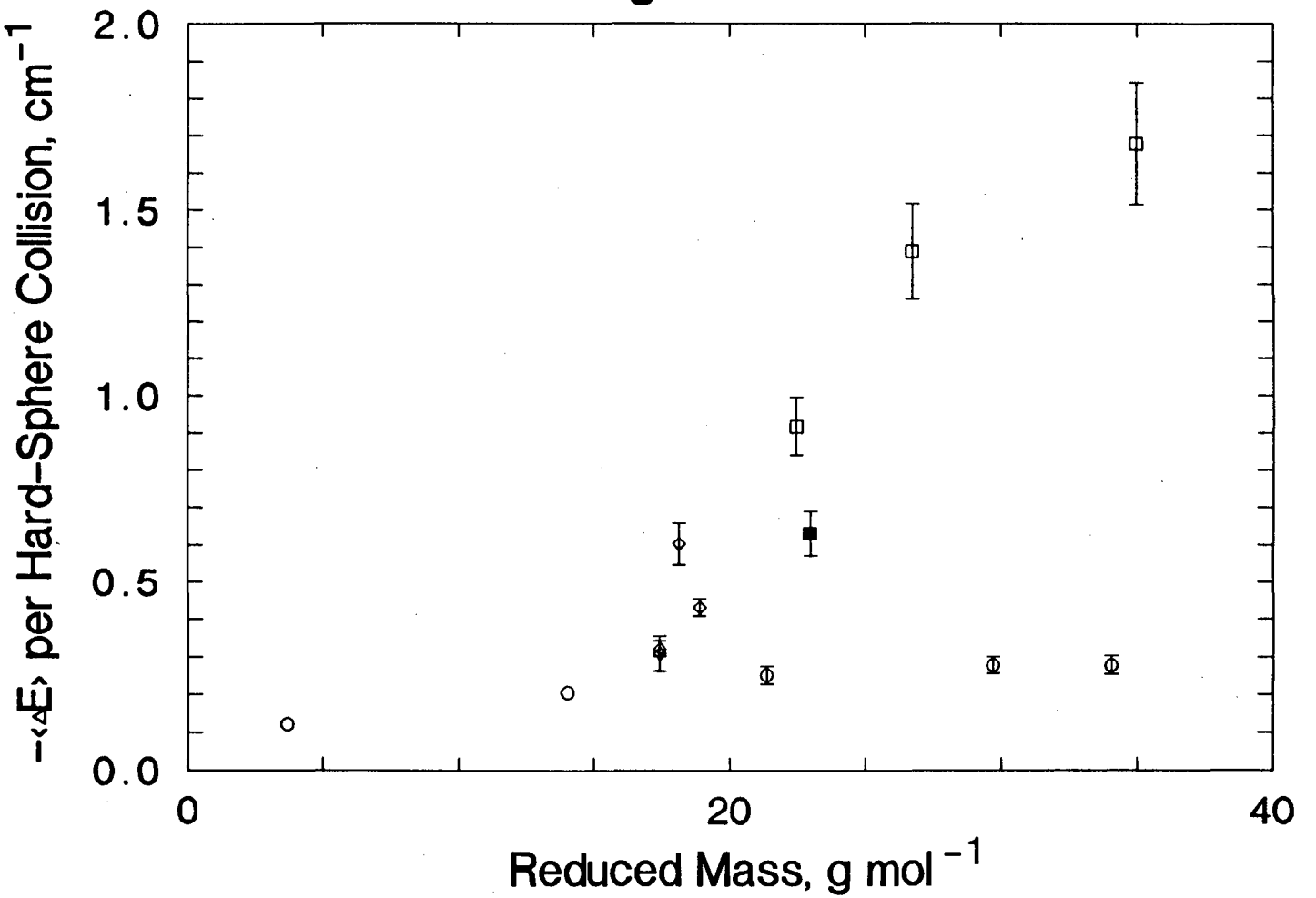
2.0
1.5
1.0
0.5
0.0
0
20
40
-<ΔE> per Hard-Sphere Collision, cm^{-1}
Reduced Mass, g mol^{-1}

Figure 2-43

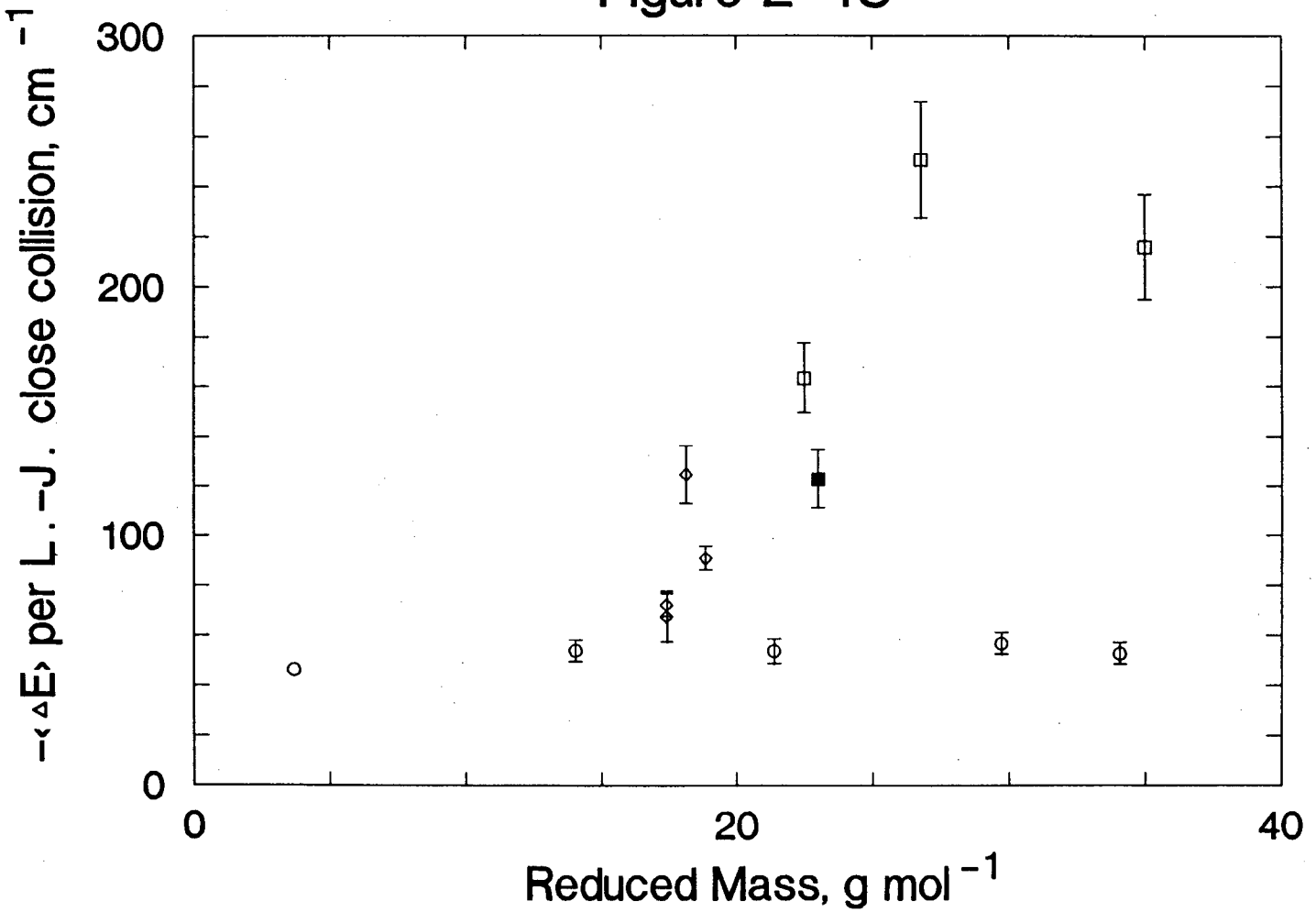
300
200
100
0
0
20
40
Reduced Mass, g mol $^{-1}$
$-\langle\Delta E\rangle$ per L.-J. close collision, cm $^{-1}$

Figure 2-44

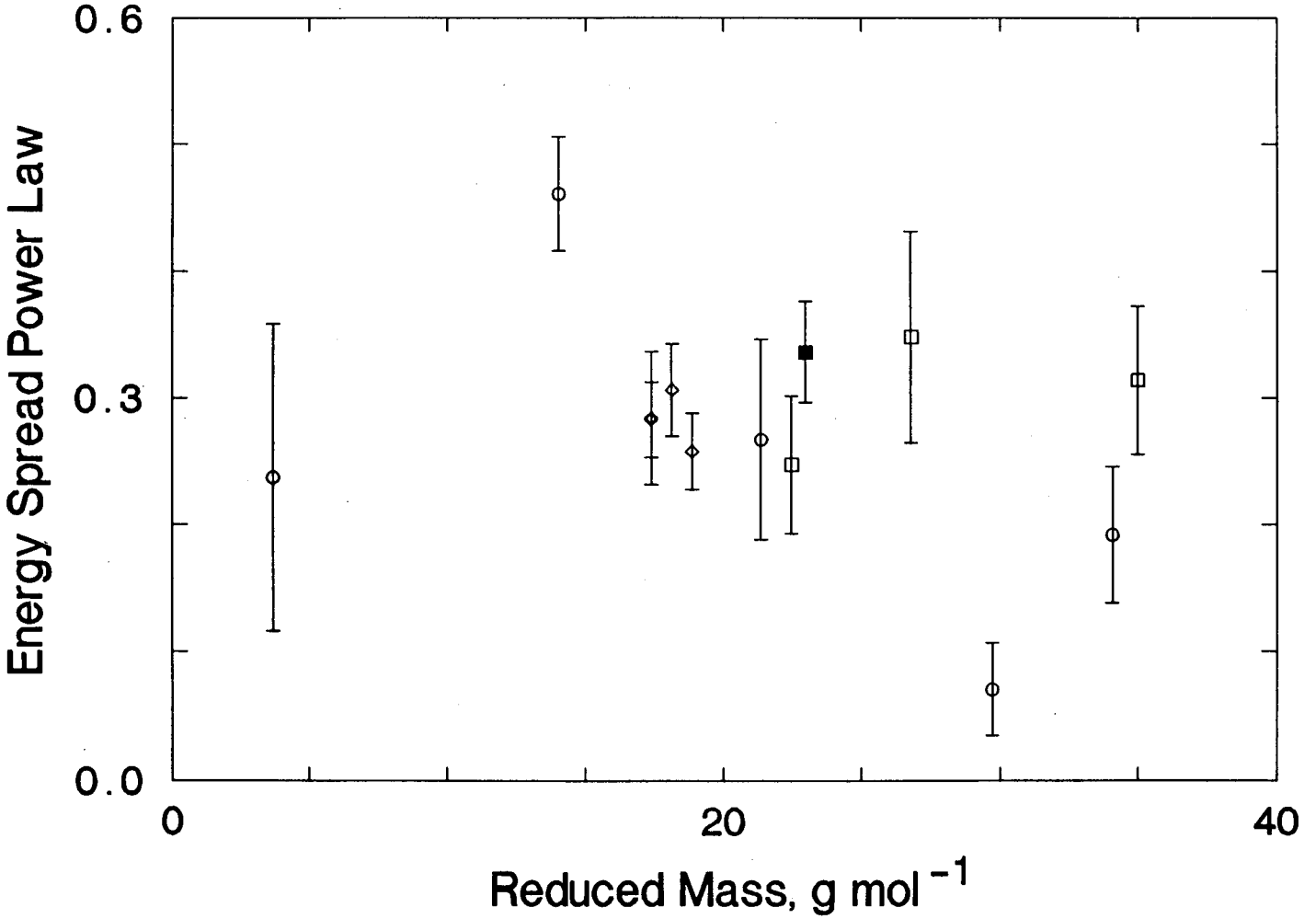

Figure 2-45

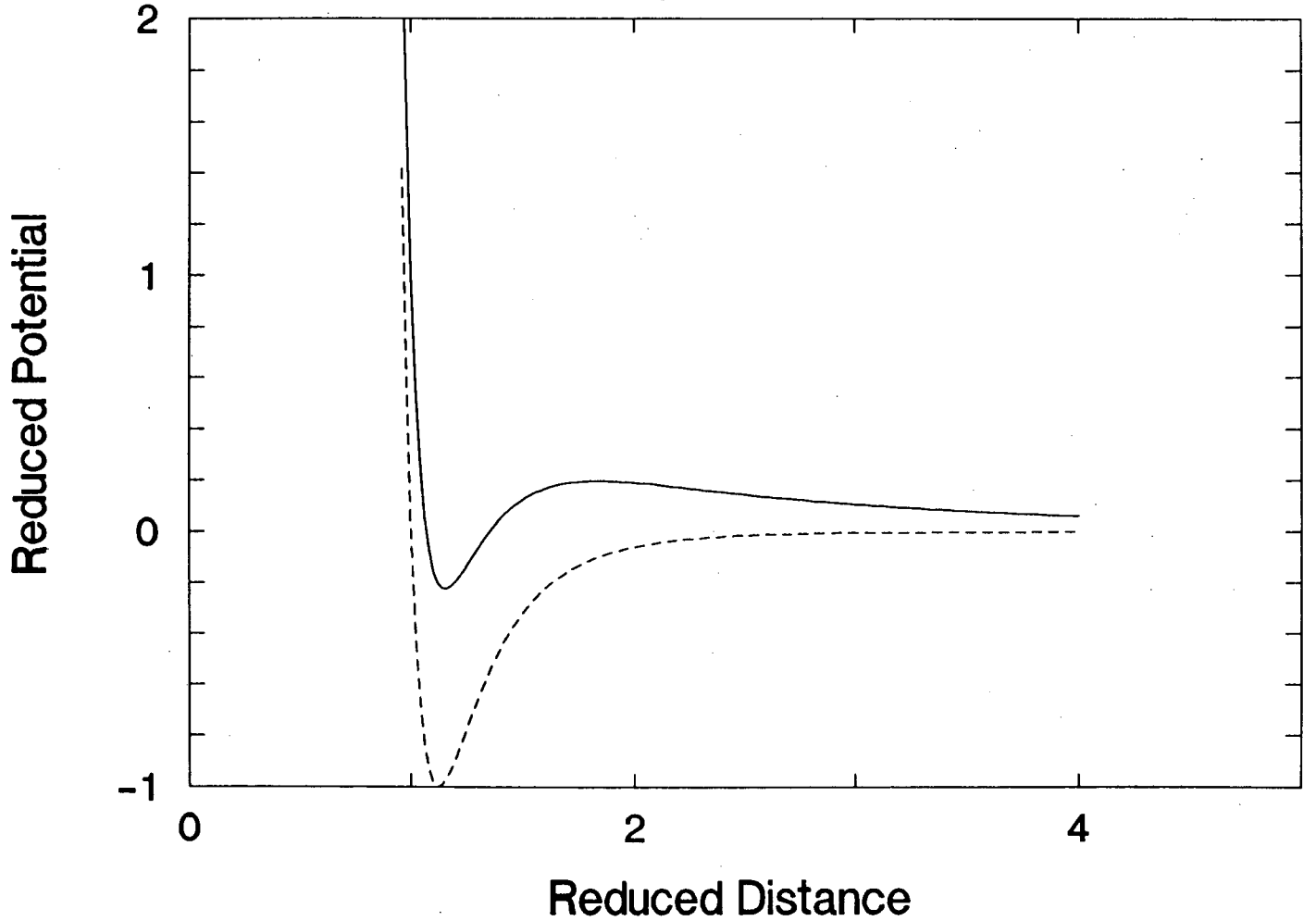

Figure 2-46

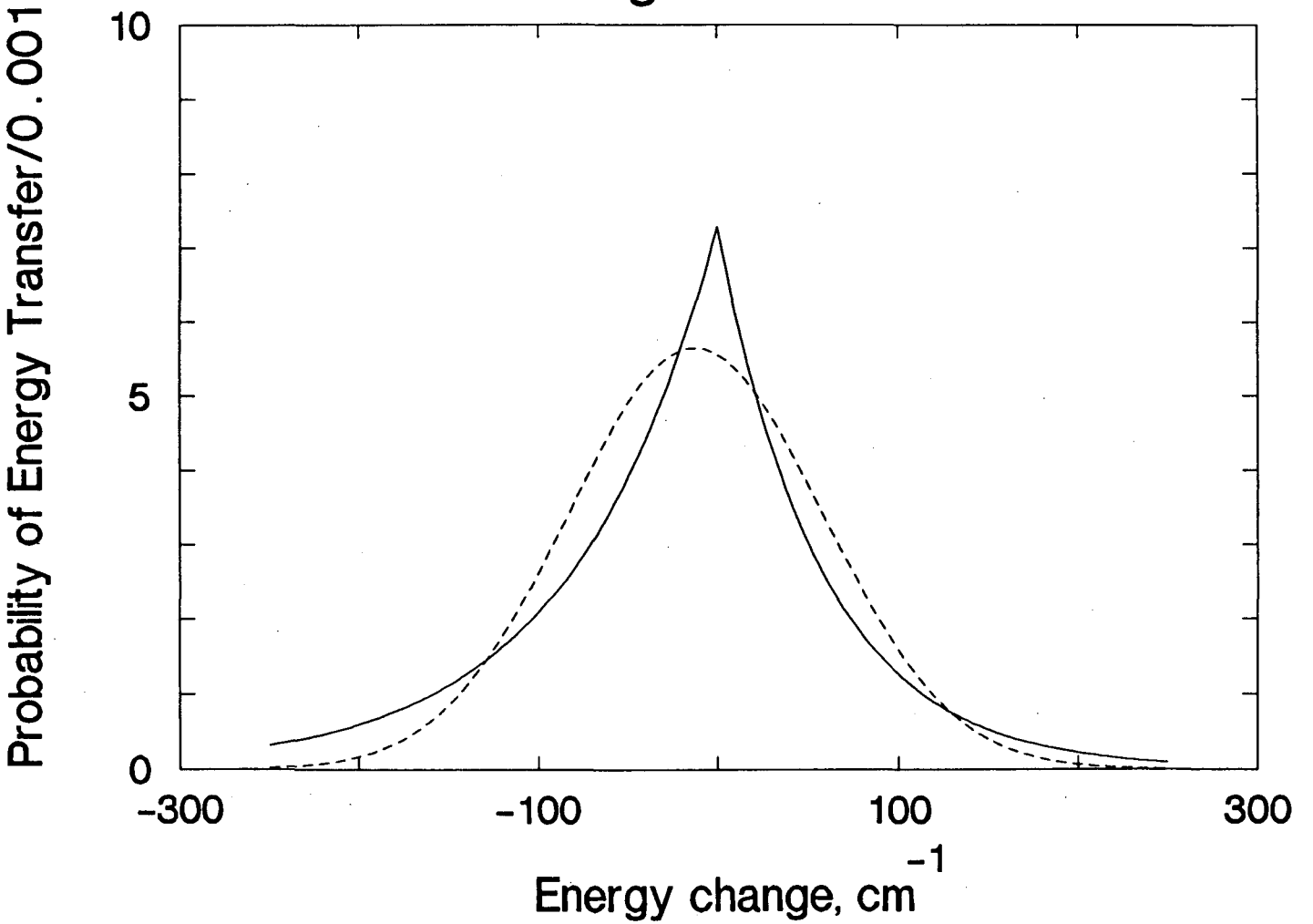
Probability of Energy Transfer/0.001
10
5
0
-300
-100
100
300
Energy change, cm^{-1}

Chapter 3

Excitation Energy Dependence of NO_2 Energy Transfer Rates

1. Introduction

The rate of energy removal from a molecule is conventionally expected to increase with increasing excitation energy. A simple explanation for this dependence is that added internal energy, particularly vibrational, stretches the chemical bonds which make up the molecule. The size of the molecule (and it collision cross-section area) thus increases with its internal energy.

Ultraviolet absorption experiments in shock tubes have provided energy dependence data on CS_2,[74] SO_2,[75] and azulene,[76] among other molecules. The energy removed from azulene per collision decreases approximately linearly with the average energy of the azulene population.[76] The smaller molecules CS_2[74] and SO_2[75] lose energy at a rate proportional to the square of the average energy instead. Excited CS_2 and SO_2 undergo similar vibrational-electronic interactions to those in excited NO_2.[7]

The time-dependent thermal lensing study of deactivation of NO_2 by Ar, Kr, and Xe from an initial excitation of 21,631 cm^{-1} has found a marked dependence of the energy removal rate upon the ensemble-averaged energy through the entire deactivation back to energies near thermal.[54] A linear dependence for energies up to 4,000 cm^{-1} gives way to a quadratic dependence for average energies between 4,000

and 10,000 cm^{-1}. Above 10,000 cm^{-1}, the energy removal rate becomes at least fifth order in the average energy, though the report states that results are uncertain near the excitation energy.

Dependence of the energy removal rate constant upon the ensemble average energy has been found to a slight extent in the delayed fluorescence studies after excitation at 532 nm (Chapter 2, Section 4.1). However, the underlying dependence of energy transfer rate constants upon the internal energy of NO_2^* is not readily obtained from these data. For any nonzero concentration-time product (collision number), the observed energy removal rate is a sum of contributions from a range of internal energies of NO_2. The average energy as a function of concentration-time product may be extrapolated back to that at zero concentration-time product given a suitable model for the dependence. Laser excitation allows the preparation of a relatively narrow range of internal energies from which the initial rate constant for energy removal can be obtained. This chapter combines the energy transfer data for NO_2 excited by 532 nm light (Chapter 2) with additional data obtained at excitation energies of 21,000, 23,000, and 25,000 cm^{-1} in order to determine the internal energy dependence of the NO_2 energy transfer rate constant.

2. Experimental Apparatus

The fluorescence collection system and electronics of Chapter 2, Section 2 are used with few changes. The changes required for the experiments at higher excitation energies are noted below.

2.1. Excitation and Fluorescence Collection

The experimental apparatus is shown in Figure 3-1. A dye laser (Lumonics HyperDye 300) is pumped by 50-100 mJ per pulse of 308 nm light from an excimer laser (Questek 2210; XeCl). The dye laser produces tunable light pulses with 5-10 mJ of energy lasting < 20 ns, and the bandwidth of the laser was found as 0.8 cm^{-1} by the manufacturer. The excitation wavelength of 400.00 nm was set with no fluorescence intensity optimization, while the wavelengths of 435.04 and 475.34 nm were selected to produce the maximum fluorescence signal. The laser dyes Exalite® 398, Coumarin 440, and Coumarin 480 (Exciton) were dissolved in p-dioxane (Exalite® 398) or in methanol (Coumarin 440, 480) according to the specifications of the dye manufacturer in order to produce 400.00, 435.04, and 475.34 nm respectively. The excitation wavelengths were checked using the monochromator position corresponding to the scattered light peak. The uncertainties in the following readings reflect the slit width of the monochromator rather than the laser bandwidth:

nominal λ/nm	measured λ/nm	excitation energy/cm^{-1}
475.34	475.57 ± 0.08	21027.5 ± 3.5
435.04	435.20 ± 0.04	22977.9 ± 2.1
400.00	400.17 ± 0.04	24989.4 ± 2.5

Further, the above measurements are uncertain to ±0.1 nm due to the monochromator wavelength calibration. Laser intensity and NO_2 pressure variations were simultaneously monitored for normalization by observing the total fluorescence intensity. An photomultiplier tube (RCA 1P21) equipped with a colored glass filter (Corning CS2-60) to block scattered laser light observed intensity through the glass wall of the fluorescence cell along the axis perpendicular to both the laser path and the optical axis of the monochromator. This intensity PMT is supplied with an independent high-voltage power supply (Fluke 412B) and a separate amplifier (Avantek GPD 461, 462, and 463 in cascade) from the dispersed fluorescence PMT mounted to the monochromator exit. Signal from the intensity PMT is sent to the third of the analog gated integrators (SR250). As in Chapter 2, all three gated integrators are triggered by the photodiode, and the first two gated integrators each collect the dispersed PMT signal at different delay times after laser excitation.

The slit widths of the monochromator (Interactive Technology CT-103) are set to 1.25 mm in order to obtain better precision of the observation wavelength; an apparent factor of 2 error in ΔX terms of the data analysis equations (Equations 2-6 through 2-18) is cancelled upon normalization. The observation wavelength is scanned from 380 to 818 nm in 2-nm steps except for 400.00 nm excitation, for

which the wavelength is started from 370 nm in order to provide 5 extra points of zero signal. The redmost observation wavelength valid for data analysis is 818 nm for excitation at 435.04 and 475.34 nm, but wavelengths greater than 796 nm are discarded for excitation at 400.00 nm because second-order transmission by the monochromator grating distorts the fluorescence profile. The spectral responsivity is obtained by a tungsten ribbon standard light source as in Chapter 2, and the responsivity used is plotted in Figure 3-2.

A possible interference in this experiment arising from the use of the dye laser is amplified stimulated emission (ASE). The contribution of this effect is determined at 475.34 nm by using an array of three 60° quartz prisms to disperse the laser excitation beam spatially. A visible greenish-blue ASE spot in addition to the blue laser beam is blocked by an iris following the prism array. Most of the experiments at this wavelength (Table 3-1) use this ASE removal, but some experiments at 475.34 nm (marked in Table 3-1) and all of those at 435.04 and 400.00 nm excitation do not use the dispersing prism array.

2.2. NO_2 Sample Handling

NO_2 (Matheson, 99.5%) is subjected to a freeze-pump-thaw cycle using liquid nitrogen to remove volatile impurities, then mixed at room temperature with one-half atmosphere of oxygen gas (Lawrence Berkeley Laboratory, 99.5%) for 12 hr. to destroy NO impurities. The excess O_2 is removed by a second freeze-pump-thaw

cycle with liquid nitrogen, after which the sample is vacuum-distilled from -20 °C to -70°C. A Dry Ice-isopropanol slush bath maintains the -70 °C temperature, while a bath containing equal volumes of ethylene glycol and water is cooled to -20 °C by a refrigerated cooling unit (Neslab RTE-4). Only the middle third of the NO_2 sample is retained in the vacuum distillation, and the resulting white solid N_2O_4 (NO_2 dimer) is maintained in the dark at -70 °C. The experiments at 475.34 nm used a static cell configuration as did those in Chapter 2, but those at 435.04 and 400.00 nm ran with an NO_2 flow rate of approximately 5 mTorr/minute because of the possibility of significant photolysis of NO_2 during the experiment.[18]

3. Results

The dispersed fluorescence spectra collected are normalized for the total fluorescence and corrected for spectral responsivity by ANALYZ.PRO under ASYST[49] as for the 532 nm data in Chapter 2. The fluorescence deconvolution procedure (see Section 3.2 of Chapter 2) of FP28 FOR and FITPRO28.FOR produces the excited state population for each experiment. Average energy $<E>$ and energy spread $<\Delta E^2>^{1/2}$ (Equations 2-16 and 2-17) are obtained provided the fraction to the red of the observation limit f_R (Equation 2-18) is less than or equal to 0.05. Further analysis is based upon these moments of the population, particularly the average energy.

3.1. 475.34 nm excitation

Table 3-1A lists the NO_2 pressure and delay time for the experiments at this excitation wavelength, while Table 3-1B lists the fit parameters, average energy $<E>$, and energy spread $<\Delta E^2>^{1/2}$. The plot of $<E>$ versus hard-sphere collision number for 475.34 nm excitation (Figure 3-3) shows significant positive curvature. The weighted linear least squares fit[58] of $<E>$ in cm^{-1} versus NO_2 concentration-time product in cm^{-3} s, shown by the dashed line in the figure, fails to model this profile:

$$<E> = -(10.35 \pm 0.71) \times 10^{-8}\, c(NO_2) \cdot t + (20580 \pm 110)$$

$$\chi^2 = 348. \qquad (3\text{-}1)$$

The χ^2 above is not an absolute test of the validity of the fit above since the uncertainties obtained in $<E>$ are based upon the deviation of data from the fit rather than upon the actual variation in the data. χ^2 nonetheless indicates the validity of the model overall; a decreasing χ^2 indicates a more satisfactory description of the data, as is obtained for a fit of $<E>^{-3}$ to concentration-time product:

$$<E>^{-3} = (2.69 \pm 0.13) \times 10^{-24}\, c(NO_2) \cdot t + (1.069 \pm 0.026) \times 10^{-13}$$

$$\chi^2 = 216. \qquad (3\text{-}2)$$

This fit is demonstrated by the solid line in Figure 3-3. The data at both ends and in the center of the plot are better represented by Equation 3-2.

The log-log plot of the energy spread versus the hard-sphere collision number shown in Figure 3-4 is fit by the line:

$$\ln \langle \Delta E^2 \rangle^{1/2} = (0.148 \pm 0.046) \ln[c(NO_2) \cdot t] + (4.3 \pm 1.1)$$

$$\chi^2 = 14600. \qquad (3\text{-}3)$$

The very high value of χ^2 is related more to the small uncertainties in the energy spread (Table 3-1B) than to disagreement between the fit and the trend in the results. The limitations of the uncertainty estimation method used throughout this study are apparent. The slope of 0.148, when combined with the tendency of the population profiles toward Biexponential (Equation 2-11) behavior, indicates marked asymmetry in the deactivated population.

Comparison of similar experiments in Table 3-1B for which ASE is allowed to pass through the fluorescence cell with the experiments for which no ASE is allowed indicates little effect of ASE. Experiments 3, 6, 7, and 8 (ASE not allowed) yield an unweighted average of $\langle E \rangle$ of 20379 $\pm$ 180 cm^{-1}, while Experiments 4 and 5 (ASE allowed) give $\langle E \rangle$ of 20164 $\pm$ 46 cm^{-1}. The difference of 200 cm^{-1} is not much larger than the estimated uncertainty in $\langle E \rangle$ for some experiments, and is three times the maximum resolution element for this experiment, (1 nm)(1.0E7

$cm^{-1}/nm)/(400\ nm)^2 = 62.5\ cm^{-1}$. The possible effect of ASE decreases as collisions proceed, as expected since any deactivated ASE-excited NO_2 becomes increasingly indistinguishable from deactivated laser-excited NO_2.

3.2. 435.04 nm excitation

Parts A and B of Table 3-2 summarize the 435.04 nm NO_2 deactivation experiments. Positive curvature in $<E>$ versus NO_2 hard-sphere collision number again appears in Figure 3-5. The linear fit,

$$<E> = -(10.30 \pm 0.98) \times 10^{-8}\ c(NO_2)\cdot t + (22140 \pm 200)$$
$$\chi^2 = 602 \qquad (3\text{-}4)$$

of the dashed line is even poorer than for 475.34 nm excitation. The solid line representing the fit to $<E>^{-3}$:

$$<E>^{-3} = (2.20 \pm 0.12) \times 10^{-24}\ c(NO_2)\cdot t + (8.25 \pm 0.25) \times 10^{-14}$$
$$\chi^2 = 256 \qquad (3\text{-}5)$$

fits the data satisfactorily.

The ln-ln plot of energy spread versus hard-sphere collision number (Figure 3-6) again shows an asymmetric population distribution:

$$\ln \langle \Delta E^2 \rangle^{1/2} = (0.136 \pm 0.024) \ln[c(NO_2) \cdot t] + (4.70 \pm 0.56)$$

$$\chi^2 = 10700. \qquad (3\text{-}6)$$

The populations derived from these experiments typically have profiles resembling the Biexponential intensity coefficient function.

3.3. 400.00 nm excitation

The summary of experiments in Table 3-3 indicates the unusual nature of this excitation wavelength. Experiments 1 and 2 are best fit by populations which are extremely narrow mostly because of the cutoff at the dissociation energy $D_0 = 25132$ cm^{-1}.[17] The positive curvature in $\langle E \rangle$ with respect to hard-sphere collision number is the most severe in this study, as shown by Figure 3-7. Accordingly, the linear fit:

$$\langle E \rangle = -(14.59 \pm 0.15) \times 10^{-8}\, c(NO_2) \cdot t + (23960 \pm 300)$$

$$\chi^2 = 697 \qquad (3\text{-}7)$$

of the dashed line does not correspond well to the data. The $\langle E \rangle^{-3}$ fit (solid line) is improved:

$$\langle E \rangle^{-3} = (2.399 \pm 0.084) \times 10^{-24}\, c(NO_2) \cdot t + (6.20 \pm 0.26) \times 10^{-14}$$

$$\chi^2 = 217. \qquad (3\text{-}8)$$

The near-nascent Experiments 1 and 2 distort the ln-ln plot of $<\Delta E^2>^{1/2}$ versus hard-sphere collision number in Figure 3-8. The reported uncertainties of these two points are small, so that the weighted least squares fit

$$\ln <\Delta E^2>^{1/2} = (1.02 \pm 0.15) \ln[c(NO_2)\cdot t] - (14.9 \pm 6.0)$$

$$\chi^2 = 295{,}000 \qquad (3\text{-}9)$$

is strongly influenced by these points. Agreement of this fit with other experiments is poorer. Populations produced by deactivation from this excitation wavelength primarily have Biexponential profiles (see Table 3-3B).

4. Discussion

4.1. Energy Removal Rate Dependence on Ensemble Average Energy

Studies in which the dependence of energy transfer rate upon the average energy of the ensemble $<E>$ often express the rate of energy removal as proportional to a power of the average energy:[54,74-76]

$$\frac{d<E>}{d(c_M t)} = -k_n <E>^n \qquad (3\text{-}10)$$

The concentration of the buffer, NO_2 for these experiments, is c_M and the delay time after excitation is t. The rate constant for the equation is designated k_n, with dimen-

sions $(\text{energy})^{1-n} \cdot (\text{concentration} \cdot \text{time})^{-1}$. n often is but need not be taken as an integer. Integration of this equation from the initial concentration-time product $c_M t = 0$ and initial average energy $\langle E \rangle_0$ to the current values of these variables produces:

$$\langle E \rangle^{1-n} - \langle E \rangle_0^{1-n} = (n-1)\, k_n c_M t \qquad (3\text{-}11)$$

where n is not equal to 1, or

$$\ln\langle E \rangle - \ln\langle E \rangle_0 = -k_1\, c_M t \qquad (3\text{-}11a)$$

when n = 1. The equation may be expressed in a y = mx + b form where y is a function of $\langle E \rangle$ and x is $c_M t$:

$$\begin{aligned} \langle E \rangle^{1-n} &= (n-1)k_n\, c_M t + \langle E \rangle_0^{(1-n)}; \quad n \neq 1 \\ \ln\langle E \rangle &= -k_1\, c_M t + \ln\langle E \rangle_0; \quad n = 1 \end{aligned} \qquad (3\text{-}12)$$

for the purposes of fitting $\langle E \rangle$ data. The quantity of relevance in determining the dependence of energy transfer rates upon excitation energy, as opposed to ensemble-average energy, is the negative of the derivative of $\langle E \rangle$ with respect to $c_M t$ at $c_M t = 0$, or:

$$k_E = -\left[\frac{d\langle E\rangle}{d(c_M t)}\right]_{c_M t=0} = k_n \langle E\rangle_0^n \qquad (3\text{-}13)$$

for all values of n including n = 1.

Each of the four sets of average energy versus NO_2 concentration-delay time product has been fit to Equation 3-12 for integer n from 0 to 5. The results of these fits are listed in Table 3-4. Inspection reveals that the value of χ^2 decreases monotonically as the order n increases. In each case, the best model of the data among those listed is n = 5, in agreement with the TDTL study.[54] Further increases in n would probably decrease χ^2 further, but not by a significant amount: the maximum difference in χ^2 between n = 4 and 5 is 57 for the excitation wavelength of 532 nm (Table 3-4D), which is less than three times the number of data points. n = 4 is selected to represent the data for the extrapolation back to $c_M t = 0$.

4.2. Energy Removal Rate Dependence on Excitation Energy

The dependence of k_E upon the excitation energy X_L is identical to that of k_E upon <E> only for narrow population distributions. The energy transfer rate constant found throughout this study, for a general population distribution, is a double sum. The contribution corresponding to the microscopic energy transfer rate constant $k(E_j, E_k)$ from each initial value of NO_2 internal energy E_k to each final value of

internal energy E_j by each population distribution element $P(E_k)dE_k$ must be summed over both initial and final internal energies:

$$k_E(E_j) = \int_0^{\infty} \int_0^{D_0} (E_j - E_k)\, k(E_j, E_k) P(E_k)\, dE_k dE_j \qquad (3\text{-}14)$$

The average energy $<E>$ is related to the above expression only through the population $P(E_k)$:

$$<E> = \int_0^{D_0} E_k P(E_k) dE_k \qquad (3\text{-}15)$$

(note that this is the more general form of this expression than Equation 2-16). Both $<E>$ and k_E depend upon the population distribution $P(E_k)$, and an analytical relation between the two quantities requires models for both the population distribution and the microscopic energy transfer rate constants.

Table 3-5 lists the excitation energies studied and the corresponding k_E values for both the linear model ($n = 0$) and the $n = 4$, $<E>^{-3}$ model of average energy behavior. The k_E dependence on excitation energy X_L is plotted in Figure 3-9. As noted above, the k_E values for $n = 4$ represent the deactivation experiments better than do $n = 0$. Generally, k_E increases with increasing X_L, though the plot shows a positive curvature to within the experimental uncertainty. A linear fit (dotted line) of k_E in $cm^{-1}\ cm^3\ s^{-1}$ versus X_L in cm^{-1}:

$$k_E = (2.96 \pm 0.47) \times 10^{-11} X_L - (4.50 \pm 7.32) \times 10^{-7}$$

$$\chi^2 = 6.45 \qquad (3\text{-}16)$$

cannot duplicate the positive curvature and further gives the unphysical result of negative energy transfer rate constants at X_L below 15,200 cm^{-1}. Fitting k_E to X_L^4, which presumes that the excitation energy dependence is identical to the ensemble average energy dependence found above, gives rise to a physically valid fit (dashed line):

$$k_E = (7.42 \pm 0.90) \times 10^{-25} X_L^4 + (1.98 \pm 4.14) \times 10^{-8}$$

$$\chi^2 = 4.85. \qquad (3\text{-}17)$$

The best fit of all is linear in ln k_E with respect to X_L:

$$\ln k_E = (1.63 \pm 0.18) \times 10^{-4} X_L - (19.0 \pm 3.6)$$

$$\chi^2 = 4.57. \qquad (3\text{-}18)$$

However, the latter two fits cannot be distinguished from each other on the basis of χ^2. The decrease in χ^2 from Equation 3-17 to Equation 3-18 is 0.28, which is considerably less than one standard deviation per data point. Either of the equations describes the observations to within experimental uncertainty.

The power in the relationship of energy removal rate constant to excitation energy may also be obtained by taking the natural logarithm of both sides of the negative of Equation (3-10). ln k_E (k_E in cm^{-1} cm^3 s^{-1}) is then linear in ln X_L (X_L in cm^{-1}) with a slope of n, the power for the rate law, and a y-intercept of ln k_n. This is obtained for the four excitation energies in Table 3-5:

$$\ln k_E = (3.5917 \pm 0.3819) \ln X_L - (51.355 \pm 356.635)$$

$$\chi^2 = 4.675. \qquad (3\text{-}19)$$

Extra figures are quoted beyond significant, particularly in the y-intercept, in order to allow the use of this equation in predicting k_E values. This analysis agrees with Equation (3-17) above to within two standard deviations in the slope n.

5. Conclusions

The dependence of the NO_2^* energy transfer rate constant k_E upon the average energy of the excited state population <E> and upon the excitation energy X_L has been determined for four excitations from 18,828 to 24,989 cm^{-1}. The rate constant increases as at least the fourth power of <E>, and the rate constant at the limit of zero NO_2 concentration-delay time product is greater than is found by assuming that the rate constant does not vary with <E> by a factor greater than 3/2 for the entire

excitation energy range studied. Either an exponential or fourth-power dependence of k_E upon the laser excitation energy satisfactorily models the observations.

Table 3-1

A. Experimental conditions for NO_2^*-NO_2 excited at 475.34 nm

index	$P(NO_2)$, mT		t, μs		$c(NO_2) \cdot t$, 10^9 cm^{-3} s		Z_{HS}		Z_{close}
1	153.8	±0.1	0.4987	±0.0325	24.9	±1.6	0.27	±0.02	1.40 ± 0.09
2	156.5	±0.5	0.4983	±0.0326	25.3	±1.7	0.28	±0.02	1.43 ± 0.09
3	307.6	±0.7	0.4939	±0.0320	49.2	±3.2	0.54	±0.04	2.78 ± 0.18
4[c]	307.9	±1.8	0.4935	±0.0325	49.2	±3.3	0.54	±0.04	2.78 ± 0.18
5[c]	309.2	±1.0	0.4935	±0.0325	49.4	±3.3	0.54	±0.04	2.79 ± 0.18
6	153.8	±0.1	0.9969	±0.0583	49.7	±2.9	0.55	±0.03	2.80 ± 0.16
7	156.5	±0.5	0.9929	±0.0574	50.3	±2.9	0.55	±0.03	2.84 ± 0.17
8	315.3	±0.5	0.4983	±0.0326	50.9	±3.3	0.56	±0.04	2.87 ± 0.19
9[c]	598.7	±1.7	0.4935	±0.0325	95.7	±6.3	1.05	±0.07	5.40 ± 0.36
10	603.1	±0.2	0.4939	±0.0320	96.5	±6.2	1.06	±0.07	5.44 ± 0.35
11[c]	604.9	±1.5	0.4935	±0.0325	96.7	±6.4	1.06	±0.07	5.46 ± 0.36
12	600.8	±0.5	0.4983	±0.0326	97.0	±6.4	1.07	±0.07	5.47 ± 0.36
13[c]	302.5	±0.8	0.9960	±0.0588	97.6	±5.8	1.07	±0.06	5.51 ± 0.33
14	301.0	±0.6	1.0177	±0.0550	99.3	±5.4	1.09	±0.06	5.60 ± 0.30
15[c]	310.1	±1.2	0.9960	±0.0588	100.1	±5.9	1.10	±0.07	5.64 ± 0.33
16	156.5	±0.5	2.0030	±0.1048	101.6	±5.3	1.12	±0.06	5.73 ± 0.30
17	313.5	±0.3	1.0137	±0.0544	103.0	±5.5	1.13	±0.06	5.81 ± 0.31
18	163.2	±0.4	1.9882	±0.1038	105.1	±5.5	1.16	±0.06	5.93 ± 0.31
19	301.0	±0.6	1.4997	±0.0810	146.3	±7.9	1.61	±0.09	8.25 ± 0.45
20	313.5	±0.3	1.4955	±0.0809	151.9	±8.2	1.67	±0.09	8.57 ± 0.46
21	1213.8	±1.3	0.4939	±0.0320	194.2	±12.6	2.14	±0.14	10.96 ± 0.71
22[c]	605.7	±2.0	0.9960	±0.0588	195.5	±11.6	2.15	±0.13	11.02 ± 0.65
23[c]	307.9	±1.8	1.9748	±0.1036	197.0	±10.4	2.17	±0.11	11.11 ± 0.59
24	1221.6	±1.2	0.4983	±0.0326	197.2	±12.9	2.17	±0.14	11.12 ± 0.73
25[c]	613.0	±1.4	0.9960	±0.0588	197.8	±11.7	2.18	±0.13	11.16 ± 0.66
26[c]	309.2	±1.0	1.9748	±0.1036	197.8	±10.4	2.18	±0.11	11.16 ± 0.59
27	602.0	±0.1	1.0177	±0.0550	198.5	±10.7	2.18	±0.12	11.20 ± 0.61
28	307.6	±0.7	2.0114	±0.1059	200.5	±10.6	2.21	±0.12	11.31 ± 0.60

Table 3-1A continued

index	$P(NO_2)$, mT		t, μs		$c(NO_2) \cdot t$, 10^9 cm^{-3} s		Z_{HS}		Z_{close}	
29	615.6	±0.4	1.0137	±0.0544	202.2	±10.9	2.22	±0.12	11.40	± 0.61
30	315.3	±0.5	2.0030	±0.1048	204.6	±10.7	2.25	±0.12	11.54	± 0.60
31	603.5	±0.1	1.2127	±0.0646	237.1	±12.6	2.61	±0.14	13.37	± 0.71
32	617.7	±0.3	1.2365	±0.0662	247.5	±13.3	2.72	±0.15	13.96	± 0.75
33	602.0	±0.1	1.4997	±0.0810	292.5	±15.8	3.22	±0.17	16.50	± 0.89
34	1206.3	±3.0	0.7596	±0.0428	296.9	±16.8	3.27	±0.18	16.74	± 0.95
35	615.6	±0.4	1.4955	±0.0809	298.3	±16.1	3.28	±0.18	16.82	± 0.91
36	1217.5	±1.1	0.7563	±0.0428	298.3	±16.9	3.28	±0.19	16.83	± 0.95
37	603.5	±0.1	1.7443	±0.0926	341.1	±18.1	3.75	±0.20	19.24	± 1.02
38	617.7	±0.3	1.7492	±0.0926	350.1	±18.5	3.85	±0.20	19.74	± 1.05
39[c]	598.7	±1.7	1.9748	±0.1036	383.1	±20.1	4.21	±0.22	21.61	± 1.14
40[c]	604.9	±1.5	1.9748	±0.1036	387.0	±20.3	4.26	±0.22	21.83	± 1.15
41	600.8	±0.5	2.0030	±0.1048	389.9	±20.4	4.29	±0.22	21.99	± 1.15
42	603.1	±0.2	2.0114	±0.1059	393.0	±20.7	4.32	±0.23	22.17	± 1.17
43	1198.9	±0.6	1.0177	±0.0550	395.3	±21.3	4.35	±0.23	22.30	± 1.20
44	1204.4	±0.5	1.0137	±0.0544	395.6	±21.2	4.35	±0.23	22.31	± 1.20
45	1206.3	±3.0	1.2510	±0.0695	488.9	±27.2	5.38	±0.30	27.58	± 1.53
46	1217.5	±1.1	1.2452	±0.0690	491.2	±27.2	5.40	±0.30	27.70	± 1.54
47	1198.9	±0.6	1.4997	±0.0810	582.6	±31.5	6.41	±0.35	32.86	± 1.78
48	1204.4	±0.5	1.4955	±0.0809	583.6	±31.6	6.42	±0.35	32.91	± 1.78
49	1213.8	±1.3	2.0114	±0.1059	791.0	±41.7	8.70	±0.46	44.62	± 2.35
50	1221.6	±1.2	2.0030	±0.1048	792.8	±41.5	8.72	±0.46	44.71	± 2.34

Note: extra figures beyond significant are included for both $P(NO_2)$ and t for use in calculations.

[c]experiment without laser dispersion prism (see Section 3.2.1)

Table 3-1 continued

B. Fit parameters and energy moments for 475.34 NO_2^*-NO_2 energy transfer

index	fit method	parameters[a] 1	2	M, cm^{-1}	$10^3 \times$ sum error	f_R[b]	<E> cm^{-1}	$<\Delta E^2>$ cm^{-1}
1	Biexp.	3.2813E+1	1.8672E+3	22438	3.2605	1.42E-03	20910 ±191	1863.1 ± 17.0
2	Biexp.	1.8750E+1	1.1531E+3	22180	1.7863	3.05E-05	21362 ±104	1221.3 ± 5.9
3	Biexp.	4.7656E+1	2.0937E+3	21938	1.0571	3.69E-03	20194 ± 63	1988.7 ± 6.2
4[c]	Biexp.	3.5156E+1	2.5078E+3	22219	1.8820	8.17E-03	20130 ±112	2238.2 ± 12.4
5[c]	Biexp.	3.5938E+1	2.4609E+3	22250	1.5453	7.56E-03	20196 ± 92	2217.4 ± 10.0
6	Biexp.	3.2031E+1	2.3125E+3	22313	2.6239	5.26E-03	20379 ±155	2146.3 ± 16.3
7	Biexp.	4.8438E+1	2.2578E+3	22219	5.0346	4.87E-03	20320 ±296	2108.7 ± 30.8
8	Biexp.	3.8000E+1	1.9050E+3	22200	1.8604	1.85E-03	20623 ±110	1879.4 ± 10.0
9[c]	Biexp.	3.6719E+1	3.2031E+3	21844	0.8703	0.0254	19319 ± 52	2441.1 ± 6.6
10	Biexp.	4.0625	2.8406E+3	21750	1.0979	0.0167	19483 ± 66	2320.4 ± 7.9
11[c]	Biexp.	3.5938E+1	3.1125E+3	21828	0.9637	0.0230	19357 ± 58	2416.4 ± 7.2
12	Biexp.	1.2500E+1	2.5547E+3	21750	1.0676	0.0107	19681 ± 64	2210.3 ± 7.2
13[c]	Biexp.	2.8906E+1	3.2266E+3	21906	1.2542	0.0255	19363 ± 75	2462.0 ± 9.6
14	Biexp.	1.6719E+1	2.8320E+3	21844	1.0525	0.0159	19559 ± 63	2331.3 ± 7.5
15[c]	Biexp.	4.6094E+1	3.2266E+3	21938	0.8377	0.0254	19377 ± 50	2462.9 ± 6.4
16	Biexp.	3.5156E+1	2.3945E+3	21828	0.8723	7.70E-03	19852 ± 52	2145.0 ± 5.6
17	Biexp.	3.8672E+1	2.4805E+3	21625	0.6902	9.87E-03	19589 ± 41	2163.4 ± 4.6
18	Biexp.	3.3594E+1	3.3672E+3	22008	2.0523	0.0287	19369 ±123	2513.3 ± 15.9
19	Biexp.	8.4766E+1	3.5000E+3	21641	0.5560	0.0367	18938 ± 34	2471.2 ± 4.4
20	Biexp.	2.7344E+1	3.0625E+3	21375	0.8527	0.0251	18989 ± 52	2331.4 ± 6.4
21	Biexp.	4.3750E+1	4.9844E+3	21125	0.8290	*0.0990*	*18029 ± 52*	*2545.9 ± 7.3*
22[c]	Biexp.	7.4219E+1	5.2031E+3	21375	0.5845	*0.1029*	*18135 ± 36*	*2618.0 ± 5.2*
23[c]	Biexp.	3.8281E+1	5.3516E+3	21445	0.6211	*0.1064*	*18178 ± 38*	*2648.4 ± 5.6*
24	Biexp.	5.0000E+1	4.5625E+3	21094	0.7854	*0.0833*	*18118 ± 49*	*2507.5 ± 6.8*
25[c]	Biexp.	5.9453E+2	5.0312E+3	21734	0.4593	*0.0991*	*18107 ± 28*	*2614.8 ± 4.1*
26[c]	Biexp.	1.1641E+2	6.2969E+3	21625	0.9075	*0.1384*	*18051 ± 56*	*2718.6 ± 8.4*

Table 3-1B continued

index	fit method	parameters[a] 1	2	M, cm^{-1}	$10^3 \times$ sum error	f_R[b]	<E> cm^{-1}	$<\Delta E^2>$ cm^{-1}
27	Biexp.	3.1250E+1	5.1094E+3	21332	0.8054	*0.0994*	*18147 ± 50*	*2608.9 ± 7.1*
28	Gamma	1.4666E+3	5.1250E-1	21563	0.9600	0.0461	18210 ± 60	2465.1 ± 8.1
29	Biexp.	1.0844E+3	3.3906E+3	21609	0.8344	0.0431	18348 ± 52	2398.1 ± 6.8
30	Biexp.	2.0313E+1	4.2891E+3	21375	0.7536	*0.0673*	*18452 ± 46*	*2550.3 ± 6.4*
31	Biexp.	1.6953E+2	6.1406E+3	21250	1.0102	*0.1417*	*17773 ± 63*	*2614.7 ± 9.3*
32	Biexp.	5.3906E+1	8.4062E+3	21188	0.9782	*0.2076*	*17514 ± 61*	*2674.1 ± 9.4*
33	Gamma	3.2354E+3	1.1094	22094	0.7429	*0.0925*	*17517 ± 47*	*2584.2 ± 7.0*
34	Biexp.	3.9258E+3	5.1875E+3	21734	0.8590	*0.1628*	*17119 ± 55*	*2561.9 ± 8.3*
35	Gauss.	1.8479E+4	3.9609E+3	21375	0.6647	0.0235	17552 ± 42	2494.9 ± 6.0
36	Biexp.	1.3699E+3	6.9062E+3	21344	0.7175	*0.1940*	*17120 ± 46*	*2523.6 ± 6.8*
37	Biexp.	1.3219E+3	8.4375E+3	21609	1.1970	*0.2297*	*17133 ± 77*	*2610.9 ± 11.7*
38	Gauss.	1.7035E+4	4.2187E+3	21625	1.0590	*0.0603*	*17051 ± 68*	*2614.0 ± 10.5*
39[c]	Gamma	5.7324E+3	1.7937	22938	1.1342	*0.1871*	*16875 ± 73*	*2652.0 ± 11.5*
40[c]	Gamma	6.5283E+3	3.1484	23813	0.9295	*0.1165*	*16980 ± 60*	*2617.3 ± 9.3*
41	Gamma	7.5732E+3	5.1094	24875	0.9345	*0.0752*	*17075 ± 61*	*2580.6 ± 9.2*
42	Gauss.	1.6773E+4	3.3828E+3	21875	1.1723	0.0274	17019 ± 77	2511.8 ± 11.3
43	Gamma	6.3379E+3	3.6250	23375	1.1951	*0.0958*	*16774 ± 79*	*2457.4 ± 11.6*
44	Gamma	5.1855E+3	1.4109	22031	1.2297	*0.2221*	*16568 ± 81*	*2520.4 ± 12.3*
45	Gauss.	1.4849E+4	4.1484E+3	22531	1.3912	*0.1341*	*16342 ± 92*	*2657.3 ± 14.9*
46	Gamma	8.8750E+3	2.6172	23813	1.2790	*0.3133*	*16262 ± 85*	*2606.6 ± 13.6*
47	Gamma	1.3391E+4	9.5625E-1	22813	1.7587	*0.5188*	*16204 ± 115*	*2713.2 ± 19.3*
48	Gamma	1.3242E+4	2.0625	24313	1.7647	*0.4942*	*16076 ± 116*	*2709.1 ± 19.6*
49	Gauss.	2.6562E+2	1.3172E+4	22438	2.1298	*0.6115*	*16372 ± 135*	*2929.9 ± 24.2*
50	Gauss.	9.6953E+3	8.6875E+3	22750	2.0404	*0.4866*	*16462 ± 129*	*2962.9 ± 23.2*

Table 3-1A continued

Notes:

[a]fit method determines identity of parameters 1 and 2; see Equations 2-9, 2-10, and 2-11.

[b]$<E>$ and $<\Delta E^2>$ are invalid if this number is over 0.05; such entries are italicized.

[c]experiment without laser dispersion prism (see Section 3.2.1)

Table 3-2

A. Experimental conditions for NO_2^*-NO_2 excited at 435.04 nm

index	$P(NO_2)$, mT		t, μs		$c(NO_2) \cdot t$, 10^9 cm^{-3} s		Z_{HS}		Z_{close}
1	149.5	±1.2	0.4905	±0.0321	23.8	±1.6	0.26	±0.02	1.34 ± 0.09
2	149.7	±0.6	0.4905	±0.0321	23.8	±1.6	0.26	±0.02	1.34 ± 0.09
3	301.6	±1.3	0.4952	±0.0335	48.4	±3.3	0.53	±0.04	2.73 ± 0.19
4	302.2	±2.9	0.4952	±0.0335	48.5	±3.3	0.53	±0.04	2.73 ± 0.19
5	149.5	±1.2	1.0126	±0.0578	49.0	±2.8	0.54	±0.03	2.77 ± 0.16
6	149.7	±0.6	1.0126	±0.0578	49.1	±2.8	0.54	±0.03	2.77 ± 0.16
7	145.8	±1.0	1.9750	±0.1026	93.3	±4.9	1.03	±0.05	5.26 ± 0.28
8	146.6	±0.7	1.9750	±0.1026	93.8	±4.9	1.03	±0.05	5.29 ± 0.28
9	600.1	±0.7	0.4935	±0.0322	96.0	±6.3	1.06	±0.07	5.41 ± 0.35
10	604.5	±3.3	0.4935	±0.0322	96.7	±6.3	1.06	±0.07	5.45 ± 0.36
11	300.5	±0.3	1.0036	±0.0544	97.7	±5.3	1.07	±0.06	5.51 ± 0.30
12	302.0	±1.0	1.0036	±0.0544	98.2	±5.3	1.08	±0.06	5.54 ± 0.30
13	901.9	±2.6	0.4935	±0.0322	144.2	±9.4	1.59	±0.10	8.13 ± 0.53
14	301.6	±1.3	1.4794	±0.0794	144.6	±7.8	1.59	±0.09	8.15 ± 0.44
15	904.4	±2.4	0.4935	±0.0322	144.6	±9.4	1.59	±0.10	8.16 ± 0.53
16	302.2	±2.9	1.4794	±0.0794	144.9	±7.9	1.59	±0.09	8.17 ± 0.45
17	1200.0	±4.1	0.4918	±0.0333	191.2	±13.0	2.10	±0.14	10.78 ± 0.73
18	300.5	±0.3	1.9732	±0.1031	192.1	±10.0	2.11	±0.11	10.84 ± 0.57
19	1206.6	±4.0	0.4918	±0.0333	192.2	±13.0	2.11	±0.14	10.84 ± 0.74
20	302.0	±1.0	1.9732	±0.1031	193.1	±10.1	2.12	±0.11	10.89 ± 0.57
21	599.2	±3.0	1.0040	±0.0549	194.9	±10.7	2.14	±0.12	10.99 ± 0.60
22	602.1	±2.3	1.0040	±0.0549	195.9	±10.7	2.15	±0.12	11.05 ± 0.61
23	599.0	±2.9	1.2001	±0.0635	232.9	±12.4	2.56	±0.14	13.14 ± 0.70
24	602.7	±2.5	1.2000	±0.0635	234.3	±12.4	2.58	±0.14	13.22 ± 0.70
25	600.1	±0.7	1.4711	±0.0795	286.0	±15.5	3.15	±0.17	16.13 ± 0.87
26	604.5	±3.3	1.4711	±0.0795	288.1	±15.7	3.17	±0.17	16.25 ± 0.88
27	1201.3	±0.3	0.7459	±0.0429	290.3	±16.7	3.19	±0.18	16.37 ± 0.94
28	1205.6	±2.9	0.7459	±0.0429	291.3	±16.8	3.20	±0.18	16.43 ± 0.95

Table 3-2A continued

index	$P(NO_2)$, mT		t, μs		$c(NO_2) \cdot t$, 10^9 cm^{-3} s		Z_{HS}		Z_{close}
29	900.0	±1.1	1.0030	±0.0550	292.5	±16.1	3.22	±0.18	16.50 ± 0.91
30	911.1	±3.0	1.0030	±0.0550	296.1	±16.3	3.26	±0.18	16.70 ± 0.92
31	599.2	±3.0	1.7308	±0.0913	336.0	±17.8	3.70	±0.20	18.95 ± 1.00
32	602.1	±2.3	1.7308	±0.0913	337.6	±17.9	3.71	±0.20	19.04 ± 1.01
33	599.0	±2.9	1.9718	±0.1025	382.7	±20.0	4.21	±0.22	21.58 ± 1.13
34	602.7	±2.5	1.9718	±0.1025	385.0	±20.1	4.24	±0.22	21.72 ± 1.13
35	1196.7	±2.5	0.9994	±0.0548	387.5	±21.2	4.26	±0.23	21.85 ± 1.20
36	1202.3	±1.6	0.9994	±0.0548	389.3	±21.3	4.28	±0.23	21.96 ± 1.20
37	901.9	±2.6	1.4711	±0.0795	429.9	±23.3	4.73	±0.26	24.24 ± 1.31
38	904.4	±2.4	1.4711	±0.0795	431.1	±23.3	4.74	±0.26	24.31 ± 1.32
39	1201.3	±0.3	1.2242	±0.0674	476.5	±26.2	5.24	±0.29	26.87 ± 1.48
40	1205.6	±2.9	1.2242	±0.0674	478.2	±26.4	5.26	±0.29	26.97 ± 1.49
41	1196.7	±2.5	1.4755	±0.0791	572.1	±30.7	6.29	±0.34	32.27 ± 1.73
42	900.0	±1.1	1.9653	±0.1026	573.1	±29.9	6.30	±0.33	32.32 ± 1.69
43	1202.3	±1.6	1.4755	±0.0791	574.8	±30.8	6.32	±0.34	32.42 ± 1.74
44	911.1	±3.0	1.9653	±0.1026	580.1	±30.3	6.38	±0.33	32.72 ± 1.71
45	1200.0	±4.1	1.9737	±0.1029	767.4	±40.1	8.44	±0.44	43.28 ± 2.26
46	1206.6	±4.0	1.9737	±0.1029	771.6	±40.3	8.49	±0.44	43.52 ± 2.27

Table 3-2 continued

B. Fit parameters and energy moments for 435.04 NO_2^*-NO_2 energy transfer

index	fit method	parameters[a] 1	2	M, cm^{-1}	$10^3 \times$ sum error	f_R[b]	<E> cm^{-1}	$<\Delta E^2>$ cm^{-1}
1	Biexp.	6.8750	1.8656E+3	24406	3.4246	4.85E-04	22856 ±194	1917.6 ± 16.3
2	Biexp.	5.0000E+1	1.9250E+3	24508	2.9459	6.12E-04	22829 ±167	1971.0 ± 14.4
3	Biexp.	1.7422E+1	2.4922E+3	24281	2.4888	3.44E-03	22123 ±141	2402.4 ± 15.4
4	Biexp.	6.0938E+1	2.2562E+3	24188	1.9117	2.09E-03	22207 ±109	2232.1 ± 10.9
5	Biexp.	3.5938E+1	1.7937E+3	23969	2.1500	4.64E-04	22481 ±122	1850.0 ± 10.1
6	Biexp.	5.3125E+1	1.9437E+3	24063	2.3530	8.27E-04	22408 ±134	1982.5 ± 11.8
7	Biexp.	3.2813E+1	2.0250E+3	23531	2.1293	1.38E-03	21812 ±122	2030.8 ± 11.4
8	Biexp.	3.6719E+1	2.3828E+3	23688	2.0897	3.45E-03	21631 ±120	2294.1 ± 12.7
9	Biexp.	2.5000E+1	3.2422E+3	23875	2.2756	0.0143	21114 ±131	2740.8 ± 17.0
10	Biexp.	1.6719E+1	3.0430E+3	23750	1.1200	0.0116	21167 ± 65	2644.9 ± 8.1
11	Biexp.	3.6719E+1	2.7812E+3	23719	1.4973	7.57E-03	21324 ± 86	2526.2 ± 10.2
12	Biexp.	2.3438E+1	3.0281E+3	23844	2.5282	0.0107	21252 ±145	2657.8 ± 18.1
13	Biexp.	2.6563E+1	4.0937E+3	23406	1.2562	0.0371	20205 ± 73	2917.0 ± 10.5
14	Biexp.	1.8125E+1	3.8984E+3	23594	1.5762	0.0299	20480 ± 91	2916.8 ± 12.9
15	Biexp.	4.0625E+1	4.2891E+3	23477	1.2188	0.0419	20143 ± 71	2960.4 ± 10.4
16	Biexp.	1.8750E+1	3.9687E+3	23594	2.1765	0.0321	20442 ±126	2931.6 ± 18.0
17	Biexp.	3.4375E+1	4.8516E+3	22969	0.8891	*0.0645*	*19506 ± 52*	*2955.0 ± 7.9*
18	Biexp.	1.1094E+2	4.4375E+3	23281	0.9746	0.0483	19858 ± 57	2950.0 ± 8.4
19	Biexp.	3.1250E+1	6.7187E+3	23344	1.2256	*0.1152*	*19230 ± 72*	*3186.8 ± 11.9*
20	Biexp.	7.3438E+1	3.9453E+3	23094	0.9942	0.0357	19958 ± 58	2827.7 ± 8.2
21	Gauss.	2.1986E+4	3.6484E+3	23125	0.8921	1.02E-03	20076 ± 53	2433.4 ± 6.4
22	Biexp.	3.1250E+1	5.6406E+3	23281	1.6906	*0.0845*	*19487 ± 99*	*3109.8 ± 15.8*
23	Biexp.	6.4063E+1	9.6875E+3	23281	3.1715	*0.1863*	*18705 ±186*	*3265.4 ± 32.5*
24	Biexp.	5.1563E+1	6.9687E+3	23141	3.3318	*0.1250*	*19031 ±195*	*3158.2 ± 32.4*
25	Biexp.	1.1250E+2	1.5094E+4	23375	3.1380	*0.2643*	*18355 ±186*	*3304.1 ± 33.5*
26	Biexp.	2.9844E+2	7.4062E+3	23000	1.7968	*0.1470*	*18711 ±107*	*3062.6 ± 17.6*
27	Biexp.	3.3281E+2	1.0000E+4	22938	1.6071	*0.2074*	*18304 ± 96*	*3101.3 ± 16.3*

Table 3-2B continued

index	fit method	parameters[a] 1	2	M, cm^{-1}	$10^3 \times$ sum error	f_R[b]	<E> cm^{-1}	$<\Delta E^2>$ cm^{-1}
28	Biexp.	5.1094E+2	1.3125E+4	23188	1.4980	*0.2549*	*18124 ± 90*	*3161.2 ± 15.7*
29	Biexp.	5.3047E+2	7.3437E+3	22906	0.9421	*0.1506*	*18499 ± 56*	*3009.6 ± 9.2*
30	Biexp.	4.6875E+1	1.0625E+4	22656	1.7324	*0.2190*	*18252 ±104*	*3096.6 ± 17.7*
31	Biexp.	1.3797E+3	1.3594E+4	23750	1.0210	*0.2668*	*18026 ± 61*	*3198.0 ± 10.9*
32	Gauss.	1.9266E+4	3.8984E+3	23156	1.1104	0.0121	18599 ± 68	2819.7 ± 10.2
33	Gauss.	1.8754E+4	4.1719E+3	23500	2.1927	0.0227	18353 ±133	2966.9 ± 21.5
34	Gamma	7.6230E+3	6.0625	26500	2.6277	0.0274	18278 ±162	2779.5 ± 24.6
35	Gamma	4.7725E+3	1.4391	23688	0.9218	*0.1302*	*17789 ± 57*	*2912.3 ± 9.3*
36	Gauss.	1.8135E+4	3.9141E+3	23094	0.9495	0.0241	17978 ± 59	2840.5 ± 9.3
37	Gauss.	1.8064E+4	3.5391E+3	23531	2.0398	0.0143	18099 ±127	2818.0 ± 19.7
38	Biexp.	7.3437E+2	3.5000E+5	23281	3.2706	*0.4461*	*17360 ±200*	*3136.0 ± 36.2*
39	Gamma	5.0508E+3	2.3438	24250	7.5128	*0.0600*	*18159 ±462*	*2825.9 ± 71.9*
40	Gauss.	1.7500E+2	1.3094E+4	24531	7.7387	*0.5999*	*16875 ±468*	*3389.3 ± 94.0*
41	Gamma	6.0625E+4	6.8125E-1	25000	2.5106	*0.5575*	*16906 ±153*	*3266.5 ± 29.6*
42	Gauss.	1.5272E+4	4.4219E+3	26500	4.8042	*0.1283*	*16861 ±302*	*3010.1 ± 53.9*
43	Gamma	8.2812E+3	1.2469	24375	2.7196	*0.3400*	*17133 ±168*	*3076.0 ± 30.2*
44	Gauss.	3.2812E+3	2.8750E+4	22469	4.3080	*0.4810*	*17114 ±267*	*3061.3 ± 47.7*
45	Gauss.	1.7297E+4	3.9375E+3	23938	3.7286	0.0380	17697 ±231	2972.9 ± 38.9
46	Gauss.	4.6875E+1	1.2125E+4	24406	3.9518	*0.6284*	*16657 ±241*	*3302.2 ± 47.9*

[a]fit method determines identity of parameters 1 and 2; see Equations 2-9, 2-10, and 2-11.

[b]<E> and $<\Delta E^2>$ are invalid if this number is over 0.05; such entries are italicized.

Table 3-3

A. Experimental conditions for NO_2^*-NO_2 excited at 400.00 nm

index	$P(NO_2)$, mT	t, μs	$c(NO_2) \cdot t$, 10^9 cm^{-3} s	Z_{HS}	Z_{close}
1	147.6 ± 0.5	0.4947 ± 0.0325	23.7 ± 1.6	0.26 ± 0.02	1.33 ± 0.09
2	148.5 ± 0.6	0.4947 ± 0.0325	23.8 ± 1.6	0.26 ± 0.02	1.34 ± 0.09
3	294.6 ± 2.0	0.4947 ± 0.0325	47.2 ± 3.1	0.52 ± 0.03	2.66 ± 0.18
4	145.1 ± 0.5	1.0131 ± 0.0581	47.6 ± 2.7	0.52 ± 0.03	2.69 ± 0.15
5	145.4 ± 0.7	1.0131 ± 0.0581	47.7 ± 2.7	0.53 ± 0.03	2.69 ± 0.16
6	298.0 ± 0.5	0.4947 ± 0.0325	47.8 ± 3.1	0.53 ± 0.03	2.69 ± 0.18
7	147.6 ± 0.5	1.9829 ± 0.1040	94.8 ± 5.0	1.04 ± 0.05	5.35 ± 0.28
8	148.5 ± 0.6	1.9829 ± 0.1040	95.4 ± 5.0	1.05 ± 0.06	5.38 ± 0.28
9	593.5 ± 2.3	0.5019 ± 0.0333	96.5 ± 6.4	1.06 ± 0.07	5.44 ± 0.36
10	298.6 ± 1.9	1.0022 ± 0.0544	96.9 ± 5.3	1.07 ± 0.06	5.47 ± 0.30
11	603.4 ± 9.8	0.5019 ± 0.0333	98.1 ± 6.7	1.08 ± 0.07	5.53 ± 0.38
12	304.4 ± 2.3	1.0022 ± 0.0544	98.9 ± 5.4	1.09 ± 0.06	5.58 ± 0.31
13	298.6 ± 1.9	1.4821 ± 0.0798	143.4 ± 7.8	1.58 ± 0.09	8.09 ± 0.44
14	897.0 ± 2.6	0.5019 ± 0.0333	145.9 ± 9.7	1.60 ± 0.11	8.23 ± 0.55
15	304.4 ± 2.3	1.4821 ± 0.0798	146.2 ± 7.9	1.61 ± 0.09	8.25 ± 0.45
16	901.7 ± 2.6	0.5019 ± 0.0333	146.6 ± 9.7	1.61 ± 0.11	8.27 ± 0.55
17	294.6 ± 2.0	1.9829 ± 0.1040	189.3 ±10.0	2.08 ± 0.11	10.68 ± 0.56
18	1192.2 ± 0.9	0.4943 ± 0.0320	190.9 ±12.4	2.10 ± 0.14	10.77 ± 0.70
19	1194.8 ± 7.0	0.4943 ± 0.0320	191.3 ±12.5	2.10 ± 0.14	10.79 ± 0.70
20	298.0 ± 0.5	1.9829 ± 0.1040	191.5 ±10.0	2.11 ± 0.11	10.80 ± 0.57
21	1203.4 ± 1.6	0.4943 ± 0.0320	192.7 ±12.5	2.12 ± 0.14	10.87 ± 0.70
22	593.9 ± 2.2	1.0052 ± 0.0545	193.4 ±10.5	2.13 ± 0.12	10.91 ± 0.59
23	596.2 ± 2.7	1.0022 ± 0.0544	193.6 ±10.5	2.13 ± 0.12	10.92 ± 0.59
24	594.4 ± 2.0	1.2066 ± 0.0639	232.4 ±12.3	2.56 ± 0.14	13.11 ± 0.70
25	594.7 ± 1.6	1.2066 ± 0.0639	232.5 ±12.3	2.56 ± 0.14	13.11 ± 0.70
26	862.6 ± 12.4	1.0065 ± 0.0543	281.3 ±15.7	3.09 ± 0.17	15.87 ± 0.89
27	593.9 ± 2.2	1.4821 ± 0.0798	285.2 ±15.4	3.14 ± 0.17	16.09 ± 0.87
28	596.2 ± 2.7	1.4821 ± 0.0798	286.3 ±15.5	3.15 ± 0.17	16.15 ± 0.87

Table 3-3A continued

index	$P(NO_2)$, mT	t, μs	$c(NO_2) \cdot t$, 10^9 cm^{-3} s	Z_{HS}	Z_{close}
29	894.0 ± 3.3	1.0065 ± 0.0544	291.5 ±15.8	3.21 ± 0.17	16.44 ± 0.89
30	1204.4 ± 4.8	0.7492 ± 0.0427	292.4 ±16.7	3.22 ± 0.18	16.49 ± 0.94
31	1205.9 ± 1.6	0.7492 ± 0.0427	292.7 ±16.7	3.22 ± 0.18	16.51 ± 0.94
32	594.4 ± 2.0	1.7349 ± 0.0919	334.1 ±17.7	3.68 ± 0.20	18.84 ± 1.00
33	594.7 ± 1.6	1.7349 ± 0.0919	334.3 ±17.7	3.68 ± 0.19	18.85 ± 1.00
34	593.5 ± 2.3	1.9793 ± 0.1025	380.6 ±19.8	4.19 ± 0.22	21.47 ± 1.11
35	603.4 ± 9.8	1.9793 ± 0.1025	387.0 ±21.0	4.26 ± 0.23	21.83 ± 1.19
36	1205.1 ± 2.6	1.0065 ± 0.0544	393.0 ±21.2	4.32 ± 0.23	22.16 ± 1.20
37	862.6 ± 12.4	1.4786 ± 0.0784	413.2 ±22.7	4.32 ± 0.23	22.17 ± 1.20
38	894.0 ± 3.3	1.4786 ± 0.0801	428.3 ±23.2	4.55 ± 0.25	23.31 ± 1.28
39	1204.4 ± 4.8	1.2294 ± 0.0678	479.7 ±26.5	4.71 ± 0.26	24.15 ± 1.31
40	1205.9 ± 1.6	1.2294 ± 0.0678	480.3 ±26.5	5.28 ± 0.29	27.06 ± 1.50
41	897.0 ± 2.6	1.9793 ± 0.1025	575.3 ±29.8	5.28 ± 0.29	27.09 ± 1.49
42	1205.1 ± 2.6	1.4786 ± 0.0801	577.3 ±31.3	6.33 ± 0.33	32.45 ± 1.68
43	901.7 ± 2.6	1.9793 ± 0.1025	578.3 ±30.0	6.35 ± 0.34	32.56 ± 1.76
44	1192.2 ± 0.9	1.9728 ± 0.1028	762.1 ±39.7	6.35 ± 0.34	32.57 ± 1.76
45	1194.8 ± 7.0	1.9728 ± 0.1028	763.7 ±40.1	6.36 ± 0.33	32.62 ± 1.69
46	1203.4 ± 1.6	1.9728 ± 0.1028	769.2 ±40.1	8.38 ± 0.44	42.98 ± 2.24

Table 3-3 continued

B. Fit parameters and energy moments for 400.00 NO_2^*-NO_2 energy transfer

index	fit method	parameters[a] 1	2	M, cm^{-1}	$10^3 \times$ sum error	f_R[b]	<E> cm^{-1}	$<\Delta E^2>$ cm^{-1}
1	Gamma	8.1250E+1	2.0000	25016	3.3381	0.00	25052 ±191	74.7 ± 0.6
2	Gamma	8.5156E+1	2.0000	24906	2.0883	0.00	24932 ±120	74.7 ± 0.4
3	Biexp.	1.5000E+2	1.2129E+3	26500	2.9363	5.02E-06	23905 ±169	1255.1 ± 8.9
4	Biexp.	5.0000E+1	9.0527E+2	25500	1.4831	7.94E-08	24111 ± 85	929.9 ± 3.3
5	Biexp.	7.5000E+1	1.1543E+3	25750	3.8449	2.70E-06	23967 ±221	1193.3 ± 11.0
6	Biexp.	1.5000E+2	1.4160E+3	26500	5.1732	2.89E-05	23689 ±298	1467.2 ± 18.4
7	Biexp.	7.5000E+1	2.2734E+3	25750	1.9689	1.47E-03	22800 ±114	2243.8 ± 11.2
8	Biexp.	5.0000E+1	2.1875E+3	25500	2.5771	1.14E-03	22765 ±149	2171.8 ± 14.2
9	Biexp.	5.0000E+1	2.7480E+3	25500	4.2160	4.48E-03	22253 ±245	2545.3 ± 28.0
10	Biexp.	5.0000E+1	2.4746E+3	25500	3.3259	2.54E-03	22503 ±193	2376.0 ± 20.4
11	Biexp.	5.0000E+1	2.6875E+3	25500	3.6081	3.97E-03	22302 ±209	2511.1 ± 23.6
12	Biexp.	7.5000E+1	2.6875E+3	25750	1.8176	3.97E-03	22414 ±105	2522.5 ± 11.8
13	Biexp.	5.6250E+1	3.4609E+3	25031	1.3744	0.0140	21710 ± 80	2869.0 ± 10.6
14	Biexp.	5.4688E+1	3.9766E+3	24875	1.5021	0.0242	21412 ± 88	3051.3 ± 12.6
15	Biexp.	6.0156E+1	3.6484E+3	25016	1.5838	0.0171	21662 ± 93	2956.6 ± 12.7
16	Biexp.	2.1094E+1	3.9531E+3	24781	1.6876	0.0241	21356 ± 99	3025.4 ± 14.1
17	Biexp.	1.2734E+2	3.7422E+3	24625	1.0018	0.0212	21361 ± 60	2950.6 ± 8.2
18	Biexp.	8.9063E+1	4.4844E+3	24188	1.1283	0.0419	20659 ± 68	3066.1 ± 10.1
19	Biexp.	7.3437E+2	3.7422E+3	24469	0.6720	0.0256	20821 ± 40	2896.7 ± 5.6
20	Biexp.	4.5313E+1	4.0547E+3	24531	1.7084	0.0281	21180 ±102	3034.9 ± 14.6
21	Biexp.	1.8750E+1	5.2422E+3	24344	1.5357	*0.0602*	*20489 ± 92*	*3212.6 ± 14.4*
22	Gauss.	2.5645E+4	5.0312E+3	24531	1.3635	2.82E-03	21146 ± 82	2760.0 ± 10.7
23	Biexp.	1.7422E+1	4.8437E+3	24406	1.6042	0.0487	20719 ± 96	3172.8 ± 14.7
24	Biexp.	1.5937E+2	5.2344E+3	24250	1.4853	*0.0634*	*20345 ± 90*	*3162.5 ± 13.9*
25	Gauss.	2.2551E+4	3.5781E+3	24594	2.2950	4.67E-04	21059 ±140	2549.4 ± 16.9
26	Biexp.	1.3672E+3	5.1875E+3	24234	0.9734	*0.0748*	*19642 ± 60*	*3077.8 ± 9.3*
27	Biexp.	9.2188E+1	6.6250E+3	24094	2.5468	*0.1030*	*19861 ±154*	*3269.5 ± 25.4*

Table 3-3B continued

index	fit method	parameters[a] 1	2	M, cm^{-1}	$10^3 \times$ sum error	f_R[b]	<E> cm^{-1}	$<\Delta E^2>$ cm^{-1}
28	Gamma	6.5219E+3	2.7450	28000	1.7919	0.0489	19627 ±109	3209.3 ± 17.8
29	Biexp.	1.9160E+3	5.1875E+3	24344	0.9009	*0.0803*	*19513 ± 55*	*3091.0 ± 8.8*
30	Biexp.	2.2539E+3	5.0937E+3	24375	0.9519	*0.0804*	*19461 ± 59*	*3084.2 ± 9.3*
31	Gamma	3.1982E+3	1.2375	24594	0.7074	0.0357	19643 ± 44	2949.1 ± 6.6
32	Biexp.	2.4980E+3	5.5937E+3	24672	0.6779	*0.0964*	*19433 ± 42*	*3172.3 ± 6.8*
33	Biexp.	3.0234E+3	5.5625E+3	24922	1.1135	*0.0969*	*19468 ± 68*	*3215.2 ± 11.3*
34	Gamma	5.7187E+3	2.0937	26125	1.0390	*0.0757*	*19025 ± 64*	*3160.9 ± 10.7*
35	Gamma	3.6904E+3	1.1812	24688	0.8894	*0.0667*	*19212 ± 55*	*3077.5 ± 8.9*
36	Gamma	5.5977E+3	2.2187	25313	0.8012	*0.0772*	*18624 ± 51*	*3015.8 ± 8.2*
37	Gauss.	1.8762E+4	4.8125E+3	24813	1.1107	0.0434	18658 ± 69	3236.4 ± 12.0
38	Gauss.	1.8794E+4	4.0937E+3	24531	2.7967	0.0210	18722 ±177	3067.8 ± 29.0
39	Gauss.	1.3898E+4	9.1250E+3	25132	3.5244	*0.3435*	*17798 ±217*	*3415.3 ± 41.6*
40	Gauss.	1.7792E+4	4.9219E+3	25132	2.7069	*0.0706*	*18244 ±169*	*3211.2 ± 29.8*
41	Gauss.	1.6543E+4	5.2031E+3	25132	1.7884	*0.1214*	*17779 ±113*	*3221.8 ± 20.4*
42	Gauss.	1.6946E+4	4.6094E+3	25132	2.1371	*0.0783*	*17828 ±137*	*3118.8 ± 23.9*
43	Gamma	4.4299E+4	4.9688E+1	60000	1.1670	*0.2306*	*17626 ± 74*	*3243.4 ± 13.6*
44	Gamma	1.0625E+7	1.1400E+2	1.25E6	3.4790	*0.6534*	*17412 ±212*	*3478.2 ± 42.4*
45	Gamma	1.7750E+7	1.0200E+2	1.25E6	2.8963	*0.6407*	*17442 ±177*	*3458.0 ± 35.1*
46	Gamma	4.1094E+6	9.0000E+1	1.00E6	2.6335	*0.6199*	*17525 ±161*	*3478.3 ± 31.9*

[a]fit method determines identity of parameters 1 and 2; see Equations 2-9, 2-10, and 2-11.

[b]<E> and $<\Delta E^2>$ are invalid if this number is over 0.05; such entries are italicized.

Table 3-4

A. Fits of Average Energy for $NO_2^{\bullet}$-NO_2 Excited at 400.00 nm

Equation 3-12:

n	m	b	$\langle E \rangle_0$/cm^{-1}	$k_E/10^{-8}$ cm^{-1}cm^{3}s^{-1}	χ^2
0	-(1.46 ±0.15)E-7	(2.396 ±0.030)E4	23960±300	14.6 ±1.5	697
1	-(7.22 ±0.61)E-12	10.097 ±0.012	24270±290	17.5 ±1.5	528
2	(3.52 ±0.24)E-16	(4.067 ±0.071)E-5	24590±430	21.3 ±1.5	405
3	(3.38 ±0.17)E-20	(1.610 ±0.050)E-9	24920±390	26.1 ±1.8	296
4	(2.399 ±0.084)E-24	(6.20 ±0.27)E-14	25270±360	32.6 ±2.2	217
5	(1.493 ±0.038)E-28	(3.32 ±0.13)E-18	25620±360	41.2 ±3.1	170

B. Fits of Average Energy for $NO_2^{\bullet}$-NO_2 Excited at 435.04 nm

Equation 3-12:

n	m	b	$\langle E \rangle_0$/cm^{-1}	$k_E/10^{-8}$ cm^{-1}cm^{3}s^{-1}	χ^2
0	-(1.030 ±0.098)E-7	(2.214 ±0.020)E4	22140±200	10.30 ±0.98	602
1	-(5.38 ±0.45)E-12	10.013 ±0.009	22310±200	12.0 ±1.0	468
2	(2.79 ±0.20)E-16	(4.440 ±0.047)E-5	22520±240	14.1 ±1.2	408
3	(2.87 ±0.18)E-20	(1.935 ±0.040)E-9	22740±230	16.9 ±1.2	326
4	(2.20 ±0.12)E-24	(8.25 ±0.25)E-14	22970±240	20.4 ±1.4	256
5	(1.482 ±0.068)E-28	(3.44 ±0.15)E-18	23220±250	25.0 ±1.8	204

Table 3-4 continued

C. Fits of Average Energy for NO_2^*-NO_2 Excited at 475.34 nm

n	Equation 3-12: m	b	$\langle E \rangle_0$/cm^{-1}	$k_E/10^{-8}$ cm^{-1}cm^{3}s^{-1}	χ^2
0	-(1.035 ±0.071)E-7	(2.058 ±0.011)E4	20580±110	10.35 ±0.71	348
1	-(5.65 ±0.36)E-12	9.937 ±0.006	20690±110	11.68 ±0.75	304
2	(3.07 ±0.18)E-16	(4.807 ±0.037)E-5	20800±160	13.28 ±0.81	274
3	(3.32 ±0.18)E-20	(2.283 ±0.035)E-9	20930±160	15.24 ±0.89	243
4	(2.69 ±0.13)E-24	(1.069 ±0.026)E-13	21070±170	17.7 ±1.0	216
5	(1.920 ±0.082)E-28	(4.93 ±0.18)E-18	21230±190	20.7 ±1.3	195

D. Fits of Average Energy for NO_2^*-NO_2 Excited at 532.00 nm

n	Equation 3-12: m	b	$\langle E \rangle_0$/cm^{-1}	$k_E/10^{-8}$ cm^{-1}cm^{3}s^{-1}	χ^2
0	-(6.92 ±0.66)E-8	(1.859 ±0.024)E4	18590±240	6.92 ±0.66	796
1	-(4.11 ±0.38)E-12	9.835 ±0.013	18670±250	7.68 ±0.71	735
2	(2.44 ±0.21)E-16	(5.332 ±0.071)E-5	18750±250	8.57 ±0.79	671
3	(2.88 ±0.24)E-20	(2.817 ±0.076)E-9	18840±250	9.63 ±0.89	609
4	(2.54 ±0.20)E-24	(1.473 ±0.060)E-13	18940±260	10.9 ±1.0	549
5	(1.99 ±0.15)E-28	(7.62 ±0.42)E-18	19040±260	12.4 ±1.3	492

Table 3-5

Collisional Energy Transfer Rate Constants for NO_2^*

Versus Excitation Energy

nominal λ / nm	measured λ / nm	excitation energy / cm^{-1}	Linear fit k_E / 10^{-8} cm^{-1} cm^3 s^{-1}	$\langle E \rangle^{-3}$ fit k_E / 10^{-8} cm^{-1} cm^3 s^{-1}
400.00	400.17	24989	14.6 ± 1.5	32.6 ± 2.2
435.04	435.20	22978	10.30 ± 0.98	20.4 ± 1.4
475.34	475.57	21027	10.35 ± 0.71	17.7 ± 1.0
532.00	531.13	18828	6.92 ± 0.66	10.9 ± 1.0

Figure Captions

Figure 3-1. Apparatus for this experiment. Note the addition of the total intensity photomultiplier tube and the differences in electronics.

Figure 3-2. Spectral responsivity for the fluorescence collection system over the wavelength range 380-820 nm.

Figure 3-3. Ensemble average energy $<E>$ versus NO_2^*-NO_2 hard-sphere collision number for excitation at 475.34 nm. The dashed line is a linear fit of $<E>$ to the concentration-delay time product (Equation 3-1), and the solid line is a fit of $<E>^{-3}$ to concentration-time product (Equation 3-2).

Figure 3-4. Log-log plot of the energy spread versus NO_2^* hard-sphere collision number for 475.34 nm excitation. The line is the linear fit to these points (Equation 3-3).

Figure 3-5. $<E>$ versus NO_2^*-NO_2 hard-sphere collision number for excitation at 435.04 nm. The linear fit (Equation 3-4) is the dashed line, and the $<E>^{-3}$ fit (Equation 3-5) is the solid line.

Figure 3-6. Log-log plot of the energy spread versus NO_2^* hard-sphere collision number for 435.04 nm excitation. The linear fit of Equation 3-6 is given by the line.

Figure 3-7. $<E>$ versus NO_2^*-NO_2 hard-sphere collision number for excitation at 400.00 nm. The dashed line corresponds to the linear fit in Equation 3-7, and the solid line represents the $<E>^{-3}$ fit in Equation 3-8.

Figure 3-8. Log-log plot of the energy spread versus NO_2^* hard-sphere collision number for 400.00 nm excitation. The line shows the linear fit in Equation 3-9.

Figure 3-9. Initial energy transfer rate constants k_E versus excitation energy X_L. Filled squares represent k_E obtained from the $<E>^{-3}$ fits, while hollow squares show the k_E in the linear fits. The dotted line shows the weighted linear least squares fit of k_E to X_L (Equation 3-16), the dashed line represents the linear fit of k_E to X_L^4 (Equation 3-17), and the solid line is the linear fit of ln k_E to X_L (Equation 3-18).

Figure 3-1

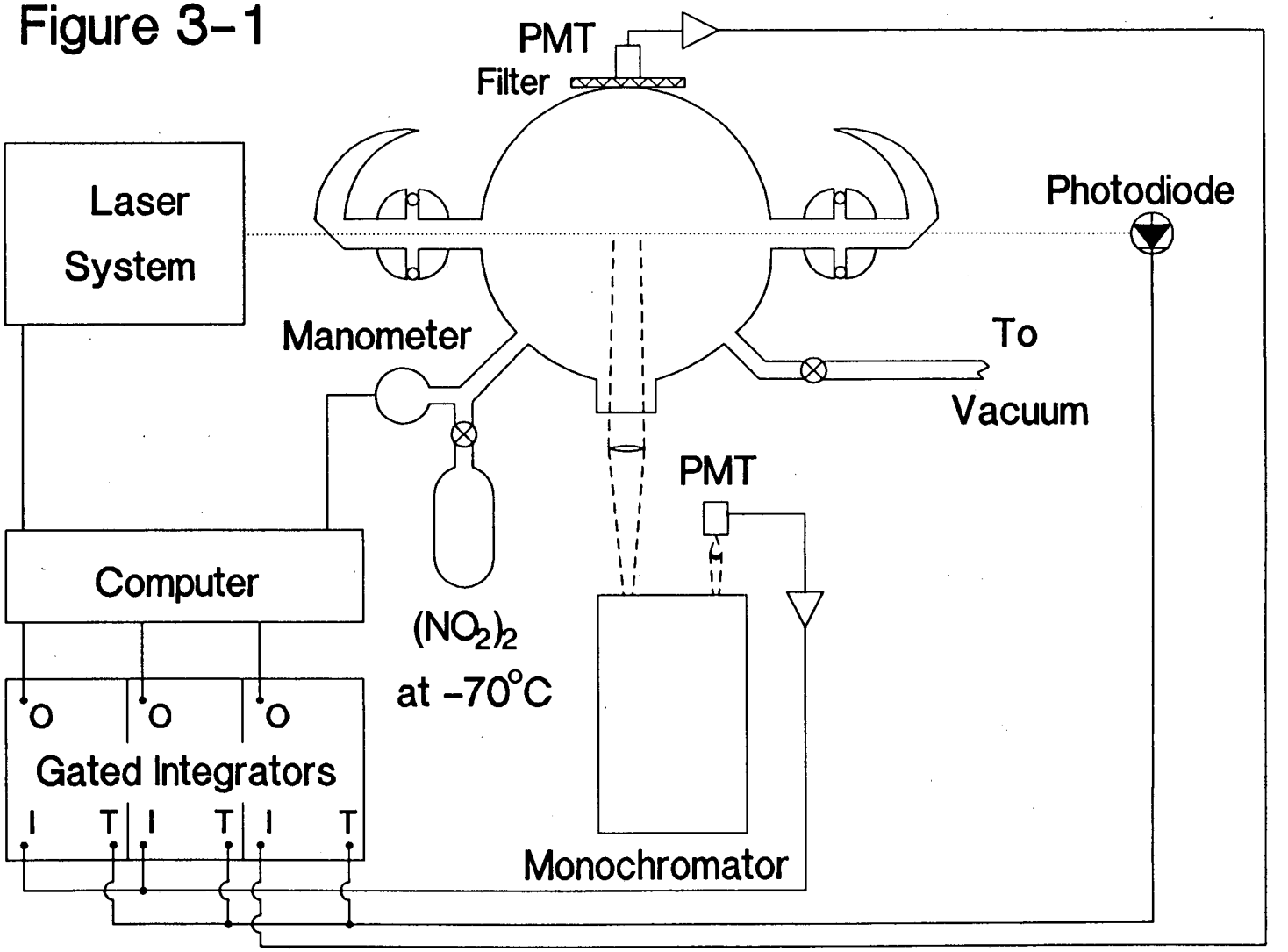
PMT
Filter
Laser System
Photodiode
Manometer
To Vacuum
PMT
Computer
$(NO_2)_2$ at -70°C
Gated Integrators
I T I T I T
Monochromator

Figure 3-2

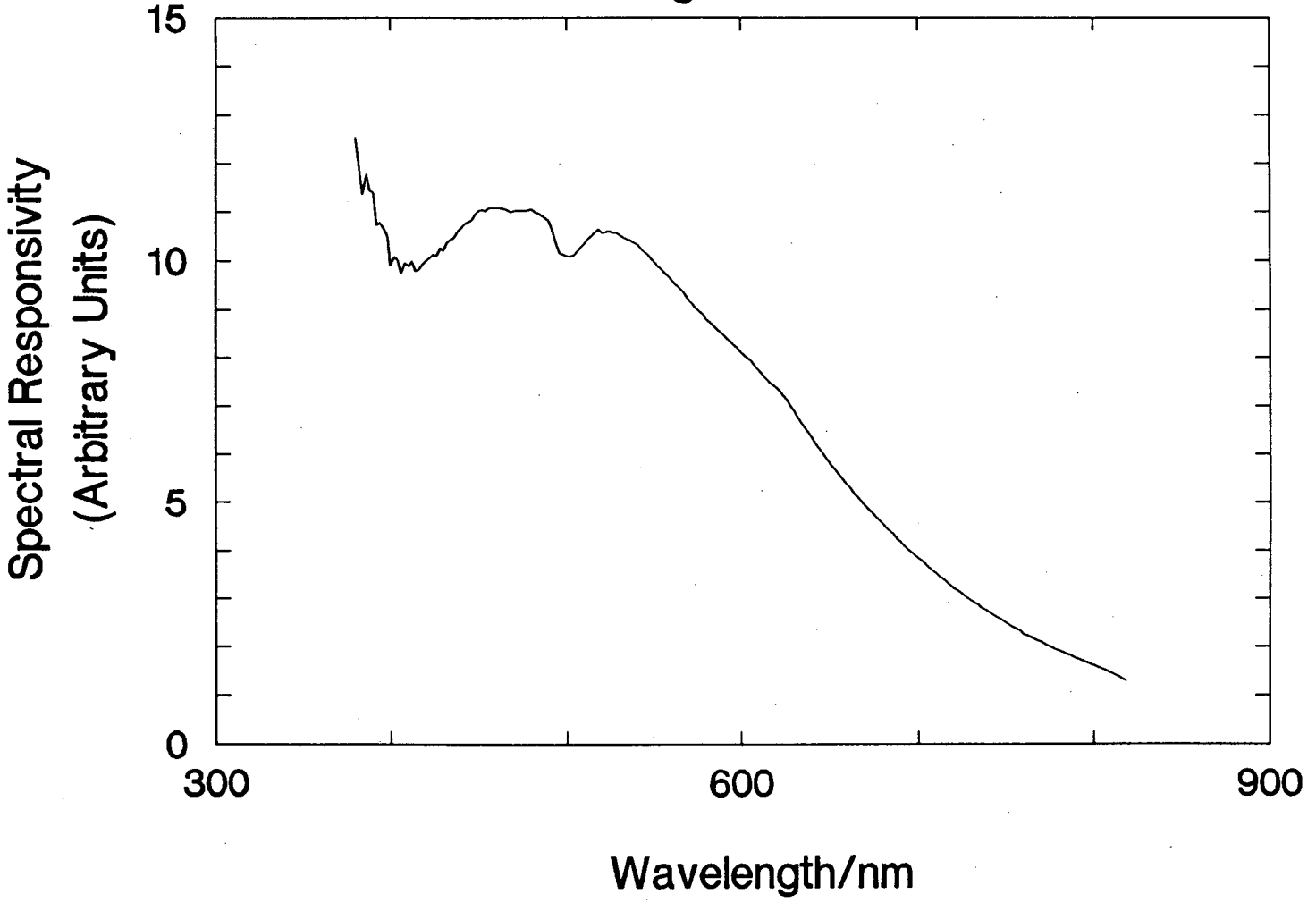
15
10
5
0
300
600
900
Spectral Responsivity
(Arbitrary Units)
Wavelength/nm

Figure 3-3

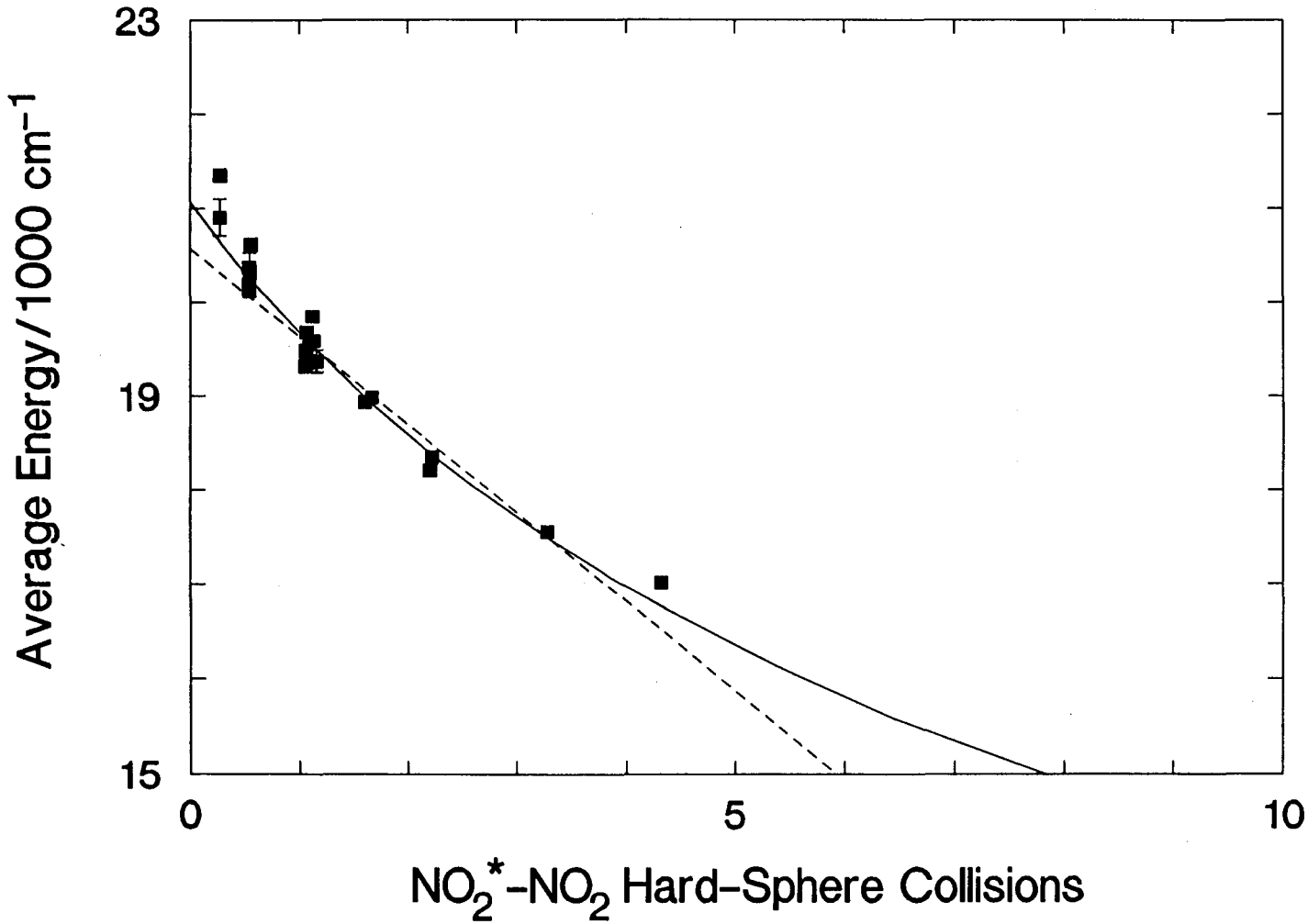
23
19
15
0
5
10
Average Energy/1000 cm^{-1}
NO_2^*-NO_2 Hard-Sphere Collisions

Figure 3-4

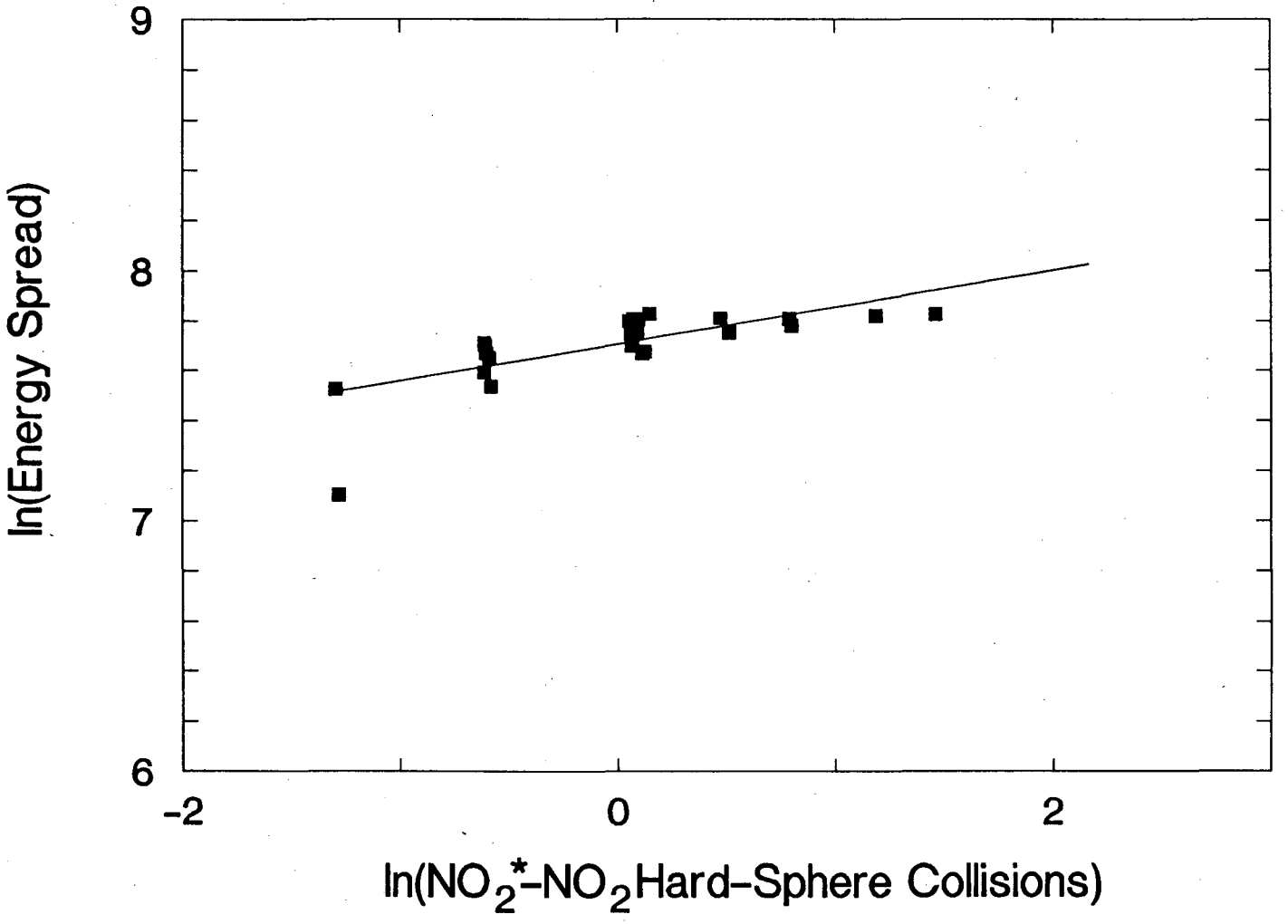

Figure 3-5

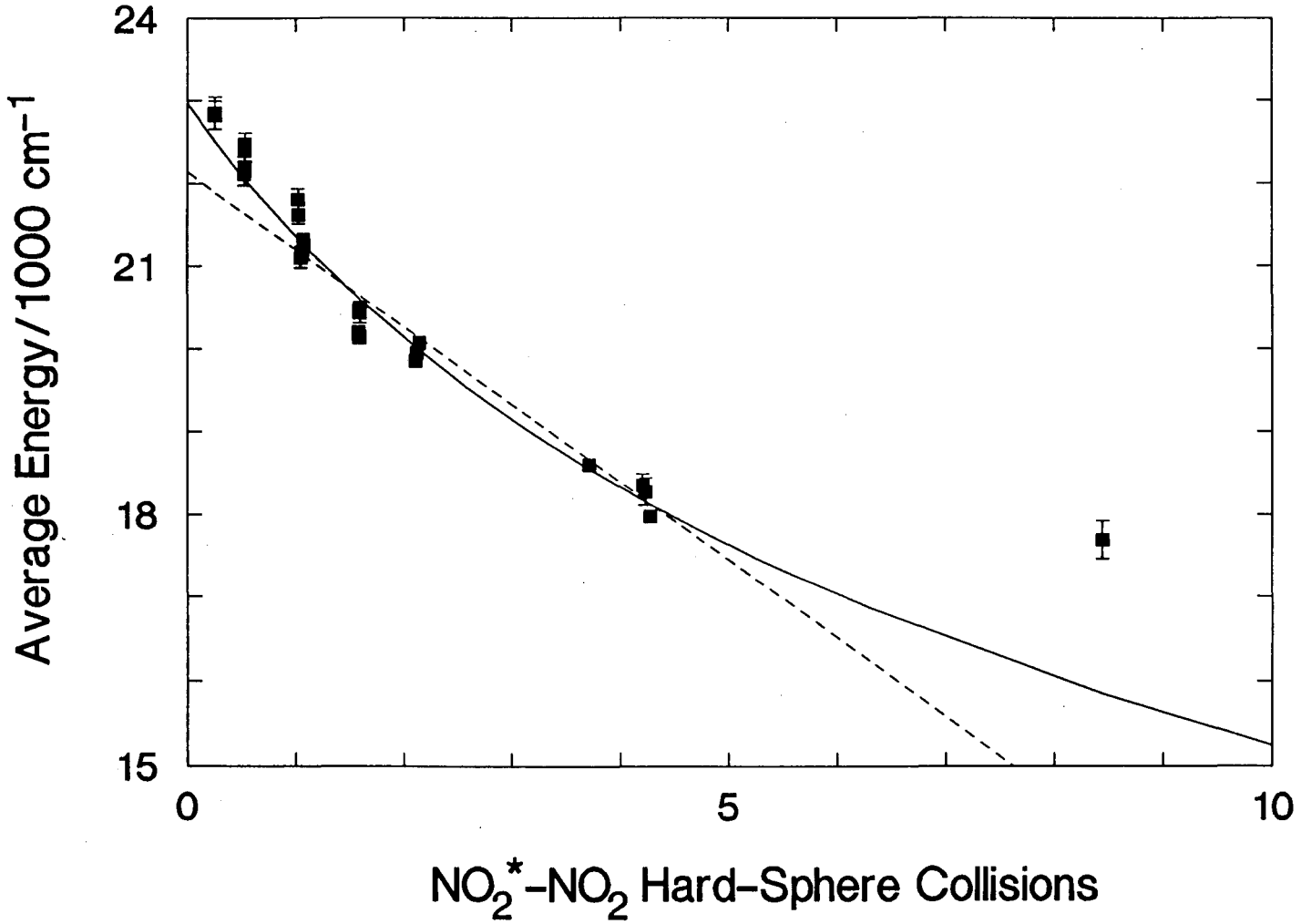
24
21
18
15
0
5
10
Average Energy/1000 cm^{-1}
NO_2^*-NO_2 Hard-Sphere Collisions

Figure 3-6

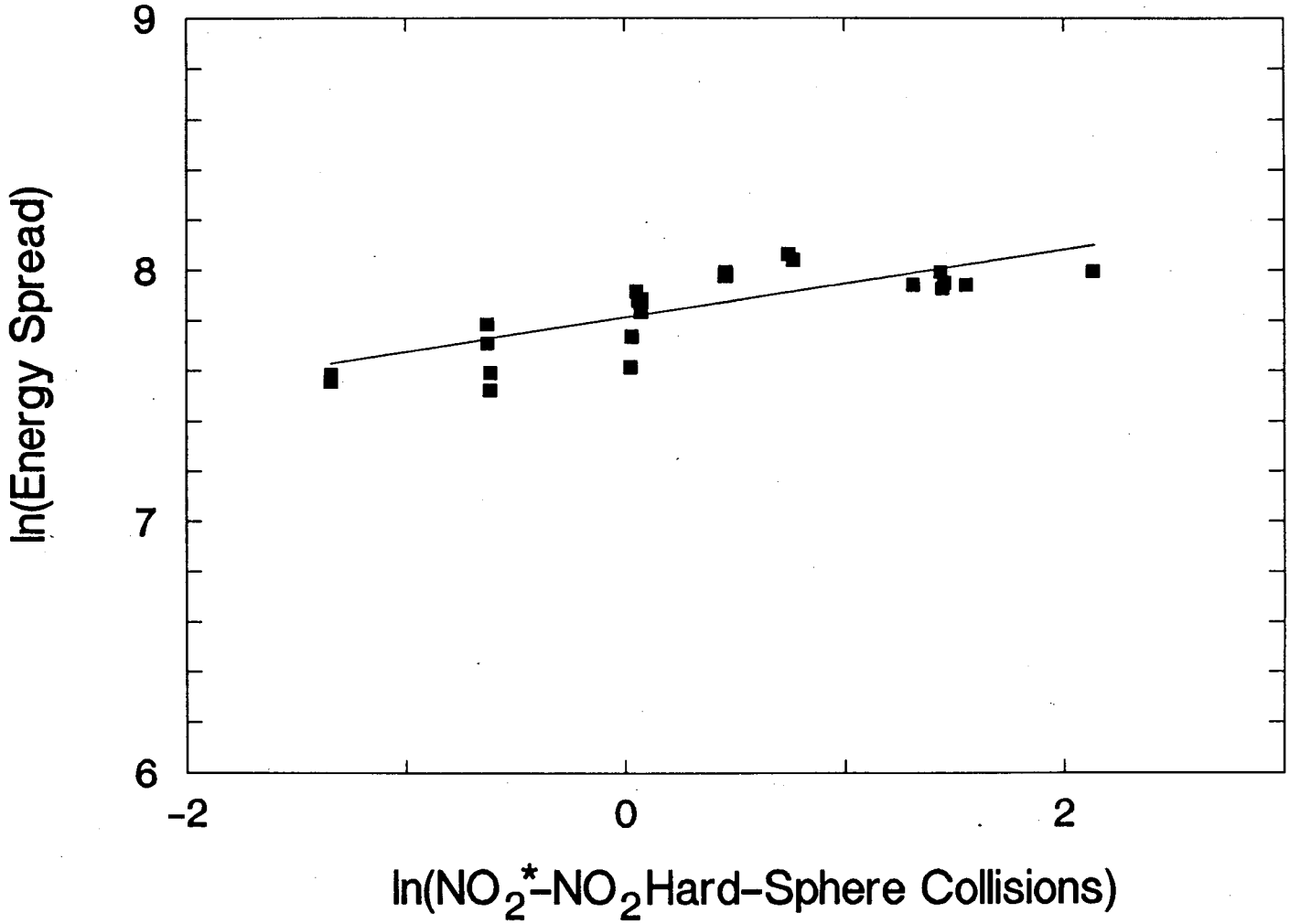

Figure 3-7

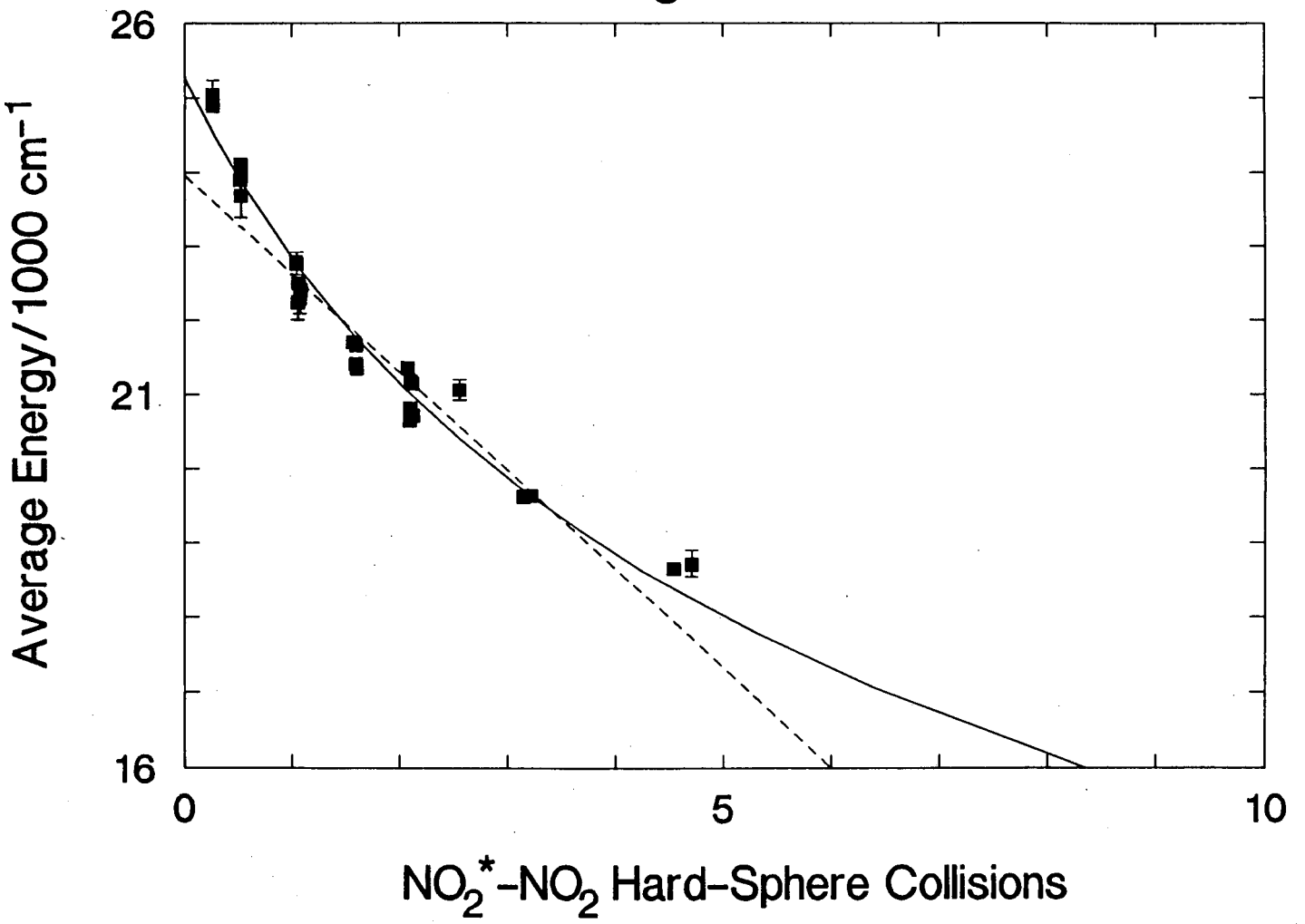
26
21
16
0
5
10
Average Energy/1000 cm^{-1}
NO_2^*-NO_2 Hard-Sphere Collisions

Figure 3-8

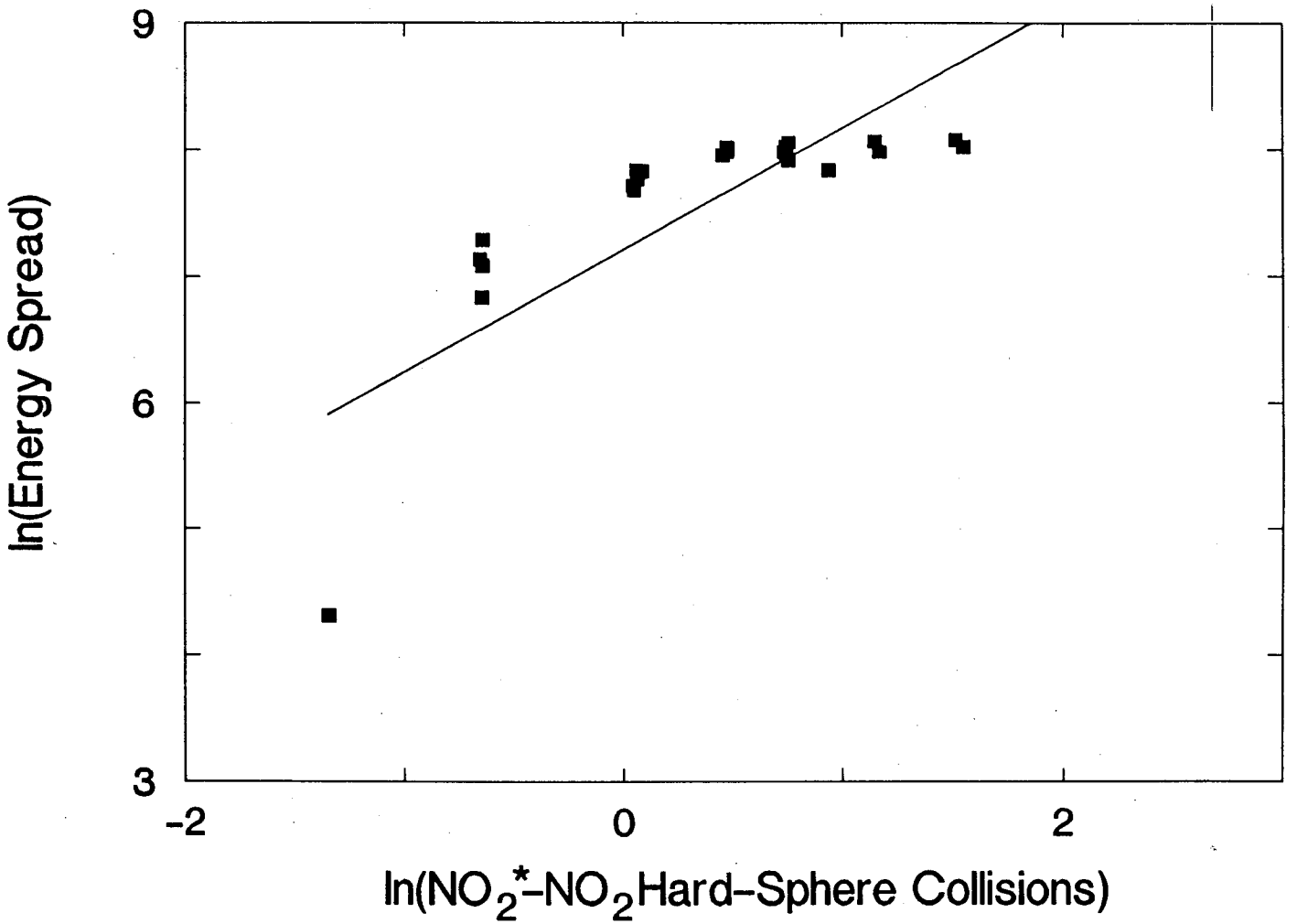

Figure 3-9

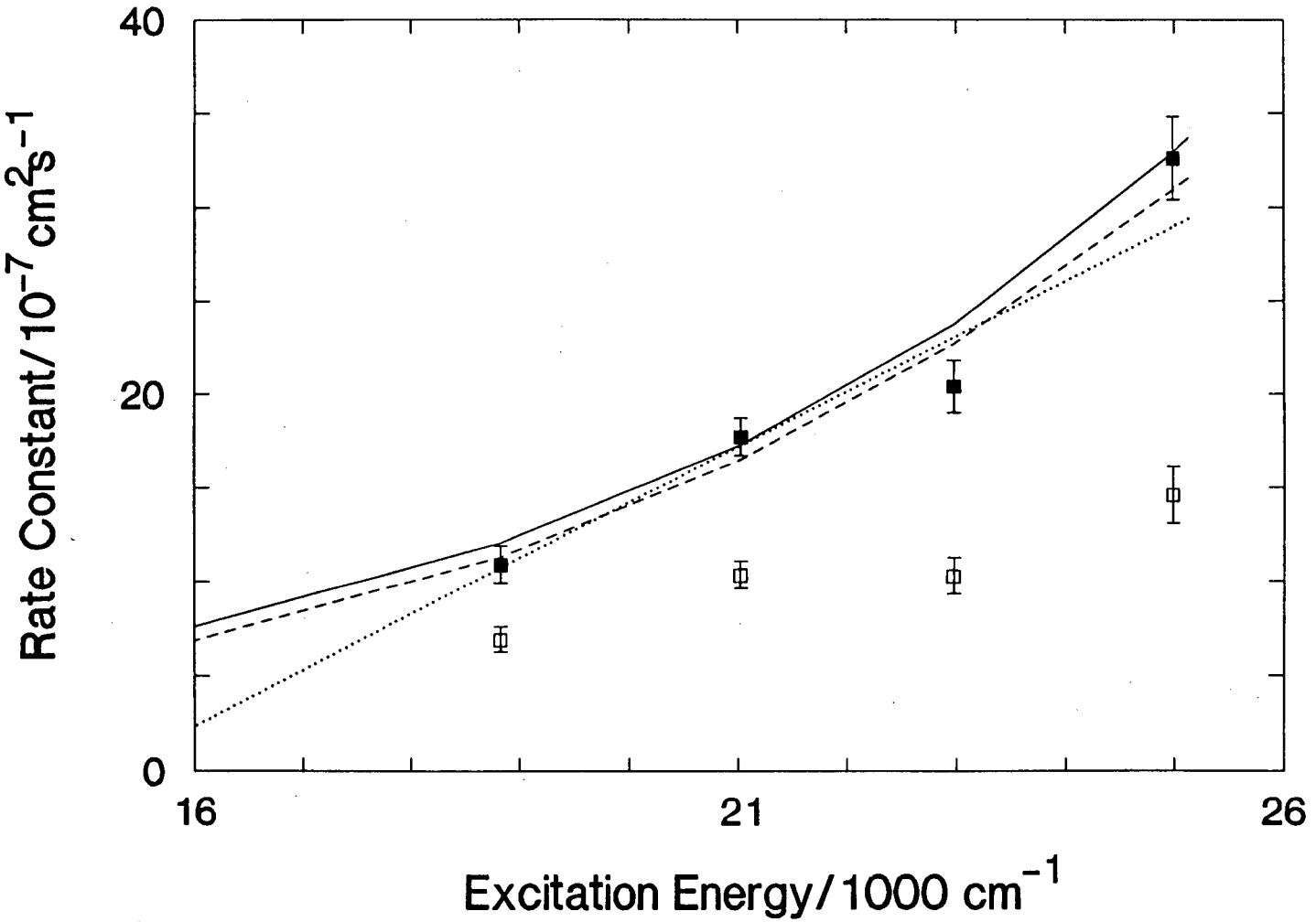
40
20
0
16
21
26
Rate Constant/10^{-7} cm^2s^{-1}
Excitation Energy/1000 cm^{-1}

References

[1]G. Herzberg Molecular Spectra and Molecular Structure I. Spectra of Diatomic Molecules (Van Nostrand Reinhold Company; New York, New York; 2nd. edition; 1950).

[2]G. Herzberg Molecular Spectra and Molecular Structure III. Electronic Spectra and Electronic Structure of Polyatomic Molecules (Van Nostrand Reinhold Company; New York, New York; 1966).

[3]"The Electronic Structure of Nitrogen Dioxide. I. Multiconfiguration Self-Consistent-Field Calculation of the Low-Lying Electronic States" G. D. Gillispie, A. U. Khan, A. C. Wahl, R. P. Hosteny, M. Krauss J. Chem. Phys. **63**, 3425-44 (1975).

[4]"Ultraviolet Photoelectron Spectrum of NO_2^-" K. M. Ervin, J. Ho, W. C. Lineberger J. Phys. Chem. **1988**, 5405-12 (1988).

[5]"Observation of the $\tilde{A}(^2B_2)$ and $\tilde{C}(^2A_2)$ States of NO_2 by Negative Ion Photoelectron Spectroscopy of NO_2^-" A. Weaver, R. B. Metz, S. E. Bradforth, D. M. Neumark J. Chem. Phys. **90**, 2070-1 (1989).

[6]"The $^2B_1 \leftarrow {}^2A_1$ System of Nitrogen Dioxide" J. L. Hardwick and J. C. D. Brand Chem. Phys. Lett. **21**, 458-61 (1973).

[7]"Anomalously Long Radiative Lifetimes of Molecular Excited States" A. E. Douglas J. Chem. Phys. **45**, 1007-15.

[8]"Long Radiative Lifetimes of Small Molecules" M. Bixon and J. Jortner J. Chem. Phys. **50**, 3284-90.

[9]D. K. Hsu, D. L. Monts, R. N. Zare Spectral Atlas of Nitrogen Dioxide 5530-6480 Å (Academic Press; New York, New York; 1978).

[10]"The Fluorescence Excitation Spectrum of Rotationally Cooled NO_2" R. E. Smalley, L. Wharton, D. H. Levy J. Chem. Phys. **63**, 4977-89 (1975).

[11]"Laser Spectroscopy of NO_2 Under Very High Resoluation: Fluorescence Spectra from Selectively Excited hfs Levels" R. Schmiedl, I. R. Bonilla, F. Paech, W. Demtröder J. Mol. Spectrosc. **68**, 236-52 (1977).

[12]"Quantum Ergodicity in Small Molecules: The Continuum Fluorescence of Nitrogen Dioxide" J. L. Hardwick J. Mol. Spectrosc. **109**, 85-98 (1985).

[13]"Absorption Cross Sections of NO_2 in the UV and Visible Region (200 - 700 nm) at 298 K" W. Schneider, G. K. Moortgat, G. S. Tyndall, J. P. Burrows J. Photochem. Photobio. A **40**, 195-217 (1987).

[14]"Rotational Analysis of the NO_2 6125-Å Region" D. L. Monts, B. Soep, R. N. Zare J. Mol. Spectrosc. **77**, 402-28 (1979).

[15]"Analysis of the Perturbed NO_2 $^2B_2 \leftarrow {}^2A_1$ System in the 591.4- to 592.9-nm Region Based on Sub-Doppler Laser Spectroscopy" H. J. Vedder, M. Schwarz, H.-J. Foth, W. Demtröder J. Mol. Spectrosc. **97**, 92-116 (1983).

[16]"Rotational Analyses and Vibrational Assignments of the 463- and 474-nm Bands of NO_2" N. Sugimoto and S. Takezawa J. Mol. Spectrosc. **106**, 307-19 (1984).

[17]"A Study of Electronically Excited Nitrogen Dioxide in its First Predissociation Region: Fluorescence Emission, Lifetimes, and Electronic Quenching" W. M. Uselman and E. K. C. Lee J. Chem. Phys. **64**(8), 3457-62 (1976).

[18]"Primary Quantum Yields of NO_2 Photodissociation" E. P. Gardner, P. D. Sperry, J. G. Calvert J. Geophys. Res. **92**, 6642-52 (1987).

[19]"Fluorescence of Nitrogen Dioxide" D. Neuberger and A. B. F. Duncan J. Chem. Phys. **22**, 1693-6 (1954).

[20]"Kinetics of Nitrogen Dioxide Fluorescence" S. E. Schwartz and H. S. - Johnston J. Chem. Phys. **51**, 1286-1302 (1969).

[21]"Dynamics of NO_2 Excited States Excited by a Tunable Dye Laser" P. B. Sackett and J. T. Yardley J. Chem. Phys. **57**, 152-67 (1972).

[22]"Fluorescence Lifetime Studies of NO_2. II. Dependence of the Perturbed $^2B_2$ State Lifetimes on Excitation Energy" V. M. Donnelly and F. Kaufman J. Chem. Phys. **69**, 1456-60 (1978).

[23]"Radiative Lifetimes of Nitrogen Dioxide for Excitation Wavelengths from 400 to 750 nm" K. O. Patten, Jr., J. D. Burley, H. S. Johnston J. Phys. Chem. **94**(20), 7960-9 (1990).

[24]"Intensities of Electronic Transitions in Molecular Spectra. I. Introduction" R. S. Mulliken J. Chem. Phys. **7**, 14-20 (1939).

[25]"Collision-Free Lifetimes of Selectively Excited Levels in the $^2B_2$-$^2A_1$ System of NO_2" G. Persch, H. J. Vedder, W. Demtröder Chem. Phys. **105**, 471-9 (1986).

[26]"Photochemical Equilibrium in Nitrogen Peroxide. Part IV. The Relation Between Fluorescence and Chemical Action" R. G. W. Norrish J. Chem. Soc. **1929**, 1611-21.

[27]"Quenching of the Fluorescence of Nitrogen Dioxide" P. W. Baxter J. Am. Chem. Soc. **52**, 3920-7 (1930).

[28]"Messung der Lebensdauer von angeregtem NO_2" O. Heil Z. Phys. **77**, 563-6 (1932).

[29]"Radiative Lifetime and Collisional Quenching of NO_2 Fluorescence and Nature of the Air Afterglow" L. F. Keyser, F. Kaufman, E. C. Zipf Chem. Phys. Lett. **2**, 523-5 (1968).

[30]"Spectral Study of NO_2 Fluorescence Excited by 11 Lines of Argon and Krypton Ion Lasers" K. Sakurai and H. P. Broida J. Chem. Phys. **50**, 2404-10 (1969).

[31]"Kinetics and Mechanism of NO_2 Fluorescence" L. F. Keyser, S. Z. Levine, F. Kaufman J. Chem. Phys. **54**, 355-63 (1971).

[32]"Lifetime Measurement of NO_2 by Dye Laser Excitation" K. Sakurai and G. Capelle J. Chem. Phys. **53**, 3764-5 (1970).

[33]"Radiative Lifetime of Nitrogen Dioxide Using a Tunable Organic Dye Laser" P. B. Sackett and J. T. Yardley Chem. Phys. Lett. **6**, 323-5 (1970).

[34]"Short-Lived Fluorescence from Nitrogen Dioxide" P. B. Sackett and J. T. Yardley Chem. Phys. Lett. **9**, 612-4 (1971).

[35]"Analysis of Polyatomic Spectra Using Tunable Laser-Induced Fluorescence: Applications to the NO_2 Visible Band System" C. G. Stevens, M. W. Swagel, R. Wallace, R. N. Zare Chem. Phys. Lett. **18**, 465-9. (1973).

[36]"Lifetime of Electronically Excited NO_2: Evidence for a Short-Lived Excited State" R. Solarz and D. H. Levy J. Chem. Phys. **60**, 842-5 (1974).

[37]"Laser Fluorescence Spectroscopy and Lifetime of the $^2B_1$ (K' > 0) Electronic State of NO_2" S. E. Schwartz and G. I. Senum Chem. Phys. Lett. **32**, 569-71 (1975).

[38]"Long-Lived $K_a = 0$, $^2B_1$ States of NO_2: A Direct Measurement Using a Tunable Dye Laser" Y. Haas, P. L. Houston, J. H. Clark, C. B. Moore, H. Rosen, P. Robrish J. Chem. Phys. **63**, 4195-7 (1975).

[39]"Ruby Laser Induced Emission from NO_2" D. F. Hakala and R. R. Reeves Chem. Phys. Lett. **38**, 510-5 (1976).

[40]"Fluorescence Lifetime Studies of NO_2. I. Excitation of the Perturbed $^2B_2$ State Near 600 nm" V. M. Donnelly and F. Kaufman J. Chem. Phys. **66**, 4100-10 (1977).

[41]"Fluorescence Lifetime Studies of NO_2. III. Mechanism of Fluorescence Quenching" V. M. Donnelly, D. G. Keil, F. Kaufman J. Chem. Phys. **71**, 659-73 (1979).

[42]"Fluorescence Lifetime Studies of NO_2. IV. Temperature Dependence of Fluorescence Spectra and of Collisional Quenching of Fluorescence" D. G. Keil, V. M. Donnelly, F. Kaufman J. Chem. Phys. **73**, 1514-20 (1980).

[43]"Collision Free Lifetimes of Excited NO_2 Under Very High Resolution" F. Paech, R. Schmiedl, W. Demtröder J. Chem. Phys. **63**, 4369 (1975).

[44]"Studies of Lifetimes of Rotationally Cooled NO_2 Using Time-Resolved Fluorescence Excitation Spectra" C. H. Chen, S. D. Kramer, D. W. Clark, M. G. Payne Chem. Phys. Lett. **65**, 419-24 (1979).

[45]"Lifetimes of Electronically Excited NO_2 in a Collision-Free Differentially Pumped Supersonic Molecular Beam" O. Cheshnovsky and A. Amirav Chem. Phys. Lett. **109**, 368-73 (1984).

[46]"Photodissociation of NO_2 - X (X = ClO, NO3, Cl) Molecules" D. Oh, Ph.D. Thesis, University of California-Berkeley (1988).

[47]"Nitrogen Dioxide Fluorescence from N_2O_5 Photolysis" D. Oh, W. Sisk, A. Young, H. Johnston J. Chem. Phys. **85**, 7146-59 (1986).

[48]G. W. Castellan Physical Chemistry, 3rd. ed. (Addison-Wesley; Reading, Massachusetts; 1983).

[49]Asyst Software Technologies; Rochester, New York (1987).

[50]"Über die Abklingungszeit der Fluoreszenz" O. Stern and M. Volmer Physik. Z. **20**, 183-8 (1919).

[51]"Accurate and Facile Approximation for Vibrational Energy-Level Sums" G. Z. Whitten and B. S. Rabinovich J. Chem. Phys. **38**, 2466-73 (1963).

[52]"Vibronic Level Density of Excited NO_2-States and its Statistical Analysis" G. Persch, E. Mehdizadeh, W. Demtröder, Th. Zimmermann, H. Köppel, L. S. Cederbaum Ber. Bunsenges. Phys. Chem. **92**, 312-8 (1988).

[53]"Diode Laser Probing of the High-Frequency Vibrational Modes of Baths of CO_2, N_2O, and CO Excited by Relaxation of Highly Excited NO_2" J. Z. Chou, S. A. Hewitt, J. F. Hershberger, B. B. Brady, G. B. Spector, L. Chia, G. W. Flynn J. Chem. Phys. **91**, 5392-401 (1989).

[54]"Time-Dependent Thermal Lensing Measurements of V-T Energy Transfer from Highly Excited NO_2" B. M. Toselli, T. L. Walunas, J. R. Barker J. Chem. Phys. **92**, 4793-804 (1990).

[55]"Internal Energy Distribution of Nitrogen Dioxide from Fluorescence. I. Method and N_2O_5 Photolysis Induced Fluorescence at 248.5 nm" H. S. Johnston, C. E. Miller, B. Y. Oh, K. O. Patten, Jr., W. N. Sisk; to be submitted for publication.

[56]"A New Determination of the Emissivity of Tungsten Ribbon" J. C. DeVos Physica **XX**, 690-714 (1954).

[57]"Spectral Emissivity of Tungsten: Analytic Expressions for the 340-nm to 2.6 μm Spectral Region" R. M. Pon and J. P. Hessler Appl. Opt. **23**, 975-6 (1984).

[58]W. H. Press, B. P. Flannery, S. A. Teukolsky, W. T. Vettering Numerical Recipes: The Art of Scientific Computing (Cambridge University Press; Cambridge, England) 1989.

[59]"Effects of Wavelength and Temperature on Primary Processes in the Photolysis of Nitrogen Dioxide and a Spectroscopic-Photochemical Determination of the Dissociation Energy" J. N. Pitts, Jr., J. H. Sharp, S. I. Chan J. Chem. Phys. **42**, 3655-62 (1964).

[60]H. S. Johnston Gas Phase Reaction Rate Theory (Ronald Press Company; New York, New York) 1966.

[61]J. T. Yardley Introduction to Molecular Energy Transfer (Academic Press; New York, New York) 1980.

[62]"Theory of Thermal Unimolecular Reactions at Low Pressures. I. Solutions of the Master Equation" J. Troe J. Chem. Phys. **66**, 4745-57 (1977).

[63]"Modeling Collisional Energy Transfer in Highly Excited Molecules" K. F. Lim and R. G. Gilbert J. Chem. Phys. **92**, 1819-30 (1990).

[64]J. O. Hirschfelder, C. F. Curtiss, R. B. Bird Molecular Theory of Gases and Liquids (John Wiley and Sons, Inc.; New York, New York) 1954.

[65]G. Herzberg Molecular Spectra and Molecular Structure II. Infrared and Raman Spectra of Polyatomic Molecules (Van Nostrand Reinhold Company; New York, New York) 1945.

[66]K.-P. Huber and G. Herzberg Molecular Spectra and Molecular Structure IV. Constants of Diatomic Molecules (Van Nostrand Reinhold Company; New York, New York) 1979.

[67]"Selected Values of Electric Dipole Moments for Molecules in the Gas Phase" R. D. Nelson, Jr., D. R. Lide, Jr., A. A. Maryott National Reference Data Series-National Bureau of Standards 10 (U. S. Government Printing Office; Washington, D. C.) as abstracted in CRC Handbook of Chemistry and Physics, R. C. Weast ed. (Chemical Rubber Company; West Palm Beach, Florida), 59th edition, 1978, pages E-63 to E-66.

[68]"Dielectric Constants of Imperfect Gases. III. Atomic Gases, Hydrogen, and Nitrogen" R. H. Orcutt and R. H. Cole J. Chem. Phys. **46**, 697-702 (1967).

[69]J. D. Lambert Vibrational and Rotational Relaxation in Gases (Clarendon Press; New York, New York) 1977.

[70]based on Van der Waals b values in the Landolt-Bornstein Physical Chemical Tables as abstracted in CRC Handbook of Chemistry and Physics, 59th ed., 1978, p. D-230.

[71]"Force Constants of N_2O_4 and NO_2 and the Viscosity of the Dissociating System $N_2O_4 \rightleftarrows 2NO_2$" A. K. Barua and T. K. RaiDastidar J. Chem. Phys. **43**, 4140-2 (1965).

[72]"Equilibrium and Transport Properties of Eleven Polyatomic Gases at Low Density" A. Boushehri, J. Bzowski, J. Kestin, E. A. Mason J. Phys. Chem. Ref. Data **16**, 445-66 (1987).

[73]"The Resonance Fluorescence and Absorption Spectrum of Nitrogen Dioxide" J. C. D. Brand, J. L. Hardwick, R. J. Pirkle, C. J. Seliskar Can. J. Phys. **51**, 2184-8 (1973).

[74]"Direct Study of Energy Transfer of Vibrationally Highly Excited CS_2 Molecules" J. E. Dove, H. Hippler, J. Troe J. Chem. Phys. **82**, 1907-19 (1985).

[75]"UV Absorption Study of Collisional Energy Transfer in Vibrationally Highly Excited SO_2 Molecules" H. Hippler, D. Nahr, H. J. Plach, J. Troe J. Phys. Chem. **92**, 5507-14 (1988).

[76]"Collisional Energy Transfer of Vibrationally Highly Excited Molecules. VI. Energy Dependence of $<\Delta E>$ in Azulene" H. Hippler, B. Otto, J. Troe Ber. Bunsenges. Phys. Chem. **93**, 428-34 (1989).

LAWRENCE BERKELEY LABORATORY
UNIVERSITY OF CALIFORNIA
INFORMATION RESOURCES DEPARTMENT
BERKELEY, CALIFORNIA 94720